

# **CHARACTERISATION OF SELECT NANOFLUID AND VEGETABLE OIL QUENCHANTS AND ASSESSMENT OF HEAT TRANSFER DURING QUENCH HARDENING OF STEELS**

Thesis

Submitted in partial fulfilment of the requirements for the degree of

**DOCTOR OF PHILOSOPHY**

by

**VIGNESH NAYAK ULLAL**



**DEPARTMENT OF METALLURGICAL AND MATERIALS  
ENGINEERING**

**NATIONAL INSTITUTE OF TECHNOLOGY KARNATAKA,  
SURATHKAL, MANGALORE – 575025**

**MAY, 2018**



## **DECLARATION**

*By the Ph.D. Research Scholar*

I hereby declare that the Research Synopsis entitled “**CHARACTERISATION OF SELECT NANOFUID AND VEGETABLE OIL QUENCHANTS AND ASSESSMENT OF HEAT TRANSFER DURING QUENCH HARDENING OF STEELS**” which is being submitted to the National Institute of Technology Karnataka, Surathkal in partial fulfillment of the requirements for the award of the Degree of Doctor of Philosophy in **Metallurgical and Materials Engineering** is a bonafide report of the research work carried out by me. The material contained in this Research Thesis has not been submitted to any University or Institution for the award of any degree.

135029MT13F03, **VIGNESH NAYAK U**

Department of Metallurgical and Materials Engineering

**Place** : **Mangalore**

**Date** :





## C E R T I F I C A T E

This is to certify that the Research Synopsis entitled “**CHARACTERISATION OF SELECT NANOFLUID AND VEGETABLE OIL QUENCHANTS AND ASSESSMENT OF HEAT TRANSFER DURING QUENCH HARDENING OF STEELS**” submitted by **Mr. Vignesh Nayak Ullal (Register Number: 135029MT13F03)** as the record of the research work carried out by him, is accepted as the Research Thesis submission in partial fulfillment of the requirements for the award of degree of **Doctor of Philosophy**.

Dr. K. Narayan Prabhu

Research Guide

(Signature with Date and Seal)

Chairman-DRPC

(Signature with Date and Seal)

## **ACKNOWLEDGEMENTS**

First and foremost, I want to thank Dr. K Narayan Prabhu. It has been an honour to do my Ph.D. under him. He has taught me how quenching experiments are done and its nuances. I appreciate the support, motivation, cooperation and most of all his time, ideas to make my Ph.D. project worth remembering for a life time. I also thank him for providing me the excellent experimental facilities during my research investigation. His professional attitude and human qualities serve as a benchmark to me.

I thank Dr. Jagannath Nayak, Professor and former head and Dr. Udaya Bhat K., Associate Professor and ex-head for providing excellent laboratory facilities. I also thank Dr. Anandhan Srinivasan, Associate Professor and present head, Department of Metallurgical and Materials Engineering, NITK, Surathkal for his support and help.

I would like to acknowledge my gratitude to my RPAC members: Dr. A. O. Surendranathan, Professor, Department of Metallurgical and Materials Engineering and Dr. Amba Shetty, Associate Professor, Department of Applied Mechanics, NITK, Surathkal for their valuable suggestions during the research work.

I am grateful to NITK for providing an opportunity to carry out my doctoral study in the Department of Metallurgical and Materials Engineering. I thank all faculty members of the Department who taught and helped me.

I thank Dr. K. Rajendra Udupa, Professor, Department of Metallurgical and Materials for permitting me to use the SEM.

I thank Dr. Gangadharan K V, Professor, Department of Mechanical Engineering and Mr. Praveen Shenoy of the SOLVE lab, NITK, Surathkal for providing the data logger.

I thank the Science and Engineering Research Board (SERB), Department of Science and Technology (DST), New Delhi, India for the research project.

I am also obliged to Mr. Vasant, Mrs. Sharmila, Mr. Sundar Shettigara, Mrs. Vinaya, for their help during the course of my work.

I especially thank Mr. Dinesh for drilling holes in steel probes and Mr. Satish for his machining services and whole-hearted help during the course of my work.

I thank our research group members Dr. Ramesh, Dr. Satyanarayan, Dr. Vijeesh, Dr. Mrunali Sona, Mr.Sudheer and Mr. Sanjay Tikale for their cooperation during the research work.

I am very much grateful to Mr. Pranesh Rao K. M. of our research group for his Matlab skills, criticisms and suggestions. I am deeply moved by his humbleness and helping nature.

Lastly, I would like to express my deepest gratitude to my parents and Late. Ullal Srinivas Nayak (Manthu) without whom I would not have pursued higher education.

Finally, I thank all those who directly / indirectly helped me to complete the research work.

**Vignesh Nayak U**

## **ABSTRACT**

The present investigation involved the characterization of nanofluids and study of heat transfer characteristics of vegetable oil quench media for heat treatment of steels. Nanoquenchants were formulated by the two-step method. The wetting kinetics and kinematics of quench media were studied by measuring the contact angle and online video imaging during quenching. CuO, MWCNT and graphene based nanofluids showed better wetting and spreading ability compared to distilled water. In nanofluids, the stabilization of the vapour phase stage resulted in low severity of quenching. Spatiotemporal heat flux transients were estimated by using a 2-D IHCP model during quenching of ISO 9950 inconel probe. The study showed increased heat extraction capabilities of graphene and MWCNT nanofluids compared to distilled water under agitated quenching conditions. Heat extraction rates were found to be lower for CuO nanofluids.

The use of edible and non-edible vegetable oils for quench hardening was investigated by comparing their heat transfer characteristics with a mineral oil. The study showed the excellent potential of non-edible vegetable oils for quench hardening of steels. Karanja oil was found to be superior compared to neem and sunflower oils. To simulate the industrial quench heat treatment, reference probes made of medium and high carbon steels were quenched and heat flux transients were estimated by taking into account the phase transformation. The cooling curves obtained with reference probes made from G 10450 and G 10900 steels showed kinks indicating enthalpy change accompanied with phase transformations during continuous cooling. This was reflected in the estimated heat flux curves. The effect of viscosity, density and surface tension of quench media on the mean peak heat flux was quantified using a power fit model. The section thickness effect on heat flux transients was examined by using probes of diameters 25 mm and 50 mm. The cooling rates measured at various locations along the cross section of reference probes of both thicknesses were related to the hardness using the Quench Factor technique. The heat transfer characteristics of the quench media, the evolved microstructure and the resulting hardness were in complete agreement.

Keyword: Nanofluids; vegetable oils; quenching; heat transfer; section thickness microstructure; hardness



## CONTENTS

<b>LIST OF FIGURES</b>	<b>i</b>
<b>LIST OF TABLES</b>	<b>xv</b>
<b>NOMENCLATURE</b>	<b>xvii</b>
<b>CHAPTER 1 INTRODUCTION</b>	<b>1</b>
1.1 Scope of the Investigation	1
1.2 Objectives of the Research Work	3
1.3 Organization of the Thesis	3
<b>CHAPTER 2 LITERATURE REVIEW</b>	<b>4</b>
2.1 Stages of Heat Transfer During Quenching	4
2.2 Variables Influencing Quenching Process	6
2.2.1 Types and characteristics of quenching media	6
2.2.1.1 Aqueous quench media	7
2.2.1.1.1 Water	7
2.2.1.1.2 Brine	8
2.2.1.1.3 Water-polymer quenchants	8
2.2.1.1.4 Carbonated water	10
2.2.1.1.5 Nanofluids	10
2.2.1.2 Oils	12
2.2.1.2.1 Mineral oil	12
2.2.1.2.2 Vegetable oils	13
2.2.1.2.2.1 Edible vegetable oils	13
2.2.1.2.2.2 Non-edible vegetable oils	17
2.2.1.3 Molten salts and metal quenchants	19

2.2.2 Characteristics of steel part	20
2.2.3 Quenching conditions	22
2.3 Assessment of Cooling Performance of Quench Media	22
2.3.1 Critical cooling parameters	23
2.3.2 Grossmann quench severity	24
2.3.3 V-value and hardening power analysis	24
2.3.4 Vs/Vc, quench uniformity analysis	25
2.3.5 Quench factor analysis	25
2.4 Interfacial Heat Flux Measurement/Computation	27
2.4.1 Lumped heat capacitance method	27
2.4.2 Temperature gradient method	28
2.4.3 Kobasko's method	28
2.4.4 Inverse heat conduction problem	29
2.5 Uniformity of Quenching	29
2.6 Summary	33
<b>CHAPTER 3 EXPERIMENTAL</b>	<b>34</b>
3.1 Quench Media	34
3.2 Quench Probe Details	35
3.3 Quenching Set-Up and Operation Details	37
3.4 Agitation Quench Set-Up	38
3.5 Measurements of Viscosity	39
3.6 Metallographic Specimen Preparation and Microstructure Examination	40
3.7 Measurement of Microhardness	41
3.8 Measurement of Thermal Conductivity	41

3.9 Density Measurements	42
3.10 Flash and Fire Point Temperature of Oils	42
3.11 Measurement of Contact Angle and Surface Tension	43
3.12 Rewetting Kinematics	44
3.13 Estimation of Interfacial Heat Flux Transients	44
<b>CHAPTER 4 RESULTS</b>	<b>50</b>
4.1 Characterisation of Liquid Quenching Media Using Inconel Probe	50
4.1.1 Un-agitated quench media	50
4.1.2 Video imaging of quenching process	51
4.1.3 Thermophysical properties of the liquid quench media	52
4.1.3.1 Thermal conductivity and viscosity of nanofluids	52
4.1.3.2 Viscosity, density, flash and fire points of oil quench media	52
4.1.4 Contact angle and spreading behaviour	54
4.1.5 Effect of agitation	55
4.2 Quenching Experiments with G 10450 and G 10900 Steel Alloys of 25 and 50 mm Section Diameters	56
4.3 Quenching Experiments with 304 SS of 25 and 50 mm Section Diameters	57
4.4 Interfacial Heat Flux Transients	58
4.5 Microstructure	59
4.6 Microhardness	61
4.6.1 G 10450 steels	61
4.6.2 G 10900 steels	62
4.7 Quench Bath Temperature	63
<b>CHAPTER 5 DISCUSSION</b>	<b>64</b>



5.1 Characterization of Liquid Quench Media Using Inconel Probe	64
5.1.1 Un-agitated quench media	64
5.1.2 Spreading behaviour of quench media on inconel and steel substrate	68
5.1.3 Spatiotemporal heat flux during quenching of inconel probe	70
5.2 Effect of Agitation on Quench Media	78
5.2.1 Spatiotemporal heat flux during quenching of inconel probe under agitated quench conditions	80
5.3 Quenching Experiments with G 10450 and G 10900 Steel Grades of Section Sizes 25 mm and 50 mm	92
5.3.1 Effect of section diameter on the interfacial heat flux transients during quenching of steels	95
5.3.2 Heat removed during quenching in oil quench media	97
5.3.3 Microstructure	988
5.3.4 Quench factor and hardness	102
5.3.5 Quench uniformity during hardening of steels	103
5.4 Quenching Experiments with 304 SS of Section Diameters of 25 and 50 mm	104
5.4.1 Heat flux transients during quenching of 25 and 50 mm section diameters of 304 stainless steel	105
<b>CHAPTER 6 CONCLUSIONS</b>	<b>107</b>
<b>REFERENCES</b>	<b>110</b>
APPENDIX A: COOLING CURVES MEASURED IN THE INCONEL PROBE DURING QUENCHING IN VARIOUS QUENCH MEDIA	117
APPENDIX B: VIDEO IMAGES OF QUENCHING PROCESS	119
APPENDIX C: CONTACT ANGLE IMAGES OF QUENCH MEDIA	121

APPENDIX D: COOLING CURVES MEASURED IN THE INCONEL PROBE DURING QUENCHING IN VARIOUS QUENCH MEDIA IN THE TENSI AGITATION SYSTEM	130
APPENDIX E: COOLING CURVES AND COOLING RATE CURVES MEASURED IN THE G 10450 STEEL OF 25 AND 50 MM SECTION DIAMETER	138
APPENDIX F: COOLING CURVES AND COOLING RATE CURVES MEASURED IN THE G 10900 STEEL OF 25 AND 50 MM SECTION DIAMETER	143
APPENDIX G: COOLING CURVES AND COOLING RATE CURVES MEASURED IN THE STAINLESS STEEL OF 25 AND 50 MM SECTION DIAMETER	148
APPENDIX H: ESTIMATED HEAT FLUX TRANSIENTS DURING QUENCHING OF INCONEL PROBE IN VARIOUS QUENCH MEDIA	153
APPENDIX I: ESTIMATED HEAT FLUX TRANSIENTS DURING QUENCHING OF INCONEL PROBE IN VARIOUS QUENCH MEDIA IN THE TENSI AGITATION SYSTEM	155
APPENDIX J: AVERAGE HEAT REMOVED WITH AVERAGE SURFACE TEMPERATURE UNDER AGITATED QUENCH MEDIUM CONDITIONS	163
<b>LIST OF PUBLICATIONS</b>	<b>166</b>
<b>BIO-DATA</b>	<b>168</b>

## List of Figures

<b>Figure No.</b>	<b>Caption</b>	<b>Page No.</b>
2.1	Stages of cooling during quenching in liquid medium	5
2.2	Categories of liquid quench media	6
2.3	Temperature measured at the centre of a silver probe of $\text{Ø}15 \times 45$ mm as a function of time during quenching in water maintained at various temperatures (Tensi and Schwalm 1980)	7
2.4	(a) Cooling curves with rapeseed oil and (b) mineral oils (Rose 1940)	14
2.5	Variation of viscosity increase with exposure time during testing for oxidation tendency of soybean oil with and without addition of various antioxidant compounds (Souza et al. 2013a)	17
2.6	Photograph of karanja tree and seeds (Karikalan and Chandrasekaran 2015)	18
2.7	Photograph of neem seeds	18
2.8	Cooling curve and cooling rate curve showing various critical cooling parameters	24
2.9	Schematic of the Liscic/Nanmac probe (Liscic et al. 2010)	28
2.10	Rewetting front motion during quenching of $\text{Ø}15$ by 45 mm steel cylinder in soybean oil (Totten et al. 1999)	30
2.11	Rewetting front photograph during quenching in (a) water and (b) carbonated water.	31
2.12	Sketch illustrating a solid substrate wetted by a sessile liquid drop	32
3.1	Flow chart showing experiments done in the present work	35
3.2	Metal quench probes (a) inconel (b) 25 mm and (c) 50 mm	36
3.3	Schematic of the pneumatic quench system	37

3.4	(a) Cooling curves and (b) cooling rates showing the effect of insulating paste on reducing heat transfer from the inconel probe during quenching in water	38
3.5	Tensi agitator	39
3.6	Photograph of Brookefield rheometer	40
3.7	Schematic of diagonal length measurements resulting from Vickers indentation	41
3.8	Photograph of KD2 pro with KS1 sensor for measuring thermal conductivity of liquid media	42
3.9	Photograph of Cleveland open cup apparatus	43
3.10	Photograph of drop shape analyzer	44
3.11	Axisymmetric model of (a) inconel (b) 25 mm and (c) 50 mm quench probe	49
4.1	Cooling curves measured in the inconel probe during quenching in distilled water	50
4.2	Video images of inconel probe obtained during quenching in distilled water	51
4.3	Viscosity behaviour of quench oils with temperature	53
4.4	Contact angle measured during spreading of 0.01 vol.% concentration of graphene nanofluids	54
4.5	Relaxation of contact angle obtained during spreading of distilled water and graphene nanofluids of various concentrations on an inconel substrate	55
4.6	Temperature vs. time plot during quenching of inconel in water under various agitation rates at thermocouple locations (a) TC(1) (b) TC(2) (c) TC(3) and TC(4)	56
4.7	Cooling curves obtained during quenching of G 10450 steel of (a) 25 mm and (b) 50 mm and G 10900 steel of (c) 25 mm and (d) 50 mm section diameters in karanja oil quench medium	57
4.8	Cooling curves measured in (a) 25 mm and (b) 50 mm SS probes during quenching in karanja oil quench medium	58

4.9	Spatiotemporal heat flux vs. surface temperature obtained during quenching of an inconel probe in distilled water	59
4.10	As-rolled microstructure of G 10450 and G 10900 steel alloys	59
4.11	Micrographs obtained from G 10450 steel at the (a) centre and (b) surface of a 25 mm section size and (c) centre and (d) surface of a 50 mm section size test piece quenched in distilled water	60
4.12	Micrographs obtained from G 10900 steel at the (a) centre and (b) surface of a 50 mm section size test piece quenched in distilled water	60
4.13	(a) Hardness profile of 25 mm and (b) 50mm section diameters of G 10450 steels and (c) average hardness bar chart of G 10450 steel of 25 and 50 mm section diameters quenched in various quench media	61
4.14	(a) Hardness profile of 25 mm and (b) 50 mm section diameters of G 10900 steels and (c) average hardness bar chart of G 10900 steel of 25 and 50 mm section diameters quenched in various quench media	62
4.15	Rise in the temperature of the (a) 4 lts. and (b) 15 lts. liquid quench media at its bulk during quenching of the steel probe	63
5.1	Cooling curves measured at the geometric centre of the inconel probe obtained during quenching in (a) MWCNT and distilled water (b) CuO and distilled water (c) graphene and distilled water and (d) oil quenching media	64
5.2	Cooling rates vs. time plot obtained at the centre of the inconel probe during quenching in (a) MWCNT and distilled water (b) CuO and distilled water (c) graphene and distilled water and (d) oil quenching media	65
5.3	Contact angle relaxation plots obtained during spreading of (a) CuO and (b) MWCNT nanofluids and (c) oil quenching media on inconel substrate	69

5.4	(a) Spreading of water and oil quench media on steel substrate and (b) dimensionless contact angle vs. dimensionless time for the spreading of oils on steel substrate	70
5.5	Relation between the mean peak heat flux and the viscosity, density and surface tension of the quench media	73
5.6	Rewetting time and temperature during quenching in (a) CuO (b) graphene and (c) MWCNT of various concentrations and (d) quench oils	73
5.7	Fraction heat removed as a function of time during quenching in (a) CuO (b) graphene and (c) MWCNT of various concentrations and (d) quench oils	74
5.8	Average heat removed vs. average surface temperature during quenching in (a) CuO (b) graphene and (c) MWCNT of various concentrations and (d) quench oils	75
5.9	Thermal profile in inconel alloy during quenching in CuO nanofluids of concentrations 0.01, 0.05, 0.1 and 1.0 vol.% (from left to right) at average surface temperature of 440 °C	76
5.10	Thermal profile in inconel alloy during quenching in CuO nanofluids of concentrations 0.01, 0.05, 0.1 and 1.0 vol.% (from left to right) at average surface temperature of 250 °C	77
5.11	Thermal profile in inconel alloy during quenching in mineral, sunflower, karanja and neem oils (from left to right) at average surface temperature of 600 °C	78
5.12	Cooling rates at critical cooling temperatures for nanofluids under (a) still (b) 500 (c) 1000 and (d) 1500 rpm agitation rates	79
5.13	Cooling rates at critical cooling temperatures for oils under (a) still (b) 500 (c) 1000 and (d) 1500 rpm agitation rates	80
5.14	Rewetting time and temperatures of quench media under still quench conditions	86
5.15	Rewetting time and temperatures of quench media at 500 rpm quench conditions	87

5.16	Rewetting time and temperatures of quench media at 1000 rpm quench conditions	88
5.17	Rewetting time and temperatures of quench media at 1500 rpm quench conditions	89
5.18	Average heat removed as a function of average surface temperature during quenching of the inconel probe in (a) MWCNT (b) graphene (c) CuO nanofluids of various concentrations and (d) oil quenching media under still quench condition	90
5.19	(a) Average heat removed vs. average surface temperature and (b) average heat removed vs. time of inconel during quenching in graphene nanofluids at agitation rate of 1500 rpm	91
5.20	Cooling curves measured at the centre and 2 mm from the surface in G 10450 steel of section diameters 25 and 50 mm during quenching in karanja oil	92
5.21	Heat flux transients obtained during quenching of 25 and 50 mm section diameters of G 10450 steels in (a) mineral (b) karanja (c) sunflower (d) neem and (e) distilled water quench media	95
5.22	Heat flux transients obtained during quenching of 25 and 50 mm section diameters of G 10900 steels in (a) mineral (b) karanja (c) sunflower (d) neem and (e) distilled water quench media	96
5.23	Heat removed by oil quenchants during quenching of G 10450 steel of section diameters (a) 25 and (b) 50 mm and G 10900 steel of section diameters (c) 25 and (d) 50 mm	97
5.24	Microstructure obtained in G 10450 steel at the (a) centre and (b) surface of the 25 mm probe and (c) centre and (d) surface of the 50 mm probe during quenching in mineral oil	98
5.25	Microstructure obtained in G 10450 steel at the (a) centre and (b) surface of the 25 mm probe and (c) centre and (d) surface of the 50 mm probe during quenching in sunflower oil	98

5.26	Microstructure obtained in G 10450 steel at the (a) centre and (b) surface of the 25 mm probe and (c) centre and (d) surface of the 50 mm probe during quenching in neem oil	99
5.27	Microstructure obtained in G 10450 steel at the (a) centre and (b) surface of the 25 mm probe and (c) centre and (d) surface of the 50 mm probe during quenching in karanja oil	99
5.28	Microstructure obtained in G 10900 steel at the (a) centre and (b) surface of the 25 mm probe and (c) centre and (d) surface of the 50 mm probe during quenching in mineral oil	100
5.29	Microstructure obtained in G 10900 steel at the (a) centre and (b) surface of the 25 mm probe and (c) centre and (d) surface of the 50 mm probe during quenching in sunflower oil	100
5.30	Microstructure obtained in G 10900 steel at the (a) centre and (b) surface of the 25 mm probe and (c) centre and (d) surface of the 50 mm probe during quenching in neem oil	101
5.31	Microstructure obtained in G 10900 steel at the (a) centre and (b) surface of the 25 mm probe and (c) centre and (d) surface of the 50 mm probe during quenching in karanja oil	101
5.32	(a) Quench factor vs. cooling rate (b) quench factor vs. hardness for the G 10450 steel samples of 25 and 50 mm and (c) quench factor vs. cooling rate (b) quench factor vs. hardness for the G 10900 steel samples of 25 and 50 mm	102
5.33	Variation of cooling rate with distance in G 10450 steel grade of (a) 25 mm and (b) 50 mm section diameter during quenching in distilled water.	103
5.34	Variation of cooling rate with distance in G 10900 steel grade of (a) 25 mm and (b) 50 mm section diameter during quenching in karanja oil.	104
5.35	Heat flux curves obtained with SS probes during quenching in (a) mineral (b) karanja (c) neem (d) sunflower and (e) distilled water quench media	106



A.1	Cooling curves measured at 2 mm below the surface of the inconel probe during quenching in 2 lts. of (a) distilled water and (b) 0.01 (c) 0.1 and (d) 0.3 vol.% graphene nanofluids	117
A.2	Cooling curves measured at 2 mm below the surface of the inconel probe during quenching in 2 lts. of (a) 0.01 (b) 0.05 (c) 0.1 and (d) 1.0 vol.% CuO nanofluids	117
A.3	Cooling curves measured at 2 mm below the surface of the inconel probe during quenching in 2 lts. of (a) 0.0003 (b) 0.003 and (c) 0.03 vol.% MWCNT nanofluids	118
A.4	Cooling curves measured at 2 mm below the surface of the inconel probe during quenching in 2 lts. of (a) mineral (b) karanja (c) neem and (d) sunflower oil quenching media	118
B.1	Video images of quenching of inconel probe in mineral oil	119
B.2	Video images of quenching of inconel probe in sunflower oil	119
B.3	Video image taken during quenching of steel probes of (a) 50 and (b) 25 mm in distilled water	119
B.4	Video images of 25 mm steel probe quenched in sunflower oil	120
B.5	Video images of 50 mm steel probe quenched in sunflower oil	120
C.1	Images of contact angle relaxation of water droplet during spreading on an inconel substrate	121
C.2	Images of contact angle relaxation of 0.01 vol.% CuO nanofluid droplet during spreading on an inconel substrate	121
C.3	Images of contact angle relaxation of 0.05 vol.% CuO nanofluid droplet during spreading on an inconel substrate	122
C.4	Images of contact angle relaxation of 0.1 vol.% CuO nanofluid droplet during spreading on an inconel substrate	122
C.5	Images of contact angle relaxation of 1.0 vol.% CuO nanofluid droplet during spreading on an inconel substrate	123
C.6	Images of contact angle relaxation of 0.1 vol.% graphene nanofluid droplet during spreading on an inconel substrate	123

C.7	Images of contact angle relaxation of 0.3 vol.% graphene nanofluid droplet during spreading on an inconel substrate	124
C.8	Images of contact angle relaxation of 0.0003 vol.% MWCNT nanofluid droplet during spreading on an inconel substrate	124
C.9	Images of contact angle relaxation of 0.003 vol.% MWCNT nanofluid droplet during spreading on an inconel substrate	125
C.10	Images of contact angle relaxation of 0.03 vol.% MWCNT nanofluid droplet during spreading on an inconel substrate	125
C.11	Images of contact angle relaxation of mineral oil droplet during spreading on an inconel substrate	126
C.12	Images of contact angle relaxation of karanja oil droplet during spreading on an inconel substrate	127
C.13	Images of contact angle relaxation of neem oil droplet during spreading on an inconel substrate	128
C.14	Images of contact angle relaxation of sunflower oil droplet during spreading on an inconel substrate	129
D.1	Measured cooling curves in the inconel probe during quenching in distilled water under agitation rates of (a) still (b) 500 (c) 1000 and (d) 1500 rpm	130
D.2	Measured cooling curves in the inconel probe during quenching in 0.01 vol.% CuO nanofluid under agitation rates of (a) still (b) 500 (c) 1000 and (d) 1500 rpm	130
D.3	Measured cooling curves in the inconel probe during quenching in 0.05 vol.% CuO nanofluid under agitation rates of (a) still (b) 500 (c) 1000 and (d) 1500 rpm	131
D.4	Measured cooling curves in the inconel probe during quenching in 0.1 vol.% CuO nanofluid under agitation rates of (a) still (b) 500 (c) 1000 and (d) 1500 rpm	131
D.5	Measured cooling curves in the inconel probe during quenching in 1.0 vol.% CuO nanofluid under agitation rates of (a) still (b) 500 (c) 1000 and (d) 1500 rpm	132

D.6	Measured cooling curves in the inconel probe during quenching in 0.01 vol.% graphene nanofluid under agitation rates of (a) still (b) 500 (c) 1000 and (d) 1500 rpm	132
D.7	Measured cooling curves in the inconel probe during quenching in 0.1 vol.% graphene nanofluid under agitation rates of (a) still (b) 500 (c) 1000 and (d) 1500 rpm	133
D.8	Measured cooling curves in the inconel probe during quenching in 0.3 vol.% graphene nanofluid under agitation rates of (a) still (b) 500 (c) 1000 and (d) 1500 rpm	133
D.9	Measured cooling curves in the inconel probe during quenching in 0.0003 vol.% MWCNT nanofluid under agitation rates of (a) still (b) 500 (c) 1000 and (d) 1500 rpm	134
D.10	Measured cooling curves in the inconel probe during quenching in 0.003 vol.% MWCNT nanofluid under agitation rates of (a) still (b) 500 (c) 1000 and (d) 1500 rpm	134
D.11	Measured cooling curves in the inconel probe during quenching in 0.03 vol.% MWCNT nanofluid under agitation rates of (a) still (b) 500 (c) 1000 and (d) 1500 rpm	135
D.12	Measured cooling curves in the inconel probe during quenching in karanja oil under agitation rates of (a) still (b) 500 (c) 1000 and (d) 1500 rpm	135
D.13	Measured cooling curves in the inconel probe during quenching in mineral oil under agitation rates of (a) still (b) 500 (c) 1000 and (d) 1500 rpm	136
D.14	Measured cooling curves in the inconel probe during quenching in neem oil under agitation rates of (a) still (b) 500 (c) 1000 and (d) 1500 rpm	136
D.15	Measured cooling curves in the inconel probe during quenching in sunflower oil under agitation rates of (a) still (b) 500 (c) 1000 and (d) 1500 rpm	137

E.1	Cooling curves obtained at various locations in (a) 25 and (b) 50 mm section diameters of G 10450 steel and their corresponding cooling rate curves in (c) and (d) respectively during quenching in mineral oil quenching medium	138
E.2	Cooling curves obtained at various locations in (a) 25 and (b) 50 mm section diameters of G 10450 steel and their corresponding cooling rate curves in (c) and (d) respectively during quenching in karanja oil quenching medium	139
E.3	Cooling curves obtained at various locations in (a) 25 and (b) 50 mm section diameters of G 10450 steel and their corresponding cooling rate curves in (c) and (d) respectively during quenching in neem oil quenching medium	140
E.4	Cooling curves obtained at various locations in (a) 25 and (b) 50 mm section diameters of G 10450 steel and their corresponding cooling rate curves in (c) and (d) respectively during quenching in sunflower oil quenching medium	141
E.5	Cooling curves obtained at various locations in (a) 25 and (b) 50 mm section diameters of G 10450 steel and their corresponding cooling rate curves in (c) and (d) respectively during quenching in distilled water quenching medium	142
F.1	Cooling curves obtained at various locations in (a) 25 and (b) 50 mm section diameters of G 10900 steel and their corresponding cooling rate curves in (c) and (d) respectively during quenching in mineral oil quenching medium	143
F.2	Cooling curves obtained at various locations in (a) 25 and (b) 50 mm section diameters of G 10900 steel and their corresponding cooling rate curves in (c) and (d) respectively during quenching in karanja oil quenching medium	144
F.3	Cooling curves obtained at various locations in (a) 25 and (b) 50 mm section diameters of G 10900 steel and their corresponding cooling	145

	rate curves in (c) and (d) respectively during quenching in neem oil quenching medium	
F.4	Cooling curves obtained at various locations in (a) 25 and (b) 50 mm section diameters of G 10900 steel and their corresponding cooling rate curves in (c) and (d) respectively during quenching in sunflower oil quenching medium	146
F.5	(a) Cooling curves and (b) cooling rate curves obtained at various locations in the 50 mm section diameter of G 10900 steel during quenching in distilled water quenching medium	147
G.1	Cooling curves obtained at various locations in (a) 25 and (b) 50 mm section diameters of stainless steel and their corresponding cooling rate curves in (c) and (d) respectively during quenching in mineral oil quenching medium	148
G.2	Cooling curves obtained at various locations in (a) 25 and (b) 50 mm section diameters of stainless steel and their corresponding cooling rate curves in (c) and (d) respectively during quenching in karanja oil quenching medium	149
G.3	Cooling curves obtained at various locations in (a) 25 and (b) 50 mm section diameters of stainless steel and their corresponding cooling rate curves in (c) and (d) respectively during quenching in neem oil quenching medium	150
G.4	Cooling curves obtained at various locations in (a) 25 and (b) 50 mm section diameters of stainless steel and their corresponding cooling rate curves in (c) and (d) respectively during quenching in sunflower oil quenching medium	151
G.5	Cooling curves obtained at various locations in (a) 25 and (b) 50 mm section diameters of stainless steel and their corresponding cooling rate curves in (c) and (d) respectively during quenching in distilled water quenching medium	152

H.1	Spatiotemporal heat flux obtained during quenching of inconel in (a) distilled water (b) 0.01 (c) 0.1 and (d) 0.3 vol.% graphene nanofluids	153
H.2	Spatiotemporal heat flux obtained during quenching of inconel in (a) 0.01 (b) 0.05 (c) 0.1 and (d) 1.0 vol.% CuO nanofluids	153
H.3	Spatiotemporal heat flux obtained during quenching of inconel in (a) 0.0003 (b) 0.003 and (c) 0.03 vol.% MWCNT nanofluids	154
H.4	Spatiotemporal heat flux obtained during quenching of inconel in (a) mineral (b) karanja (c) neem and (d) sunflower oils	154
I.1	Spatiotemporal heat flux estimated at the inconel/water interface at impeller agitation rates of (a) still (b) 500 (c) 1000 and (d) 1500 rpms	155
I.2	Spatiotemporal heat flux estimated at the inconel/0.01 vol.% CuO nanofluid interface at impeller agitation rates of (a) still (b) 500 (c) 1000 and (d) 1500 rpms	155
I.3	Spatiotemporal heat flux estimated at the inconel/0.05 vol.% CuO nanofluid interface at impeller agitation rates of (a) still (b) 500 (c) 1000 and (d) 1500 rpms	156
I.4	Spatiotemporal heat flux estimated at the inconel/0.1 vol.% CuO nanofluid interface at impeller agitation rates of (a) still (b) 500 (c) 1000 and (d) 1500 rpms	156
I.5	Spatiotemporal heat flux estimated at the inconel/1.0 vol.% CuO nanofluid interface at impeller agitation rates of (a) still (b) 500 (c) 1000 and (d) 1500 rpms	157
I.6	Spatiotemporal heat flux estimated at the inconel/0.01 vol.% graphene nanofluid interface at impeller agitation rates of (a) still (b) 500 (c) 1000 and (d) 1500 rpms	157
I.7	Spatiotemporal heat flux estimated at the inconel/0.1 vol.% graphene nanofluid interface at impeller agitation rates of (a) still (b) 500 (c) 1000 and (d) 1500 rpms	158

I.8	Spatiotemporal heat flux estimated at the inconel/0.3 vol.% graphene nanofluid interface at impeller agitation rates of (a) still (b) 500 (c) 1000 and (d) 1500 rpms	158
I.9	Spatiotemporal heat flux estimated at the inconel/0.0003 vol.% MWCNT nanofluid interface at impeller agitation rates of (a) still (b) 500 (c) 1000 and (d) 1500 rpms	159
I.10	Spatiotemporal heat flux estimated at the inconel/0.003 vol.% MWCNT nanofluid interface at impeller agitation rates of (a) still (b) 500 (c) 1000 and (d) 1500 rpms	159
I.11	Spatiotemporal heat flux estimated at the inconel/0.03 vol.% MWCNT nanofluid interface at impeller agitation rates of (a) still (b) 500 (c) 1000 and (d) 1500 rpms	160
I.12	Spatiotemporal heat flux estimated at the inconel/karanja oil interface at impeller agitation rates of (a) still (b) 500 (c) 1000 and (d) 1500 rpms	160
I.13	Spatiotemporal heat flux estimated at the inconel/mineral oil interface at impeller agitation rates of (a) still (b) 500 (c) 1000 and (d) 1500 rpms	161
I.14	Spatiotemporal heat flux estimated at the inconel/neem oil interface at impeller agitation rates of (a) still (b) 500 (c) 1000 and (d) 1500 rpms	161
I.15	Spatiotemporal heat flux estimated at the inconel/sunflower oil interface at impeller agitation rates of (a) still (b) 500 (c) 1000 and (d) 1500 rpm	162
J.1	Average heat removed as a function of average surface temperature during quenching of the inconel probe in (a) MWCNT (b) graphene (c) CuO nanofluids of various concentrations and (d) oil quenching media under 500 rpm quench condition	163
J.2	Average heat removed as a function of average surface temperature during quenching of the inconel probe in (a) MWCNT (b) graphene	164

	(c) CuO nanofluids of various concentrations and (d) oil quenching media under 1000 rpm quench condition	
J.3	Average heat removed as a function of average surface temperature during quenching of the inconel probe in (a) MWCNT (b) graphene (c) CuO nanofluids of various concentrations and (d) oil quenching media under 1500 rpm quench condition	165



## List of Tables

<b>Table No.</b>	<b>Caption</b>	<b>Page No.</b>
2.1	Flash point and viscosity of various edible vegetable oils (Simencio Otero et al. 2012, Souza et al. 2009)	15
3.1	Details of quench media	34
3.2	Chemical composition of the metal probes	35
3.3	Thermophysical properties of the inconel 600 alloy quench probe (Penha et al. 2010)	45
3.4	Thermophysical properties for SS probes (JMatPro, Sente Software Ltd., UK))	46
3.5	Thermophysical data for G 10450 grade steel probes (JMatPro, Sente Software Ltd., UK))	47
3.6	Thermophysical properties for G 10900 grade steel probes (JMatPro, Sente Software Ltd., UK))	48
4.1	Thermophysical properties of nanofluids	52
4.2	Thermophysical properties of quench oil	53
4.3	Viscosity index of quench oils	54
4.4	Surface tension (mN/m) of nanofluids	55
4.5	Surface tension (mN/m) of oils	55
5.1	Critical cooling parameters obtained during quenching of inconel probe in various liquid quench media	66
5.2	Estimated peak heat flux at various boundary segments during quenching of the inconel probe in various quench media	72
5.3	Peak heat flux at various interfacial heat segments under still quench condition	81
5.4	Peak heat flux at various interfacial heat segments under 500 rpm quench condition	83
5.5	Peak heat flux at various interfacial heat segments under 1000 rpm quench condition	84

5.6	Peak heat flux at various interfacial heat segments under 1500 rpm quench condition	85
5.7	Maximum cooling rate and latent heat start parameters during quenching of G 10450 steel of section diameters 25 and 50 mm	93
5.8	Maximum cooling rate and latent heat start parameters during quenching of G 10900 steel of section diameters 25 and 50 mm	93
5.9	Maximum cooling rate parameters during quenching of 304 SS of section diameters 25 and 50 mm	105

## NOMENCLATURE

### Symbols

$\hat{T}$	temperature computed for a few future time steps, °C
$\hat{T}^+$	$\hat{T}$ with enhanced heat flux at the selected segment, °C
$\phi$	sensitivity coefficient, Km <sup>2</sup> /W
A	area, m <sup>2</sup>
C <sub>p</sub>	specific heat, J/KgK
CR	cooling rate, °C/s
$m$	product of the slope of the kink in the cooling curve due the evolution of the latent heat and the average cooling rate from the peak of kink to the bainite start temperature given by the CCT curve for the steel, °C <sup>2</sup> /s <sup>2</sup>
q	heat flux, MW/m <sup>2</sup>
$QF$	quench factor
R	radius of probe, m
T	temperature, °C
t	time, s
Y	measured temperature, °C
z, r	coordinate direction, m
v	kinematic viscosity, m <sup>2</sup> /s
$\Delta Q_{60}$	difference in the average heat removed between the bottom half portion and the top half portion of the inconel probe obtained at the average surface temperature of 60 °C, MJ/m <sup>2</sup>

$\theta$	contact angle, $^{\circ}$
$\lambda$	thermal conductivity, W/mK
$\rho$	density, kg/m <sup>3</sup>
$\sigma$	surface tension, mN/m

### **Subscripts**

b	future time step, s
i	time step, s
j	temperature sensor location, m
k	number of unknown heat flux components
max	maximum
sl	start of transformation

## **Chapter 1 INTRODUCTION**

The history of hardening steel has been reported to date back to about 800 BC (MacKenzie 2006). Since these times, the technology of quench hardening steel has come a long way from quenching of steel in blood to using water, synthetic oils, vegetable oils, aqueous polymers, their blends and others. The process involves heating steel in the range of 850-870 °C for austenitizing followed by introduction of the metal into a suitable quench medium for strengthening (Ramesh and Prabhu 2012). The outcome of the quenching process depends on: (i) characteristics of the steel being quenched (ii) characteristics of the quench medium used and (iii) the conditions prevailing during the process (Grum et al. 2001). The main objective of the hardening operation is to obtain maximum hardness in the steel and minimize the evolution of internal stresses. Quench medium that is used to extract heat must be carefully chosen to meet the objectives of the hardening process. The ability of the quench medium to harden steel is limited by its characteristics. Spatiotemporal heat flux estimated at the metal/quenchant interface with the aid of cooling curves measured in accordance with ISO 9950 standard provides valuable information that helps in the selection of the medium. However, such information is limited as it does not consider the heat evolved due to phase transformation and the effect of section size of the steel being quenched. The section size of the quenched steel influences the cooling rate during quenching (Fernandes and Prabhu 2007, Grum et al. 2001) and is an important variable that must be considered during assessment of heat transfer.

### **1.1 Scope of the Investigation**

A review of the literature suggests a significant increase in the thermal conductivity of nanofluids compared to water. This has an important implication in quench hardening. Although water has high severity of quenching, its use is not recommended in thin sections having high quench sensitivity and complex shaped components. Moreover, water has poor wettability compared to other quench media which causes distortion and crack formation in the quench parts. Water based nanofluids have shown higher wetting ability compared to water. The suitability of water based nanofluids as quench media requires the estimation of both quench severity and quench uniformity of nanofluids. The estimation of spatiotemporal heat flux transients by solving the inverse heat

conduction problem (IHCP) is a useful tool for assessing both the cooling power and cooling uniformity of quench media.

Mineral oils are the most widely used quench media to heat treat steels (Ramesh and Prabhu 2014a). However, their use causes environmental problems (Totten et al. 1999). An alternative solution to using mineral oil is the use of vegetable oils as quenching media because of their favourable bio-degradability. A significant work has been carried out to assess the suitability of vegetable oils as quench media. Most of the vegetable oils investigated were edible. India, imported nearly 127 lakh tones of vegetable oil during the year 2014-2015 (Department of Food and Public Distribution 2018). Presently, 2.5% of India's oil bill accounting to about 65,000 Crores is used in importing edible vegetable oils (Ghosal 2017). The use of edible oils in industrial heat treatment is thus not recommended, in the Indian context. A more feasible solution to this would be the use of non-edible vegetable oils that are produced in the country. Assessment of their quench characteristics and comparing them with those obtained for mineral oils would enable the assessment of the viability of non-edible oils for quench hardening applications.

Inconel/stainless steel probes machined to ISO 9950 or similar standard are useful only for the characterization of quench media. Their use is limited in predicting the microstructure and hardness as they do not undergo phase transformation. Moreover, the data obtained from such probes do not provide information concerning the effect of section size on heat transfer characteristics of carbon steels. It is well known fact that the surface of the steel cools faster compared to its interior because of its proximity to the quench medium. The differential cooling influences heat transfer at the metal/quenchant interface affecting microstructure and hardness. To assess these effects, the inverse solution to heat conduction problem must consider the phase transformation during quenching of reference probes made from carbon steels of different section sizes.

## **1.2 Objectives of the Research Work**

The following are the objectives of the present investigation:

1. To prepare nanofluids of various concentrations and determine their wetting characteristics.
2. To assess the suitability of nanofluids as quench media by estimating spatially dependent heat flux transients using a standard inconel probe and to compare their heat transfer characteristics with conventional quench media.
3. To use non-edible vegetable oils for quench hardening and assess their cooling power, thermal and heat transfer characteristics.
4. To determine the effect of section thickness and agitation on heat transfer during quenching.
5. To estimate heat flux transients during quenching of reference probes of carbon steels in non-edible oils by considering phase transformation.
6. To study the effect of cooling rate on microstructure and hardness of reference probes.

## **1.3 Organization of the Thesis**

The thesis is divided into six chapters. Chapter 1 presents introduction, followed by the scope and objectives of the present research work. Chapter 2 provides the literature reviewed on quenching, nanofluids, oil quench media and quenching of steels. Chapter 3 describes the experimental set-up, materials used and the methodology followed during the investigation. Chapter 4 presents the results of the experiments carried out. Chapter 5 gives a detailed analysis of the results, interpretation and the related discussion. Chapter 6 lists the conclusions drawn based on the discussion and experimental findings.

## **Chapter 2 LITERATURE REVIEW**

Steel alloys in their as produced condition consist of ferrite-pearlite microstructure. The mechanical properties of such steels are limited in their capability to handle load. Quench hardening is a solid-state transformation process. It consists of heating steels that contain carbon content ranging from 0.4 to 2% to temperatures that are 50-60°C above their austenitizing temperature and maintaining that temperature to homogenize the alloy followed by introducing the red-hot steel into a quenching medium. In India, the era during which steels were first quenched is unknown. However, Wootz steel that was used to produce swords and daggers by quenching in water were carried out till the 19<sup>th</sup> century (Srinivasan and Ranganathan 2017). The science of quantifying the outcome of quenching and the effect of alloying addition on steel properties was developed after approximately 1850 AD (MacKenzie 2006). At present our understanding of quench hardening shows that, the operation of quenching involves heat transfer from the metal alloy to the quenching medium. Heat transfer is an imperative process that leads to the development of microstructure and formation of stress. Hence, the objective of quenching heat treatment is to enhance the mechanical properties while minimizing the accompanying ill-effects of distortion and crack formation in steels. The rate and the uniformity at which heat is transferred during quenching decides the extent of enhancement and/or degradation and must be understood by the heat treater before commencement of the operation.

### **2.1 Stages of Heat Transfer During Quenching**

The three heat transfer modes that operate during quenching process are radiation, conduction and convection. These modes occur either individually or in combination. Depending on the dominating mode each stage during quenching is classified into (i) vapour phase stage (ii) nucleate boiling stage and (iii) convective cooling stage. The steel alloys to be hardened is heated to an elevated temperature that generally ranges between 850 - 1200°C. The hot steel is then immersed into a liquid quench medium. The instant at which the steel contacts the medium, the liquid wets the metal surfaces and immediately vaporises, forming an envelope around the metal. This symbolises the first stage of heat transfer known as the vapor phase stage. Heat is transferred primarily by conduction and radiation mode during the vapor phase stage. A pictorial



representation of the quenching stages and the cooling curves obtained during the immersion cooling process is shown in Figure 2.1. Heat transferred during stage one is slow and low shown by the gradual sloping portion at the beginning of the cooling curve. The initial slow cooling of the metal is due to the insulating nature of the vapor medium. With continued cooling, the temperature at the surface of the probe falls below the Leidenfrost temperature of the liquid. At this instant, the liquid medium rewets the metal surface. Rewetting of the metal surface by the liquid is an important thermophysical phenomenon as it significantly influences the remaining stages. On rewetting, heat transfer from the metal accelerates and numerous bubble nucleate, collapse and depart from the metal surface. The cooling stage thus enters the nucleate boiling stage. Heat transfer during this stage primarily occurs by conduction and boiling. The slope of the cooling curve during the second stage is markedly different from the first stage and shows an increased rate of decrease in temperature. As the metal cools, its temperature drops below the boiling point of the liquid quench medium. The boiling of the liquid then ceases to occur and the cooling stage exits into the convective stage. Heat transfer occurs primarily by convection during this stage with the metal surface in complete contact with the surface of the metal.

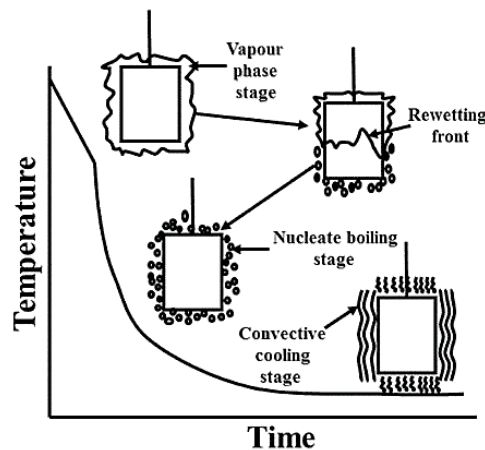


**Figure 2.1: Stages of cooling during quenching in liquid medium**

The cooling curve during the convective stage shows a gradual reduction in temperature with the surface temperature of the metal reaching that of the liquid medium temperature.

## 2.2 Variables Influencing Quenching Process

The variables that influence the quenching operation are broadly categorized into

- The types and characteristics of quenching media used
- Characteristics of steel part to be quench hardened and
- The quenching condition under which the hardening operation is done

### 2.2.1 Types and characteristics of quenching media

The various liquid quench media are broadly classified under aqueous and non-aqueous quench media and are shown in Figure 2.2. The quench severity of aqueous media is higher compared to those under the non-aqueous category. Further, aqueous and oil quench media vaporize during the quench hardening operation compared to the molten media. these two class of quench media undergo boiling resulting in faster heat removal than molten salts and metal quench media (Luty 2010). In other words, aqueous and oil media undergo boiling causing more and faster heat extraction from steels compared to the molten media.

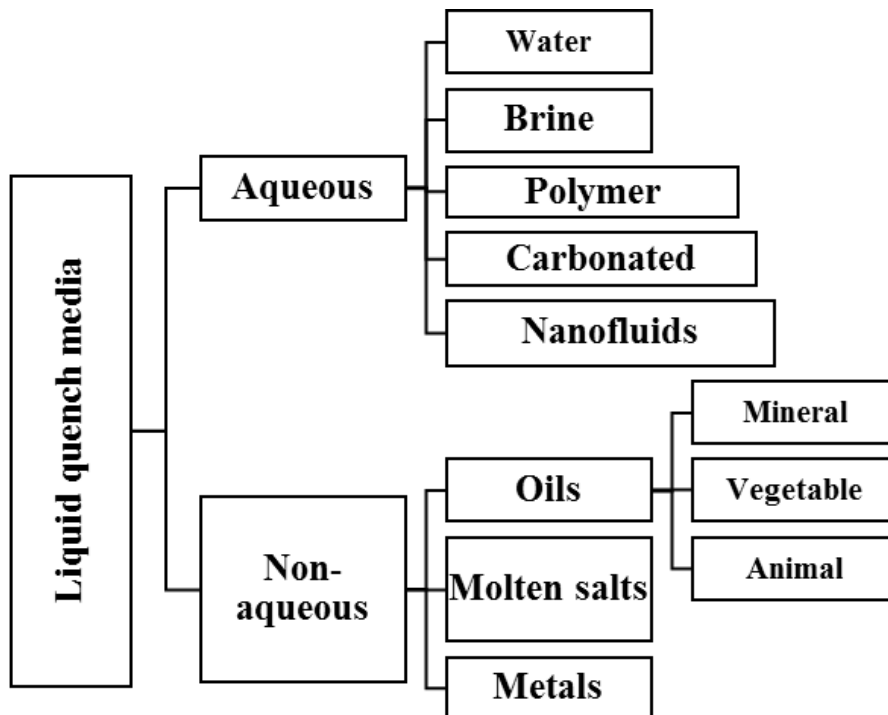
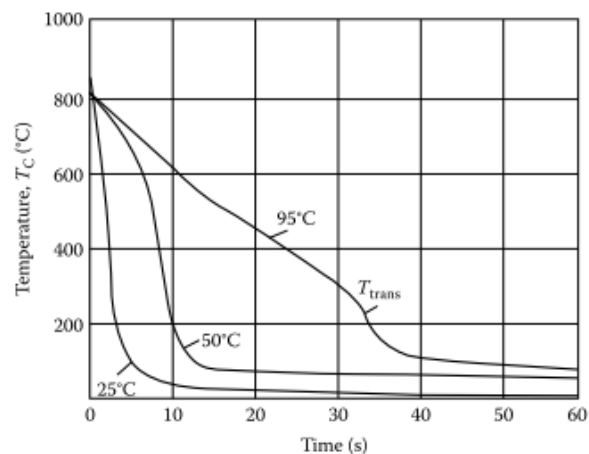


Figure 2.2: Categories of liquid quench media

### 2.2.1.1 Aqueous quench media

#### 2.2.1.1.1 Water

Water is the most widely used quenching medium because of its availability, cost and simplicity in use. Water is eco-friendly and does not cause harm to the operator. However, its uses are limited to quench hardening of only medium carbon steels (with about 0.4% C) of simple shapes. This is because of its high cooling rates coupled with non-uniform heat extraction characteristic. To obtain uniform and lower cooling rates, researchers in the past have tried agitation and heating of water respectively. Agitation, helps early break down of the vapor phase. It aids to obtain a more uniform heat extraction from the metal. However, agitation increases the cooling rate during convective cooling leading (martensite transformation range) to increased propensity towards distortion and cracking in the metal. Water heated to elevated temperature lowers its heat extraction ability significantly as shown in Figure 2.3. It shows that increasing the water temperature from 25 to 50°C would increase the vapor phase duration by about 200° C. Further, steel components quenched in hot water developed soft spots which occur because of non-uniformity in quenching.



**Figure 2.3: Temperature measured at the centre of a silver probe of  $\text{Ø}15 \times 45$  mm as a function of time during quenching in water maintained at various temperatures (Tensi and Schwalm 1980)**

The combined effect of agitation and elevated water temperature failed in obtaining the desired results. This was because of the higher stability of the vapor phase at elevated

water temperatures and difficulty associated with control over the flow during quenching. In addition to these factors, the cooling performance of water is significantly influenced by the presence of contaminants such as cutting fluids, oils, metal filings, and others.

#### **2.2.1.1.2 Brine**

Brine quench media are obtained by adding and mixing of sodium chloride (NaCl), sodium hydroxide (NaOH), chlorides of magnesium, calcium and lithium in water. NaCl and NaOH solutions of varying concentrations were used as quench media by Kobasco. The heat transfer coefficient was found to be highest at the 10% concentration for these two salts. Further, NaOH showed higher heat transfer coefficient compared to NaCl (Kobasko 1968). Compared with water, the temperature increase from 20 to 60° C for these salts at 5% concentration did not significantly affect their cooling behavior (French and Hamill 1929). The vapor phase stage was shortened during quenching with brine. The rewetting front motion for quenching in brine compared to water causing faster cooling of the metal. However, brine has poor wettability and is corrosive (Ramesh and Narayan Prabhu 2014). Moreover, the use of brine to heat treat steel is limited to quench harden small and simple shaped components (French and Hamill 1929).

#### **2.2.1.1.3 Water-polymer quenchants**

The quench media formulated in this category are made from polymerization of synthetic polymers. Polymers that are used are derived from petroleum. They are produced in the form of concentrated liquids or powders. The required quench medium is obtained by mixing the polymers with desired concentration in water. The limitations of oil quench media such as smoke, fire and handling difficulty were the main reason behind the development and use of aqueous polymer media for immersion quench hardening heat treatment (Ikkene et al. 2010). These quenchants are nonflammable and do not cause harm to the operator. Polymer quenchants have shown to offer satisfactory distortion control with eliminates of soft spots and achievement of the desired mechanical properties. Wide range of cooling rates, between that of water and oils, would be obtained by varying the polymer type, its concentration, quenchant

temperature and the agitation rate used. Synthetic polymers used as quenchants by combining with water include polyvinyl alcohol (PVA), polyalkylene glycol (PAG), polyethyl oxazoline (PEOX), polysodium acrylate (PSA) and polyvinyl pyrrolidone (PVP) etc. PVA or PVA+PAG are less popular and were shown to form a rubber-like film on the quenched part. Such films require post heat treatment cleaning operation and are difficult to remove. Also, PVA undergoes thermal decomposition giving acetic acid. Acetic acid is a known corrosive and its formation would alter the cooling power of the polymer quenchant. Among the polymers available to form aqueous quench media PAG is most popular (Troell and Kristoffersen 2010). It is nonionic (unlike PSA) (Totten et al. 1993). It exhibits inverse solubility behavior. Polymer quenchants whose bath temperature when exceeds 60-85 °C separate-out of water exhibiting inverse solubility leading to polymer rich and water rich regions (Deval 2009). Quenching of hot metal in PAG causes the liquid polymer to coat the metal surface (Canter 2010). The polymer coat provides more uniform heat transfer than the vapor phase formed during the first stage of quenching observed with oils and water. The coated layers provide higher quench rate compared to water that was heated to 60°C or above during the vapor phase stage (Croucher and Schuler 1970). The precipitated polymers re-dissolves in water when the quenchant falls below the inverse solubility temperature range for the polymer. Fire safety, distortion control, desirable mechanical properties, cooling rate flexibility (Sarmiento et al. 2010) are obtained with polymer quenchants. (Totten et al. 1998) demonstrated inverse hardening in AISI 4140 steel of 50 mm diameter. This steel was quenched in a 25% PAG solution that was maintained at 40°C under an agitation rate of 0.8 m/s. It was proposed that, such an outcome occurs, because of the delayed quenching process. The heat transfer condition (on quenching in aqueous polymer quench media) during delayed quenching would be such that, stable phases other than martensite would develop on the surface while martensite would form at the centre. The disadvantages of implementing polymer based water quenchants are corrosion of the quench tank, bacterial degradation of the polymer, drag-out losses, periodic evaluation of the quenchant etc.

#### **2.2.1.1.4 Carbonated water**

Carbonated water is prepared by dissolving carbon dioxide in water. This is achieved by (i) injecting carbon dioxide gas into water (ii) addition of carbonic acid to water and (iii) addition of organic or inorganic acid to water. Examples of inorganic acids include –  $\text{CaCO}_3$ ,  $\text{K}_2\text{CO}_3$ ,  $\text{NaCO}_3$ . (Yu et al. 1997) made carbonated water by dissolving carbon dioxide at 0.001-0.2 standard cubic feet of gas per 3.8 lts of water to quench heat treat aluminium metal objects. (Nayak et al. 2016) showed evolution of gas bubbles during the convection stage causes faster cooling of the inconel probe compared to quenching in water. The peak cooling rate reported by them showed reduction of about 50 % during quenching in the carbonated water medium compared to water. When carbon dioxide was injected in the 10 vol.% PAG solution their results showed that the peak rate was reduced by three times compared to the solution without carbon dioxide addition. A notable feature of quenching in carbonated media was the movement of a uniform rewetting front implying uniform heat transfer from the metal quenched in carbonated media and their possible implementation to heat treat thin, short and simple shaped metal objects.

#### **2.2.1.1.5 Nanofluids**

Nanofluids are heat transfer media obtained by dispersing nano sized particles (1 to 100 nm) of solid materials in base fluids. The base fluids that have been used are water, oil and ethylene glycol (Philip and Shima 2012). They were conceived because of the limitations of heat transfer liquids that contained microparticles. Heat transfer liquids containing microparticles were used primarily to remove heat from components of miniature size. However, the use of such liquids were plagued by issues such as erosion of the flow path, increased pumping losses, rapid settling of the particles in the suspended fluid, buildup of particles in flow channels (Murshed et al. 2008). The miniature components produced high densities of heat and had the need for a coolant with superior heat transfer abilities. Evolution in nanoscience technology has enabled nanoparticles to be made from different metallic and nonmetallic materials such as copper, titanium, multiwall carbon nanotubes (MWCNT), silicon carbide and others (Ramesh and Prabhu 2011). Nanofluids can be produced either by the one-step or the two-step method. In the single step method, nanoparticles are simultaneously produced

and added to the base fluid while in the two-step process nanofluids are first generated and then dispersed in the base fluid. Techniques for producing nanoparticles include chemical solution method (Wei and Wang 2010), direct evaporation, submerged arc, inert gas condensation, microwave irradiation (Sureshkumar et al. 2013), chemical vapor deposition, direct evaporation and condensation, micro emulsion, ball milling and others (Das et al. 2007). The two-step method is most used due to the availability and production of nanopowders in large quantities (Murshed et al. 2008) and works well for oxide nanoparticles (Sureshkumar et al. 2013). It was envisioned by Choi that since the nanoparticles have higher thermal properties compared to the base fluid their introduction in the base fluid would significantly enhance the thermal performance of base fluids (Choi and Eastman 1995). Heat transfer characteristics of nanofluids can be obtained by measuring the thermal conductivity, heat transfer coefficient and other thermophysical properties. Factors influencing the thermal performance of nanofluids are its material, shape, size and volume fraction. Temperature, acidity, sonication time, distribution, surfactants used, flow velocity and rate of agitation are the other factors that affect heat transferred by the nanofluids. Thermal conductivity of nanofluids can be measured using: transient hot-wire method, parallel plate technique and the temperature oscillation technique. Research data on thermal conductivity of various nanofluids shows increased thermal conductivity relative to base fluids. For example: Eastman, one of the pioneers in nanofluid research reported an enhancement of 60% in thermal conductivity by suspending 5 vol. % of copper oxide (36nm) particles in water. However, mechanism related to the enhancement of thermal conductivity is unknown (Khedkar et al. 2012). The possible mechanisms stated are: Brownian motion, liquid layer formation around the nanoparticles, nature of the heat transport and clustering of nanoparticles (Ramesh and Prabhu 2011). In quenching heat treatment, the performance of the quenchant is measured by its ability to extract heat from the hot metal surface. At low concentrations of nanoparticles, the cooling curves measured for water and nanofluids showed no increase in cooling with nanofluids. Repetitive quenching experiments with water based alumina, silica and diamond nanoparticles (Kim et al. 2009) showed the deposition of particles on the quench probe surface. The effect of deposition was to increase the cooling rate during quenching and was also observed in the works of (Ciloglu and Bolukbasi 2011). (Župan et al. 2011) reported increase in the

peak heat transfer coefficient in nanofluids relative to their base fluids (water and PAG solution, 5, 10 and 20 Vol.%) with the addition of 0.2g/l of nanoparticles under unagitated quench condition. These studies highlight the shortening of the film boiling stage indicating early wetting of the cooling metal surface. Quenching of unfouled fresh probe in water-clay nanofluids of various concentrations lowered the peak heat flux compared to quenching in water (Ramesh and Prabhu 2012). These outcomes indicate the importance of selecting the material type while formulating the nanoquenchant.

### **2.2.1.2 Oils**

Oil media are the most widely used quenching media for heat treatment of steel components. Based on the source, oils used to heat treat steels are classified into mineral, animal and vegetable. They can be classified into naphthenic, paraffinic etc. depending on composition. Other modes of classification are based on the operational requirement like cooling rate, quenchant temperature and ease of removal (Totten et al. 1993) (Ma 2002).

#### **2.2.1.2.1 Mineral oil**

The first petroleum based mineral oil for quenching steel was developed by researchers in the year 1880 at E.F. Houghton and Co. (MacKenzie and Lazerev). Mineral oil media are the most preferred media and are being used to heat treat steels since the industrial revolution. They have higher thermal stability compared with oils derived from other sources (Pedišić et al. 2005). They offer wide range of cooling rates and they last for many quench cycles. Chromatographic studies have shown that the mineral oils are made up of complex formulations containing several components. These components include various paraffinic, naphthenic, and various oxygen-, nitrogen-, and sulfur-derived open chain and cyclic derivatives and other volatile components (Totten et al. 1993). A high quality mineral oil is obtained from refined petroleum stock that has high paraffinic content (MacKenzie and Lazerev). Further, additives and stabilizers are added to the base oil to obtain satisfactory quench performance. Various concentrations of polyisobutylene polymer were added to mineral oil to eliminate film boiling and reduce distortion in the metal during quenching (Kobasko et al. 2016). Various mineral oils of viscosities ranging from 10 to 120 cP, operating at temperatures from ambient



to 150 °C were tested for their quenching performance using a 4140-medium carbon steel of dimensions  $\text{Ø } 6.35 \times 38 \text{ mm}$ . Cooling rate curves reported in their study showed that the two quench oils that were designated to have moderate quench speeds widely differed in their peak cooling rates (120 and 208 °C/s). The researchers showed that higher viscosity and lower operating temperature caused reduced cooling rates compared to the oils that were operated at higher temperature and had lower viscosity and showed that the cooling rate was found to be maximum at 700 °C for most of the oils used (Ma 2002). The effect of oil composition on the cooling curve behaviour of mineral oil was shown by (Pedišić et al. 2005). Their results showed that the addition of sodium, calcium sulfonates and emulsifiers significantly altered the cooling behaviour of base oils. Vegetable oil containing sodium and calcium sulfonates tested by them showed faster cooling rates compared to mineral oils containing these additives. Wetting characteristics, kinetics and heat transfer ability of normal, accelerated and hot mineral oils were investigated by (Ramesh and Prabhu 2014a). They witnessed occurrence of a double rewetting front during quenching of inconel in mineral oil. Rewetting front was more uniform during quenching with mineral oils of lower viscosity ( $< 56 \text{ cP}$ ) compared to those that had higher viscosity. Though mineral oil is widely used because of its perceived benefits, its use causes environmental issues and needs an alternative solution to address this concern.

#### **2.2.1.2.2 Vegetable oils**

##### **2.2.1.2.2.1 Edible vegetable oils**

Mineral oils are produced from non-renewable resources and cause environment pollution. They are toxic and their disposability concerns have driven the need of obtaining a more eco-friendly alternative. Vegetable oils are the oils derived from leaves, seeds and other parts of plants. Such oils when used as quenchants, could provide a sustainable and eco-friendly alternative to mineral oils. The cooling curves obtained with rapeseed oil were investigated by Rose in the year 1940 (Rose 1940). It was one of the earliest investigations on the viability of vegetable oils as quench media. Cooling curves with rapeseed oil and their comparison to three different mineral oils are shown in Figure 2.4. The findings of this study showed that an unstable vapour blanket stage occurred during quenching with the rapeseed oil compared to mineral oil

resulting in higher heat transfer during the initial cooling stage of quenching. Based on these investigations on the quenching ability of rapeseed oil, vegetable oils such as cotton seed oil, castor, canola, soyabean, palm kernel, palm, sunflower etc. were tried as quenching media by various researchers. The flash point and viscosity of various vegetable oils are given in Table 2.1. Of the vegetable oils tried as quenchants, high oleic fat containing canola oil has the highest oxidation resistance. Further its biodegradability measured using the CEC L-33-T-82 test was found to be higher (80-100) compared to mineral oil (10-40) (MacKenzie 2003).

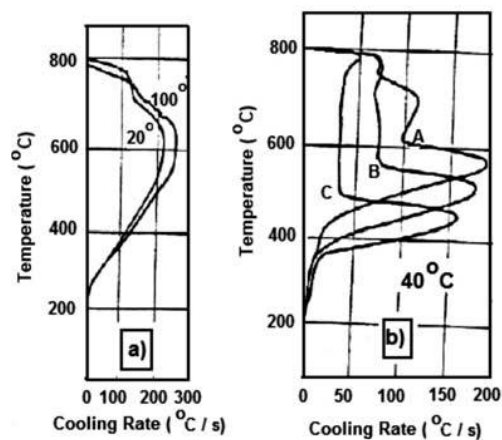


**Figure 2.4: (a) cooling curves with rapeseed oil and (b) mineral oils (Rose 1940)**

Critical cooling parameters of canola oil are similar to that of sunflower and cotton seed oil while those of corn and soyabean oil are higher and lower compared to canola oil respectively (de Souza et al. 2009). Crude and partially hydrogenated and winterized soyabean oil were tested for their quenching ability at an agitation rate of 0.3 m/s at 40 °C in a tensi agitaion system by (Totten et al. 1999) using oxidised steel probes. Their investigation showed that hydrogenated and winterized soyabean oil had similar cooling characteristics compared to the minerl oil while the crude vegetable oil had cooling characteristics that were higher than the mineral oil used. Sunflower oil had higher peak cooling rate of 50 °C/s compared to mineral oil (40 °C/s) in the work of (Prabhu and Prasad 2003). Vegetable oils made from groundnut and coconut were also investigated by them. Their results clearly showed higher peak flux during quenching in vegetable oils compared to mineral oil. One explanation for their superior

performance over mineral oil was due to their lower viscosity and higher flash point in comparison to mineral oil.

Quenched microstructure in the AISI 1040 steel consisted of martensite and mixed microstructure comprising of bainite, pearlite, and ferrite, for the vegetable oil quenched test pieces while pearlite and ferrite structures were observed in the mineral oil quenched steel specimen. The lower viscosity of vegetable oils led to enhanced wetting with lower contact angle compared to mineral oils (Prabhu and Fernandes 2007). The activation energy shown for the sunflower and coconut oils were found to be lower while that for castor, palm and cashew nut shell oil were higher compared to the mineral oil tested.

**Table 2.1: Flash point and viscosity of various edible vegetable oils (Simencio Otero et al. 2012, Souza et al. 2009)**

Vegetable oil	Flash point (°C)	Viscosity (cst)	
		Temperature (°C)	cst
Canola oil	335	40	24.9
Coconut oil	288	37.8	29.8
Corn oil	340	40	33.5
Cottonseed oil	234	37.8	37.9
Crambe oil	274	40	49
Gingelly oil	260	37.8	39.6
Groundnut oil	340	37.8	42
Hazelnut oil	221	38	24
Linseed oil	222	37.8	30.5
Olive oil	225	37.8	43.2
Palm oil	320	37.8	47.8
Peanut oil	340	37.8	32
Rapeseed oil	246	37.8	54.1
Soybean oil	343	40	31.5
Sunflower oil	274	40	33.2
Tea seed	252	40	36

The peak heat transfer coefficient of sunflower oil was found to be the highest and was about 8% higher than that obtained during quenching in mineral oil. Various vegetable oils such as cotton, canola, soybean sunflower and canola were assessed for their cooling performance and compared with mineral oils by (de Souza et al. 2009). An unstable vapor phase stage with reduced duration leading to faster cooling of the metal probe was observed from their reported cooling curves for the vegetable oils compared to mineral oils. However, their study also showed that the vegetable oils have poor oxidation stability. The potential to oxidize was the highest for soybean oil (1.9 %) followed by sunflower (1.85 %), cotton (1.6 %), corn (1.43 %) and canola (1%) had the least oxidation potential because of their higher linoleic and linolenic content.

A study on the oxidation stability was conducted by (Said et al. 2013). The report demonstrated the poor oxidation resistance of soybean and palm oil. These oils underwent rapid and increased viscosity due to oxidation compared to the tested fast and slow speed quench mineral oil. The peak heat transfer coefficient of the oxidized soybean oil on ageing for 60h were lowered by about 28 % compared to the fresh oil indicating the need to develop antioxidants to minimize oxidation tendency (Souza et al. 2013a). The oxidation instability of vegetable oils was due to their molecular composition (Souza et al. 2013b). Figure 2.5 shows the effect of oxidation on the viscosity of soyabean quench oil compared to mineral oils (Souza et al. 2013a). The mechanical properties of soyabean oil quenched EN 19 steel was compared with that of mineral oils. The results obtained clearly show the viability of soyabean to quench harden EN 19 steel grade (Shinde 2013).

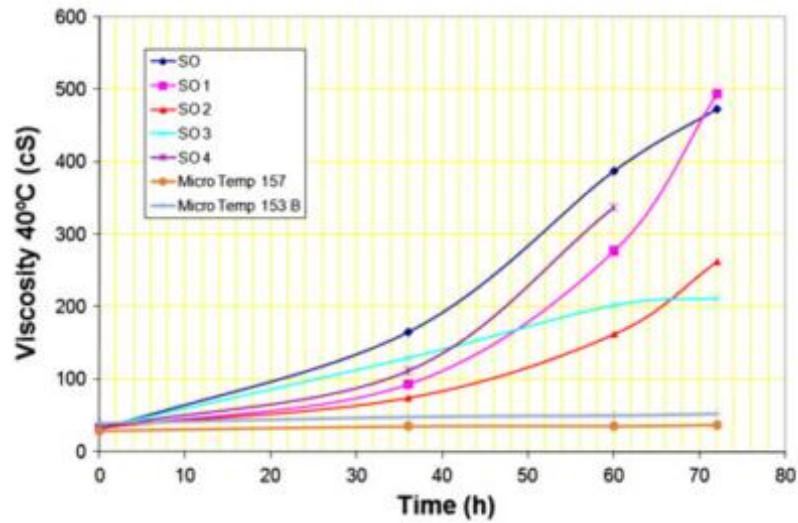


**Figure 2.5: Variation of viscosity increase with exposure time during testing for oxidation tendency of soybean oil with and without addition of various antioxidant compounds (Souza et al. 2013a)**

#### 2.2.1.2.2.2 Non-edible vegetable oils

The oils discussed in the previous section are edible and their use in heat treating industry will negatively impact the food processing industry. This is especially true in the case of India, which imports large tonnage of edible oil to be used in the food processing industry. The spreading kinetics, rewetting behaviour and critical cooling parameters of pongamia pinnata, a non-edible vegetable oil was found to be faster, more uniform and higher compared with mineral oil (Ramesh and Prabhu 2014b). In India, pongamia oil is obtained by crushing the seeds of the Hongai tree, Figure 2.6. It is used more popularly in hair oil products and is presently explored for the production of biodiesel (Vivek and Gupta 2004).



**Figure 2.6: Photograph of karanja tree and seeds (Karikalan and Chandrasekaran 2015)**

Another potential bio-quenchant that requires investigation from the Indian perspective is neem oil (Figure 2.7) and is investigated in the present study along with pongamia oil. Neem oil is also known as *Azadirachta indica*. Neem tree is grown throughout India mainly in the states of Uttar Pradesh, Tamilnadu, Karnataka, Madhya Pradesh, Maharashtra, Andhra Pradesh, and Gujarat. A neem tree roughly produces about 31 to 55 kg of fruit per year having 40% seed constitute (Rao 1991). A tone of neem seed when processed produces nearly 200 kg of neem oil indicating an annual production of nearly 59500 m<sup>3</sup> of neem oil.



**Figure 2.7: Photograph of neem seeds**

The potential of neem oil as quench medium has not been explored by the cooling curve method using ISO 9950 inconel probe and its cooling and heat transfer characteristics

have not been determined. The Government of India has recently increased its focus on the production, research and development activities for non-edible oils in its Mini Mission-III-Tree Borne Oil seeds to be taken up in the states of Arunachal Pradesh, Chhattisgarh, Jammu & Kashmir, Madhya Pradesh, Maharashtra, Mizoram, Rajasthan, Tamil Nadu, Tripura and Uttar Pradesh (Government of India 2016-2017).

### **2.2.1.3 Molten salts and metal Quenchants**

Molten salts are most suitable quench medium when hot metal is to be rapidly quenched to high temperatures (Chandler 1996) such as those used in austempering and martempering (Totten et al. 1993). Molten salt bath comprises of one or more chemical salts which are melted to form a liquid into which metal is quenched by immersion (Dexter). The goal in such type of quenching is to obtain rapid heat transfer to elevated temperature to favour formation of tempered hard phases of martensite and/or bainite (Verhoeven 2007). Salts in this category are made from mixtures of sodium and potassium nitrates, sodium nitrate and nitrite, potassium nitrate and sodium nitrate and nitrite and sodium-potassium and barium chlorides (Dexter) and potassium-lithium-sodium chlorides (Chandler 1996). The melting temperatures of these salts can be adjusted by varying the relative proportion of constituent chemical compounds and by the addition of water content. Their operating temperature limit ranges from 500 °C to as low as 80 °C by the addition of approximately 10% water (Chandler 1996). Addition of water lowers the viscosity and increases the quench severity of salt bath. Quench severity can further be altered by the bath temperature and the agitation rate (Dubal 2003). Molten salts are preferred over oil quench oils when the steels are to be quenched to elevated temperature as the operating temperature of the oils cannot be extended beyond 250°C (Liscic et al. 2010). The other advantages offered by salt baths are they provide rapid heating, uniform temperature distribution, oxidation prevention and surface decarburization (Verhoeven 2007), reduced distortion and cracking in high-speed tool steel (Dexter) and uniform hardness (Liscic et al. 2010). Apart from austempering and martempering molten salt bath can be utilized for other processes like isothermal annealing, hardening, nitriding, carbonitriding etc. (Kopeliovich). However, molten salt bath usage suffers from disadvantages like disposal of salts, contaminations in the salt alter their quenching ability. The racks, fixtures and the steel parts quenched

in salt bath requires post quenching cleaning operation to remove the adhered salts. This is achieved by dipping the metal components in hot water and/or using a water spray (Dubal 2003). Overheating and quenching incompatible materials would lead to explosion and safety issues. The salts baths require periodic monitoring to remove sludge, addition of the water content and makeup salt to compensate for drag-out losses. In the case of operation under humid environment conditions, preheating of the bath to remove the absorbed water would be needed (Totten et al. 1993). Rao and Prabhu (2017) conducted quenching experiments using eutectic  $\text{NaNO}_3\text{-KNO}_3$  quench medium at various bath temperatures ranging from 200 to 450 °C in steps of 50 °C. It was shown that the mean peak flux was lowered and the corresponding temperature increased with increase in the bath temperature. Further, the study showed that the uniformity in the theoretical hardness parameter ' $t_{85}$ ' was reduced with increased bath temperature.

Molten metals like lead, tin, bismuth and their eutectics or alloys have also been used as quenchants for heat treating steel. The melting temperature of lead is about 327 °C while that of tin-lead eutectic is about 183 °C and that of eutectic lead-bismuth alloy is around 125 °C. Quenching in molten metal does not exhibit vapor stage (Verhoeven 2007) and higher thermal conductivity of these metals compared to the molten salts make them a good high temperature quenchant. However, toxicity of lead and lead bearing metals do not make them favourable quench media. A limitation of molten metal quenchants is that their surface must be covered using graphite powder to prevent surface oxidation (Verhoeven 2007). The use of graphite could affect the heat transfer properties of the bath. Also, molten metal quenchants have specific heat capacity about 10 folds lower than that of molten salts (Liscic et al. 2010) which makes them less popular quenchants compared to molten salts.

### **2.2.2 Characteristics of steel part**

The speed at which a steel part is cooled depends on the characteristics of the metal part being quenched and dictates the selection of the quenching medium. The features of the part being quenched that must be considered are: the chemical composition (carbon content and alloying elements) of steel being quenched, the shape of the component, its size (surface area, volume and specific heat), surface conditions and presence of weld etc.



The effect of carbon content on hardness was shown by (Çalik 2009). His work showed that, quenching of AISI 1020, 1040 and 1060 steels having carbon contents of 0.2, 0.4 and 0.6 % respectively in water showed pearlite + ferrite, pearlite + ferrite and pearlite + ferrite + martensite microstructures. (French and Klopsch 1925) conducted quenching experiments with spheres, cylinder and plates of various sizes. They showed that the cooling rate measured at 720 °C is inversely proportional to their characteristic dimension (diameter and thickness). Further, the cooling times were shown to be inversely proportional to the cooling rate at 720 °C. The effect of quenching probes of AISI 304 steel of section diameters 25, 38 and 51 mm in fast oil were shown by (Monroe and Bates 1983). Their experiments showed that the peak cooling rate at the centre was reduced with increased section size and were 34, 21 and 14 °C/s for 25, 38 and 51 mm section diameters. Higher peak heat flux transients were obtained during quenching with Ø 28 mm compared to Ø 44 mm of AISI 1040 steel of  $l/d=2$  during quenching in aqueous media (water and brine). Quenching of these probes in oil showed higher peak heat flow with Ø 44 mm steel (Fernandes and Prabhu 2007). The effect of steel mass during studied quenching was studied by (Grum et al. 2001). Quenching experiments with 42CrMO4 steel specimens of diameter 35 mm having heights of 5 and 15 mm were performed by them. The quench media that were used are 10% aqueous polymer solution and a rapid quenching oil. Their experiments showed better quenching of the larger test piece in the polymer solution than in the oil medium. Superimposition of the cooling curves on the CCT diagram for 42CrMO4 showed that the microstructure of the polymer quenched samples consisted of bainite and martensite (for both the test samples) compared to bainite, martensite and ferrite observed in the case of the 15 mm sample quenched in oil. AISI 5160 in the hardened and tempered condition showed higher mechanical properties for the 50 mm diameter specimen compared to the 140 mm round corner specimen (Perla et al. 2017). They showed that grain size of the raw stock used during quenching has a significant influence on the microstructure and mechanical properties. ASTM grain size 7 was shown to have a tempered martensite structure compared to the mixed microstructure for the ASTM 9 grain sized test piece. The study clearly showed the suitability of larger grain sized steel over steels with smaller grain size to develop higher mechanical properties during quenching of shallow hardening steel grades.

### **2.2.3 Quenching conditions**

The operating conditions that affect the quenching outcomes are: agitation, racking arrangement and quenching medium temperature. Monroe and Bates (1983) studied the effect of temperature and agitation velocity on the cooling severity of AISI 304 steel. They used fast oil, water and 16% aqueous polymer as quenching media. The severity of cooling reported by the researchers shows that effect of these parameters was limited in the case of quenching with oil while the polymer solution was most sensitive to changes in the operating conditions. The effect of agitation on the cooling rate of a 38 mm steel probe was investigated by Monroe and Bates (1983) during quenching in water that was maintained at 50 °C. The cooling curves reported by them show that with increased flow rate of the quenching medium, there was an increase in the peak cooling rate. The peak cooling rates obtained were 27, 30 and 33 °C/s for quenchant flow rates of 0, 0.4 and 0.8 m/s. Operating temperature significantly affected the cooling rates provided by the mineral oil. They used a mineral quench oil that showed repeatable cooling rate vs. temperature behaviour and heated it to temperatures of 25, 40, 60 and 80 °C. Cooling rates plots published by them showed that temperature of the oil affected the cooling rates during the nucleate boiling regime. The peak cooling rate in their study increased with operating temperature upto a temperature of 60 °C and thereafter declined when the oil was operated at 80 °C (Ma 2002). The effect of oxidation on the cooling behaviour of 4140 steel probes of  $\text{Ø } 9.5 \times 38.1$  mm was done by Ma (Ma 2002). Argon gas at a flow rate of 12.77 cm<sup>3</sup>/min was supplied to displace oxygen in the furnace during heating of the 4140 steel quench probe. The results of this study showed that the cooling behaviour of the oxidized probe did not exhibit vapor phase stage and caused increased cooling rate compared to the unoxidized probe. He attributed the increase in the cooling rates to the increase in the surface roughness which in turn increased the nucleation sites leading to faster cooling.

### **2.3 Assessment of Cooling Performance of Quench Media**

The techniques to quantify the cooling performance of liquid quench medium have evolved considerably from (i) The laborious U-curve and Jominy end quench test method to (ii) The quick measurement techniques such as The General motors (GM) quenchemeter (nickel ball test), the hot wire test, and the 5-second interval test. In

between these two extremes lies the now familiar and most popular cooling curve method.

Cooling curve method requires a thermocouple inserted metal probe that is heated and subjected to cooling by the quench medium. Temperature data from the thermocouple is recorded and is analyzed in the following one or more ways to draw conclusions about the quenching process.

### **2.3.1 Critical cooling parameters**

The following parameters obtained from the cooling curve and the cooling rate curve (Figure 2.8) allow comparison of the various quench media available. The critical cooling parameters may also be used to check the quality of the quench media at various intervals during production to assess deviations in the behaviour of the medium due to use over an extended time frame.

- The transition temperature between the film and nucleate boiling phase ( $T_{f-b}$ )
- The time at which transition from the film boiling phase to nucleate boiling phase occurs ( $t_{f-b}$ )
- Cooling rate at 705 °C ( $CR_{705}$ ), describes the rate required to avoid austenite to pearlite transformation for most steels.
- Maximum or the peak cooling rate ( $CR_{max}$ ) and the temperature at the peak cooling rate ( $T_{max}$ ), both these must be high to prevent pearlite transformation during continuous cooling and to avoid the nose of the CCT curve.
- Cooling rates at 300°C ( $CR_{300}$ ) and 200°C ( $CR_{200}$ ), represent the cooling rate in the martensite transformation range and need to be slow enough to prevent distortion and cracking in the steel.

These parameters though important from the perspective of quantifying a quench medium do not provide any information regarding the properties developed in steel. Further, they are discrete information taken from the cooling curve and the cooling rate curve and do not represent quench curve in its entirety.

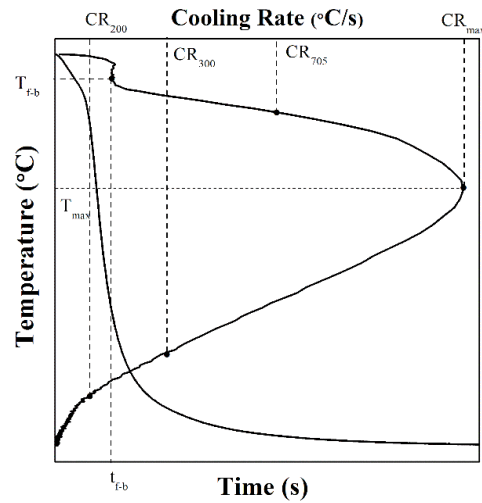


**Figure 2.8: Cooling curve and cooling rate curve showing various critical cooling parameters**

### 2.3.2 Grossmann quench severity

In this method, known heat flux are provided to the surface of the metal that is to be quenched. Cooling curves are generated using a finite difference program. From the curves produced the cooling rate at 705°C is obtained. Temperature of 705°C was chosen since it lies in the pearlite transformation range for most steels (Totten et al.). The cooling rates at 705°C is related to the Grossmann's H factor according to the equation:  $H = \frac{h}{2k}$  (m<sup>-1</sup>), where 'h' is the heat transfer coefficient and 'k' is the thermal conductivity of the metal. The limitations of this technique are it does not describe the agitation conditions adequately. It does not provide information regarding the time required to complete the quenching process. Moreover, Prabhu and Prasad 2003 showed that mineral oil that had higher H value of 0.46 compared to a H value of 0.45 for the sunflower oil resulted in lower hardness compared to that obtained for sunflower oil quenched steel.

### 2.3.3 V-value and hardening power analysis

V-value was originally developed for oil quench media by Tamura and is expressed as

$$V = \frac{T_c - T_d}{T_s - T_f} \quad (2.1)$$

Where  $T_c$  is the  $T_{f-b}$  temperature,  $T_d$  is the temperature at the start of convective boiling stage,  $T_s$  is the temperature at the start of austenite to pearlite transformation and  $T_f$  is the temperature at the start of martensite transformation.

Hardening power method developed by Segerberg for polymer media and oil are expressed by the following equation

For polymers,

$$HP=3.54CR_{550}+12.3CR_{330}-168 \quad (2.2)$$

For oils,

$$HP=91.5+1.34T_{f-b}+10.88CR_{600-500}-3.85T_d \quad (2.3)$$

These equations were obtained by regression analysis of a series of cooling curves obtained during quenching under various agitation rates.

### 2.3.4 $V_s/V_c$ , quench uniformity analysis

The degree of uniformity in cooling was expressed as a dimensionless number by measuring the difference in the cooling rate between 300°C and 200°C at the centre and surface of the steel being quenched. These temperatures were chosen as they represent the martensite start and finish of many steels. Mathematically,  $V_s/V_c$  ratio is expressed as

$$\frac{V_s}{V_c} = \frac{(t_{200} - t_{300})_c}{(t_{200} - t_{300})_s} \quad (2.4)$$

The uniformity of cooling improves as the  $V_s / V_C$  ratio approaches 1.0 and deteriorates as it moves towards zero.

### 2.3.5 Quench factor analysis

In this approach, the cooling curve is combined with the time-temperature-transformation (TTT) to give a number than is related to the hardness developed in the steel during quenching. The start of transformation curve is represented by the following equation.

$$C_T = -K_1 * K_2 * \exp\left[\frac{K_3 * (K_4)^2}{RT(K_4 - T)^2}\right] * \exp\left(\frac{K_5}{RT}\right) \quad (2.5)$$

where  $C_T$  is the locus of points forming the time-temperature curve at which a constant amount of a new phase would be formed during quenching. The constants  $K_1$  to  $K_5$  define the shape of the TTT curve.  $K_1$  is a constant that equals the natural logarithm of the phase fraction that remains untransformed during quenching. Typically, a value of 0.995 is assigned to  $K_1$ ,  $K_2$  is another constant related to the reciprocal of the number of nucleation sites, the constant  $K_3$  is related to the energy required to form a nucleus,  $K_4$  is a constant related to the solvus temperature of the steel used and  $K_5$  relates to the activation energy of diffusion,  $R = 8.3143$  J/K mol, the universal gas constant and  $T$  is the temperature in Kelvin.

An incremental quench factor,  $q$ , for each time step in the cooling curve is calculated as follows to obtain the incremental quench factor ( $\bar{q}$ )

$$\bar{q} = \frac{\Delta t}{C_T} \quad (2.6)$$

where  $\Delta t$  is the time step used during the quenching experiment.

Thus  $\bar{q}$ , the incremental quench factor is defined as the ratio of the time that an alloy spends at a particular temperature during quenching to the time required for transformation to begin at that temperature. The incremental quench factors are summed over the entire transformation range to produce the cumulative quench factor ( $\bar{Q}$ ) according to:

$$\bar{Q} = \sum \bar{q} = \sum_{T_2}^{T_1} \frac{\Delta t}{C_T} \quad (2.7)$$

The cumulative quench factor reflects the heat removal characteristics of the quenchant as indicated by the cooling curve. It is inversely related to the developed hardness due to quenching of the steel. Hardness and strength of the steel increases with the decrease in the numerical value of the quench factor (Totten et al. 1993).

## 2.4 Interfacial Heat Flux Measurement/Computation

The basis of the quenching process rests on the heat flux that is generated at the metal/quenchant interface. It is this heat that flows from the hot metal into the quenchant which causes phase transformation, mechanical properties development, and the accompanying ill-effects of residual stress and distortion. Estimation of heat flux evolved during quenching operation is thus a crucial necessity to predict the effects of quenching. It also facilitates computation of temperature distribution in the metal providing insights that aid to optimize the quench requirement. Methods that facilitate, the calculation or measurement of the interfacial heat flux are either direct or indirect. The direct method uses a heat flux gauge made in the form of foils and films that are attached to the surface of the metal. foils are preferred over films as they are thick enough to be representatives of the bulk metal whose heat flow needs to be assessed (Mocikat and Herwig 2009). Typically, these gages consist of temperature sensors that are separated by a layer of insulation. The gage is attached to the surface by means of adhesives. These gages produce an output signal in volts when subjected to temperature filed indicating the heat flux values. The indirect method comprises of (1) lumped heat capacitance (2) temperature gradient (3) Kobasko's method and (4) Inverse heat conduction problem (IHCP).

### 2.4.1 Lumped heat capacitance method

This method is valid under the condition that the temperature gradient does not exist in the metal during cooling. It is limited to small metal components and thin components in which the temperature gradient will be negligible during quenching. The governing equation that is used to compute the heat flux is:

$$q = h(T_p - T_f) = -\frac{V\rho C_p}{A} \frac{dT_p}{dt} \quad (2.8)$$

where 'h' is the heat transfer coefficient obtained at the probe surface, 'A' is the surface area of the probe, 'T<sub>p</sub>' is the probe temperature, 'T<sub>f</sub>' is the quenchant temperature, 'C<sub>p</sub>' is the specific heat of the probe material, 'ρ' is the specific density of the probe material,

'V' is the volume of the probe, 't' is the time and ' $\frac{dT_p}{dt}$ ' is the cooling rate of the probe.

### 2.4.2 Temperature gradient method

This method was developed by Liscic using a probe called Liscic/Nanmac probe. Figure 2.9 shows the probe and the arrangement/positions of the thermocouples embedded in the probe to measure the temperature gradient. The heat flux was calculated using the equation  $q = k \frac{\Delta T}{\Delta x}$ , where all the parameters have their usual meaning.

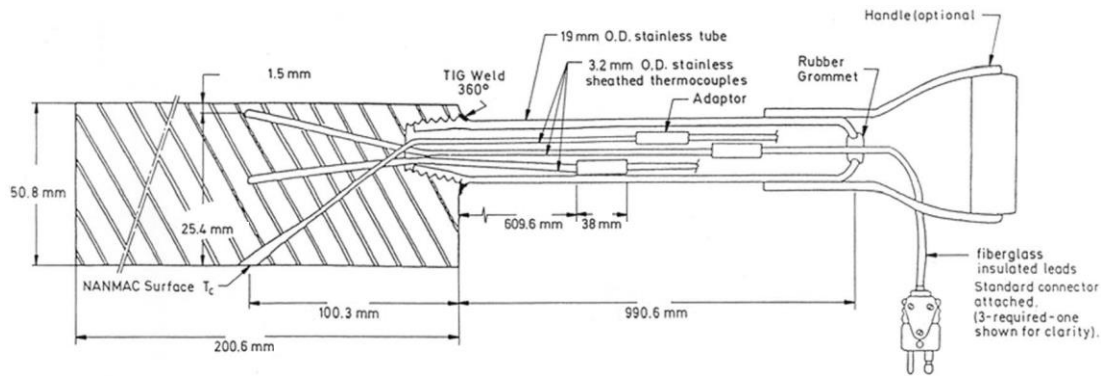


Figure 2.9: Schematic of the Liscic/Nanmac probe (Liscic et al. 2010)

### 2.4.3 Kobasko's method

The heat transfer coefficient was calculated in this method based on the following mathematical expression:

$$h = \frac{Bi_v k V}{KA} \quad (2.9)$$

Here  $Bi_v$  is the generalized Biot number,  $k$  is thermal conductivity of the probe, 'V' the volume of the probe. The Biot number is related to ' $K_n$ ' the Kondratjev number by equation

$$K_n = \frac{Bi_v}{(Bi_v^2 + 1.437 Bi_v + 1)^{1/2}} \quad (2.10)$$

And the  $K_n$  number is obtained from the Kondratjev form factor using the relation,

$$K_n = CR \frac{K}{\alpha} \quad \text{where } CR \text{ is defined as } CR = \frac{\ln(T_1 - T_q) - \ln(T_2 - T_q)}{t_2 - t_1} \text{ and } \alpha \text{ is the}$$

thermal diffusivity of the probe material where  $T_q$  is the temperature of the quenchant



and  $T_1$  and  $T_2$  are the temperature corresponding to the times  $t_1$  and  $t_2$  respectively in the probe during quenching (Liscic et al. 2010).

#### **2.4.4 Inverse heat conduction problem**

This method consists of obtained the heat flux transients at the metal/quenchant interface by using the temperature measurements taken at the interior of the metal. It considers the entire temperature during quenching. It considers the temperature gradient that are developed in the metal during quenching and is preferable over other method mentioned above. In general, the solution comprises of one or more optimization techniques for solving the Fourier equation.

#### **2.5 Uniformity of Quenching**

The nature of contact of the liquid quench medium with the metal surface during quenching has significant implications on the developed properties. The progress of the rewetting front determines the temperature distribution and its understanding is of fundamental importance to describe the quenching process as uniform or non-uniform (Tensi and Lainer). Depending on the rewetting time the rewetting process is described as Newtonian or non-Newtonian. The rewetting is said to be Newtonian if the wetting is completed in a short period of time otherwise it is called non-Newtonian. Newtonian wetting promotes uniform heat removal and is preferred over the non-Newtonian category (Ramesh and Narayan Prabhu 2013). The Newtonian type of quenching is exhibited by brine quenching media (Ramesh and Prabhu 2015) while oils and most of the water based media shows non-Newtonian type of rewetting. The nature of the rewetting front is studied by the following methods:

1. Measurement of temperature measurements just beneath the surface of the steel
2. Recording the development and progress of the rewetting front motion during quenching by video imaging
3. Measurement of contact conductance
4. Measurement of contact angle to analyse the wetting and spreading behaviour of the liquid medium

Hollow cylinders made from high chromium carbon steel was quenched in mineral oil to obtain the influence of shape of the metal surface on the rewetting phenomenon. Near surface temperature measurements showed wide rewetting temperatures resulted between the inner and the outer surface of the cylinder. The rewetting temperatures were found to be higher at the inner surface compared to the outer surface of the cylinder causing differential cooling. The rewetting velocity at the inner surface was insignificantly affected by the liquid agitation upto a fluid velocity of 0.6 m/s (Tensi and Lainer). Photographs (Figure 2.10) during quenching of CK 45 steel in soybean in shows the sequence of rewetting front motion (Totten et al. 1999).

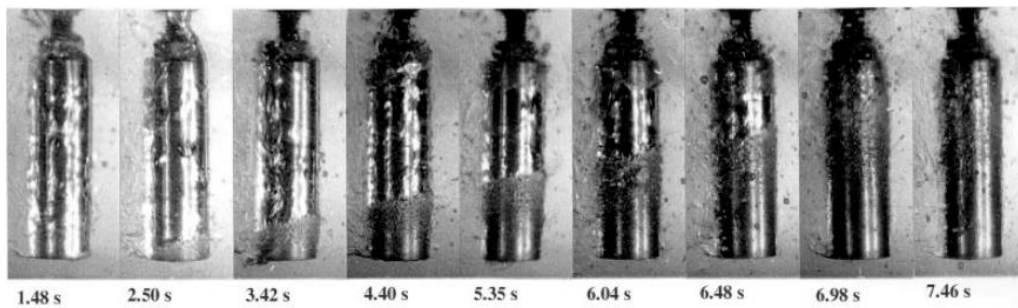


**Figure 2.10: Rewetting front motion during quenching of  $\phi 15$  by 45 mm steel cylinder in soybean oil (Totten et al. 1999)**

It shows the dynamic process of rewetting. The front movement from the bottom to the top portion along the probe surface is clearly observed here. The soybean oil rewetted the probe surface in about 6 s. The time to completely rewet a standard inconel probe quenched from 850 °C in aqueous PAG media of 5, 10, 25, 50, 75 and 100 concentrations were found to increase with concentration and were 6.4, 6.4, 12.7, 16.8, 24.8 and 44.2 respectively (Ramesh and Narayan Prabhu 2016). The corresponding values for quenching in pongamia, palm and mineral oil quenching media were found to be 10.9, 10.2 and 12.7 s (Ramesh and Prabhu 2014b). The rewetting time was shown to be dependent on the viscosity of the oil. Shorter time resulted for oils with lower viscosity compared to the more viscous mineral oils. (Ramesh and Prabhu 2014a). The effect of gaseous content present in water on the rewetting kinematics is shown in Figure 2.11 during quenching of inconel probe (Nayak et al. 2016). Carbonated media showed more uniform rewetting front boundary compared to water. However, the rewetting time was increased because of higher gaseous content in the medium.

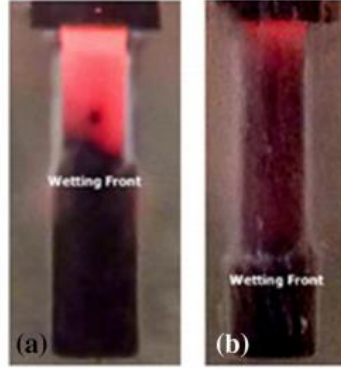


**Figure 2.11: Rewetting front photograph during quenching in (a) water and (b) carbonated water.**

To quantify rewetting into uniform and non-uniform regimes, the following dimensionless wetting time parameter was developed and is given by.

$$\tau_{wet} = 1 - \frac{\sqrt{\frac{1}{n} \sum \frac{1}{n} (t_{avg} - t_n)^2}}{1 + t_{max} - t_{min}} \quad (2.11)$$

where  $\tau_{wet}$  is dimensionless rewetting time,  $n$  is number of radial locations,  $t_n$  is rewetting time at  $n$ th radial location,  $t_{avg}$  is the average rewetting time (s).  $t_{max}$  is maximum rewetting time (s). The numerator of the above equation is the standard deviation of rewetting time which determines the variation of rewetting times. The value of standard deviation of rewetting time was normalized with the range of rewetting time ( $t_{max}-t_{min}$ ) to make it dimensionless. The nature of wetting front is more uniform as the  $\tau_{wet}$  approaches the value of 1 (Ramesh and Prabhu 2015) and showed that quenching with brine was more uniform than polymer and water.

The degree by which a quench medium wets the surface is given by the contact angle it makes with the metal surface. It is measured using a charge-coupled device camera. Wetting angle is defined as the angle made by a sessile drop of a liquid medium at the triple line of contact formed between the liquid-air-solid surface (Figure 2.12).

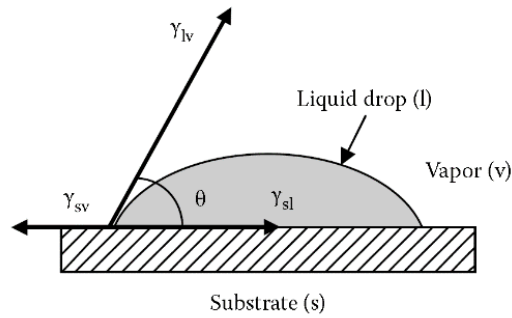


**Figure 2.12: Sketch illustrating a solid substrate wetted by a sessile liquid drop**

The equation facilitating computation of the degree of wetting is known as the Young's equation and is expressed as:

$$\cos \theta_e = \frac{\gamma_{sv} - \gamma_{sl}}{\gamma_{lv}} \quad (2.12)$$

where  $\theta_e$  is equilibrium contact angle,  $\gamma$  represents the surface energy and the subscripts s, v, and l designate solid, liquid and vapour phases. The rate at which the contact angle changes gives the ability of the liquid to spread on the surface. Lower the value of the angle implies better wetting and more uniform heat removal. Various researchers have determined the wetting angle of a myriad of quenching media that have been used till date. It was shown that water had poor wettability while oil quench media had higher ability to wet the surface indicating viscosity of the quench medium affects its wetting ability. Prabhu and Fernandes (2007) measured the activation energy for spreading of oils by conducting wetting experiments at various temperatures. They showed that oils having lower activation energy during wetting had higher heat extraction ability compared to those which had higher activation energy.

## 2.6 Summary

Quench hardening is an essential technological process for hardening of steel alloys. Of the various factors that affect the quenching operation, the size of the metal alloy being quenched and the liquid medium used are most important. To assess the influence of these factors an analysis of the interfacial heat flux transients is necessary. Further, heat flow during quenching is a localised surface process influenced by the wetting of the liquid media. Spatiotemporal assessment of heat flow from steels, wetting kinematics and kinetics would be helpful for better understanding of the outcome of the quench hardening process.

Various conventional liquid quench media have been discussed in the literature. Their quenching ability has been characterized using the standard ISO 9950 probe. The drawbacks and/or limitations of the conventional media have been dealt with. The literature review clearly outlines the need to develop eco-friendly media capable of hardening steel. In light of this requirement, nanofluids have shown promising results. However, the discrepancies observed during quenching of inconel probe in nanofluids necessitates further investigation. Non-edible vegetable oils, derived from plant matter are environmental friendly and are obtained from renewable sources. Their ability to quench harden steel are relatively unexplored and warrant investigation.

The focus during the quenching experiments were more towards the characterization of liquid media used for hardening. In most of the publications cited, the quench part material used was restricted to inconel, stainless steel or silver. These alloys do not consider the complexity intertwined during quenching of steel alloys. Unlike these alloys, steels undergo phase transformation during quenching. Phase transformation causes evolution of latent heat leading to deviation in the cooling curves compared to those reported using non-transforming alloys. Further, the size of the steel quenched markedly affects the cooling process and must be considered during the design of the quenching process.

The above stated necessities provide the framework for carrying out experiments directed at the collective issue of section size effect and the use of eco-friendly quenchant for hardening steels.

## Chapter 3 EXPERIMENTAL

### 3.1 Quench Media

In the present investigation water based nanofluids of MWCNT, CuO and Graphene nanoparticles were used. Neem, karanja and sunflower vegetable oils, distilled water and a mineral oil (fast quenching oil) were investigated. The nanofluids used were prepared by the two-step method. In the two-step method, nanoparticles were procured from commercial suppliers and then dispersed in water. The details of the nanofluid media used and their preparation methods are given in Table 3.1.

**Table 3.1: Details of quench media**

SI no.	Nanoparticles	Size	Concentrations (vol.%)	Mode of preparation	Source
1	Distilled water				Prepared in the laboratory
2	Multi Wall Carbon Nanotube (MWCNT)	Upto 500 nm	0.0003 0.003 0.03	Mechanical mixing using a hand held stirrer	Timesnano Co., Chengdu, China
3	CuO	Average particle size: 40 nm	0.01 0.05 0.1 1.0		Sisco Research Laboratories Pvt. Ltd., India
4	Graphene	1 to 5 nm thick	0.01 0.1 0.3	Ultrasonication at 30kHz for 30 minutes	Reinste Nano Ventures Pvt. Ltd.

The vegetable oils used were procured from local suppliers in Mangalore, India. The mineral oil was purchased from Thin Chemie formulations, Tamil Nadu, India.

### 3.2 Quench Probe Details

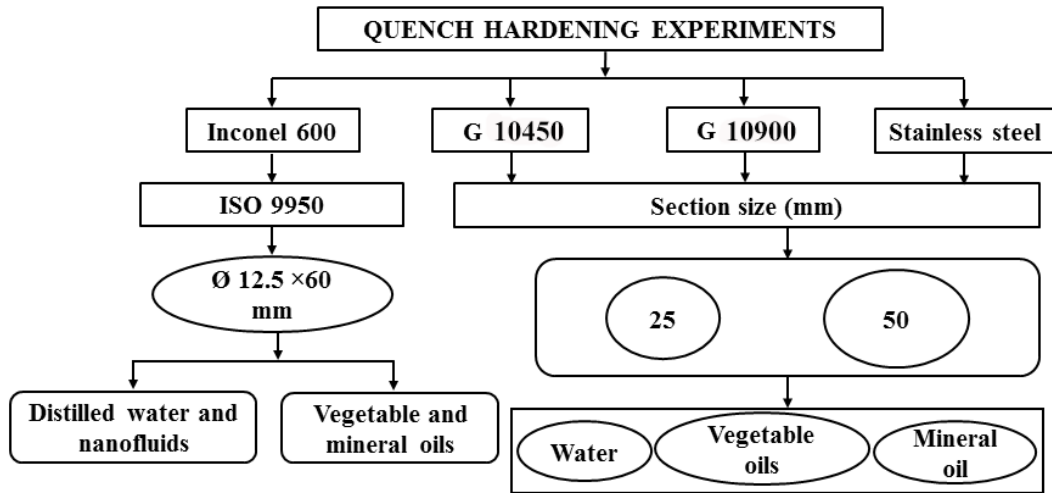


**Figure 3.1: Flow chart showing experiments done in the present work**

Cooling characteristics of the quench media were obtained using inconel 600 alloy probe. The probe was machined to dimensions in accordance with the ISO 9950 standard ( $\text{Ø } 12.5 \times 60 \text{ mm}$ ). The 304-stainless steel (SS) and steel probes of diameters 25 and 50 mm were used to study the effect of section thickness during quenching. These probes were machined to have a height of 30 mm. The flow chart in Figure 3.1 shows the probe-quenchant combination used in the present study. The chemical composition of the metal probes used is given in Table 3.2.

**Table 3.2: Chemical composition of the metal probes**

Metal grades	Elements (%)								
	C	Si	Mn	S	P	Cr	Cu	Ni	Fe
<b>Inconel 600</b>	0.006	0.012	0.027	0.002	-	15.22	0.26	75.67	8.77
<b>304 SS</b>	0.08	-	2	-	-	19	0.3	9.5	69.12
<b>G 10450</b>	0.446	0.187	0.740	0.0330	0.0220	0.01	0.0022	0.0068	98.5
<b>G 10900</b>	0.960	0.204	0.362	<0.001	0.0081	1.4	0.0077	0.0180	97.0

The metal probes were drilled at various locations to accommodate  $\text{Ø } 1.0 \text{ mm}$  K-type thermocouples. A schematic sketch of quench probes indicating thermocouple locations are given in Figure 3.2. The drilled holes in the inconel probe had a diameter of 1.0 mm whereas those in the stainless steel and steel probes were of 1.1 mm in diameter. The

reason for this was that the steel probes underwent phase transformation causing the hole diameter to shrink and this posed problem in removing thermocouples from the quenched specimens. The inconel probe has a 10 mm screw section to fasten the probe to a connecting pipe.

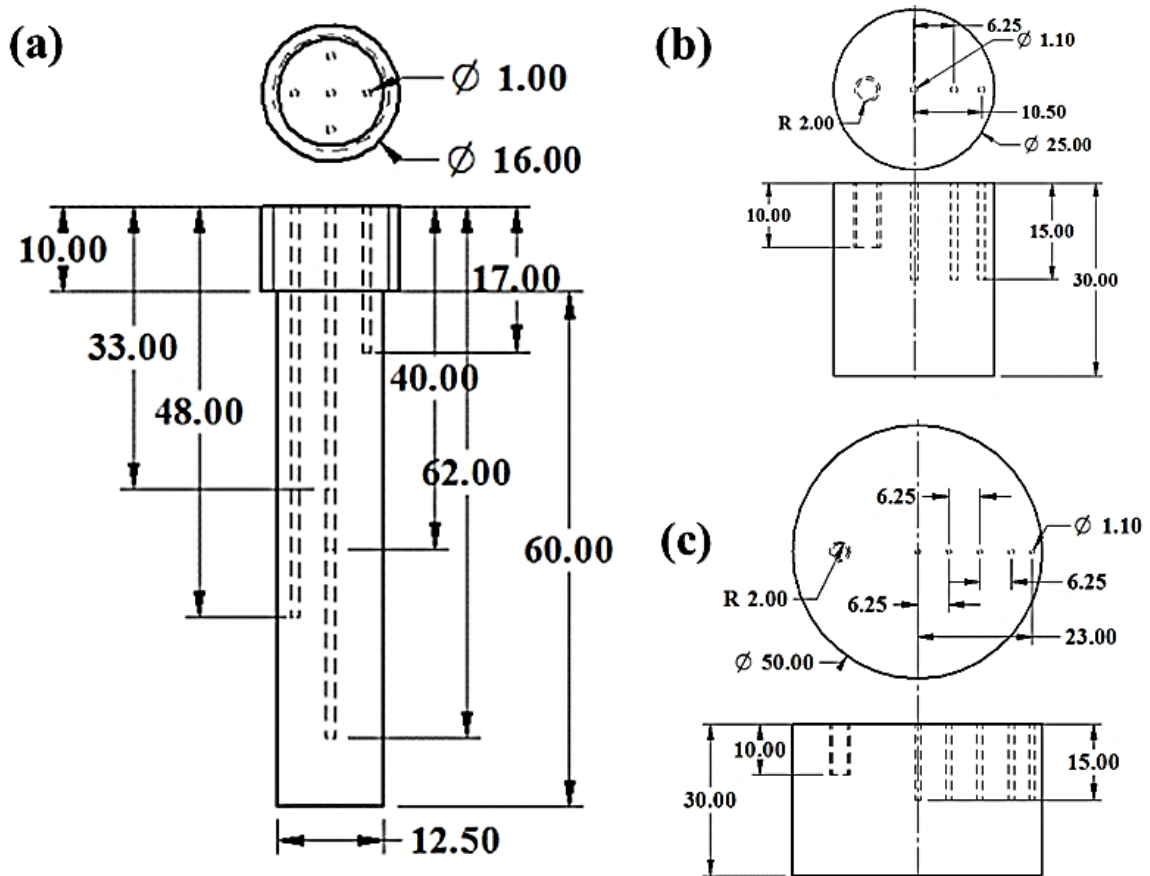


**Figure 3.2: Metal quench probes (a) inconel (b) 25 mm and (c) 50 mm**

The pipe conceals the entry of liquid medium into the drilled holes and facilitates lateral quenching of the probe. In the case of stainless steel and steel probes, a stainless-steel rod replaces the connecting pipe and is fastened to the probe at the threaded hole marked as R 2.00.



### 3.3 Quenching Set-Up and Operation Details

The probes were quenched from 860°C. Quenching experiments were conducted using a pneumatic quench system. A schematic of the quenching facility is shown in Figure 3.3. It consists of a pneumatic cylinder, a 3/2 solenoid valve, an electric resistance furnace, and a quench tank. Such a system helps to control the speed at which the metal probe is immersed into the quench medium and also aids in immersing the probe vertically into the medium. The inconel probe was quenched in 2 lts. of the quench medium (ISO 9950) while the steel probes of section diameters 25 and 50 mm were quenched into a tank containing 4 lts and 15 lts respectively. of quench medium. The embedded thermocouples were interfaced with a PC via a data acquisition (DAQ) module (NI 9213). During quenching experiments, the temperature data was measured and recorded at an interval of 0.1 s. The inconel and SS probes were cleaned with water and acetone after each experiment. Quenching with probes having L/D ratio less than four results in loss of heat from the end faces. This would affect the temperature measurements taken along the radial direction and would not be useful for assessing the effect of section thickness on cooling behaviour.

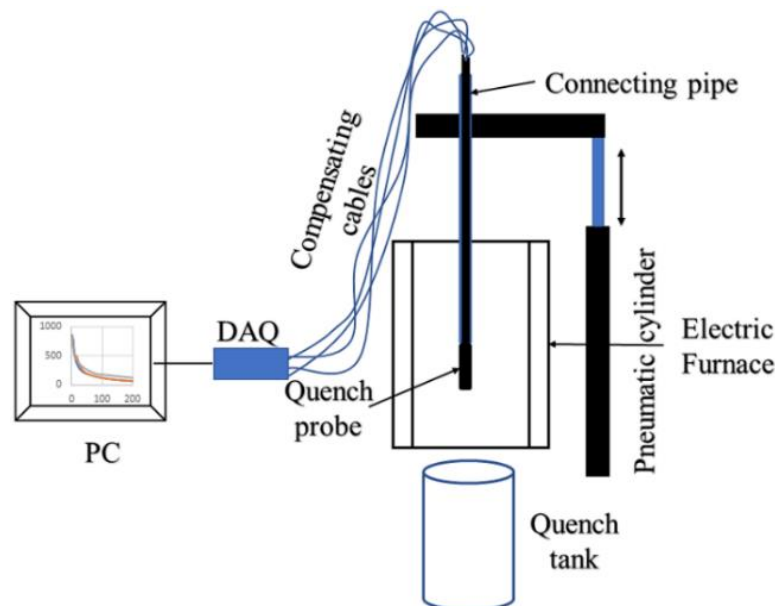


**Figure 3.3: Schematic of the pneumatic quench system**

To minimize this, an insulating paste made of zirconia, alumina and sodium silicate (2:0.5:1) was developed. The top and bottom faces of the steel probes were coated with

this paste. After application of the paste, it was cured by heating it with the probe to a temperature of about 180 °C. The height of the solidified insulation coating ranged from 3 to 10 mm. In addition to providing insulation, the cured paste served as an entry barrier to the quench medium preventing its contact with thermocouples at the top face. The effectiveness with which heat transfer was reduced due to the application of the paste is depicted in Figure 3.4. These cooling curves were obtained using a near surface thermocouple positioned at a depth of 33 mm from the top surface as shown in Figure 3.2a. It shows that the peak rate obtained during quenching with the uncoated probe in distilled water was about 400 °C/s. The corresponding rate with the coated probe was found to be about 16 °C/s. The outcome implies that the insulation coating on the probe surface reduced the peak cooling rate by about 96 % and the probe took a longer time to reach the ambient temperature.

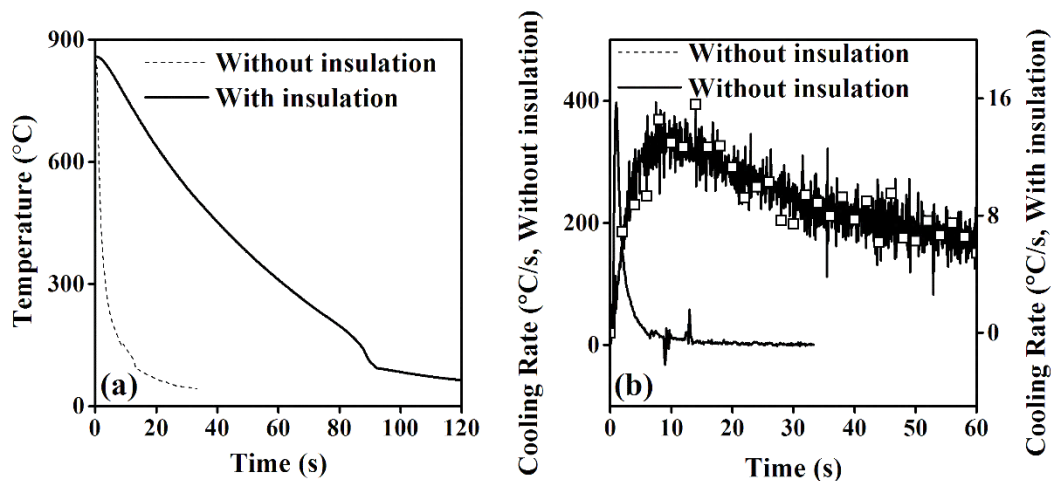


**Figure 3.4: (a) Cooling curves and (b) cooling rates showing the effect of insulating paste on reducing heat transfer from the inconel probe during quenching in water**

### 3.4 Agitation Quench Set-Up

The quench experiments under agitation were done using a Tensi agitation system (Figure 3.5). The set-up consists of a plexiglass quench tank of dimensions shown in the figure and contained 1.5 lts. of the quench medium. The furnace, thermocouples, DAQ (data acquisition system), compensating cables and probe (Figure 3.3) described in the preceding paragraph were used along with the Tensi system to measure the

thermal history during the quench process. The quench medium was agitated using a four-bladed propeller. Three propeller speeds of 0, 500, 1000 and 1500 rpm were provided during the lateral quench experiments. During the quenching process, the system was placed beside the furnace and the probe was manually transferred from the electric furnace to the Tensi quench tank. The probe was heated to about 880°C before transferring it to the Tensi system. The surface temperature of the probe as measured by the near surface sensors dropped by about 10 to 15°C during the transfer. The hot probe was quenched in the liquid medium when one of the near surface sensor read about 860°C. In all the experiments, the impeller was operated prior to the immersion of the hot probe and the temperature of the quenching medium at the start of the quenching process was in the range of  $28 \pm 3$  °C for nanofluids and  $33 \pm 2$  °C for oil quenching media. The thermal data was recorded at intervals of 0.1 s and the probe was cleaned after each experiment as stated earlier.

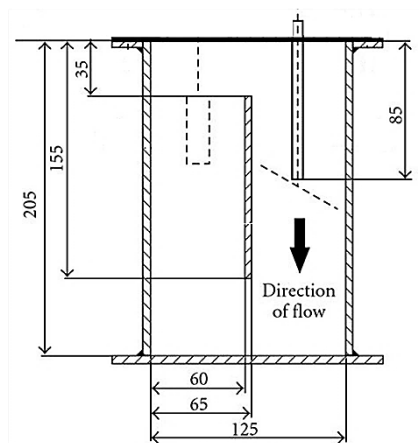


**Figure 3.5: Tensi agitator**

### 3.5 Measurements of Viscosity

Viscosity of the quench medium was measured using a programmable rheometer (Brookfield LDV-IIIU, Brookfield Engineering Laboratories, Inc., USA). A photograph of the rheometer taken during measurement of viscosity of mineral oil is shown in Figure 3.6. The principle of operation of the instrument is to drive a spindle (which is immersed in the test fluid) through a calibrated spring. A rotary transducer was used to measure the spring deflection. The viscous drag of the fluid against the

spindle is measured by the spring deflection. The instrument comes with different spindles for measuring the varying range of viscosities.

The viscosity of water and nanofluids were measured using ultra low adapter (ULA) spindle. The spindle was immersed into specially designed sample chamber containing 16 ml of test liquid was used to measure the viscosity. To measure the viscosity of oils, 800 ml of test liquid was used. Viscosity measurements were made using LV1 spindle. The spindle used is capable of measuring viscosity in the range of 15 – 20,000 cP. Viscosity of oil quench media at high temperature was determined using the Thermosel accessory with SC4-27 spindle (LPA-127) (Figure b). In these cases, the measurement was made using 7ml of test oil at temperatures ranging from 30°C to 210°C.

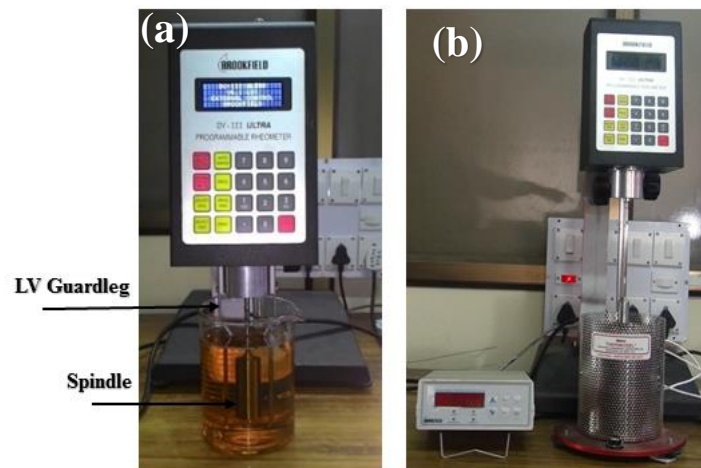


**Figure 3.6: Photograph of Brookfield rheometer**

### **3.6 Metallographic Specimen Preparation and Microstructure Examination**

The quenched steel probes were transversely sectioned at their mid-plane and were subsequently ground and polished to facilitate observation of the evolved microstructure. Sectioning was done with the aid of a silicon carbide abrasive cutting wheel. The sectioned samples were ground using silicon carbide abrasive papers of grit sizes 80, 400, 600, 1000 and 2000 to obtain a flat surface. The flattened surface was polished using diamond pastes of mesh sizes 3 – 4  $\mu\text{m}$  and 1 –  $\frac{1}{2}$   $\mu\text{m}$  to obtain a mirror finished surface.

The polished surface of the G 10450, was etched using a 2% nital etchant. Nital etchant was made by mixing 2 wt.% concentrated nitric acid with 98 wt.% ethanol. The

polished surface was etched using a cotton swab. The etching time was limited to 2 to 5 s. The etched test piece was washed with water and ethanol and dried using a hand held drier. For the G 10900 steels, the etchant used was 10 wt. % potassium metabisulphate solution with distilled water. Etching of the polished surface was done by immersing the surface in the etching medium. The etching time in this case was restricted to about 13 s. The excess etchant was washed and dried as stated before to obtain a dry surface.

Bright field images of the etched surface were observed and captured using a Zeiss microscope (Axioimager.A1m Zeiss microscope).

### 3.7 Measurement of Microhardness

To determine the hardness of the quenched specimens and to obtain its variation along the radius of the sectioned surface, a series of Vickers micro hardness measurements were made on the mirror polished plane. Indentations were made using a load of 1 kgf and 20 s holding time. Figure 3.7 presents a schematic sketch showing the measurement of the indentation diagonal length to calculate hardness.

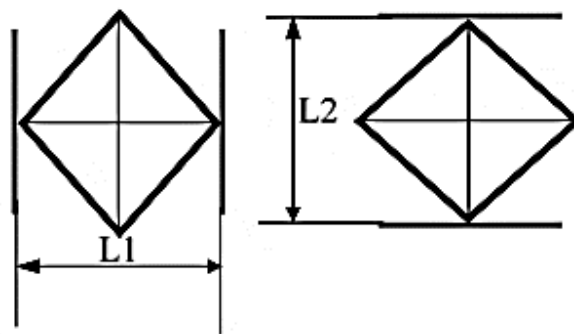


**Figure 3.7: Schematic of diagonal length measurements resulting from Vickers indentation**

### 3.8 Measurement of Thermal Conductivity

Thermal conductivity of nanofluids was measured using KD2-Pro device with KS-1 sensor as shown in Figure 3.8. The instrument consists of a control module and a KS-1 sensor connected to the module. The instrument works on the principle of hot-wire transition method. To make measurements, the sensor was dipped in a 100 ml beaker containing 90 ml of nanofluid medium. The portable module supplies a constant current

to the KS-1 sensor to heat the liquid. The heating time applied was kept short enough to prevent convection to occur. Along with heating, the sensor serves to measure the temperature loss because of the conduction of heat by the liquid. Using the temperature data, the module performs inverse calculations to obtain the thermal conductivity of the nanofluids.



**Figure 3.8: Photograph of KD2 pro with KS1 sensor for measuring thermal conductivity of liquid media**

### **3.9 Density Measurements**

Density of oils was measured by the weight displacement method. For this purpose, a 50 ml specific gravity bottle was used.

### **3.10 Flash and Fire Point Temperature of Oils**

Flash and fire points of oil quench media were determined using the Cleveland open cup apparatus. The apparatus used is shown in Figure 3.9. It consisted of a brass cup, a thermometer, and a heating rate control knob. The cup was filled with 70 ml of test oil and heated. At regular intervals, during heating a flame was introduced over the cup to check for flash and fire points. The lowest temperature at which intermittent flash (2 to 3) occurred was taken as the flash point of the oil. The temperature at which the hot oil caught fire that lasted for at least five seconds after the flame was removed was noted as the fire point of the oil.



**Figure 3.9: Photograph of Cleveland open cup apparatus**

### **3.11 Measurement of Contact Angle and Surface Tension**

Wetting of the liquid quench medium on the probe surface has been reported to influence the cooling process. The arrangement used to dispense a controlled liquid quenchant droplet and measure its spreading behaviour is shown in Figure 3.10. A 1 ml surgical syringe fitted with a needle having 0.5 mm diameter was used to dispense a droplet of quench medium on the substrate. The amount of droplet dispensed was controlled using a precision pump. The spreading phenomenon of the droplet on the metal substrate was recorded by a high-speed camera operated at 26 fps and the images were analysed in KRUSS Advance software. Elliptical curve fitting method inbuilt in the software was used to measure the contact angle of the dispensed drop. For measuring the surface tension, the syringe was fitted with a needle of 1.83 mm in diameter. To make measurements, a pendant of the quench medium was formed and suspended from the tip of the needle. Density and viscosity of the liquid used were provided as inputs to the Advance software to obtain the surface tension. The ambient temperature during experiments was maintained at 26°C. The captured images were analysed in the Advance software to measure the dynamic contact angle.

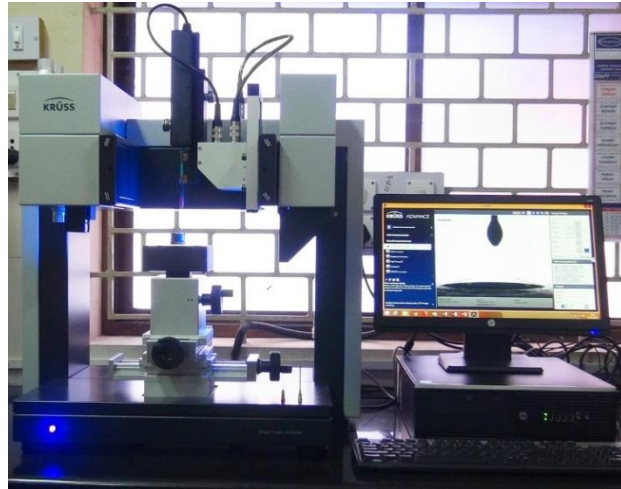


**Figure 3.10: Photograph of drop shape analyzer**

### **3.12 Rewetting Kinematics**

Information regarding the nature of the rewetting front was obtained by means of video imaging and thermal history during quenching. Images of the rewetting front motion during quenching were recorded using a high-speed video camera (Sony HDR-PJ660VE) with a frame rate of 50 fps. The extracted images of rewetting showed the nature of the front. The temperature and time at which the quenchant rewetted a specific location along the surface of the probe was obtained by assessing the estimated temperature data obtained from solution to IHCP.

### **3.13 Estimation of Interfacial Heat Flux Transients**

The spatiotemporal heat flux transients at the metal/quenchant interface were estimated by inverse heat conduction technique using the near surface thermocouples data. For this purpose, the thermal conductivity, specific heat and density of the quench probe given in Table 3.3 (for inconel), Table 3.4 (For SS), Table 3.5 (for G 10450 steels), and Table 3.6 (for G 10900 steels). The thermophysical properties in Tables 3.3 to 3.6 were used as input to the TmmFe inverse solution software (TherMet Solutions Pvt. Ltd., Bangalore).



**Table 3.3: Thermophysical properties of the inconel 600 alloy quench probe  
(Penha et al. 2010)**

Temperature (°C)	Thermal conductivity $\lambda$ (W/mK)	Specific heat $C_p$ (J/kgK)	Density $\rho$ (kg/m <sup>3</sup> )
50	13.4	451	8400
100	14.2	467	8370
150	15.1	-	-
200	16	491	8340
250	16.9	-	-
300	17.8	509	8300
350	18.7	-	-
400	19.7	522	8270
450	20.7	-	-
500	21.7	533	8230
600	-	591	8190
700	25.9	597	8150
800	-	602	8100
900	30.1	611	8060

The equation governing two-dimensional heat conduction in the solid that the software used is mathematically expressed as:

$$\frac{1}{r} \frac{\partial}{\partial r} \left( \lambda r \frac{\partial T}{\partial r} \right) + \frac{\partial}{\partial z} \left( \lambda \frac{\partial T}{\partial z} \right) = \rho C_p \frac{\partial T}{\partial t} \quad (3.1)$$

The following initial and boundary conditions were respectively applied to the above governing equation for estimating the surface heat flux.

$$T(r, z) = T_i \text{ at } t = 0 \quad (3.2)$$

$$-\lambda \frac{\partial T}{\partial r} n_r - \lambda \frac{\partial T}{\partial z} n_z = q_k(r, z, t) \text{ on } q_1, q_2, q_3 \text{ and } q_4 \quad (3.3)$$

$$k = 1, 2, \dots, p, \dots, l$$

$$-\lambda \frac{\partial T}{\partial r} n_r - \lambda \frac{\partial T}{\partial z} n_z = 0 \text{ on } q = 0 \quad (3.4)$$

**Table 3.4: Thermophysical properties for SS probes (JMatPro, Sente Software Ltd., UK)**

Temperature (°C)	Thermal conductivity $\lambda$ (W/mK)	Specific heat $C_p$ (J/kgK)	Density $\rho$ (kg/m <sup>3</sup> )
52	21.25	584	7628.9
152	22.5	648	7596.29
202	23.1	671.4	7580.4
252	23.72	738.4	7563.6
302	24.3	801.4	7546.4
352	24.87	886	7528.9
402	25.42	840.8	7511.17
452	25.97	760.2	7493.07
502	26.53	721.8	7474.66
552	27.1	702	7455.96
602	27.67	691.8	7436.96
652	28.25	687.4	7417.6
702	28.84	687.2	7398.1
752	29.42	689.4	7378.25
802	30	693.8	7358.12
852	30.59	699.6	7337.74
902	31.18	706.6	7317.06

TmmFe adopts the following methodology to estimate the unknown heat flux at the quenchant/metal interface (Kumar 2004). The unknown heat fluxes are first vectorized at the metal/quenchant interface surfaces as  $(q_{k_i})$ ;  $k = 1, 2, \dots, p, \dots, l$  and  $i = 1, 2, \dots, m, \dots, n$  (where  $k$  denotes the boundary segment, and  $i$  denotes the time step), and these heat fluxes are considered to be constant over the small interval of time  $\Delta t$ . The material properties (such as density, specific heat, and thermal conductivity as functions of temperatures), the initial condition, the boundary conditions, and the thermal histories at known locations are the required input parameters for the inverse program.

Similar to the heat flux components, the thermal histories at the known locations are also vectorized into  $Y_j(i)$ ;  $j = 1, 2, \dots, s$  and  $i = 1, 2, \dots, n$  (where  $j$  denotes the temperature sensor location). The multiple heat flux components are calculated serially, one after the other, for every time step. The calculation procedure starts by assuming the flux vectors  $(q_k)_i$ , where  $k = 1, 2, \dots, p, \dots, l$ ,  $i = 1, 2, \dots, m - 1$ ; and  $k = 1, 2, \dots, p - 1$ ;  $i = 1, 2, \dots, m$  are the known entities, and the aim is to find the heat flux  $(q_p)_m$  (where  $p$  and  $m$  are the current segment and time step, respectively) for the time interval  $t_{m-1} < t < t_m$ .

**Table 3.5: Thermophysical data for G 10450 grade steel probes (JMatPro, Sente Software Ltd., UK))**

Temperature (°C)	Thermal conductivity $\lambda$ (W/mK)	Specific heat $C_p$ (J/kgK)	Density $\rho$ (kg/m <sup>3</sup> )
30	55.65	460	7820
500	37.14	691	7669
710	31.77	960	7588
715.54	29.88	6844	7590
720	29.88	6840	7596.4
723.6	27.9	1112	7610
777.69	26.17	595.8	7619
780	26.17	600	7620
880	27.37	610	7570

The sensitivity coefficients for all the sensor locations for ‘b’ future time steps are now computed using the following equation:

$$\phi_{j,k,i} = \frac{(\hat{T}_{j,k,i}^+ - \hat{T}_{j,k,i})}{q_{k,i}}; i = m, \dots, m+r-1 \quad (3.5)$$

The numerator in the above equation is computed by solving the direct heat-conduction equation and is denoted as

$$\hat{T}_{j,k,i}^+ = T_{j,k,i} | (q_k)_{m, \dots, m+r-1} = (q_k)_{m-1}; k = 1, \dots, p-1 \quad (3.6)$$

$$\hat{T}_{j,k,i} = T_{j,k,i} | (q_k)_{m, \dots, m+r-1} = (q_k)_{m-1}; k = 1, \dots, p-1 \quad (3.7)$$

The quantity  $(q_p)_i$  is the updated heat flux in the current unknown boundary at the pth segment, which converges after a few iterations. The initial condition is taken as the thermal field resulting from the current distribution of the heat flux, and the direct solution is obtained by finite-element method for the time steps  $t_m$  to  $t_{m+r-1}$ .

The heat flux at the p<sup>th</sup> boundary segment alone is then incremented by the value given by

$$(\nabla q_k)_m = \frac{\sum_{j=1}^J \sum_{i=1}^r [Y_{j,m+r-1} - \hat{T}_{j,k,m+r-1}] \phi_{j,k,i}}{\sum_{j=1}^J \sum_{i=1}^r (\phi_{j,k,i})^2} \quad (3.8)$$

**Table 3.6: Thermophysical properties for G 10900 grade steel probes (JMatPro, Sente Software Ltd., UK)**

<b>Temperature (°C)</b>	<b>Thermal conductivity <math>\lambda</math> (W/mK)</b>	<b>Specific heat <math>C_p</math> (J/kgK)</b>	<b>Density <math>\rho</math> (kg/m<sup>3</sup>)</b>
30	46.2	480	7810
250	40	560	7747
370	37.43	616	7710
500	34.02	690	7664
734.7	29.63	973	7580
740	27	7670	7601
745.25	25.12	783	7620
870	27.19	620	7530

The iteration is repeated until the absolute value of the ratio of the flux increment to the current value reaches a minimum. The remaining unknown heat flux components are computed in a similar manner.

Figure 3.11 shows 2-D axisymmetric models of various probes. These models were used to estimate the boundary heat flux transients ( $q$ ). The models were meshed uniformly with 4 node quadrilateral elements. Measured temperature data obtained during quenching experiment was provided as input to these models at nodes corresponding to the locations given in Figure 3.2. In the inconel probe model, TC(1) represents the temperature readings measured at a depth of 17 mm while TC(2), TC(3) and TC(4) represent the temperatures recorded at depths of 33, 48 and 52 mm respectively and were at 2 mm below the surface. In the case of 25 mm steel quench probe, TC, T1 and T2 represent the thermocouples placed at a depth of 15 mm and were positioned at the geometric centre, 6.25 mm and 10.5 mm from the centre. TC, T1, T2, T3 and T4 in Figure 3.11c represent temperatures obtained at the geometric centre, 6.25, 12.5, 18.75 and 23 mm from the centre and were obtained at a depth of 15 mm. The meshing of models resulted in 3500 elements for the inconel probe while the number of elements in the case of steel probes were 1500 (for 25 mm section diameter) and 3000 (for 50 mm section size). The inconel probe model was divided into 4

boundary heat flux segments and only one heat flux was estimated in the case of steel probes. The convergence limit in the Gauss-Siedel iterations was set as  $10^{-6}$ .

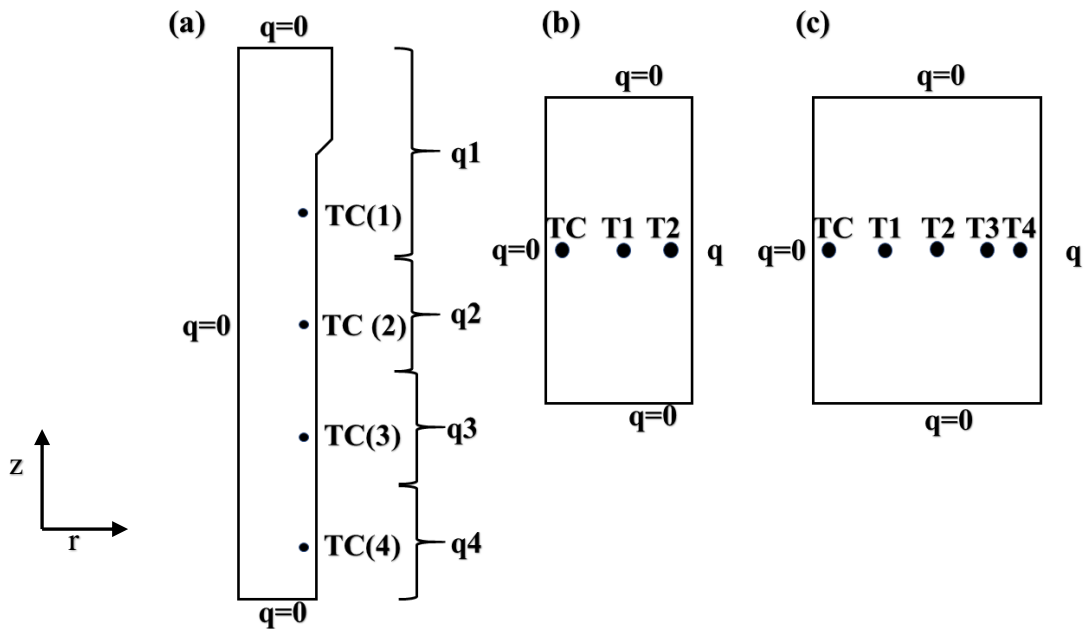


**Figure 3.11: Axisymmetric model of (a) inconel (b) 25 mm and (c) 50 mm quench probe**

## Chapter 4 RESULTS

### 4.1 Characterisation of Liquid Quenching Media Using Inconel Probe

#### 4.1.1 Un-agitated quench media

Typical cooling curves recorded during immersion quenching of inconel 600 alloy probe are shown in Figure 4.1. These curves were obtained during quenching of the probe from 860 °C in distilled water. The legend TC(C) represents the thermocouple readings obtained at the geometric centre of the probe. TC(1) to TC(4) represent the temperature readings recorded at depths of 17, 33, 48 and 62 mm and were located at 2 mm from the probe surface (Figure 3.2).

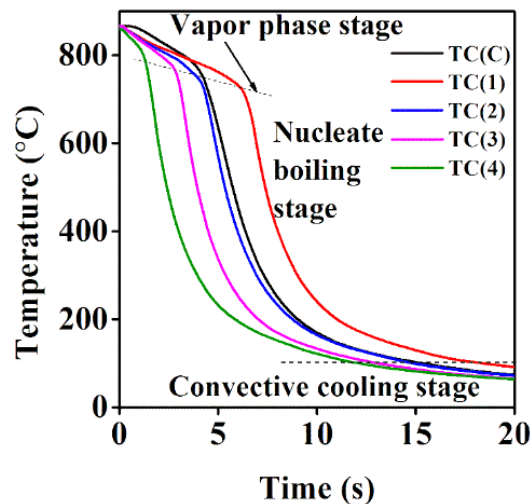


**Figure 4.1: Cooling curves measured in the inconel probe during quenching in distilled water**

The instant when inconel probe contacts the quench medium, its temperature begins to decrease. Each location in the probe experiences three distinct heat transfer modes. Initially, the temperature loss was slow because of the vapor phase formed around the probe. With continued cooling, the vapor phase collapsed, accelerating the cooling process and transferring heat to the medium by nucleate boiling mechanism. Following the rapid heat loss, the cooling process again slowed down and heat was removed by convection in the liquid medium. It is clearly observed that the vapor phase stage exists for different durations at different thermocouple locations, which implies varying rewetting time at each location on the probe surface. This phenomenon, causes

simultaneous existence of all the three modes of heat transfer on the probe surface leading to non-uniform heat transfer from the probe. Appendix A provides the cooling curves obtained for quenching of the inconel probe in nanofluids of various concentrations and oil quench media.

#### 4.1.2 Video imaging of quenching process

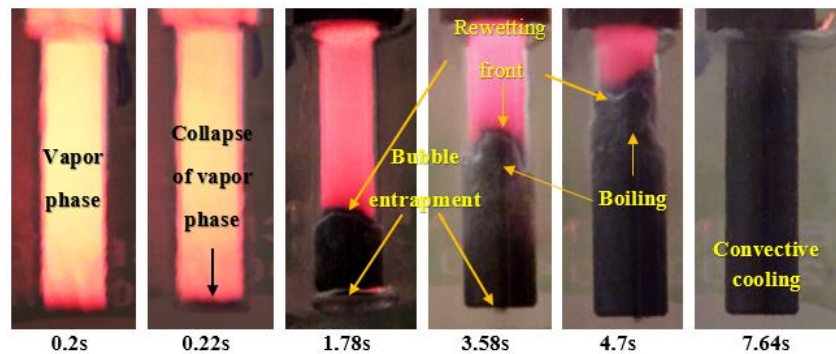


**Figure 4.2: Video images of inconel probe obtained during quenching in distilled water**

Figure 4.2 shows the images extracted from the video recorded during quenching of the inconel probe in distilled water. It shows that the vapor phase begins to break at the bottom portion of the probe. The collapse of the vapor phase stage lead to the formation of a rewetting front that moved upwards towards the top portion of the probe. Numerous bubbles were formed, departed and some collapsed on the surface of the probe during the movement of the rewetting front. Bubble entrapment on the lateral face is clearly observed and is indicative of reduced heat loss from the lateral face. At 7.64s, the final remnant vapor phase that was trapped between the support rod and the probe begins to escape bringing an end to the rewetting front motion. Convective cooling was also observed at this instant at the bottom portion of the probe. The video images obtained during quenching of inconel and steel probes with other quench media are presented in Appendix B.

### 4.1.3 Thermophysical properties of the liquid quench media

#### 4.1.3.1 Thermal conductivity and viscosity of nanofluids

The measured viscosity, thermal conductivity and density of nanofluids are shown in Table 4.1.

**Table 4.1: Thermophysical properties of nanofluids**

Quenchants		Viscosity, $\times 10^{-3}$ (Pa.s)	Thermal conductivity (W/mK)	Density ( $\text{kg/m}^3$ )
Distilled water		$1.32 \pm 0.01$	$0.5965 \pm 0.06$	867.8
MWCNT	0.0003 vol. %	$1.29 \pm 0.01$	$0.61425 \pm 0.02$	868.3
	0.003 vol. %	$1.32 \pm 0.01$	$0.59075 \pm 0.05$	868.4
	0.03 vol. %	$1.31 \pm 0.01$	$0.59819 \pm 0.096$	868.6
Graphene	0.01 vol. %	$1.31 \pm 0.03$	$0.5389 \pm 0.047$	868.4
	0.1 vol. %	$1.35 \pm 0$	$0.5908 \pm 0.062$	868.5
	0.3 vol. %	$1.34 \pm 0.02$	$0.6151 \pm 0.078$	868.6
CuO	0.01 vol. %	$1.31 \pm 0.01$	$0.5783 \pm 0.021$	868.9
	0.05 vol. %	$1.33 \pm 0.02$	$0.5683 \pm 0.016$	869.9
	0.1 vol. %	$1.36 \pm 0$	$0.5643 \pm 0.022$	871.3
	1.0 vol. %	$1.29 \pm 0.01$	$0.5627 \pm 0.042$	874.2

The measured viscosity at room temperature was found to be only slightly higher for nanofluids relative to water. Moreover, the measured thermal conductivities of the nanofluids were found to be of similar magnitude compared to that of distilled water. The density of nanofluids increased with concentration. Nanofluids of low concentrations had densities slightly higher compared to distilled water.

#### 4.1.3.2 Viscosity, density, flash and fire points of oil quench media

The thermophysical properties of oil quench media are presented in Table 4.2. Sunflower oil used had the least viscosity while the viscosity of mineral oil was found to be the highest. Viscosities of Neem and karanja oil was found to be between those of sunflower and mineral oil quench media. The flash point temperature was nearly the same for sunflower and neem oil media while that of mineral oil was found to be the least. Fire point was the highest for sunflower oil followed by karanja, neem and mineral oil respectively. The density of vegetable oil medium was found to be higher



than that of mineral oil quenching medium. The behaviour of viscosity of oil quenching media with temperature is shown in Figure 4.3.

**Table 4.2: Thermophysical properties of quench oil**

Quenchant	Viscosity, $\times 10^{-3}$ (Pa.s)	Flash point ( $^{\circ}\text{C}$ )	Fire point ( $^{\circ}\text{C}$ )	Density ( $\text{kg/m}^3$ )	Thermal conductivity (W/mK)
Mineral oil	94	238	244	873	0.132
Sunflower oil	48	336	370	918	0.155
Neem oil	81	332	360	808	0.154
Karanja oil	69	290	348	930	0.164

It shows that the viscosity of oil quenching media reduces with increase in temperature. Mineral oil quenching medium and the non-edible vegetable oils showed significant decrease in their viscosity with increase in temperature compared to that for sunflower oil quenching medium.

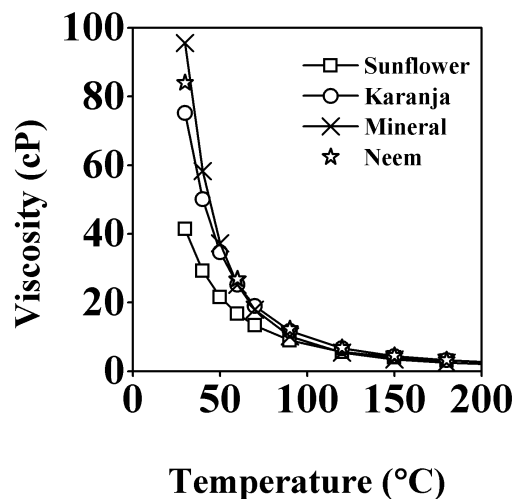


**Figure 4.3: Viscosity behaviour of quench oils with temperature**

Using the viscosity vs. temperature data, viscosity index (ASTM D2270-10(2016)) was calculated and is shown in Table 4.3 for the tested oils. In the Table, ‘L’ is defined as the kinematic viscosity at 40  $^{\circ}\text{C}$  of an oil of 0 viscosity index having the same kinematic viscosity at 100  $^{\circ}\text{C}$  as the oil whose viscosity index is to be calculated,  $\text{mm}^2/\text{s}$ . ‘H’ is

kinematic viscosity at 40 °C of an oil of 100 viscosity index having the same kinematic viscosity at 100 °C as the oil whose viscosity index is to be calculated, mm<sup>2</sup>/s. ‘U’ is the kinematic viscosity at 40 °C of the oil whose viscosity index is to be calculated, mm<sup>2</sup>/s. The Table shows that the viscosity of sunflower oil was more stable with temperature change followed by karanja, and neem and mineral oil was found to be the least stable quenching oil.

**Table 4.3: Viscosity index of quench oils**

Quenchant	Viscosity index $\left(\frac{(L-U)}{(L-H)}\right)$
Mineral	122
Neem	136
Sunflower	172
Karanja	151

#### 4.1.4 Contact angle and spreading behaviour

The angle of wetting made by the liquid drop on its contact with an inconel substrate was measured and its spreading was recorded to obtain the behaviour of the liquid as it wets the surface. Typical contact angle images recorded during measurements of contact angle are shown in Figure 4.4. Contact angle images obtained during spreading of other quench media on Inconel substrate are shown in Appendix C.

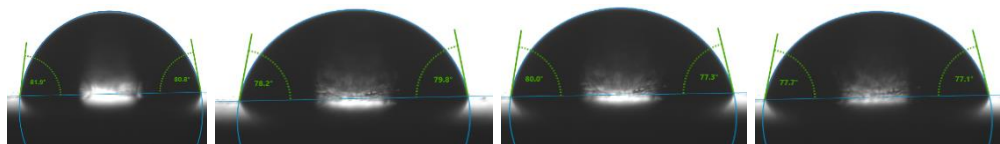


**Figure 4.4: Contact angle measured during spreading of 0.01 vol.% concentration of graphene nanofluids**

A liquid quench medium drop formed a spherical cap on contacting the surface of the substrate. A triple line of contact formed (shown with blue) which advanced with time causing increase in the base diameter of the cap and decrease in the height. The advance

of the contact line along the substrate surface caused the contact angle to decrease from its initial value leading to spreading of the drop on the solid surface. The relaxation of contact angle with time for spreading of the drop is shown in Figure 4.5.

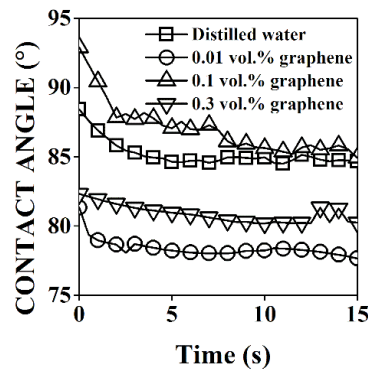


**Figure 4.5: Relaxation of contact angle obtained during spreading of distilled water and graphene nanofluids of various concentrations on an inconel substrate**

It shows that, initially, the reduction in contact angle was rapid. After the initial stage, the relaxation of contact angle slows down becoming more gradual as it approached a state of quasi-equilibrium. The surface tension of the quench media was assessed using the pendant drop technique. The surface tensions of various quench media are tabulated in Table 4.4 and 4.5.

**Table 4.4: Surface tension (mN/m) of nanofluids**

Distilled water	MWCNT			CuO				Graphene		
	0.0003	0.003	0.03	0.01	0.05	0.1	1.0	0.01	0.1	0.3
72	63	48	58	61	56	62	61	62	63	63

**Table 4.5: Surface tension (mN/m) of oils**

Neem	Mineral	Karanja	Sunflower
28	29	32	32

#### 4.1.5 Effect of agitation

Cooling curves obtained during quenching of inconel in water agitated under various impeller speeds in a Tensi agitation system are shown in Figure 4.6. The nature of the cooling curves obtained are similar to those observed during experiments under still

quenching conditions. However, the agitation of the medium resulted in reduced duration of the vapor phase stage and increased the rate of cooling during quenching. The impact of agitation on the increase in cooling rate was the least at TC(4) while it is observed to have the highest impact at TC(1) thermocouple location. The overall use of agitation is to reduce the total time of quenching, increase the cooling rate and improve the uniformity of heat removal from the metal. The cooling curves obtained under various agitation rates for different quenching media used in this study are given in Appendix D.

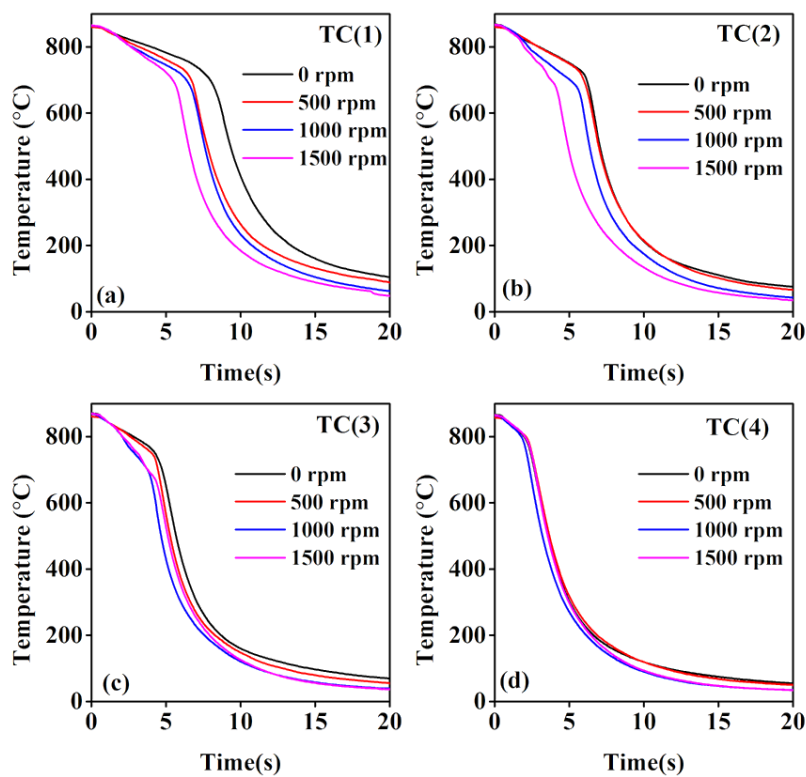


**Figure 4.6: Temperature vs. time plot during quenching of inconel in water under various agitation rates at thermocouple locations (a) TC(1) (b) TC(2) (c) TC(3) and TC(4)**

#### **4.2 Quenching Experiments with G 10450 and G 10900 Steel Alloys of 25 and 50 mm Section Diameters**

The cooling curves obtained in 25 mm G 10450 steel and 50 mm G 10900 steel quenched in karanja oil are shown in Figure 4.7. The cooling curves show momentary inflexion during the quenching process because of the evolution of latent heat due to

phase transformation during continuous cooling. Such a characteristic was not observed for quenching of the 25 mm test pieces of G 10900 indicating no transformation of parent austenite into pearlite or ferrite during quenching. The cooling curves with other oil quench media and water quenched G 10450 and 10900 steels are given in Appendices E and F respectively.

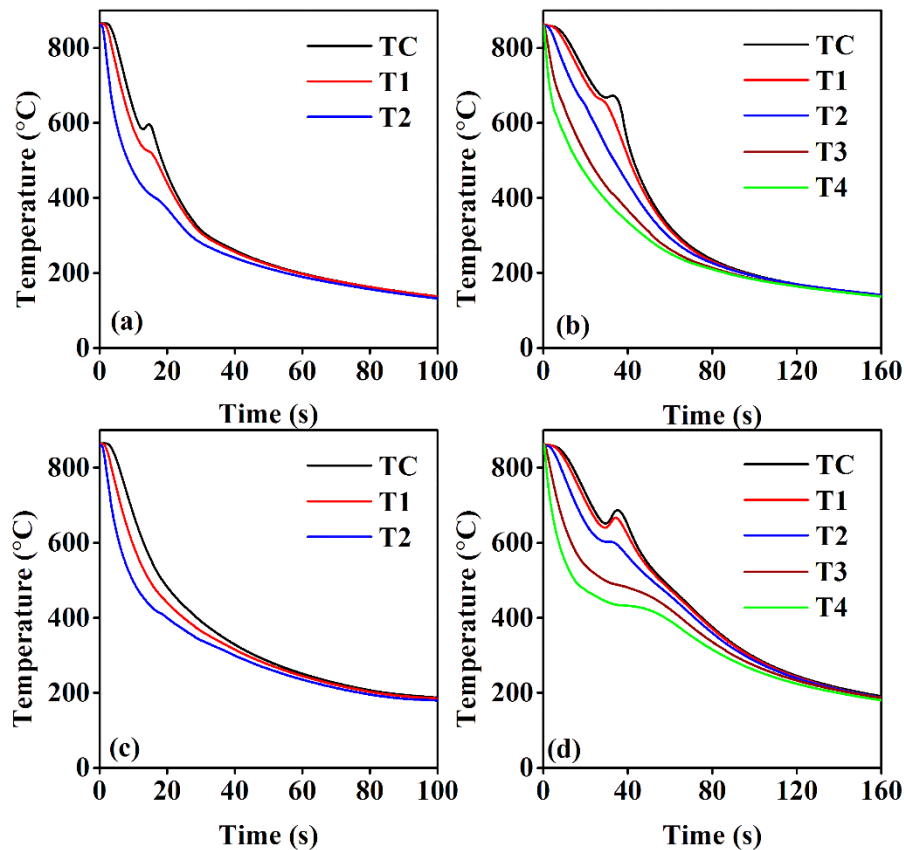


**Figure 4.7: Cooling curves obtained during quenching of G 10450 steel of (a) 25 mm and (b) 50 mm and G 10900 steel of (c) 25 mm and (d) 50 mm section diameters in karanja oil quench medium**

### 4.3 Quenching Experiments with 304 SS of 25 and 50 mm Section Diameters

The measured cooling curves during quenching of the 25 and 50 mm SS probe in karanja oil are shown in Figure 4.8. The curves show that the surface of the probe cools faster compared to its centre. For the 50 mm probe, the cooling curves measured at a distance of 6.25 mm (T1) from the centre was nearly the same as that of centre cooling curve (TC). Quenching in other oils showed similar nature of cooling curves as shown in the Figure 4.8 and are given in Appendix G.

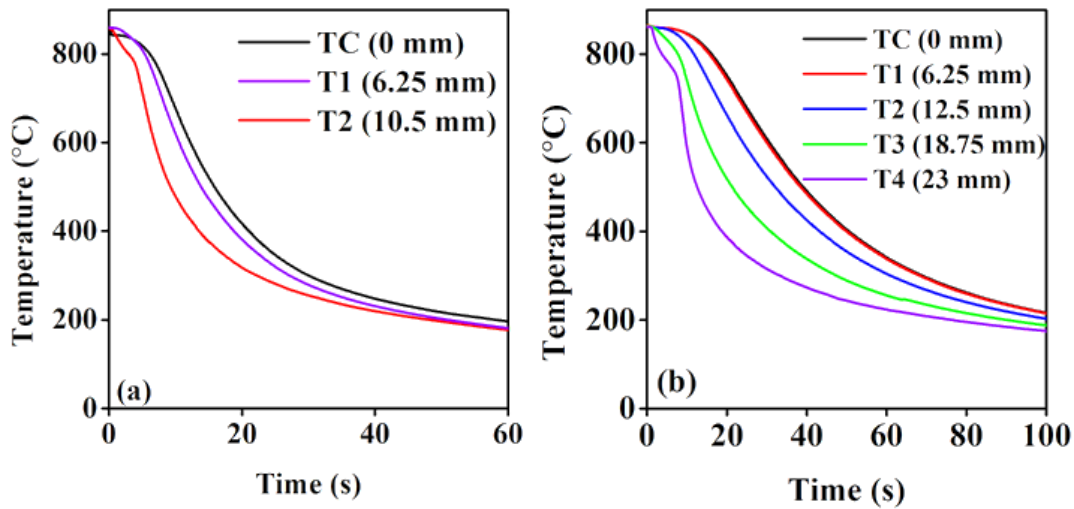


**Figure 4.8: Cooling curves measured in (a) 25 mm and (b) 50 mm SS probes during quenching in karanja oil quench medium**

#### 4.4 Interfacial Heat Flux Transients

The measured temperature recorded during experiments were provided as input to the TmmFe software (TherMet Solutions Pvt. Ltd., Bangalore) to obtain the interfacial spatiotemporal heat flux. Figure 4.9 shows typical heat flux transient curves obtained at different heat flux segments plotted against estimated surface temperature for quenching of the inconel probe in distilled water. The estimated flux had an initial low value because of the insulated vapor phase encapsulating the probe. With subsequent cooling, the vapor phase collapses causing an increase in the heat transfer from the probe to the liquid quench medium as shown by the rapid rise in the heat flux transients. The peak flux attained because of the rapid heat transfer was due to the nucleate boiling mechanism. After attainment of its peak, the heat flux rate decreased with further reduction in the surface temperature of the probe. Thereafter, the heat flux transients became more uniform and gradual heat loss is experienced by the probe as the surface temperature of the probe drops below the boiling temperature of the quench medium bringing an end to the quenching operation. The spatiotemporal heat flux obtained during quenching with inconel quenched in 2 lts and under agitation are shown in Appendices H and I respectively.

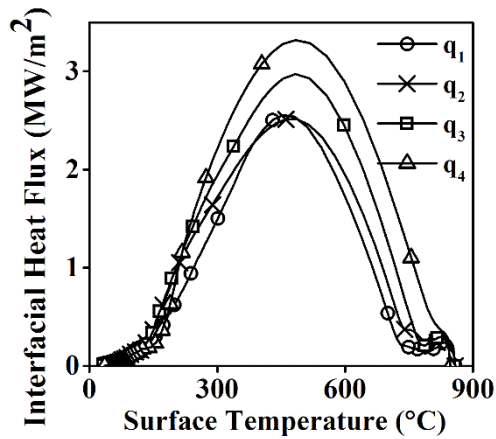


**Figure 4.9: Spatiotemporal heat flux vs. surface temperature obtained during quenching of an inconel probe in distilled water**

#### 4.5 Microstructure



**Figure 4.10: As-rolled microstructure of G 10450 and G 10900 steel alloys**

The as-received microstructure observed is shown in Figure 4.10 for the G 10450 and 10900 grades of steel. G 10450 steel showed the microstructure comprising of pearlite (darker) and ferrite (brighter) phase. Microstructure of G 10900 structure comprised of carbides (dark spots) in a ferrite matrix. The microstructures developed in the G 10450 grade steel of 25 and 50 mm diameter during quenching in water are shown in Figure 4.11. Water quenched 25 mm sample showed ferrite and pearlite structure at its centre while martensite laths were observed at the surface. The microstructures evolved during quenching of G 10900 alloy steel of diameter 50 mm are shown in Figure 4.12. It shows that the micrographs consisted of carbides, martensite and bainite. Micrographs



obtained for quenching of steels in other quenching media are shown in Figure 5.24 to 5.31.

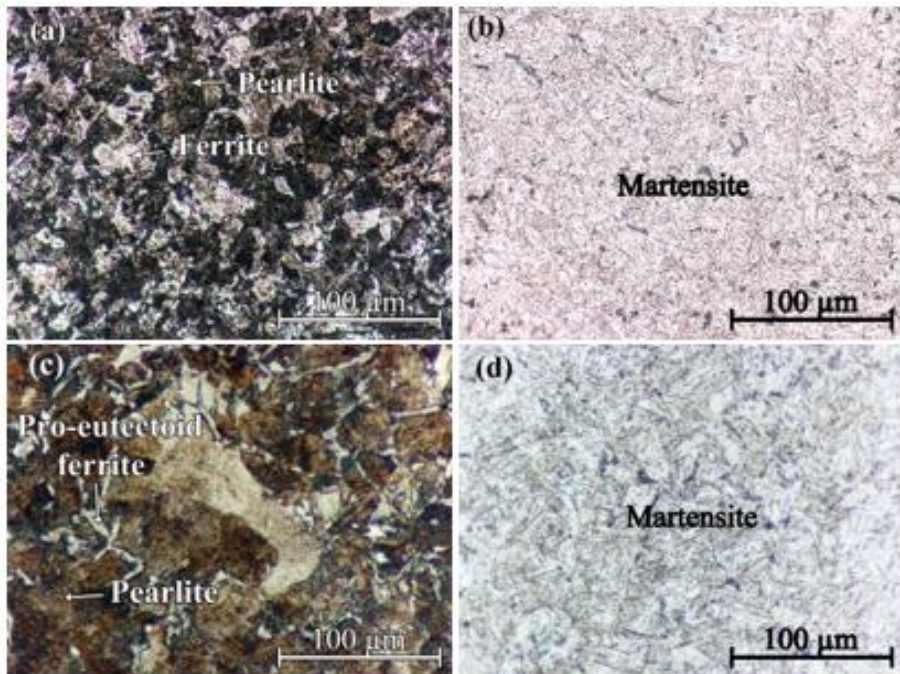


**Figure 4.11: Micrographs obtained from G 10450 steel at the (a) centre and (b) surface of a 25 mm section size and (c) centre and (d) surface of a 50 mm section size test piece quenched in distilled water**

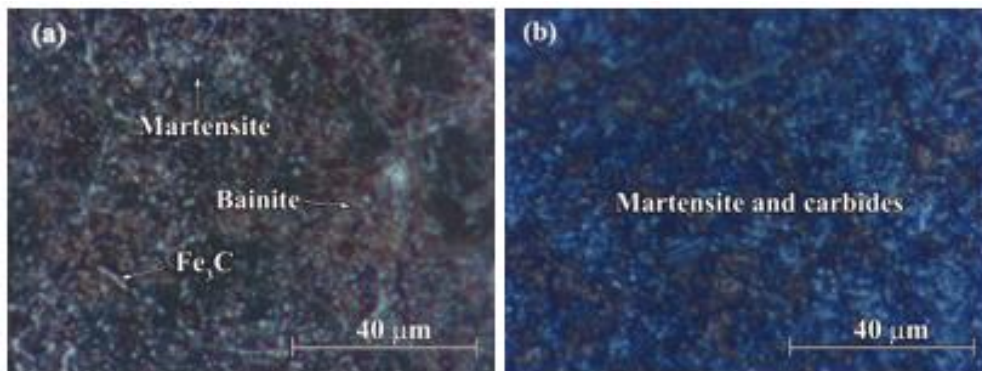


**Figure 4.12: Micrographs obtained from G 10900 steel at the (a) centre and (b) surface of a 50 mm section size test piece quenched in distilled water**



## 4.6 Microhardness

### 4.6.1 G 10450 steels

Vickers microhardness measured at every 0.5 mm distance from the centre of the sectioned test piece towards the surface for the G 10450 steels of diameter 25 and 50 mm are shown in Figure 4.13.

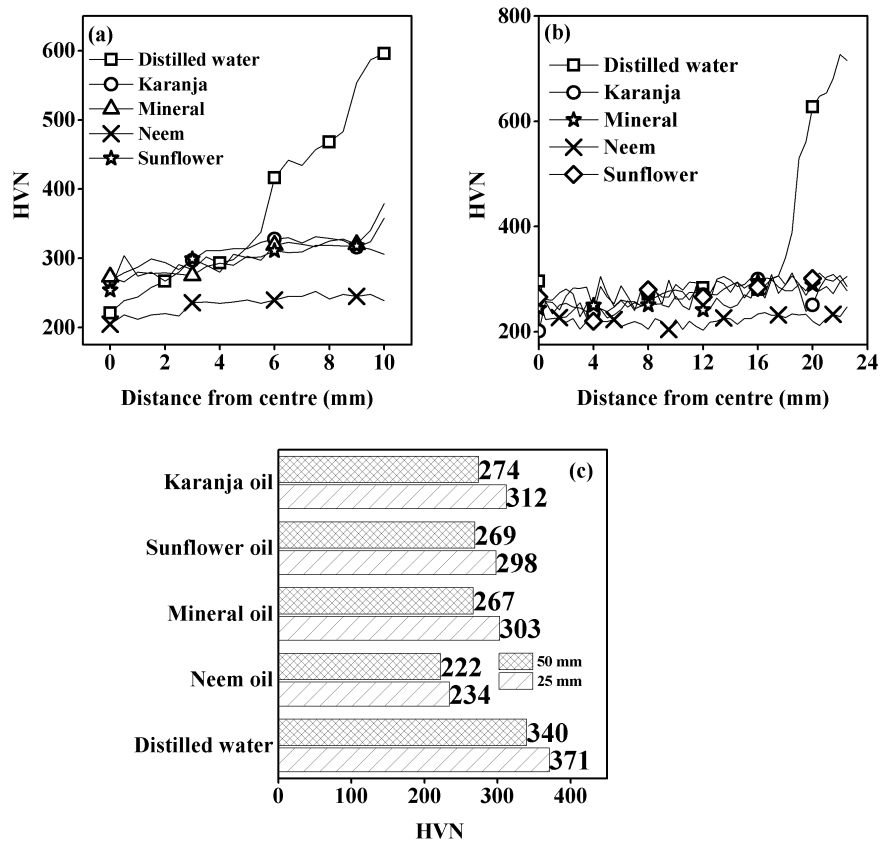


**Figure 4.13: (a) Hardness profile of 25 mm and (b) 50 mm section diameters of G 10450 steels and (c) average hardness bar chart of G 10450 steel of 25 and 50 mm section diameters quenched in various quench media**

Hardness obtained at the centre of the workpiece was lower compared to its surface in each of the quenched samples. The distribution of hardness was more uniform with oil quenching media compared to distilled water quenched test pieces. Water quenching produced harder phases with hardness ranging from 300 to 800 HVN at about 5 mm and 18 mm from the centre for the 25 mm and 50 mm section diameters. The average hardness shown in the bar chart in Figure 4.13c, shows that hardness of 50 mm section

diameters were lower compared to that of 25 mm diameter test pieces. Furthermore, test pieces quenched in karanja had higher hardness compared to mineral oil quenched samples. Hardness obtained with sunflower oil quenching medium were found to be comparable to those obtained with mineral oil quenching medium. The hardness obtained with neem oil quenching medium was found to be the lowest among the oil quenchants used.

#### 4.6.2 G 10900 steels

The hardness profile and the average hardness obtained on quenching G 10900 steels grade of 25 and 50 mm section diameters in various quenching media are shown in Figure 4.14. Hardness obtained at the centre of the workpiece was lower compared to that at the surface. The average hardness of neem oil quenched sample was found to be same as that of mineral oil quenched steel. Karanja oil quenched sample showed higher hardness compared to the mineral oil quenched sample. The hardness obtained for the sunflower oil media quenched steel showed similar hardness compared to the mineral oil quenched steel.

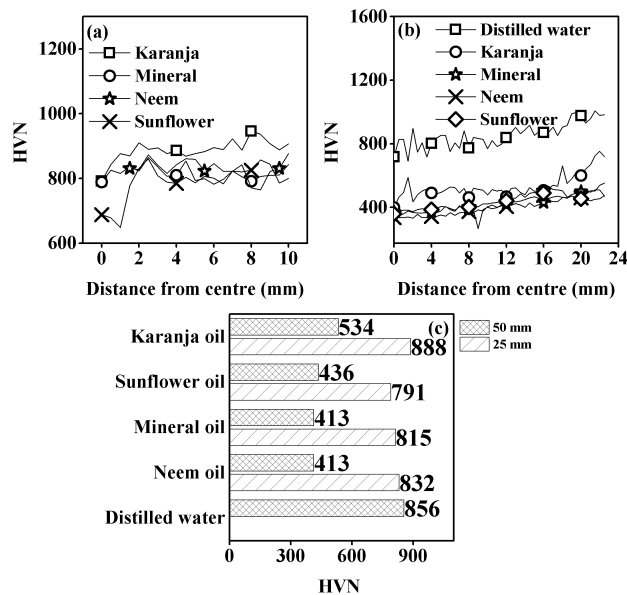


**Figure 4.14: (a) Hardness profile of 25 mm and (b) 50 mm section diameters of G 10900 steels and (c) average hardness bar chart of G 10900 steel of 25 and 50 mm section diameters quenched in various quench media**

## 4.7 Quench Bath Temperature

To measure the temperature rise, thermocouple was positioned in the bulk of the quench medium. For the quench tank that housed 4 lts of quench medium, temperature was measured at a depth of 2 cm from the free surface and was located at 3.2 cm away from the quench tank wall. The corresponding locations in the tank that had 15 lts of quench medium were about 7.4 cm and 6 cm respectively. Figure 4.15 shows the increase in temperature of the liquid during quenching in oils and water. It shows that at the onset of quenching the temperature at the bulk rises rapidly and attains a maximum value and then begins to reduce gradually to room temperature. The figure shows that the temperature rise in the case of quenching in distilled water was the least followed by oils. Karanja and sunflower oils were heated to higher temperatures compared to neem oil during quenching. Generally, quench media that do not show an increased temperature rise during quenching operation are preferred over the one where an excessive increase in temperature would increase the risk of fire hazard. Further, the use of such quench media would need a heat exchanger to cool the quenchant to its operating temperature before commencement of each successive batch quenching operation. However, because of the better viscosity stability of karanja and sunflower oils over neem and mineral oils and their higher flash and fire temperatures compared to mineral oil, the rise in temperature of these oils during quenching will not pose operational challenges for the heat treater.

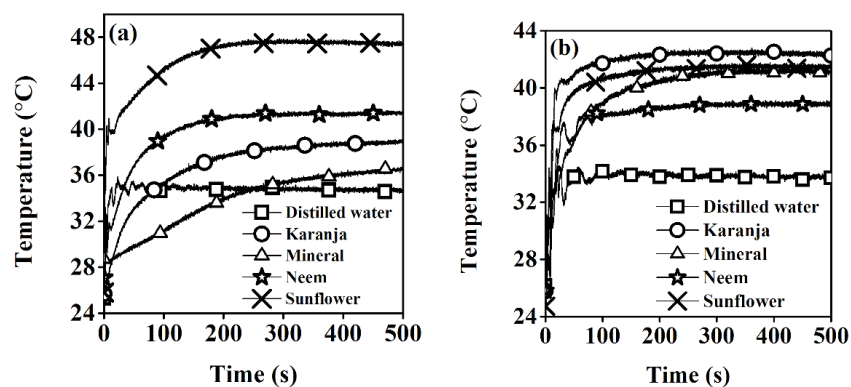


**Figure 4.15: Rise in the temperature of the (a) 4 lts. and (b) 15 lts. liquid quench media at its bulk during quenching of the steel probe**

## Chapter 5 DISCUSSION

### 5.1 Characterization of Liquid Quench Media Using Inconel Probe

#### 5.1.1 Un-agitated quench media

The cooling curves at the geometric centre of the inconel probe during immersion into various quenching media are shown in Figure 5.1. For each of the quench medium tested, the presence of vapour, nucleate boiling and convective cooling was clearly observed. During quenching in nanofluids, the vapour phase stage was longer compared to distilled water. Further, the duration of the vapour phase stage increased with increase in the concentration of nanoparticles added to distilled water. In the case of quenching with oils, sunflower oil quenched inconel probe cooled faster compared to all the other oils. Slowest quenching of inconel probe was observed during immersion in mineral oil quenching medium.

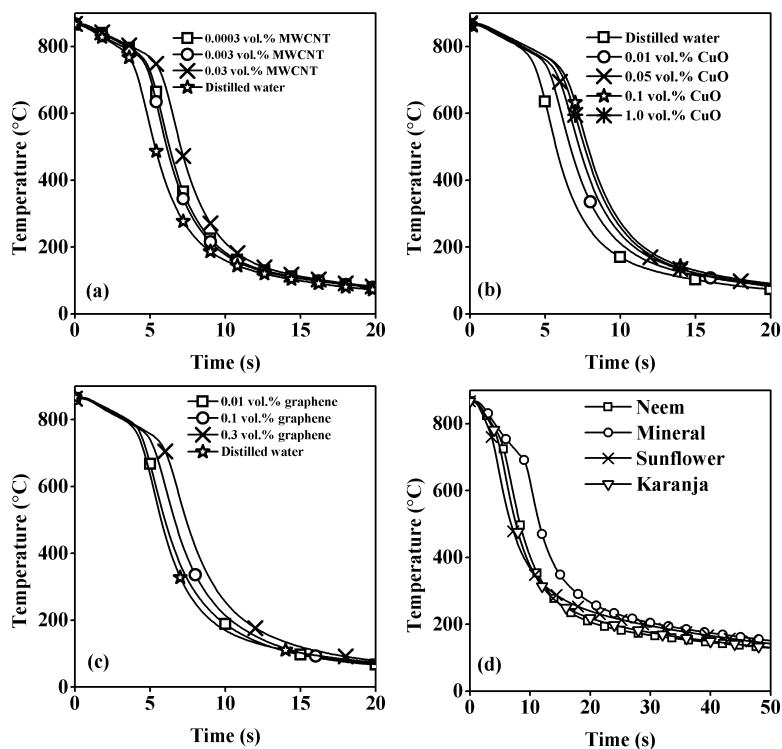


**Figure 5.1: Cooling curves measured at the geometric centre of the inconel probe obtained during quenching in (a) MWCNT and distilled water (b) CuO and distilled water (c) graphene and distilled water and (d) oil quenching media**

Karanja and neem oils quenched the inconel probe slower than sunflower oil but faster than mineral oil. Cooling rate curves obtained at the geometric centre of the inconel probe during quenching in nanofluids and oil quench media are shown in Figure 5.2. The change in the slope of the rate curves clearly shows the three distinct phases of heat transfer namely the vapour phase stage, nucleate boiling stage and the convective cooling stage. The duration of the vapour phase stage ( $t_{A-B}$ ) was found to be 3.2, 3.5, 3.6 and 4.6s for distilled water, 0.0003, 0.003 and 0.03 vol.% MWCNT nanofluids respectively. The corresponding values for quenching in CuO nanofluids were found to be 4.1, 4.2, 4.8 and 4.6s at concentrations of 0.01, 0.05, 0.1 and 1.0 vol.% respectively. For the graphene nanofluids,  $t_{A-B}$  was found to be about 3.5, 4.2 and 4.6s at concentrations of 0.05, 0.1 and 1.0 vol.% respectively. In the case of neem, mineral, sunflower and karanja oil quenching media the vapour phase stage to nucleate boiling stage transition occurred at 4.3, 8.6, 3.3 and 3.8s respectively. The cooling curves presented in Figure 5.1 and the cooling rate curves shown in Figure 5.2 were used to obtain the critical cooling parameters shown in Table 5.1

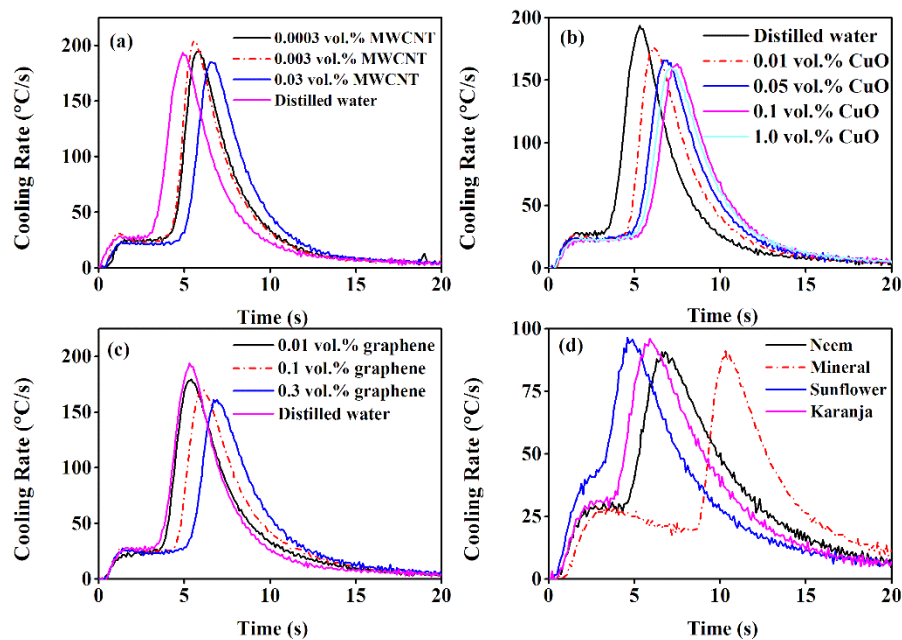


**Figure 5.2: Cooling rates vs. time plot obtained at the centre of the inconel probe during quenching in (a) MWCNT and distilled water (b) CuO and distilled water (c) graphene and distilled water and (d) oil quenching media**

$CR_{max}$  is the maximum cooling rate obtained during the quenching process and  $T_{max}$  refers to the temperature at which the cooling rate becomes maximum.  $CR_{705}$  is the cooling rate at 705 °C and it represents the temperature at which austenite in most steels transforms into ferrite and pearlite.  $CR_{550}$  is the cooling rate at 550 °C and it is representative of the temperature near the nose of the TTT curve for many steels.  $CR_{300}$  and  $CR_{200}$  represents the temperatures in the region of martensitic transformation for many steels.

**Table 5.1: Critical cooling parameters obtained during quenching of inconel probe in various liquid quench media**

<b>Quench Media</b>	<b><math>CR_{max}</math> (°C/s)</b>	<b><math>T_{maxcr}</math> (°C)</b>	<b><math>CR_{705}</math> (°C/s)</b>	<b><math>CR_{550}</math> (°C/s)</b>	<b><math>CR_{300}</math> (°C/s)</b>	<b><math>CR_{200}</math> (°C/s)</b>
<b>Distilled water</b>	192.4	578.9	147.7	189.5	84.7	39.0
<b>0.0003 vol.% MWCNT</b>	194.8	587.7	148.5	188.5	83.5	39.9
<b>0.003 vol.% MWCNT</b>	203.3	614.2	155.0	194.7	83.9	39.9
<b>0.03 vol.% MWCNT</b>	185.1	595.7	130.2	182.4	85.5	40.6
<b>0.01 vol.% CuO</b>	175.7	596.4	131.8	170.7	76.5	35.4
<b>0.05 vol.% CuO</b>	165.8	590.8	106.0	163.7	75.6	35.0
<b>0.1 vol.% CuO</b>	162.5	569.2	94.8	161.2	74.6	34.6
<b>1.0 vol.% CuO</b>	159.6	579.7	104.2	158.3	76.6	36.1
<b>0.01 vol.% graphene</b>	178.8	614.6	152.0	171.0	74.4	36.1
<b>0.1 vol.% graphene</b>	170.0	600.2	127.5	164.0	72.6	36.6
<b>0.3 vol.% graphene</b>	160.0	592.5	99.8	156.8	72.4	34.4
<b>Neem</b>	90.2	625.5	76.7	80.2	25.1	5.3
<b>Mineral</b>	89.7	601.5	19.8	83.4	15.6	3.1
<b>Sunflower</b>	95.3	679.8	89.8	74.5	14.4	3.5
<b>Karanja</b>	95.3	644.7	85.9	80.5	21.6	5.0

In the case of MWCNT nanofluid quenching media, the maximum cooling rate showed an increase of 1.2 and 5.6 % at concentrations of 0.0003 and 0.003 vol.% respectively

and was lower by 3.8% with addition of 0.003 vol.% MWCNT to water. However, the temperature at which the maximum cooling rate occurred was higher with MWCNT nanofluids compared to water. This is beneficial as it aids to avoid austenite to pearlite transformation. During quenching in CuO nanofluids, the peak cooling rate was reduced by 8.6 % to 17 % for the 0.01 and 1.0 vol.% concentrations respectively. Their cooling rates in the martensitic transformation region were lower compared to water. This would reduce the propensity of distortion and cracking especially during hardening of quench sensitive steels that require lower cooling rates compared to those provided by water. Similar to the CuO nanofluids, graphene nanofluids also provided lower peak cooling rates compared to water. According to literature, the reduction in cooling rates was due to the formation of a porous layer that adhered on the quenched metal surface. This may be true in the case of repetitive quenching of a nanoparticle fouled probe. However, in our case involving single quench experiments no such layer was observed. To account for the reduction in the cooling rates, boiling points of nanofluids were measured. It was found that MWCNT and CuO nanofluids had very much similar boiling points (99.5 °C) compared to distilled water used in their preparation. The boiling point of graphene nanofluids were lower only by a degree compared to that of water. To check for phase transformation of nanoparticles due to localised heating during quenching, the nanoparticles were heated upto 860 °C in a furnace and it was observed that they did not undergo any change in phase. The thermal conductivity and viscosity of nanofluids were comparable with water. Hence, the reduction in the cooling rates was attributed to the formation of a barrier by nanoparticles suspended between water in the bulk of the quench tank and the region immediate in the vicinity of the quench probe causing prolonged vapor phase stage during quenching.

Quenching of the inconel probe in oils showed that the peak cooling rate of sunflower and karanja oil were higher compared to mineral oil quenching medium. The peak cooling rate of neem oil was comparable to that obtained with mineral oil. The vegetable oils used showed higher cooling rates at 705 °C. The increased critical cooling parameters were observed during quenching in vegetable oil quenching media compared to mineral oil and was due to their better thermophysical properties. The thermophysical properties of the oils presented in the Table 4.2 showed that the

vegetable oils had higher flash and fire points compared to the mineral oil. Vegetable oils of sunflower and karanja had lower viscosity while the viscosity of neem oil is comparable to that of the mineral oil. Also, the viscosity index of vegetable oils was higher than mineral oil implying better viscosity stability of these oils. The higher flash and fire point temperatures work well for quench medium as they can be operated over a wider temperature range.

### **5.1.2 Spreading behaviour of quench media on inconel and steel substrate**

The spreading behaviour of nanofluids and oil quench media measured on an inconel substrate is shown in Figure 5.3. The spreading of distilled water was very poor with contact angle varying only by  $4^\circ$  from  $88^\circ$  at the start to  $84^\circ$  after 15s of spreading. The contact angle measurements for nanofluids showed lower contact angle compared to distilled water. Nanofluids were found to wet the surface of inconel better compared to that by water. Quench media having lower contact angle are preferred as it would enhance more uniform heat extraction from the metal because of more spreading on its surface. Of the nanofluids used, 0.003 vol.% MWCNT had the least contact angle. There was no definite trend emerged in the contact angle data with respect to the concentration of the nanofluids used. At 15s of spreading, contact angle obtained with CuO nanofluids were  $77^\circ$ ,  $81^\circ$ ,  $76^\circ$  and  $83^\circ$  for 0.01, 0.05, 0.1 and 1.0 vol.% concentrations respectively. The corresponding values for the 0.01, 0.1 and 0.3 vol.% graphene nanofluids were  $77^\circ$ ,  $84^\circ$  and  $80^\circ$  and for the 0.0003, 0.003 and 0.03 vol.% MWCNT were  $76^\circ$ ,  $73^\circ$  and  $77^\circ$  respectively. Oil quench media showed faster spreading behaviour compared to the aqueous quench media. Of the oils, sunflower and mineral oil had similar wetting behaviour with lower angle of nearly  $17^\circ$  at 1.7s of spreading. The corresponding wetting angles with neem and karanja oils were found to be  $21^\circ$  and  $24^\circ$  respectively. The average contact angle was about  $32^\circ$ ,  $25^\circ$ ,  $26^\circ$  and  $33^\circ$  for neem, sunflower, mineral and karanja oils respectively. Surface tension of sunflower and karanja were higher while that of neem oil was nearly the same than mineral oil and are provided in Table 4.2.



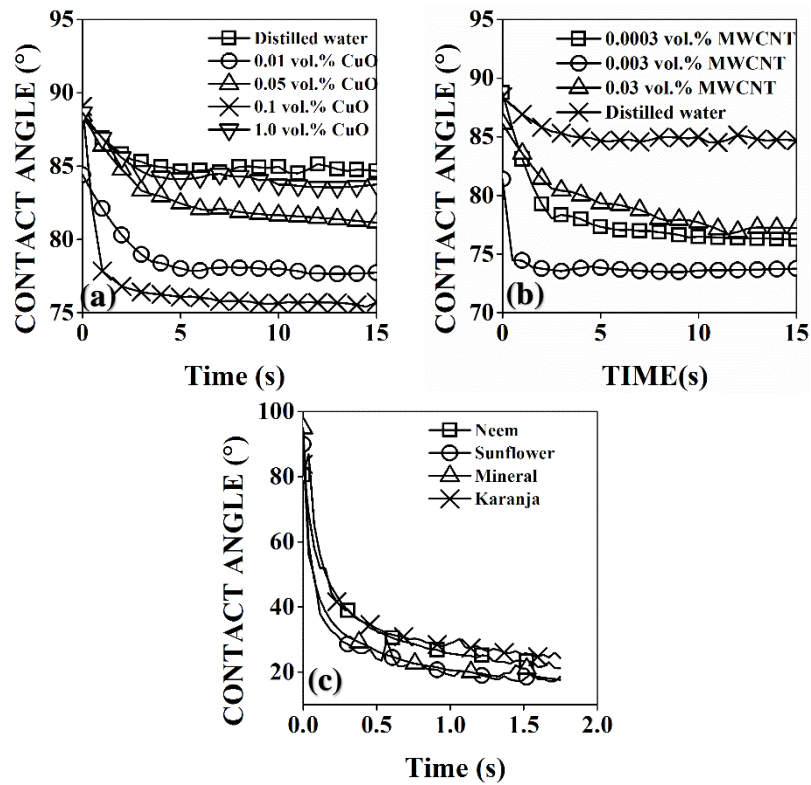


**Figure 5.3: Contact angle relaxation plots obtained during spreading of (a) CuO and (b) MWCNT nanofluids and (c) oil quenching media on inconel substrate**

Figure 5.3a show the spreading behaviour of oil on steel substrate. It shows that the spreading behaviour was similar to that observed in the case of wetting on inconel substrate. The wetting of sunflower oil was faster and had lower contact angle compared to the other oils. Karanja and mineral oil had similar contact angle of about 20 and 22° while that of neem oil was slightly higher and was 25° at 3.6s of wetting. The corresponding value in the case of sunflower oil was 13°. Figure 5.4b shows the dimensionless contact angle plot ( $\Phi$ ) vs. dimensionless time ( $t/t_r$ ) where  $\Phi = \frac{\theta - \theta_e}{\theta_i - \theta_e}$  and 't' is the transient time and 't<sub>r</sub>' is the time taken for the drop to spread from  $\theta_i$  to  $\theta_e$ .  $\theta_e$  is the contact angle at 2.5s of spreading at which  $\frac{d\theta}{dt} < 0.001 \text{ } ^\circ/ms$ . The dimensionless plot obtained is shown in Figure 5.4b. Such curve makes the spreading behaviour independent of the initial contact angle formed on the substrate. The dimensionless contact angle shows that spreading was better in the case of sunflower oil upto a dimensionless time of 0.2. This was because of the lower viscosity of sunflower oil compared with other oils.

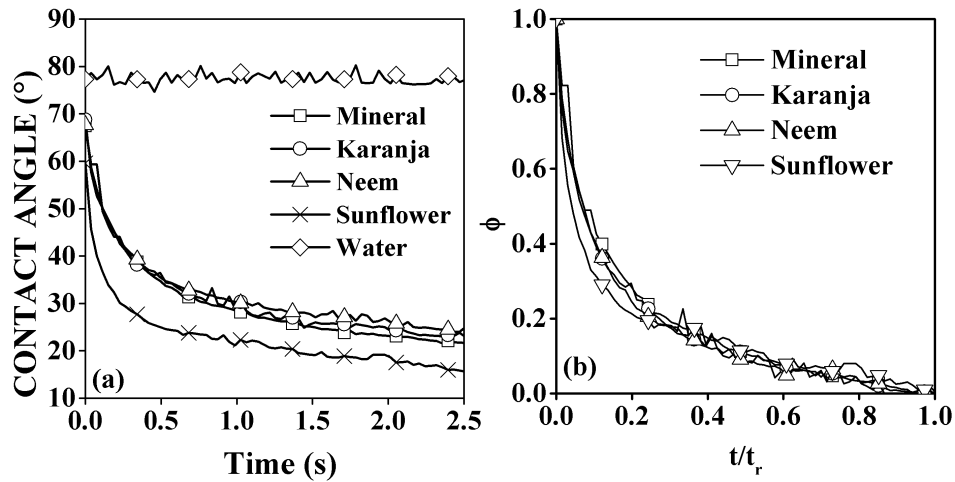


**Figure 5.4: (a) Spreading of water and oil quench media on steel substrate and (b) dimensionless contact angle vs. dimensionless time for the spreading of oils on steel substrate**

### 5.1.3 Spatiotemporal heat flux during quenching of inconel probe

The outcome of a quench hardening operation relies on the heat extracted during quenching. The cooling curves measured at various near surface locations in the probe and the video images recorded during quenching are shown in Appendices A and B respectively. They show the complexity involved during the quenching process. The formation of rewetting front and its subsequent breakdown causes heat flow to vary with location and time along the probe surface. Due to this and the dynamic nature of heat transfer occurring during the quenching operation, it is necessary to assess the heat removed from the quench probe using multiple heat flux estimated at various locations. The estimated spatiotemporal heat flux during quenching in various liquid quench media are presented in Appendix H. The error between the measured and estimated temperatures at the thermocouple locations during computation was less than 7%. The estimation of such heat flux transients would enable the determination of heat transfer rates from the metal probe to the quench media and facilitate the selection of quench medium to be used. The nature of the spatiotemporal heat flux curves remains the same for all the cases and showed the existence of vapor, nucleate boiling and convective cooling mechanisms as evident from the change in the slope. However, due to the

dynamic nature of heat flow involved and the variation of heat flux with time and space a comparison of heat transfer during quenching based on the spatiotemporal heat flux curves alone is difficult as the magnitude of flux varies in each of the considered heat flux segments. Nevertheless, they are useful in the determination of the interfacial temperature, temperature distribution and heat removed at various locations which may be used as the basis for comparison of quench media.

The spatiotemporal heat flux obtained during quenching clearly shows that the maximum variation in the heat flux occurs at the peak in the curves because of the varying nucleate boiling bubble dynamics and rewetting front effect. The video images showed that the rewetting front breaks at the bottom edge and progressed upwards along the probe surface. This implies that the bottom segment  $q_4$ , is the region where the front approaches first (generally) and then moves over other regions along the probe surface. Such motion causes the heat flux to first rise in this segment and attain higher magnitude compared to other segments. However, this is not the sole criterion that would lower or cause higher peak flux in the probe at the various boundary heat flux segments. The flux is also affected by bubble dynamics which causes bubbles to nucleate, grow, depart and collapse during the nucleate boiling stage removing larger magnitude of heat relative to the other stages in the quench hardening operation. The peak heat flux obtained at various heat flux segments along the inconel probe surface are presented in Table 5.2. It shows that the addition of nanoparticles to water reduced the average peak flux. The average peak flux further reduced as the concentration of nanoparticles in water was increased. The peak heat flux during quenching in oils were found to be nearly half of that observed for the aqueous quench media. The standard deviation among the peak heat fluxes estimated for oils were much lower to those obtained for the aqueous quench media and indicate more uniform heat removal by them. The lower peak heat flux observed during oil quenching was due to their higher viscosity. The mean peak flux was found to be related to the viscosity, density and surface tension of the quench media according to a power function ( $\bar{q}_{max} = 3.035 * \left(\frac{\nu}{\sigma}\right)^{-0.171}$ ) and is shown in Figure 5.5. It shows that the mean heat flux was significantly influenced by the viscosity of the quench medium. The mean peak heat flux was lowered with increase in the viscosity of the quench medium.

**Table 5.2: Estimated peak heat flux at various boundary segments during quenching of the inconel probe in various quench media**

Quench Media	q <sub>1</sub>	q <sub>2</sub>	q <sub>3</sub>	q <sub>4</sub>	Average	Standard deviation
	(MW/m <sup>2</sup> )					
<b>Distilled water</b>	2.55	2.51	2.97	3.32	2.84	0.38
<b>0.0003 vol.% MWCNT</b>	2.09	2.52	2.53	3.19	2.58	0.46
<b>0.003 vol.% MWCNT</b>	2.00	2.56	2.46	3.15	2.54	0.47
<b>0.003 vol.% MWCNT</b>	1.92	2.46	2.58	2.89	2.46	0.41
<b>0.01 vol.% CuO</b>	2.17	2.87	2.75	2.70	2.62	0.24
<b>0.05 vol.% CuO</b>	1.68	2.81	2.57	3.00	2.52	0.58
<b>0.1 vol.% CuO</b>	1.60	2.46	2.66	2.73	2.36	0.52
<b>1.0 vol.% CuO</b>	2.33	2.79	2.71	3.00	2.71	0.28
<b>0.01 vol.% graphene</b>	2.47	2.54	3.00	2.50	2.63	0.25
<b>0.1 vol.% graphene</b>	1.93	2.65	2.71	2.57	2.46	0.36
<b>0.3 vol.% graphene</b>	2.15	2.79	2.57	2.76	2.57	0.30
<b>Neem</b>	1.14	1.20	1.16	1.28	1.20	0.06
<b>Mineral</b>	1.07	1.03	1.10	1.31	1.13	0.13
<b>Sunflower</b>	1.13	1.09	1.11	1.21	1.14	0.05
<b>Karanja</b>	1.19	1.14	1.14	1.36	1.21	0.11

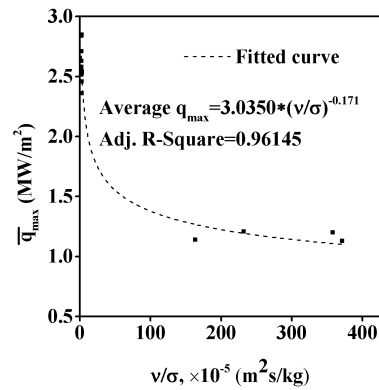


**Figure 5.5: Relation between the mean peak heat flux and the viscosity, density and surface tension of the quench media**

The temperature and time at which the liquid quench medium rewets the various locations of the quench probe surface are shown in Figure 5.6.

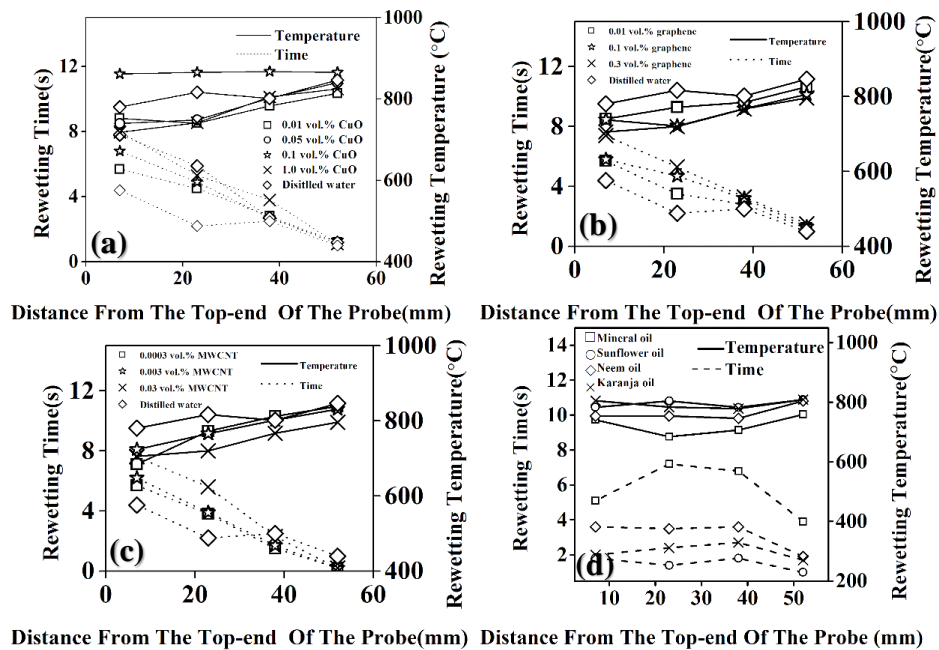


**Figure 5.6: Rewetting time and temperature during quenching in (a) CuO (b) graphene and (c) MWCNT of various concentrations and (d) quench oils**

For the nanofluids, the rewetting temperature was lower and it took longer time to rewet the probe compared with distilled water. Higher rewetting temperatures resulted at the upper top portion compared to the bottom end because of the rewetting front motion from the bottom to the top end of the probe. In the case of quenching in oil media,

sunflower oil showed the least rewetting time while mineral oil had the highest with karanja and neem oil showing intermediate values. Lower rewetting time is preferred as it is associated with faster cooling thereby avoiding the transformation to pearlite during quenching. Further, the rewetting time for mineral oil is about 5s at 7.5 mm (near the top) and was observed to be lower than that obtained at 23 mm (see Figure 5.6d) indicating the existence of a second rewetting front that forms at the top and propagates along the probe surface and was confirmed by video images shown in Appendix B (Figure B.1).

The temperature at which the oils rewet the probe surface was more uniform with higher values for the vegetable oils compared to mineral oil quench medium. The effect of delayed rewetting by nanofluids is more clearly observed in Figure 5.7a-c. Figure 5.7d shows the fraction heat removed as a function of time during quenching in oil media. To obtain these curves, the quench data was considered from the start of quenching upto the time at which the surface node corresponding to TC(1) thermocouple location showed 60 °C. The interfacial heat flux curves at each of the segments were integrated to obtain the area under them.

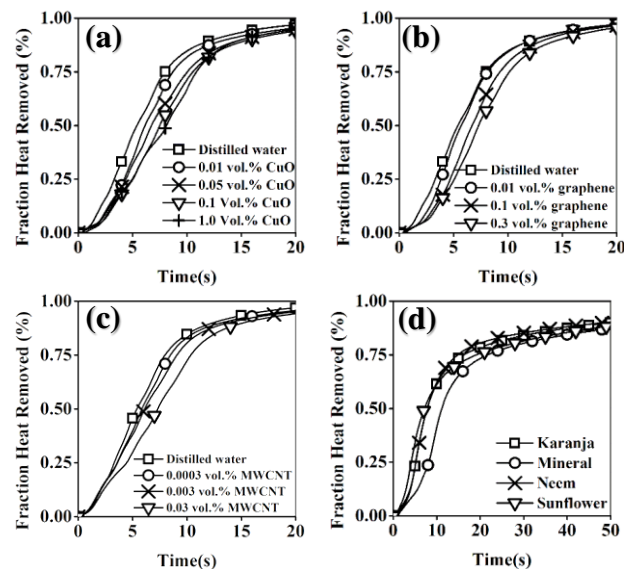


**Figure 5.7: Fraction heat removed as a function of time during quenching in (a) CuO (b) graphene and (c) MWCNT of various concentrations and (d) quench oils**

The average area was obtained and was normalised to obtain the fraction heat removed. The plots for nanofluids clearly show that the fraction of heat removed reduced for nanofluids in comparison to distilled water. The reduction in the fraction of heat removed increased with increase in the nanoparticle concentration. The implication of this is akin to that of quenching in aqueous polymer quench media where heat transfer reduces with increase in the polymer concentration to water. The addition of nanoparticles helps to lower the heat transfer rates provided by water making it better suited for quenching steels that require lower quench speeds. For the oil quenchants, longer duration was taken by the mineral oil to rewet the probe surface and showed lower fraction of heat removed compared to the vegetable oil quench media. Sunflower oil showed higher while more or less similar fraction of heat was removed by neem and karanja oils upto 12s into the quenching process.

To further understand the effect of delayed rewetting, the average heat removed during quenching was plotted as a function of the average surface temperature and is shown in Figure 5.8.

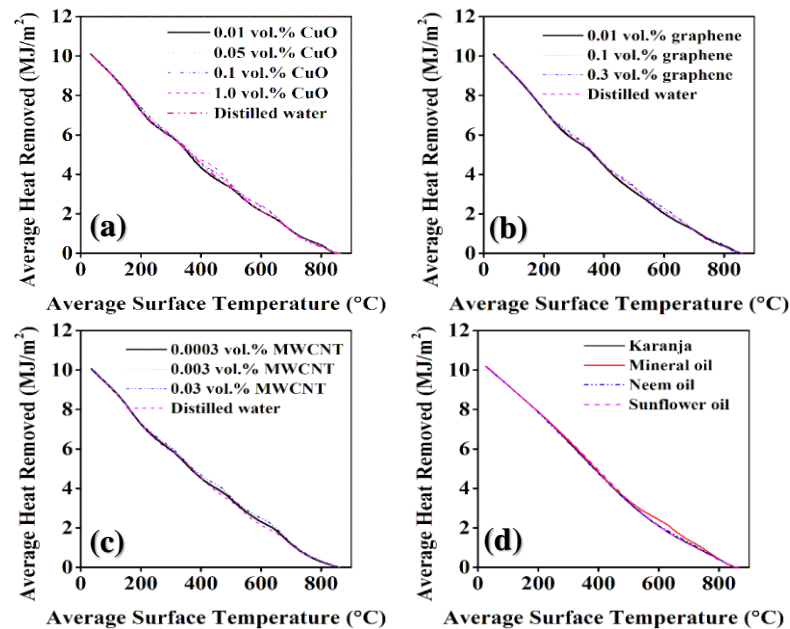


**Figure 5.8: Average heat removed vs. average surface temperature during quenching in (a) CuO (b) graphene and (c) MWCNT of various concentrations and (d) quench oils**

The discussion in the case of nanofluids are restricted to CuO nanofluids as other nanofluids showed similar results. The lowest concentration of 0.01 vol.%, showed very much similar magnitude of heat removed compared to water while that with higher concentrations showed deviations. The deviation between the curves were observed to be larger near 440 °C. With increased delay in rewetting, the temperature distribution in the probe was more uniform across its cross section (Figure 5.9). This figure shows flattening of the gradient at the interface between the temperatures represented in dark blue and light blue colours.



**Figure 5.9: Thermal profile in Inconel alloy during quenching in CuO nanofluids of concentrations 0.01, 0.05, 0.1 and 1.0 vol.% (from left to right) at average surface temperature of 440 °C**

The distribution of temperature in the probe during quenching in distilled water was similar to that shown for the 0.01 vol.% CuO nanofluid. Figure 5.10 shows the distribution in temperature of the probe at the average surface temperature of 250 °C. This temperature was chosen as it lies in the martensitic transformation range for most steels. At this average surface temperature, no difference in temperature distribution is observed between the CuO nanofluids. This implies that quenching in nanofluids would result in different property compared with quenching in water because of the deviations occurring at temperatures such as that observed at 400 °C.





**Figure 5.10: Thermal profile in Inconel alloy during quenching in CuO nanofluids of concentrations 0.01, 0.05, 0.1 and 1.0 vol.% (from left to right) at average surface temperature of 250 °C**

In the case of quenching oils, the deviation between the curves for mineral and vegetable oils is observed near 600 °C. Below 400 °C the thermal profile of all the oils are similar and cool the probe in a uniform manner. The distribution of temperature in the probe at 600 °C average surface temperature is shown in Figure 5.11. Mineral oil cooled the bottom portion of the probe more uniformly at 600 °C average surface temperature as evident from the region represented by blue in the probe. The comparative slower quenching of the probe in mineral oil thus resulted in higher temperature gradient between the top and bottom portion of the probe. Quenching in vegetable oils was found to be more uniform along the length of the probe compared to mineral oil. Among the vegetable oils, sunflower oil had better (600 to 680 °C temperature region more, shown as green) quench uniformity followed by karanja and neem oils.

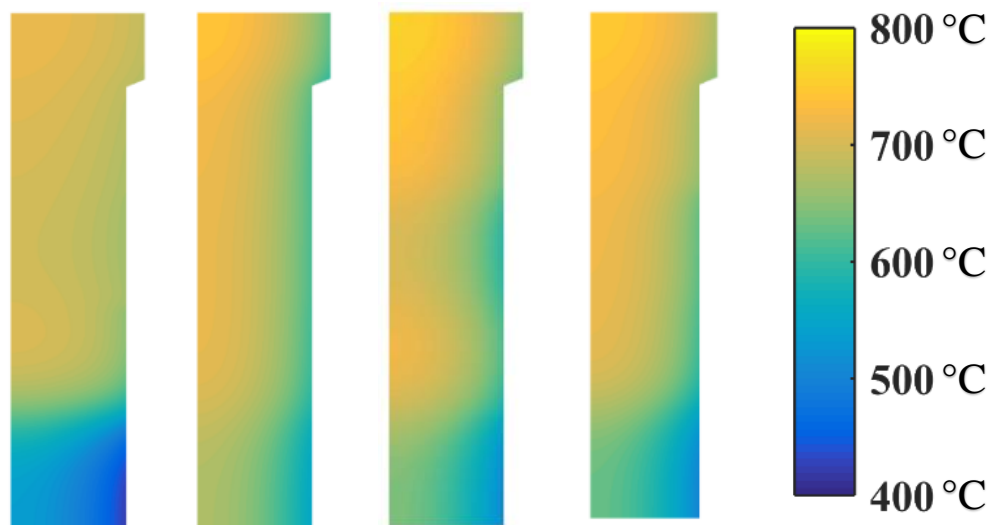


**Figure 5.11: Thermal profile in inconel alloy during quenching in mineral, sunflower, karanja and neem oils (from left to right) at average surface temperature of 600 °C**

## 5.2 Effect of Agitation on Quench Media

The measured cooling curves obtained during quenching in nanofluids and oil quenching media with various quench media under agitated conditions are presented in Appendix D. The critical cooling rates obtained at the geometric centre of the inconel probe during quenching in nanofluids of various concentrations under various agitated quenching conditions are shown in Figure 5.12. The critical cooling parameters showed an increase relative to that for distilled water for the MWCNT and graphene nanofluids while those of CuO were lower compared to distilled water. Of the nanofluids, 0.1 vol.% graphene nanofluid had the highest peak cooling rate at 1500 rpm and was nearly 32 % higher than that compared to water quenching. The results show that copper oxide based nanofluids showed lower cooling rates compared to MWCNT and graphene nanofluids whose cooling rates were considerably enhanced under agitated quenching conditions relative to that of distilled water. Nanofluids have shown to wet the surface better than water and when coupled with agitation, causes higher metal/quenchant interfacial heat transfer in the case of MWCNT and graphene. However, this seems to be not true in the case of copper oxide nanofluids which showed lower values at the

critical temperature especially at lower concentrations as oxides have lower conductivity.

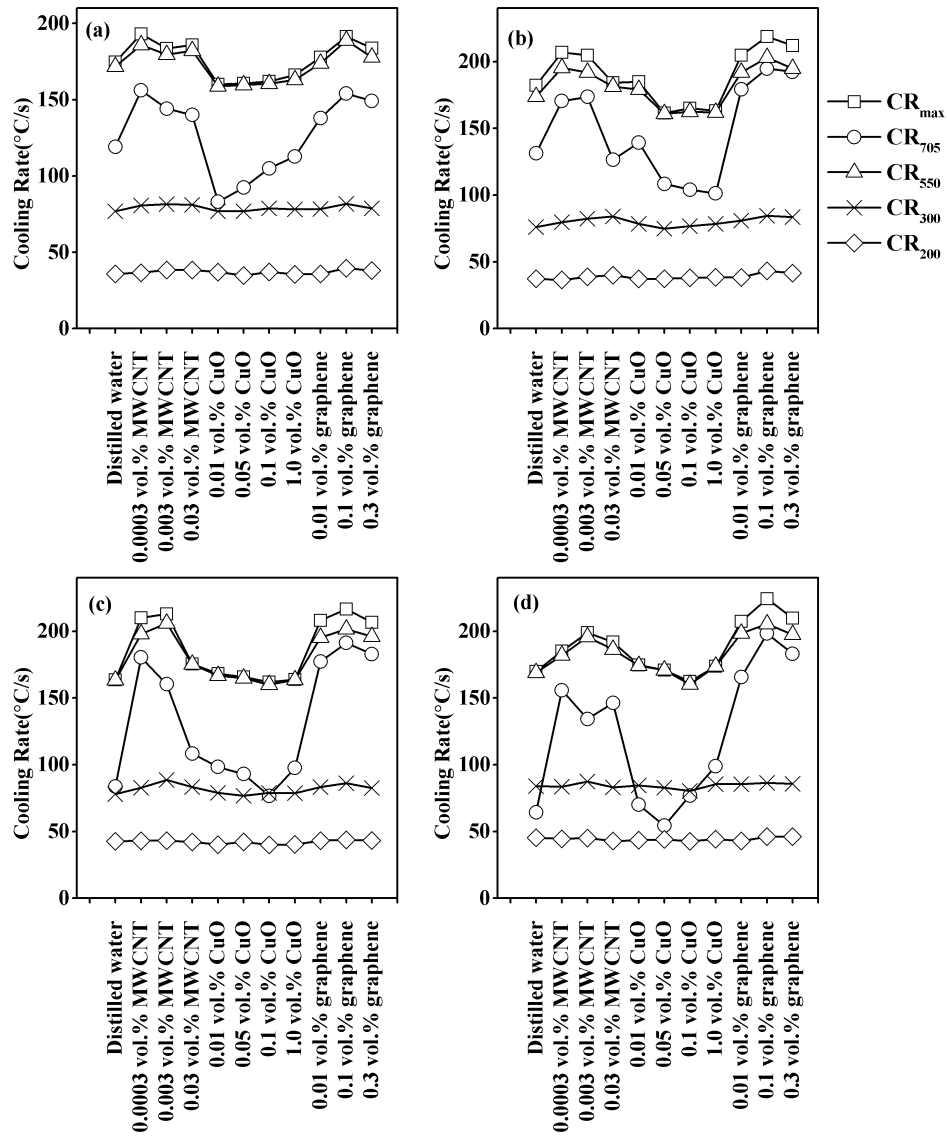


**Figure 5.12: Cooling rates at critical cooling temperatures for nanofluids under (a) still (b) 500 (c) 1000 and (d) 1500 rpm agitation rates**

The critical cooling rates for oil quench media under various agitation rates is shown in Figure 5.13. They show that at all the agitation rates the cooling rates were higher for sunflower oil and was followed by karanja, neem and mineral oil quenching media. Further, agitation rates of 500, 1000 and 1500 rpms did not have any significant effect

on the magnitudes of the cooling rates. This was because of the higher viscosity of oil quenching media.

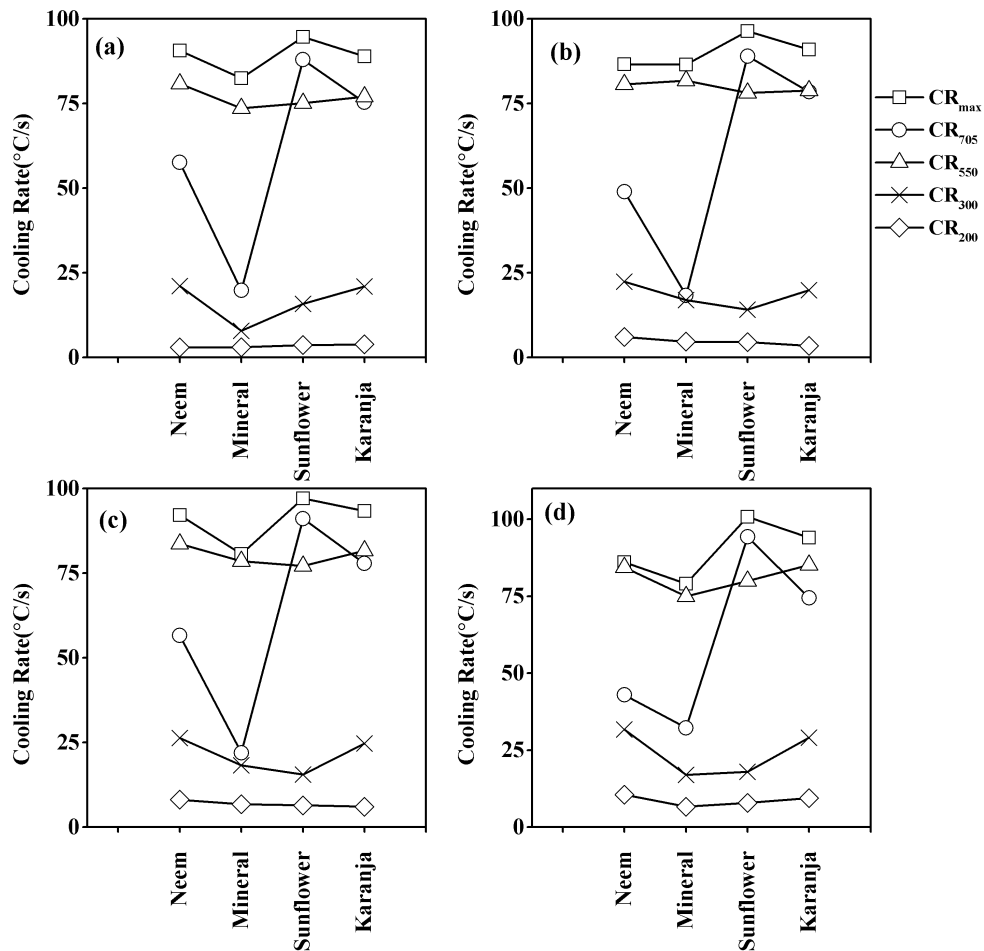


Figure 5.13: Cooling rates at critical cooling temperatures for oils under (a) still (b) 500 (c) 1000 and (d) 1500 rpm agitation rates

### 5.2.1 Spatiotemporal heat flux during quenching of inconel probe under agitated quench conditions

The heat flux curves obtained at various interfacial heat flux segments during quenching under agitation are presented in Appendix I. The maximum heat flux obtained at the metal/quenchant interfacial heat flux segments under various agitation rates are shown in Table 5.3 to 5.6. The uniformity with which heat is removed from the bottom half of the probe relative to its top half is given by the parameter  $\Delta Q_{60}$ .  $\Delta Q_{60}$  is defined as the difference in the average heat removed between the bottom half portion and the top half portion of the inconel probe obtained at the average surface

temperature of 60 °C. A positive value of  $\Delta Q_{60}$  indicates higher heat extracted from the bottom half portion of the probe while a negative value implies that the top portion of the probe removed higher heat compared with the bottom half portion. Further, lower the magnitude of  $\Delta Q_{60}$  implies more uniform heat removal from the probe during quenching.

Table 5.3 shows the peak heat flux values obtained under still quenching conditions for the various liquid quench media.

**Table 5.3: Peak heat flux at various interfacial heat segments under still quench condition**

<b>still</b>							
<b>Quench Media</b>	<b>Top half</b>		<b>Bottom half</b>		<b>Average</b>	<b>Standard deviation</b>	<b><math>\Delta Q_{60}</math></b>
	<b>q<sub>1</sub></b>	<b>q<sub>2</sub></b>	<b>q<sub>3</sub></b>	<b>q<sub>4</sub></b>			
	<b>(MW/m<sup>2</sup>)</b>						<b>(MJ/m<sup>2</sup>)</b>
<b>Distilled water</b>	2.00	2.76	2.50	2.73	2.50	0.35	0.249
<b>0.0003 vol.% MWCNT</b>	2.23	2.52	3.04	3.18	2.74	0.45	0.852
<b>0.003 vol.% MWCNT</b>	2.14	2.40	2.72	3.21	2.62	0.46	1.035
<b>0.03 vol.% MWCNT</b>	2.09	2.40	2.97	2.91	2.59	0.42	0.686
<b>0.01 vol.% CuO</b>	2.02	2.41	2.29	2.90	2.40	0.36	0.461
<b>0.05 vol.% CuO</b>	2.03	2.30	2.41	3.00	2.43	0.41	0.927
<b>0.1 vol.% CuO</b>	2.02	2.61	2.28	2.73	2.41	0.33	0.354
<b>1.0 vol.% CuO</b>	2.22	2.29	2.83	2.88	2.56	0.35	0.872
<b>0.01 vol.% graphene</b>	2.01	2.42	2.70	3.19	2.58	0.49	0.85
<b>0.1 vol.% graphene</b>	1.92	2.63	3.01	3.21	2.69	0.57	0.689
<b>0.3 vol.% graphene</b>	1.99	2.54	2.91	3.12	2.64	0.50	0.94
<b>Neem</b>	1.09	1.12	1.14	1.32	1.17	0.10	0.385
<b>Mineral</b>	1.00	1.00	1.00	1.16	1.04	0.08	0.668
<b>Sunflower</b>	1.12	1.19	1.12	1.39	1.20	0.13	0.381
<b>Karanja</b>	1.07	1.06	1.07	1.38	1.15	0.15	0.353

It shows that the heat flux boundary segment  $q_1$  has lower peak flux values compared to the other segments. This was because of the rewetting front formed during quenching, that breaks at the bottom edge of the probe and progressed along the surface and reached the  $q_1$  heat flux segment last. The highest peak flux values were obtained at the  $q_4$  segment because this is the segment where the quenchant rewets the probe first. The average heat flux for the quench media under still quench conditions in a Tensi agitation set-up showed highest values obtained with 0.0003 vol.% MWCNT while 0.01 vol.% CuO had the least average heat flux, differing with water only by 0.1 MW/m<sup>2</sup>.  $\Delta Q_{60}$  values showed that uniformity was highest with the water and the least with 0.003 vol.% MWCNT nanofluid and all other aqueous quench media had intermediate values. Of the oil quench media used, higher average heat flux was obtained with sunflower oil followed by neem, karanja and mineral oils respectively. Among the quench oils, more uniformity in heat extraction was obtained with karanja oil followed by sunflower, neem and mineral oil respectively.

Table 5.4 shows the peak flux and  $\Delta Q_{60}$  values obtained at 500 rpm impeller agitation rate in the Tensi arrangement. The trend in the heat flux values from  $q_1$  to  $q_4$  for a given quench media remains the same as before with lower flux values at  $q_1$  and higher at  $q_4$  with  $q_2$  and  $q_3$  showing intermediate values. At an impeller speed of 500 rpm, the average heat flux was found to be highest with 0.1 vol.% graphene nanofluid. CuO nanofluid of 0.05 vol.% concentration had the least average heat flux value. Further, the average value for all the quench media were found to be higher at 500 rpm agitation rate compared with quenching under still quench conditions.  $\Delta Q_{60}$  showed least uniformity with 0.05 vol.% CuO nanofluid and maximum uniformity with 0.0003 vol.% MWCNT. The standard deviation in the peak flux values at 500 rpm was found to be lower than those obtained in the case of still quenching implying agitation of the quench medium increases the uniformity with which heat is removed during quenching. The data obtained for oil quench media showed a slight improvement in the peak flux values at 500 rpm with sunflower oil having the highest average peak heat flux followed by karanja, neem and mineral oils respectively.

**Table 5.4: Peak heat flux at various interfacial heat segments under 500 rpm quench condition**

500 rpm							
Quench Media	Top half		Bottom half		Average	Standard deviation	$\Delta Q_{60}$
	q <sub>1</sub>	q <sub>2</sub>	q <sub>3</sub>	q <sub>4</sub>			
	(MW/m <sup>2</sup> )						
<b>Distilled water</b>	2.37	2.50	2.75	2.68	2.58	0.17	0.678
<b>0.0003 vol.% MWCNT</b>	2.06	2.67	2.97	3.20	2.72	0.50	0.364
<b>0.003 vol.% MWCNT</b>	2.56	2.58	2.72	3.24	2.78	0.32	0.817
<b>0.03 vol.% MWCNT</b>	2.02	2.73	2.95	2.86	2.64	0.42	0.499
<b>0.01 vol.% CuO</b>	1.85	3.14	2.97	2.89	2.71	0.58	0.456
<b>0.05 vol.% CuO</b>	1.98	2.53	2.44	2.90	2.46	0.38	0.823
<b>0.1 vol.% CuO</b>	2.32	2.59	2.47	2.89	2.57	0.24	0.647
<b>1.0 vol.% CuO</b>	2.21	2.61	2.66	2.99	2.62	0.32	0.958
<b>0.01 vol.% graphene</b>	2.24	2.77	3.07	3.13	2.80	0.41	0.659
<b>0.1 vol.% graphene</b>	2.59	2.83	3.47	3.25	3.04	0.40	0.569
<b>0.3 vol.% graphene</b>	2.38	2.80	3.14	3.12	2.86	0.36	0.693
<b>Neem</b>	0.98	1.13	1.08	1.34	1.13	0.15	-0.049
<b>Mineral</b>	1.14	1.02	0.96	1.21	1.08	0.11	0.166
<b>Sunflower</b>	1.21	1.22	1.17	1.41	1.25	0.11	0.026
<b>Karanja</b>	1.08	1.08	1.09	1.39	1.16	0.15	-0.627

The peak flux values obtained at various interfacial heat flux segments at an agitation rate of 1000 rpm are presented in Table 5.5. Compared to the values obtained at 500 rpm and still quench conditions, the flux values were higher and more uniform at 1000 rpm. Graphene nanofluids showed higher average heat flux values compared to MWCNT nanofluids while CuO nanofluids showed the least average heat flux.

**Table 5.5: Peak heat flux at various interfacial heat segments under 1000 rpm quench condition**

1000 rpm							
Quench Media	Top half		Bottom half		Average	Standard deviation	$\Delta Q_{60}$
	q <sub>1</sub>	q <sub>2</sub>	q <sub>3</sub>	q <sub>4</sub>			
	(MW/m <sup>2</sup> )						
<b>Distilled water</b>	2.48	2.87	2.94	2.93	2.80	0.22	0.730
<b>0.0003 vol.% MWCNT</b>	2.45	2.72	3.18	3.08	2.86	0.34	0.721
<b>0.003 vol.% MWCNT</b>	2.75	3.13	2.88	3.22	2.99	0.22	0.061
<b>0.03 vol.% MWCNT</b>	2.42	2.50	2.51	2.93	2.59	0.23	0.648
<b>0.01 vol.% CuO</b>	2.25	2.94	2.81	2.78	2.70	0.30	0.771
<b>0.05 vol.% CuO</b>	2.06	2.33	2.82	3.12	2.59	0.48	0.871
<b>0.1 vol.% CuO</b>	2.20	2.45	2.55	2.91	2.53	0.30	0.849
<b>1.0 vol.% CuO</b>	2.66	2.29	2.74	3.21	2.72	0.38	1.035
<b>0.01 vol.% graphene</b>	2.50	2.57	3.42	3.15	2.91	0.45	0.537
<b>0.1 vol.% graphene</b>	2.55	3.34	3.18	3.19	3.07	0.35	0.52
<b>0.3 vol.% graphene</b>	3.10	2.81	3.21	3.23	3.09	0.19	0.411
<b>Neem</b>	1.04	1.16	1.18	1.36	1.18	0.14	-0.131
<b>Mineral</b>	1.07	1.19	1.01	1.23	1.13	0.10	-0.105
<b>Sunflower</b>	1.21	1.19	1.18	1.50	1.27	0.15	-0.046
<b>Karanja</b>	1.24	1.16	1.08	1.46	1.23	0.16	-0.207

These results are contrary to those observed under unagitated quenching conditions. The obtained peak heat flux values suggest that under agitated quenching conditions, aqueous quench media of graphene and MWCNT nanofluids provide faster quenching ability compared to distilled water and oxide based nanofluids. The oil quenching media showed higher average peak flux values compared with earlier conditions. The  $\Delta Q_{60}$  is observed to be negative for water, neem, sunflower and karanja oils at 1000 rpm quench condition implying higher heat was removed from the top half portion of the probe



compared with the bottom half. For the nanofluids,  $\Delta Q_{60}$  was the least with 0.003 vol.% suggesting more uniform heat was removed from the top and bottom half portion of the probe compared with quenching in 1.0 vol.% CuO nanofluid that had higher value of  $\Delta Q_{60}$ .

The peak heat flux values obtained at 1500 rpm quench conditions for the various quench media at the interfacial heat flux segments are shown in Table 5.6.

**Table 5.6: Peak heat flux at various interfacial heat segments under 1500 rpm quench condition**

1500 rpm							
Quench Media	Top half		Bottom half		Average	Standard deviation	$\Delta Q_{60}$
	q1	q2	q3	q4			
	(MW/m <sup>2</sup> )						
<b>Distilled water</b>	2.63	2.93	2.52	2.91	2.75	0.20	-0.142
<b>0.0003 vol.% MWCNT</b>	2.79	2.99	3.13	3.04	2.99	0.14	0.247
<b>0.003 vol.% MWCNT</b>	2.87	2.95	2.92	3.07	2.95	0.09	0.465
<b>0.03 vol.% MWCNT</b>	2.44	2.56	2.70	2.99	2.67	0.24	0.88
<b>0.01 vol.% CuO</b>	2.77	2.75	2.58	2.93	2.76	0.14	0.179
<b>0.05 vol.% CuO</b>	2.54	2.14	2.79	3.06	2.63	0.39	0.511
<b>0.1 vol.% CuO</b>	2.92	2.70	2.65	2.91	2.79	0.14	0.742
<b>1.0 vol.% CuO</b>	2.71	2.58	2.96	2.90	2.79	0.17	0.467
<b>0.01 vol.% graphene</b>	2.54	2.97	3.04	3.14	2.92	0.26	0.241
<b>0.1 vol.% graphene</b>	2.92	3.27	3.35	3.38	3.23	0.21	0.384
<b>0.3 vol.% graphene</b>	3.12	3.02	3.21	3.26	3.15	0.11	0.477
<b>Neem</b>	1.13	1.16	1.03	1.32	1.16	0.12	-0.165
<b>Mineral</b>	1.06	1.10	0.96	1.23	1.09	0.11	0.246
<b>Sunflower</b>	1.32	1.27	1.25	1.48	1.33	0.11	-0.115
<b>Karanja</b>	1.26	1.26	1.15	1.51	1.30	0.15	-0.195

Compared to the other agitation rates the interfacial peak heat flux had higher values and the magnitude between  $q_1$  and  $q_4$  was more uniform due to agitation. Similar to 1000 rpm agitation condition, graphene had the highest average peak flux values showing marked improvement in heat extraction over distilled water. CuO nanofluids had slightly lower average peak heat flux compared with that of water. Average peak heat flux obtained with MWCNT were higher than distilled water. For the oil quench media, sunflower showed the highest average peak heat flux compared with the other oil quenching media. The rewetting time and temperature obtained with nanofluids and oil quench media during immersion quenching of the inconel probe in 1.5 lts of quench medium in a Tensi agitation system under still conditions are shown in Figure 5.14.

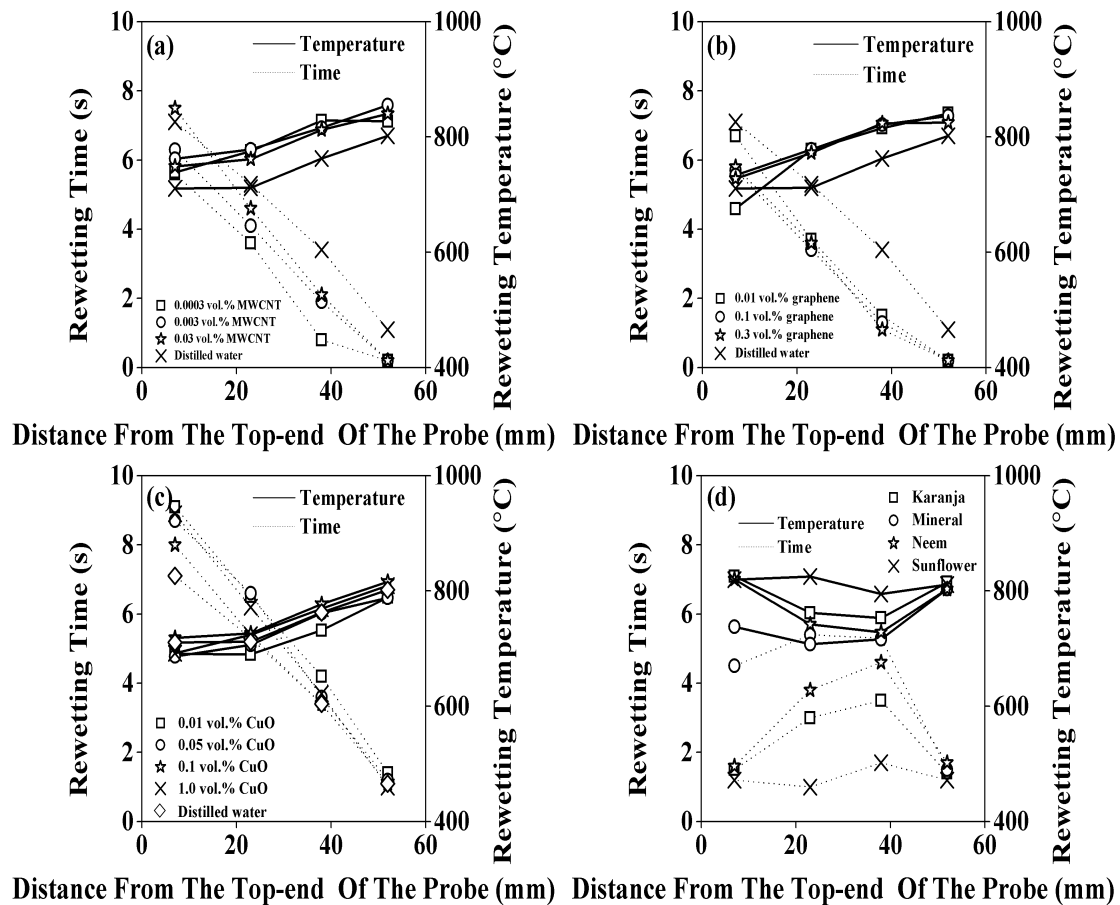


**Figure 5.14: Rewetting time and temperatures of quench media under still quench conditions**

It is clearly observed that MWCNT and graphene nanofluids rewets the surface of the inconel probe at higher temperature and at shorter times compared with water while the CuO took longer times and lower temperatures. This is contrary to the results obtained with 2 lts of quench medium where nanofluids showed longer rewetting time and lower rewetting temperatures. However, the design of the Tensi quench tank is different from the 2 lts capacity quench tank used for still quenching experiments and hence cannot be strictly compared with each other. For the oil quenchant used, sunflower oil had higher rewetting temperatures while mineral oil showed the least. The rewetting temperatures of karanja and neem oil had intermediate values in comparison to sunflower and mineral. The rewetting times were the least for sunflower oil followed by karanja, neem and mineral oils respectively.

The rewetting plots for quenching at an agitation rate of 500 rpm of impeller speed is shown in Figure 5.15.

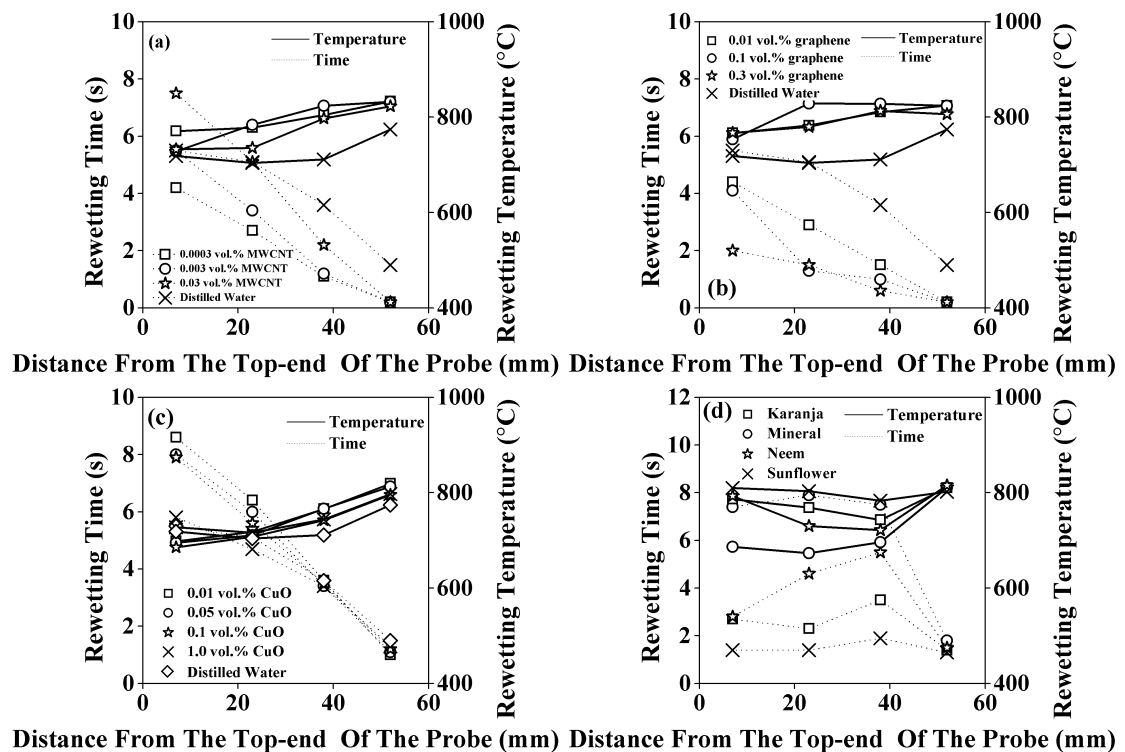


**Figure 5.15: Rewetting time and temperatures of quench media at 500 rpm quench conditions**

The result obtained is similar to those under still condition with slightly higher temperatures for graphene and MWCNT and lower for CuO indicating better rewetting of graphene and MWCNT nanofluids due to the agitation of the quench medium. For the oils, the rewetting time increased with agitation from 0 to 500 rpm while the temperature of rewetting was similar. The rewetting parameters at 1000 rpm agitation rate are shown in Figure 5.16.

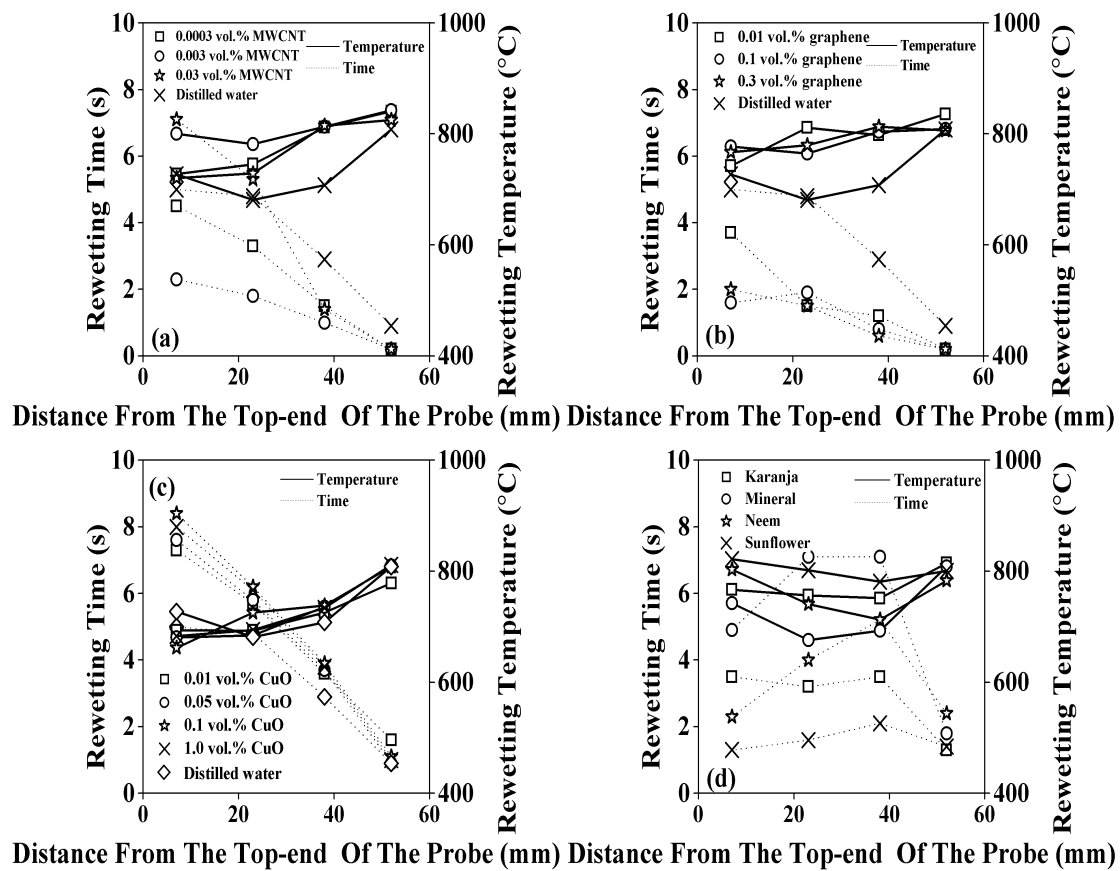


**Figure 5.16: Rewetting time and temperatures of quench media at 1000 rpm quench conditions**

It shows that better rewetting occurred for the graphene nanofluids with higher rewetting temperatures and lower rewetting times compared to the other nanofluids. These parameters confirm the higher peak flux obtained at 1000 rpm for the graphene nanofluids observed earlier. The rewetting plots obtained at the agitation rate of 1500 rpm are shown in Figure 5.17. They show that the rewetting temperatures in the case of MWCNT, graphene and CuO nanofluids were also found to be higher than water. The

rewetting times were higher for CuO and were lower for MWCNT and graphene nanofluids at most of the locations compared with water. For the oil quench media, the trend was similar to that observed earlier with higher temperature observed for sunflower followed by karanja, neem and mineral oil respectively.

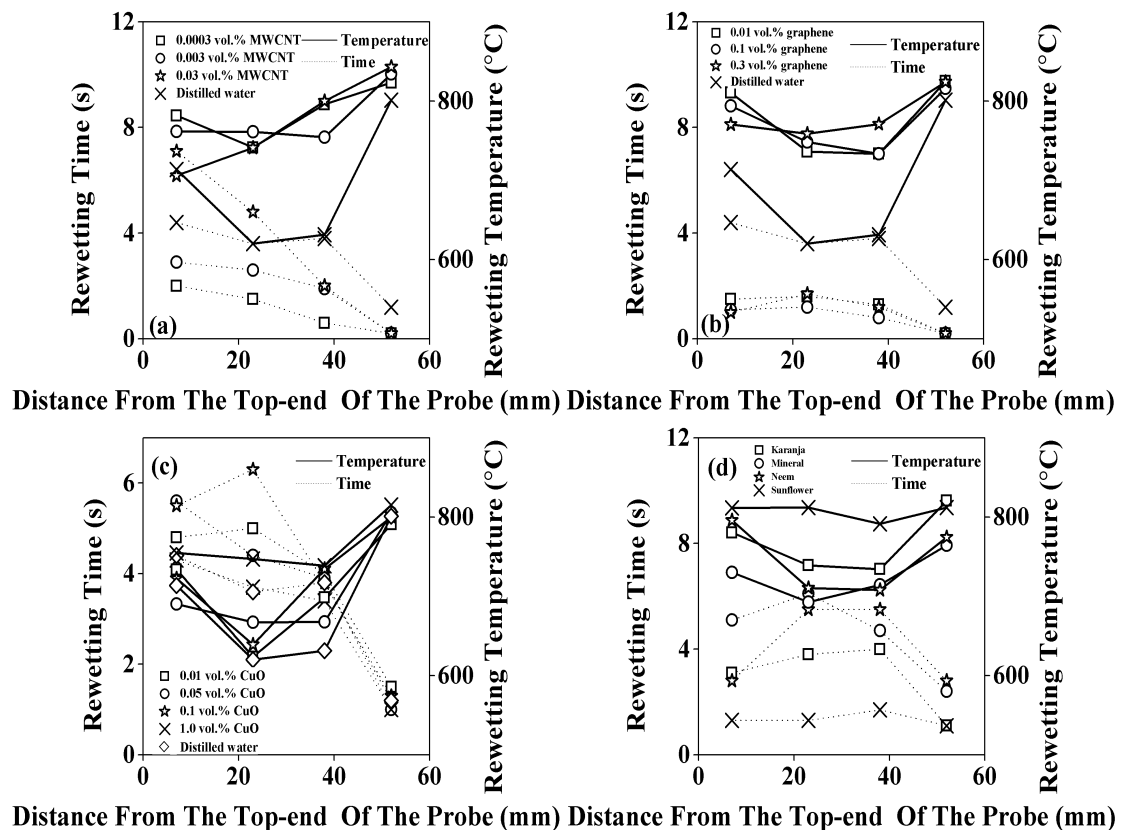


**Figure 5.17: Rewetting time and temperatures of quench media at 1500 rpm quench conditions**

The variation of average heat extracted from the inconel probe during quenching in various liquid quench media under still quench conditions are shown in Figure 5.18. The average heat removed from the inconel probe by MWCNT nanofluids were similar to that of distilled water upto a temperature of about 560 °C. Thereafter, the heat extracted with average surface temperature was lower for water upto a temperature of about 330 °C, implying faster heat removal by water compared to MWCNT in this temperature range. The average heat flow below 330 °C was observed to be similar for water and MWCNT nanofluids with the 0.03 vol.% exhibiting higher average heat extracted with temperature compared to the other MWCNT nanofluids and water.

Variations such as these can be clearly observed in the case of other nanofluids when compared with water under still quench conditions. For the oil quench media, sunflower oil removed lower amount of heat upto about 580 °C compared to other oils as the heat removed by it was faster compared with other oils during quenching upto this temperature. Faster heat removal at the onset of quenching is desirable to minimize transformation into pearlite and/or ferrite and to facilitate maximum martensite phase transformation during quenching.

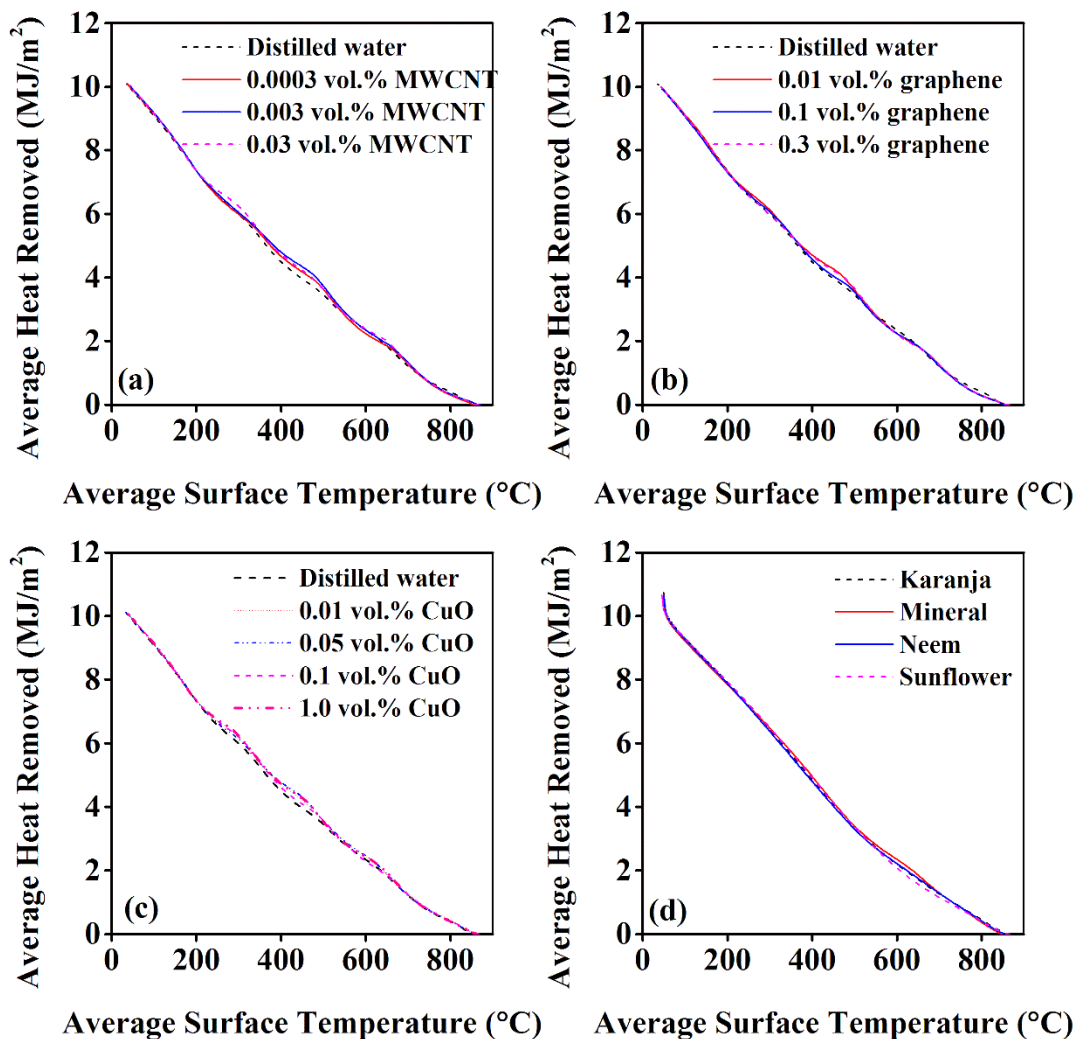


**Figure 5.18: Average heat removed as a function of average surface temperature during quenching of the inconel probe in (a) MWCNT (b) graphene (c) CuO nanofluids of various concentrations and (d) oil quenching media under still quench condition**

However, this criterion varies between steel grades and other aspects of the part to be quenched. For example, faster rate provided by water are desirable during quenching of a medium carbon steel than for a high carbon steel owing to its chemistry. In the case of oil quench media, similar to the trend observed under still quench condition, sunflower oil showed lower amount of heat to be removed at the onset of quenching compared to the other oils used, implying faster heat removal rate by sunflower oil compared to other oils.

Figure 5.19a shows the plot of average heat removed vs. average surface temperature and Figure 5.19b shows the plot of heat removed with time during quenching with graphene nanofluids of various concentrations at the agitation rate of 1500 rpm.

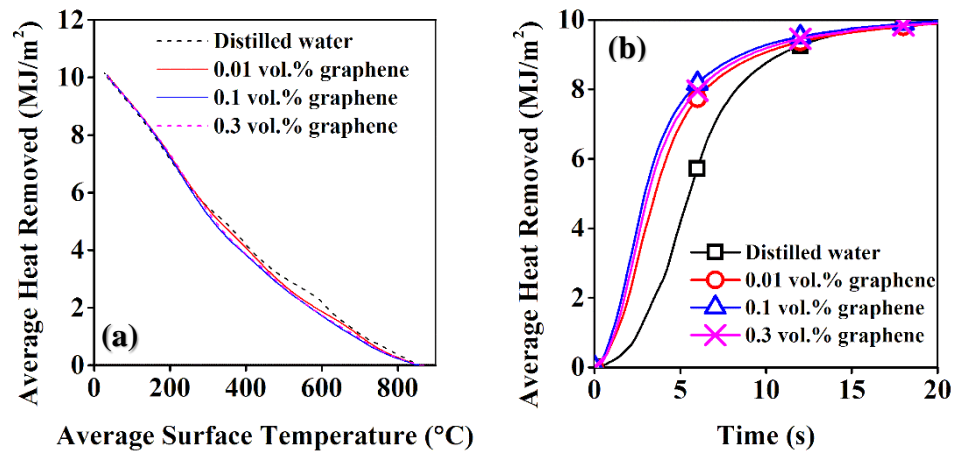


**Figure 5.19: (a) Average heat removed vs. average surface temperature and (b) average heat removed vs. time of inconel during quenching in graphene nanofluids at agitation rate of 1500 rpm**

The average heat removed with temperature were lower for the graphene nanofluids compared with water from the start of quenching till 200 °C. The reason for the same is clearly shown in Figure 5.19b which shows that the rate at which heat is removed from the inconel probe was significantly higher for graphene nanofluids compared with water. This was due to the better rewetting parameters obtained with graphene nanofluids at 1500 rpm agitation rate compared with water. Further, 0.1 and 0.3 vol.% graphene nanofluids quenched inconel probe faster compared to the 0.01 vol.% graphene and distilled water. The plots of average heat removed with respect to the average surface temperature for other quench conditions, nanofluids and oils at the

agitation rates of 500, 1000 and 1500 rpms are given in Appendix J and show larger variations in heat removed by the MWCNT and graphene nanofluids compared to water at 1000 and 1500 rpm. A comparison of these results and the average heat removed curves shown in Appendix J for the MWCNT and graphene nanofluids showed lower average heat removed with average surface temperature and was a result of faster quenching by the nanofluids when compared to water.

### 5.3 Quenching Experiments with G 10450 and G 10900 Steel Grades of Section Sizes 25 mm and 50 mm

The cooling curves measured in the test pieces of 25 and 50 mm section diameters of G 10450 and G 10900 steels are shown in the Appendices E and F respectively. The corresponding cooling rate curves are shown in these Appendices. It was observed that the rate of cooling reduces from the surface to the centre of the probe during cooling and quenching results in faster cooling at the surface of the probe compared to its centre.

Figure 5.20 shows the cooling curve obtained at the geometric centre and at 2 mm from the surface in a 25 and 50 mm probe of G 10450 steel quenched in karanja oil quench medium. its shows that because of the larger section diameter, the 50 mm probe cools much slower than the smaller section diameter 25 mm probe. The maximum cooling rates obtained at the centre and 2 mm from the surface of the 25 and 50 mm section specimens of G 10450 and G 10900 steels are given in Table 5.7 and 5.8 respectively.

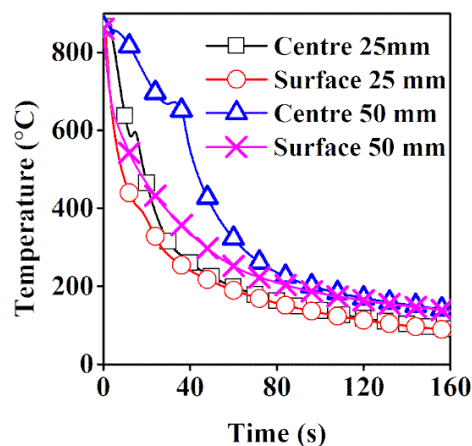


**Figure 5.20: Cooling curves measured at the centre and 2 mm from the surface in G 10450 steel of section diameters 25 and 50 mm during quenching in karanja**



**Table 5.7: Maximum cooling rate and latent heat start parameters during quenching of G 10450 steel of section diameters 25 and 50 mm**

Quenchants	G 10450							
	25 mm section diameter							
	Centre				Surface			
	CR <sub>max</sub> (°C/s)	T <sub>max</sub> (°C)	t <sub>max</sub> (s)	T <sub>ls</sub> (°C)	t <sub>ls</sub> (s)	CR <sub>max</sub> (°C/s)	T <sub>max</sub> (°C)	t <sub>max</sub> (s)
Distilled water	137	562	8.1	638	6.6	268	612	2.6
Karanja oil	38	749	6.7	583	12.8	86	792	1.8
Mineral oil	37	733	7.8	616	12.4	72	758	2.7
Neem oil	25	806	6.1	665	14.6	68	805	2.1
Sunflower oil	35	785	5.9	625	12.8	62	806	2.0
50 mm section diameter								
Distilled water	63	531	23.1	626	19.5	232	628	3.7
Karanja oil	32	589	38.4	667	29.5	71	835	0.6
Mineral oil	23	597	41	664	32.2	60	806	2.2
Neem oil	22	603	47	674	33.3	56	819	1.1
Sunflower oil	23	614	46.5	667	35.2	82	827	1.2

**Table 5.8: Maximum cooling rate and latent heat start parameters during quenching of G 10900 steel of section diameters 25 and 50 mm**

Quenchants	G 10900							
	25 mm section diameter							
	Centre				Surface			
	CR <sub>max</sub> (°C/s)	T <sub>max</sub> (°C)	t <sub>max</sub> (s)	T <sub>ls</sub> (°C)	t <sub>ls</sub> (s)	CR <sub>max</sub> (°C/s)	T <sub>max</sub> (°C)	t <sub>max</sub> (s)
Karanja oil	32	723	8.4	-	-	67	785	2.1
Mineral oil	33	753	7.7	-	-	66	800	2
Neem oil	30	741	8.7	-	-	71	795	2.7
Sunflower oil	33	733	8.1	-	-	67	785	2
50 mm section diameter								
Distilled water	21	735	14.3	-	-	299	715	1.4
Karanja oil	14	612	42.6	651	29.4	67	825	1
Mineral oil	13	621	55.7	675	38.6	50	807	3.7
Neem oil	17	634	43.4	649	31.8	57	819	3.2
Sunflower oil	14.9	631	48.4	664	33.2	57	812	1.9

In these tables  $CR_{max}$  refers to the maximum cooling rate,  $T_{max}$  refers to the temperature at which the maximum cooling rate occurs,  $t_{max}$  is the time at which the cooling rate becomes maximum,  $T_{ls}$  is the temperature at which latent heat evolution begins during continuous cooling and  $t_{ls}$  is the time corresponding to  $T_{ls}$ . For quenching of G 10450 steel of diameters 25 and 50 mm in distilled water, it is observed that the maximum cooling rate at the centre reduced by 54% for the 50 mm test piece compared to the 25 mm diameter specimen. The time taken to reach the peak rate was increased nearly 3 times for the 50 mm section diameter relative to the 25 mm diameter specimen. A reduction in the maximum cooling rate at the surface by about 11% was experienced in the case of the 50 mm test piece compared to the 25 mm section diameter for quenching in water. The temperature at which the latent heat evolution starts was slightly higher for 25 mm section diameter compared to the 50 mm section diameter steel. At the centre, of the 25 and 50 mm test pieces quenched in karanja oil the maximum cooling rate was nearly the same. The temperature at which the maximum occurred in the case of 25 mm section size was higher than the  $T_{ls}$  temperature and was higher than that observed in the case of the 50 mm section diameter. This implies lesser influence of phase transformation in the 25 mm section diameter compared to the 50 mm section diameter. In the case of the 50 mm diameter,  $T_{max}$  was lower than the  $T_{ls}$  temperature implying larger effect of phase transformation on cooling. The latent heat evolution caused increased cooling rate during transformation leading to the attainment of a maximum cooling rate during the transformation. For other oils, it was found that the maximum cooling rates at the centre of the 50 mm section diameter was lower than those obtained with the 25 mm section diameter. On comparing the value obtained at the surface, it was observed that the maximum cooling rates in the case of quenching of 50 mm section diameters were lower compared to the 25 mm section diameter and occurred at temperatures higher than those obtained for the 25 mm diameter specimens.

The maximum cooling rate and latent heat start parameters for the G 10900 steel grades of diameters 25 and 50 mm quenched in distilled water and oil quenching media are given in Table 5.8. Heat flux transients could not be estimated for the 25 mm section diameter quenched in distilled water as the probe cracked because of the faster cooling rate exerted by water on it. At the centre,  $CR_{max}$  for the 50 mm section diameter was

reduced by nearly 50% when compared to that observed for the 25 mm diameter quenched in the corresponding quench medium. Similar to quenching of the G 10450 steels,  $T_{\max}$  was lower for the larger diameter specimen compared with the smaller test pieces used. Contrary to the observation in the G 10450 steel for 25 mm diameter quenched in oils, the 25 mm section diameters of G 10900 steels did not undergo austenite transformation into pearlite/ferrite and hence did not show latent heat evolution. This signifies that the oil quench media are more suitable to quench harden small diameter (below 25 mm section size) workpieces of high carbon steels such as the G 10900 compared to the G 10450 steel grade. The larger diameter specimens showed latent heat evolution during the course of quenching similar to that observed for the 50 mm section size of G 10450 steel and had  $T_{\text{Is}}$  temperatures that were comparable among the oil quench media.

### 5.3.1 Effect of section diameter on the interfacial heat flux transients during quenching of steels

The effect of section diameter on the heat flux transients obtained during quenching of 25 and 50 mm section diameters of G 10450 steel in oil and distilled water quenching media is shown in Figure 5.21.

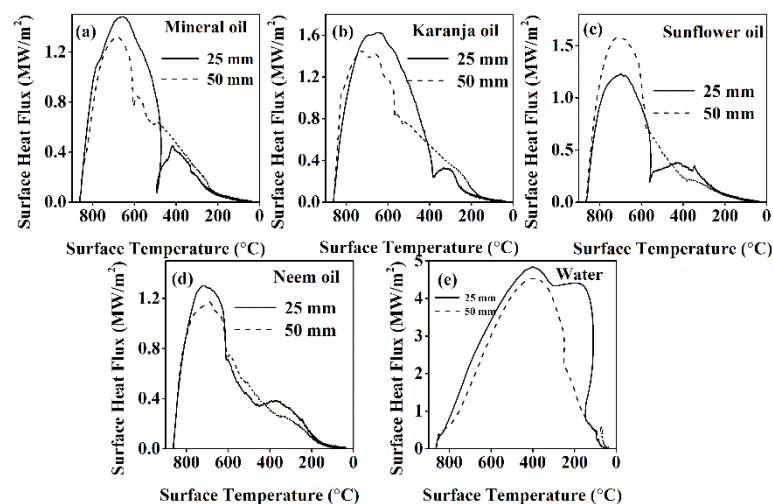


**Figure 5.21: Heat flux transients obtained during quenching of 25 and 50 mm section diameters of G 10450 steels in (a) mineral (b) karanja (c) sunflower (d) neem and (e) distilled water quench media**

It shows that the smaller diameter probe attains a higher peak flux value in the case of quenching with oils and water compared with the larger diameter samples because of the lower transformation heat evolved during their quenching. The peak heat flux obtained during quenching of the 25 mm section diameter in karanja, mineral, neem, sunflower oils and water were 1.6, 1.48, 1.3, 1.2 and 4.8 MW/m<sup>2</sup> respectively. The corresponding values for the 50 mm section diameter were found to be 1.45, 1.3, 1.17, 1.54 and 4.53 MW/m<sup>2</sup> respectively.

The heat flux obtained with 25 and 50 mm section sizes of G 10900 steel quenched in oil and water quench media are shown in Figure 5.22. These curves show similar trend to those observed in the case of the G 10450 steels. They show lower peak heat flux in the case of the 50 mm section compared to the 25 mm diameter specimens during quenching in oil quench media. The peak heat flux was found to vary between 1.1 to 1.3 MW/m<sup>2</sup> for the oil quenched steels. The corresponding value for distilled water was about 5 MW/m<sup>2</sup>.

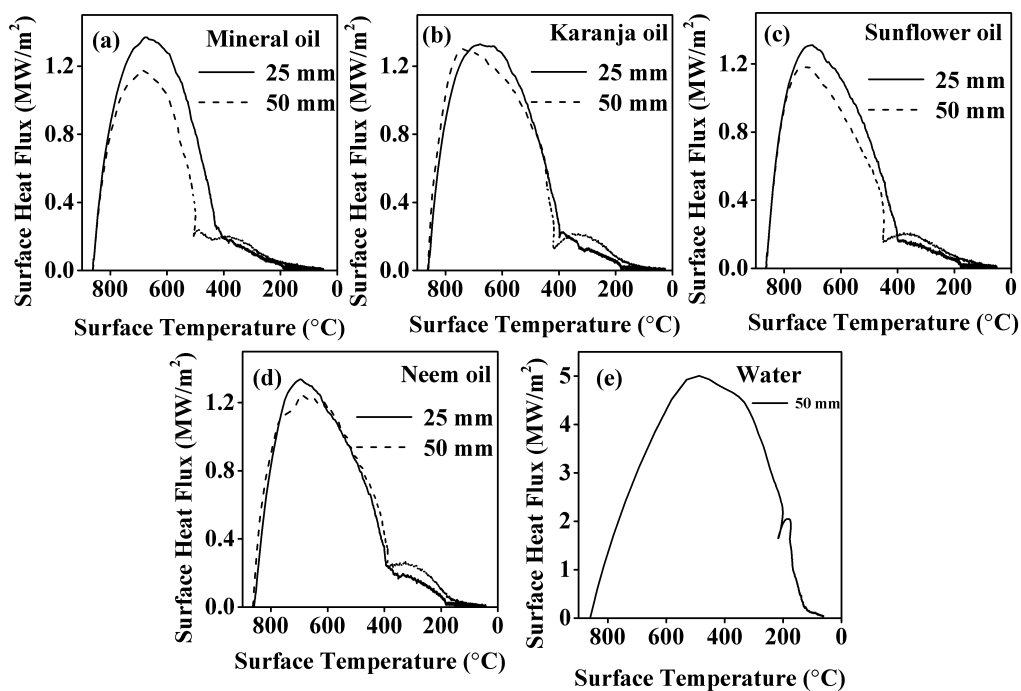


**Figure 5.22: Heat flux transients obtained during quenching of 25 and 50 mm section diameters of G 10900 steels in (a) mineral (b) karanja (c) sunflower (d) neem and (e) distilled water quench media.**

### 5.3.2 Heat removed during quenching in oil quench media

Figure 5.23 shows the effect of quench medium on heat extraction during quenching of G 10450 and G 10900 steel grades in mineral and vegetable oils.

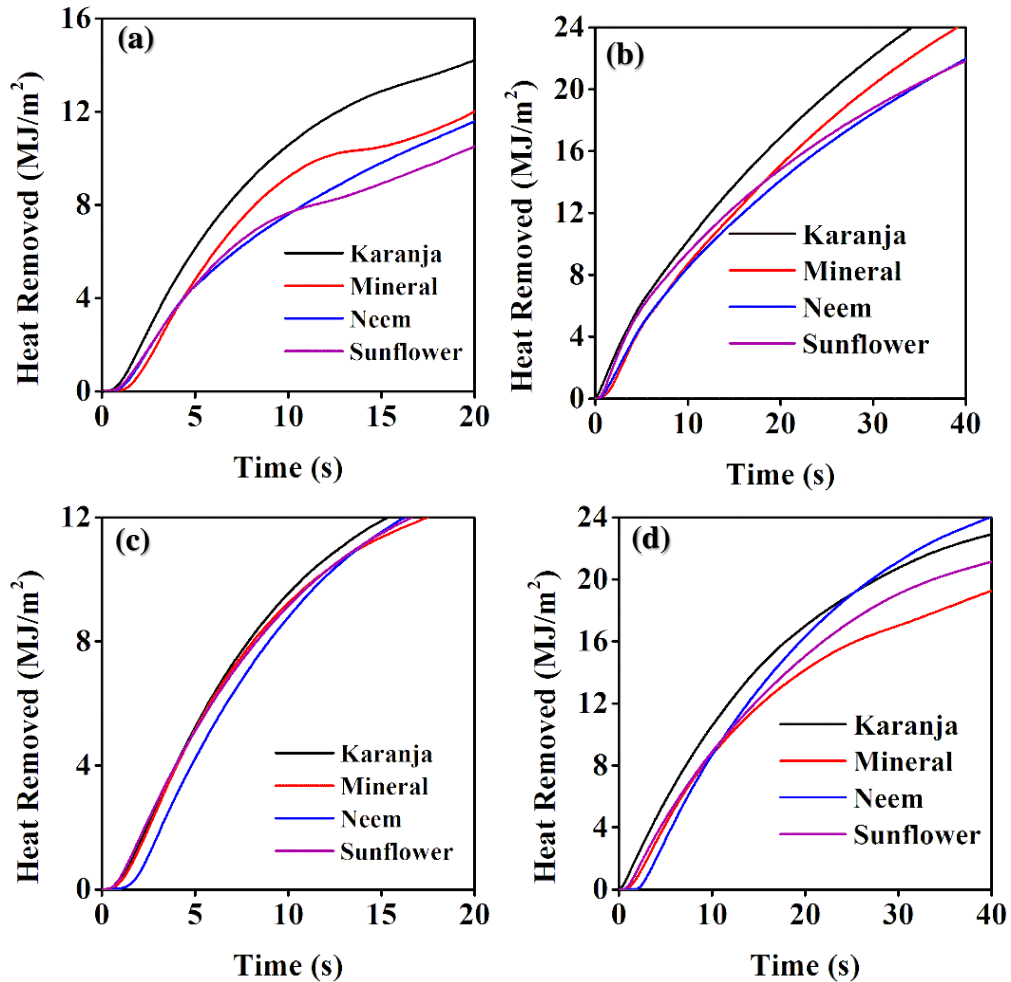


**Figure 5.23: Heat removed by oil quenchants during quenching of G 10450 steel of section diameters (a) 25 and (b) 50 mm and G 10900 steel of section diameters (c) 25 and (d) 50 mm**

In all the cases, the heat removed by karanja oil was higher compared with other oil quenching media followed by sunflower, mineral and neem oil. This resulted in higher hardness in the test pieces quenched in karanja oil followed by sunflower, neem and mineral oil as shown in Figure 4.14 and 4.15.

### 5.3.3 Microstructure

The microstructures obtained during quenching of G 10450 and G 10900 steels of diameters 25 and 50 mm in oil quench media are shown in Figures 5.24 – 5.31.

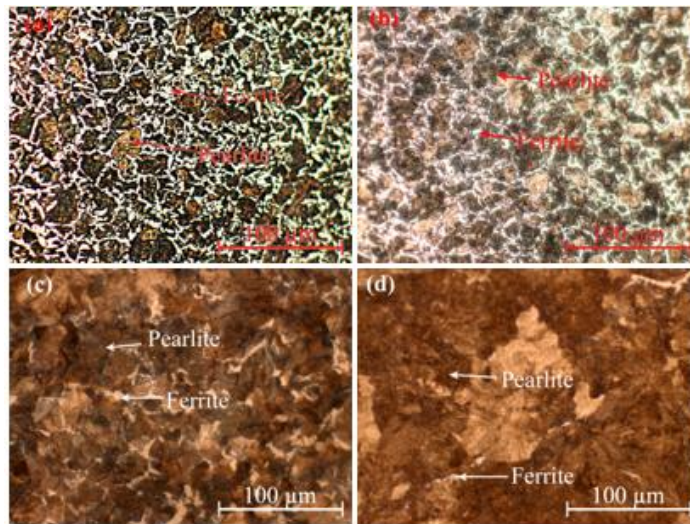


**Figure 5.24: Microstructure obtained in G 10450 steel at the (a) centre and (b) surface of the 25 mm probe and (c) centre and (d) surface of the 50 mm probe during quenching in mineral oil**

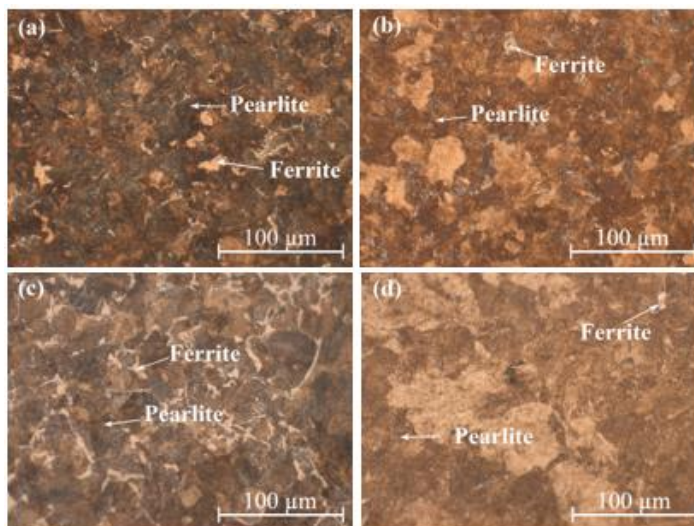


**Figure 5.25: Microstructure obtained in G 10450 steel at the (a) centre and (b) surface of the 25 mm probe and (c) centre and (d) surface of the 50 mm probe during quenching in sunflower oil**



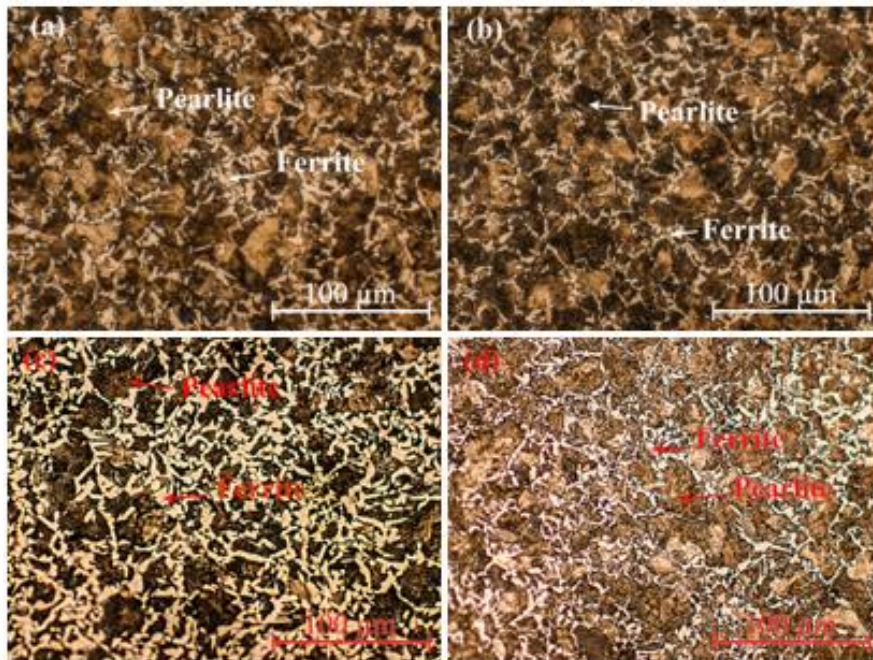


**Figure 5.26: Microstructure obtained in G 1045 steel at the (a) centre and (b) surface of the 25 mm probe and (c) centre and (d) surface of the 50 mm probe during quenching in neem oil**

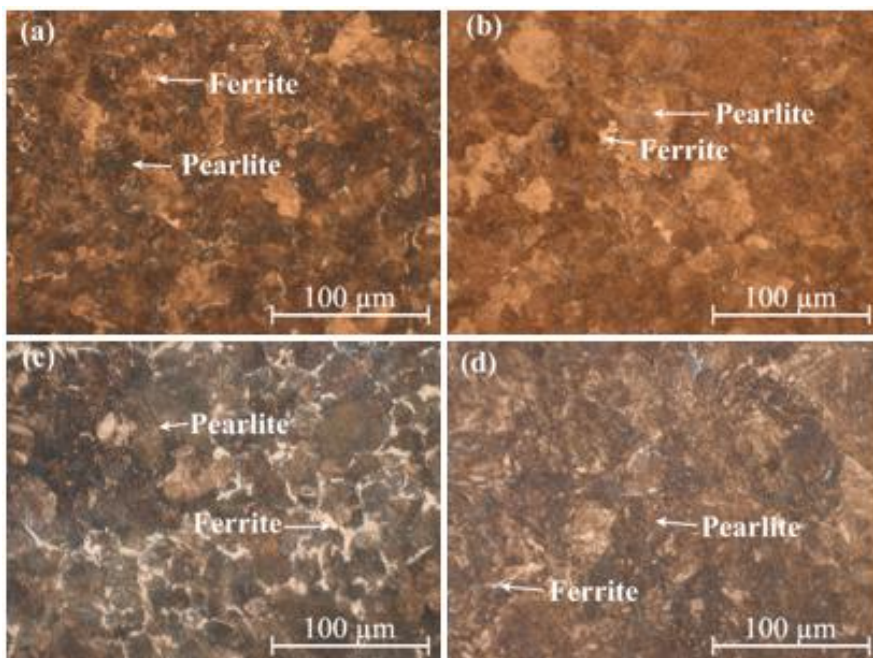


**Figure 5.27: Microstructure obtained in G 1045 steel at the (a) centre and (b) surface of the 25 mm probe and (c) centre and (d) surface of the 50 mm probe during quenching in karanja oil**

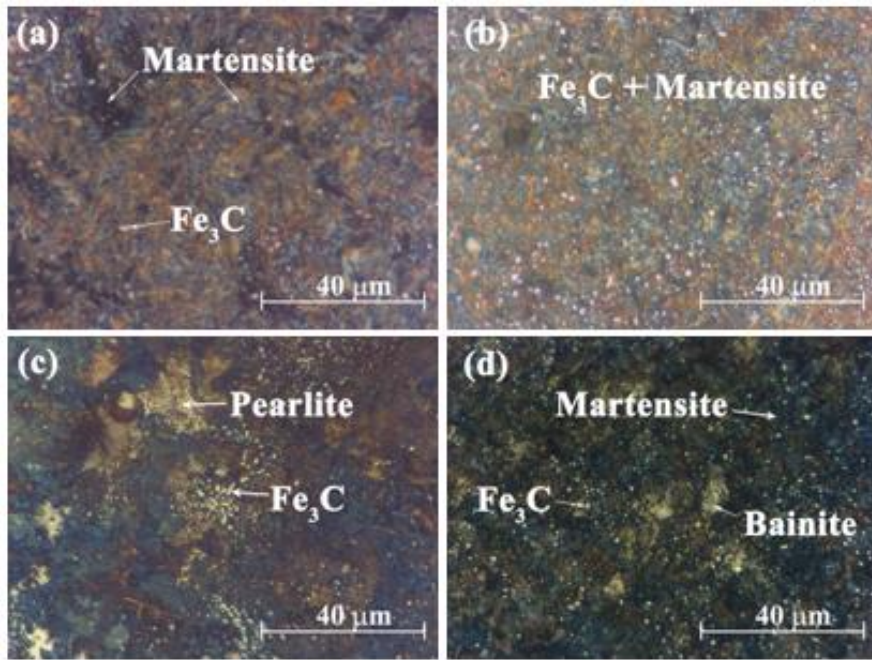


**Figure 5.28: Microstructure obtained in G 10900 steel at the (a) centre and (b) surface of the 25 mm probe and (c) centre and (d) surface of the 50 mm probe during quenching in mineral oil**

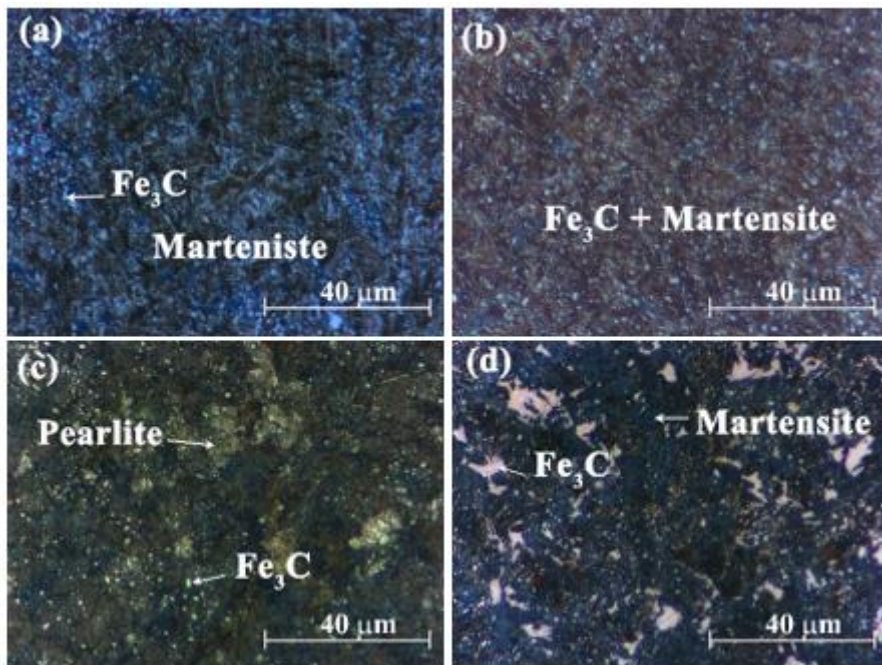


**Figure 5.29: Microstructure obtained in G 10900 steel at the (a) centre and (b) surface of the 25 mm probe and (c) centre and (d) surface of the 50 mm probe during quenching in sunflower oil**



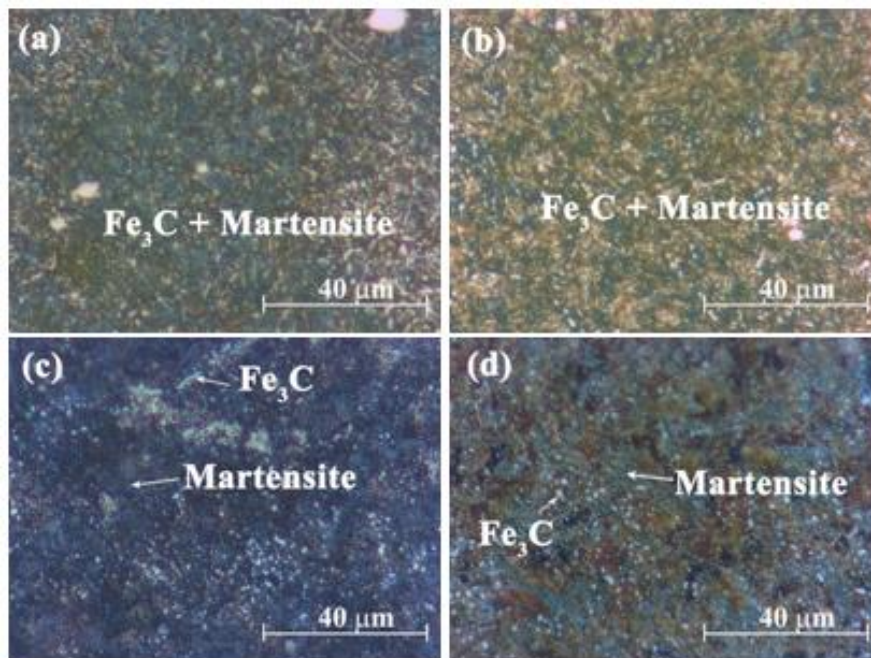


**Figure 5.30: Microstructure obtained in G 10900 steel at the (a) centre and (b) surface of the 25 mm probe and (c) centre and (d) surface of the 50 mm probe during quenching in neem oil**

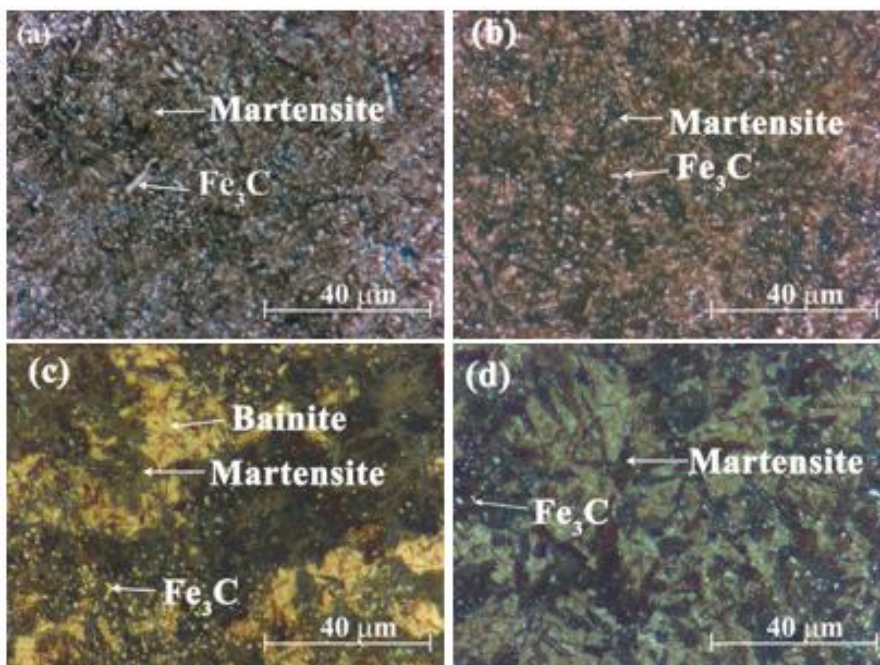
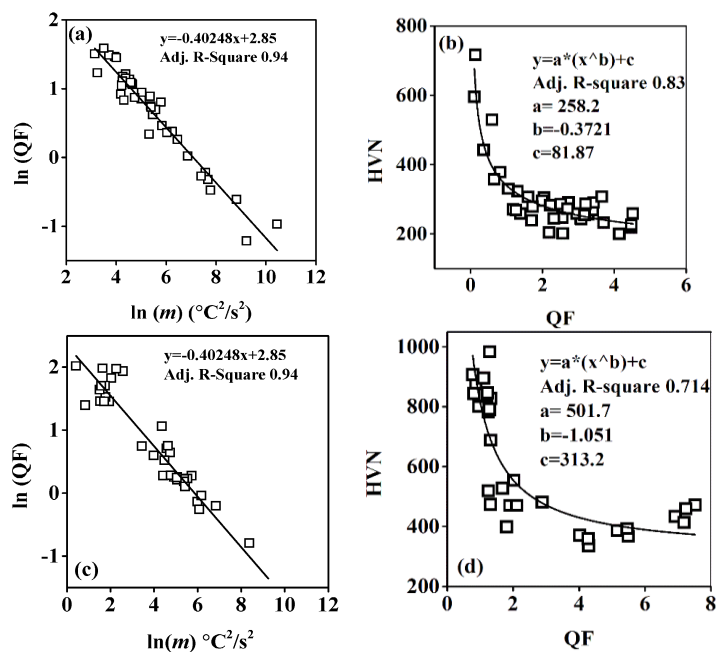


**Figure 5.31: Microstructure obtained in G 10900 steel at the (a) centre and (b) surface of the 25 mm probe and (c) centre and (d) surface of the 50 mm probe during quenching in karanja oil**

G 10450 steel showed microstructure consisting of ferrite and pearlite. The microstructure in G 10900 steel of 25 mm consisted of cementite, martensite and bainite (brown coloured phase). G 10900 steel of 50 mm diameter showed mixed microstructure at their centre consisting of pearlite, bainite, martensite and cementite. Martensite, bainite and cementite microstructures were obtained near the surface of G 10900 steel probe of 50 mm diameter.

### 5.3.4 Quench factor and hardness

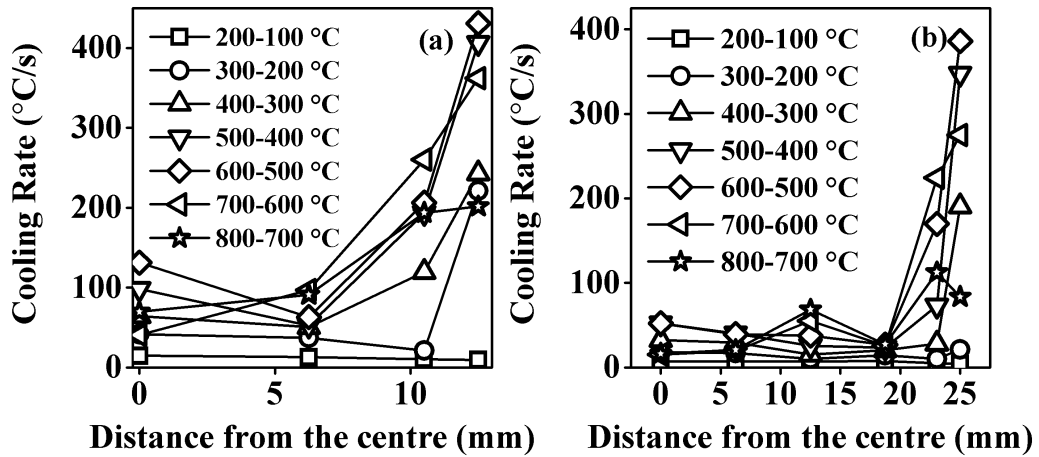
The measured hardness across the cross section of the quenched specimens were correlated with cooling curves using Quench Factor technique and are shown in Figure 5.32. Quench factor is mathematically defined as:  $QF = \Sigma \frac{\Delta t}{Ct}$  and is the ratio of the time taken to reach each temperature on the cooling curve from the start of transformation till the bainitic start temperature to the critical time required for phase transformation to occur. By knowing the average cooling rate, a heat treater may make use of Figure 5.32a to obtain the QF value. From the QF value, the heat treater will be able to estimate the hardness developed in the metal using Figure 5.32b.



**Figure 5.32: (a) Quench factor vs. cooling rate (b) quench factor vs. hardness for the G 10450 steel samples of 25 and 50 mm and (c) quench factor vs. cooling rate (b) quench factor vs. hardness for the G 10900 steel samples of 25 and 50 mm**

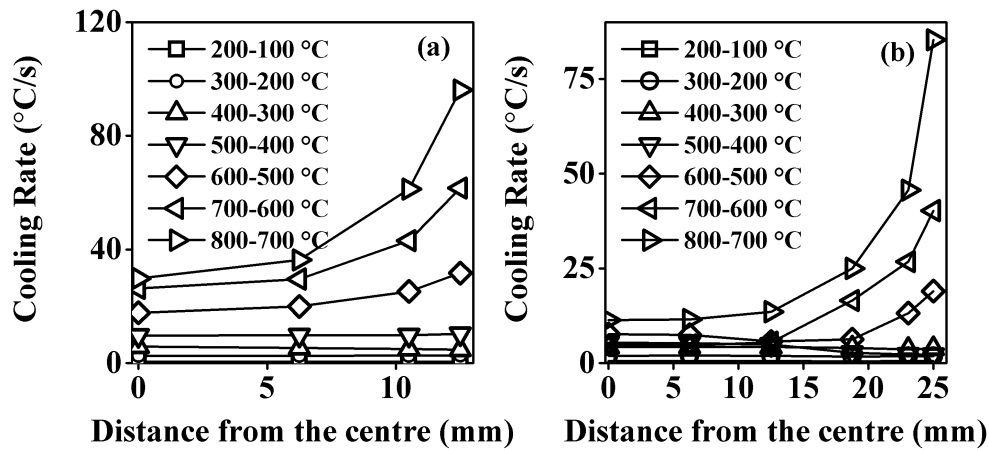
### 5.3.5 Quench uniformity during hardening of steels

Figure 5.33 shows the variation in cooling rate with distance in 25 and 50 mm section diameters specimens of G 10450 steel during quenching in distilled water.



**Figure 5.33: Variation of cooling rate with distance in G 10450 steel grade of (a) 25 mm and (b) 50 mm section diameter during quenching in distilled water.**

During continuous cooling, between temperatures 600 to 500 °C in the 25 mm probe the cooling rates experienced were found to be the highest with 437 °C/s at its surface and 63 °C/s at 6.25 mm from the centre (Figure 5.33a). The second highest was found in the temperature range of 500 to 400 °C with 406 °C/s at the surface and 52 °C/s at 6.25 mm from the centre. Within both these temperature ranges, the cooling rate increased from 6.25 mm to the centre. This was because of the effect of heat released due to phase transformation during the continuous cooling process. Had there been no phase transformation, the cooling rate would have dropped from 6.25 mm to the centre as observed in the case of cooling rate experienced in the temperature range of 700 to 600 °C. The other curves are similar to that observed for 600-500 °C because of continuous transformation of parent austenite into other phases during quenching. The curves obtained with 50 mm section diameter in Figure 5.33b show highest decrease in the cooling rate in the temperature range of 600 to 500 °C upto 18.5 mm from the centre and cools much earlier than other locations in the probe causing transformation of austenite to martensite as shown in the micrograph Figure 4.11d. The cooling rates produced during quenching of the G 10900 steel of diameters 25 and 50 mm in karanja oil quench medium are shown in Figure 5.34.



**Figure 5.34: Variation of cooling rate with distance in G 10900 steel grade of (a) 25 mm and (b) 50 mm section diameter during quenching in karanja oil.**

It shows that quenching in oil quenching media lowers the magnitude of the cooling rate variation producing a more uniform quench relative to that provided with water. The cooling rate vs. distance curves during quenching of G 10450 and 10900 steel probes for other quench media showed similar results as shown in Figure 5.33 and Figure 5.34 respectively.

#### **5.4 Quenching Experiments with 304 SS of Section Diameters of 25 and 50 mm**

The cooling curves obtained during quenching with 25 and 50 mm section sized 304 SS workpieces are shown in Appendix G. They show that the cooling curves obtained at 2 mm below the surface showed existence of a vapor phase stage during quenching. This was due to the presence of a chromium oxide film on the surface of the stainless-steel specimens. The maximum cooling rate parameters obtained during quenching are shown in Table 5.9. It shows that the cooling rate at the centre of the 50 mm section diameter was reduced by over 50 % during quenching compared with the corresponding values observed for the 25 mm section diameter. The decrease in the magnitude obtained in the cooling rate curves for the stainless-steel probes was similar to those observed in the case of steels. However, the temperature at which the maximum cooling rate occurred and the time at which cooling rate attains its maximum were not comparable to those with steels.

**Table 5.9: Maximum cooling rate parameters during quenching of 304 SS of section diameters 25 and 50 mm**

Quenchants	304 Stainless steel					
	25 mm section diameter					
	Centre			Surface		
	CR <sub>max</sub> (°C/s)	T <sub>max</sub> (°C)	t <sub>max</sub> (s)	CR <sub>max</sub> (°C/s)	T <sub>max</sub> (°C)	t <sub>max</sub> (s)
Distilled water	73	681	6.9	202	649	3.1
Karanja oil	39	691	9.6	71	720	4.9
Mineral oil	37	626	14.6	75	667	9.6
Neem oil	39	694	12	69	696	7.8
Sunflower oil	39	700	10.4	62	666	6.4
50 mm section diameter						
Distilled water	31	705	12.1	212	674	2.1
Karanja oil	16	666	25.9	74	682	8.6
Mineral oil	17	682	26	67	643	11.7
Neem oil	17	702	22.7	63	679	8.8
Sunflower oil	15	750	21.1	83	659	9.1

#### 5.4.1 Heat flux transients during quenching of 25 and 50 mm section diameters of 304 stainless steel

The heat flux curves obtained during quenching with stainless steel probes of diameters 25 and 50 mm are shown in Figure 5.35. The heat flux curves initially show a lower value due to the existence of a vapor phase enveloping the probe. The heat flux values after this stage begins to rise and attains a maximum value as the cooling enters the nucleate boiling stage. The heat flux transients thereafter decrease and again attain a low value as the cooling occurs by convection in the liquid medium. Compared with the heat flux curves of steel probes, stainless steel probes show higher values because of the absence of phase transformation during quenching. Furthermore, the heat flux curves for the 50 mm probe has higher peak flux compared with the 25 mm probe. In the case of steel, 25mm probes showed higher peak flux compared to the 50 mm probes during quenching in a quench medium.

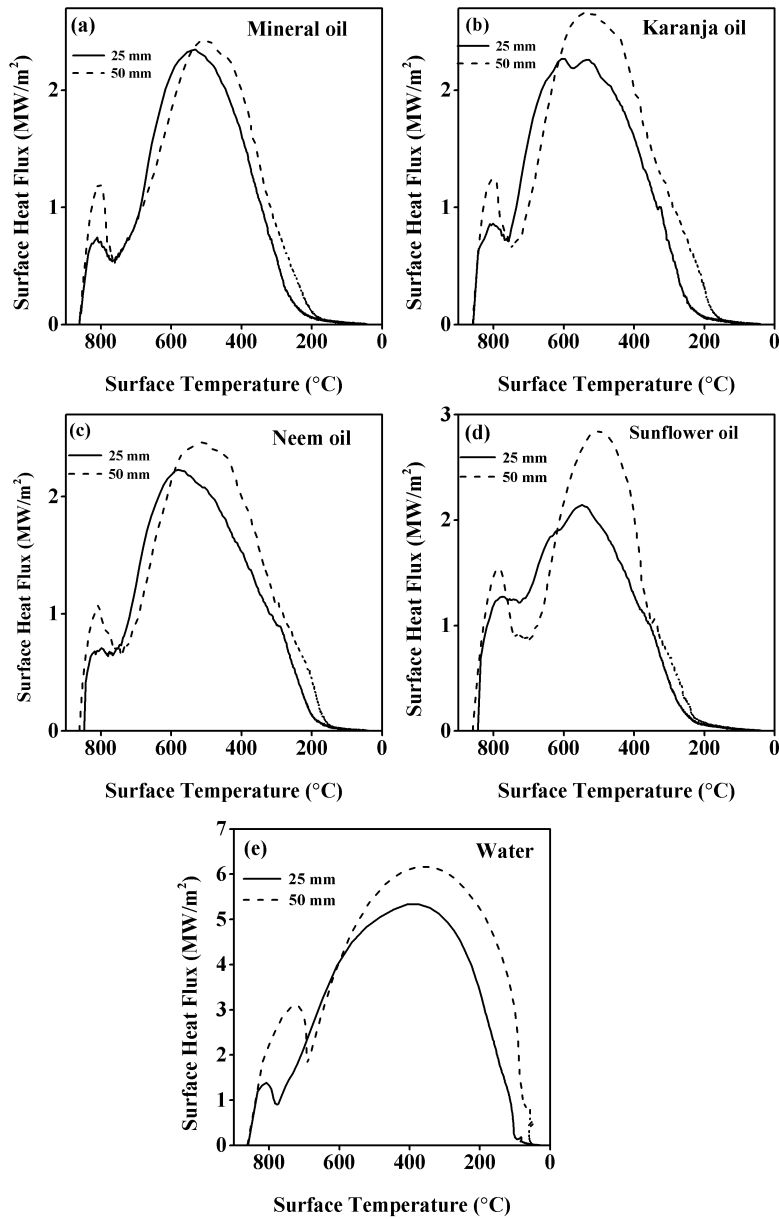


**Figure 5.35: Heat flux curves obtained with SS probes during quenching in (a) mineral (b) karanja (c) neem (d) sunflower and (e) distilled water quench media**

The peak heat flux was 2.35, 2.27, 2.14 and 2.22 MW/m<sup>2</sup> during quenching of 25 mm probe in mineral, karanja, sunflower and neem oils respectively. The corresponding values for the 50 mm probe were 2.43, 2.67, 2.84 and 2.46 MW/m<sup>2</sup> respectively. These results clearly show that heat transfer during quenching with SS probes cannot be used to predict heat transfer from carbon steels as it will lead to incorrect interpretations since SS probes will not undergo phase transformation during quenching.

## Chapter 6 CONCLUSIONS

Based on the results and discussions, the following conclusions were drawn:

1. CuO , MWCNT and graphene based nanofluids were prepared and showed better wetting and spreading ability compared to distilled water.
2. The addition of nanoparticles to distilled water resulted in longer vapour phase stage. The vapour phase stage of quenching was stabilized leading to reduction in the severity of quenching in nanofluids.
3. The thermal conductivity of nanofluids was not significantly affected by the addition of nanoparticles. This is contrary to that reported in the literature.
4. The estimated spatiotemporal heat flux along the inconel probe surface showed reduced heat removal rates with nanofluids compared to water. The maximum reduction in the rate of heat extraction was obtained with 0.1% CuO nanofluid (~57%) The rate of heat removal was comparable with water for quenching with MWCNT based nanofluid at low concentration. Graphene based nanofluids showed intermediate heat extraction rates.
5. The effect of viscosity ( $\mu_l$ ), density ( $\rho_l$ ) and surface tension ( $\sigma_l$ ) of quench media on mean peak heat flux was modelled using a power fit equation given by:

$$\bar{q}_{max} = A \left( \frac{\mu_l}{\rho_l * \sigma_l} \right)^B$$

where A and B are constants.

6. On agitation, the mean peak heat flux obtained with 0.1 vol.% graphene (3.23 MW/m<sup>2</sup>) and 0.0003 vol.% (2.99 MW/m<sup>2</sup>) and 0.003 vol.% MWCNT (2.95 MW/m<sup>2</sup>) nanofluids were higher compared to that of water (2.75 MW/m<sup>2</sup>).
7. Heat extraction rate was lower for CuO nanofluids compared to water even under agitated quench conditions. This was attributed to the agglomeration of the dispersed nanoparticles around the probe and the resistance offered by agglomerated nanoparticles to the contact of fresh liquid during quenching.

8. The mean rewetting temperature was found to be highest for the edible sunflower oil (794.7°C). Mineral oil showed the lowest rewetting temperature (722.7°C). Non-edible karanja and neem vegetable oils showed rewetting temperatures of 794°C and 764.5°C respectively.

9. Shortest rewetting times were obtained with sunflower oil (1.5 s). Rewetting time was maximum with mineral oil (5.8s). Rewetting times of 2.2 s and 3.2 s were obtained with karanja and neem vegetable oils respectively.

10. An analysis of heat flux transients revealed lower heat flow rates for mineral oil during all quenching stages compared to vegetable oils. Heat removal rates for karanja and Sunflower oils were comparable. Lower contact angles were obtained with mineral and sunflower oils (~17°) compared to that for karanja (24°) and neem (21°) oil quench media.

11. Karanja, neem and sunflower oils have better viscosity stability than mineral oil. The flash and fire points of edible sunflower oil and non-edible karanja oil were found to be comparable. Karanja oil is thus superior compared to neem and sunflower oils.

12. The cooling curves obtained with reference probes made from G 10450 and G 10900 steels showed kinks indicating enthalpy change accompanied with phase transformations during continuous cooling. The cooling of reference probes was faster with karanja oil compared to mineral and other vegetable oils.

13. Higher peak heat flux transients were obtained with the 25mm section sized samples compared to the 50 mm samples during quenching with distilled water and oil quenching media.

14. The cooling rates measured at various locations across the cross section of reference probes of both thicknesses were related to the hardness using the Quench Factor technique. The following equations were proposed for the prediction of hardness:

For G 10450 steel:  $\ln(QF) = -0.40248 * \ln(m) + 2.85$   
 $HVN = 258.2 * (QF)^{-0.3721} + 81.87$

For G 10900 steel:  $\ln(QF) = -0.40248 * \ln(m) + 2.85$   
 $HVN = 501.7 * (QF)^{-1.051} + 313.2$



where ' $m$ ' is the product of the slope of the kink in the cooling curve during the evolution of the latent heat and the average cooling rate from the peak of kink to the bainite start temperature given by the TTT curve for the steel.

## REFERENCES

- Çalik, A. (2009). "Effect of cooling rate on hardness and microstructure of AISI 1020, AISI 1040 and AISI 1060 Steels." *Int. J. Phys. Sci.*, 4(9), 514–518.
- Canter, N. (2010). "Cover story, MWF heat treatment: Options for a critical process." *TLT*, 9.
- Chandler, H. (1996). "Heat Treater's Guide: Practices and procedures for nonferrous alloys." *ASM Int.*, 657.
- Choi, S. U. S., and Eastman, J. A. (1995). "Enhancing thermal conductivity of fluids with nanoparticles." *ASME Int. Mech. Eng. Congr. Expo.*, 66(March), 99–105.
- Ciloglu, D., and Bolukbasi, A. (2011). "The quenching behavior of aqueous nanofluids around rods with high temperature." *Nucl. Eng. Des.*, 241(7), 2519–2527.
- Croucher, T. R., and Schuler, M. D. (1970). *Distortion control of aluminum products using synthetic quenchants*. Ft. Belvoir: Defense Technical Information Center.
- Das, S. K., Choi, S. U. S., Yu, W., and Pradeep, T. (2007). *Nanofluids: Science and Technology*. *Nanofluids Sci. Technol.*
- Department of food and public distribution, government of India. "Oil division." <<http://dfpd.nic.in/oil-division.htm>> (Jan. 22, 2018).
- Deval, P. . (2009). "New generation polymer quenchant for heavy forgings." *Conf. Forg. Technol. Purs. Excell. Pune, India, 9-10 Sep.*
- Dexter, G. W. "Hardening high speed steels: Metallurgical benefits of salt."
- Dubal, G. P. (2003). "The basics of molten salt quenchants." *Heat Treat. Prog.*, 3(August), 81–86.
- Fernandes, P., and Prabhu, K. N. (2007). "Effect of section size and agitation on heat transfer during quenching of AISI 1040 steel." *J. Mater. Process. Technol.*, 183(1), 1–5.
- French, H. J., and Hamill, T. E. (1929). "Hot aqueous solutions for the quenching of steels." *Bur. Stand. J. Res. Vol. 3*, R. P. Lamont and G. E. Burgess, eds., Washington:

U.S. Department of commerce, 399–418.

French, H. J., and Klopsch, O. Z. (1925). *Initial temperature and mass effects in quenching*. *Natl. Bur. Stand.*, Washington.

Ghosal, S. (2017). “India still highly dependent on edible oil imports: ICRA.” *Econ. Times*, <<https://economictimes.indiatimes.com/news/economy/agriculture/india-still-highly-dependent-on-edible-oil-imports-icra/articleshow/60360710.cms>> (Jan. 22, 2018).

Grum, J., Božič, S., and Zupančič, M. (2001). “Influence of quenching process parameters on residual stresses in steels.” *Mater. Process. Technology*, 114(1), 57–70.

Ikkene, R., Koudil, Z., and Mouzali, M. (2010). “Measurement of the cooling power of polyethylene glycol aqueous solutions used as quenching media.” *ASTM Spec. Tech. Publ.*, 1523 STP(December), 977–990.

Government of India, (2016-2017). *Annual report, Department of agriculture, cooperation and farmers welfare*, Ministry of Agriculture and Farmer Welfare, pages 194.

Karikalan, L., and Chandrasekaran, M. (2015). “Karanja oil biodiesel: A potential substitution for diesel fuel in diesel engine without alteration.” *ARPJ. Eng. Appl. Sci.*, 10(1), 152–163.

Khedkar, R. S., Sonawane, S. S., and Wasewar, K. L. (2012). “Influence of CuO nanoparticles in enhancing the thermal conductivity of water and monoethylene glycol based nanofluids.” *Int. Commun. Heat Mass Transf.*, 39(5), 665–669.

Kim, H., DeWitt, G., McKrell, T., Buongiorno, J., and Hu, L. wen. (2009). “On the quenching of steel and zircaloy spheres in water-based nanofluids with alumina, silica and diamond nanoparticles.” *Int. J. Multiph. Flow*, 35(5), 427–438.

Kobasko, N. I. (1968). “Thermal processes during quenching of steel.” *Met. Term Obrab Met*, 3(2).

Kobasko, N., Moskalenko, A., Lohvynenko, P., Karsim, L., and Riabov, S. (2016). “An effect of PIB additives to mineral oil resulting in elimination of film boiling during steel

parts quenching.” *EUREKA Phys. Eng.*, (3), 17–24.

Kopeliovich, D. “Salt bath heat treatment.”  
<[http://www.substech.com/dokuwiki/doku.php?id=salt\\_bath\\_heat\\_treatment&s=salt\\_bath\\_treatment](http://www.substech.com/dokuwiki/doku.php?id=salt_bath_heat_treatment&s=salt_bath_treatment)> (Oct. 17, 2017).

Kumar, T. S. (2004). “A serial solution for the 2-d inverse heat conduction problem for estimating multiple heat flux components.” *Numer. Heat Transf. Part B Fundam.*, 45(6), 541–563.

Liscic, B., Tensi, H. M., Canale, L. C. F., and Totten, G. E. (2010). *Quenching Theory and Technology, Second Edition*. CRC Press., (B. Liscic, H. M. Tensi, L. C. F. Canale, and G. E. Totten, eds.), Boca Raton, Florida, USA: Taylor & Francis Group.

Luty, W. (2010). “Cooling Media and Their Properties.” *Quenching Theory Technol. Second Ed.*, CRC Press., (B. Liscic, H. M. Tensi, L. C. F. Canale, and G. E. Totten, eds.), Boca Raton, Florida, USA: Taylor & Francis Group.

Ma, S. (2002). “Characterization of the performance of mineral oil based quenchants using the CHTE quench probe system.” Worcester polytechnic Institute, Columbus, Ohio.

MacKenzie, D. S. (2003). “Advances in quenching.” *Proc. 22nd Heat Treat. Soc. Conf. 2nd Int. Surf. Eng. Congr.*, 228–239.

MacKenzie, D. S. (2006). “The history of quenching.” *Adv. Mater. Process.*, 164(9), 39.

MacKenzie, D. S., and Lazerev, I. “Care and maintenance of quench oils.”  
<[https://www.houghtonintl.com/sites/default/files/resources/article\\_-\\_care\\_and\\_maintenance\\_of\\_quench\\_oils.pdf](https://www.houghtonintl.com/sites/default/files/resources/article_-_care_and_maintenance_of_quench_oils.pdf)> (Oct. 11, 2017).

Mocikat, H., and Herwig, H. (2009). “Heat transfer measurements with surface mounted foil-sensors in an active mode: a comprehensive review and a new design.” *Sensors*, 9(4), 3011–3032.

Monroe, R. W., and Bates, C. E. (1983). “Evaluating quenchants and facilities for hardening steel.” *J. Heat Treat.*, 3(2), 83–99.

- Murshed, S. M. S., Leong, K. C., and Yang, C. (2008). "Thermophysical and electrokinetic properties of nanofluids - A critical review." *Appl. Therm. Eng.*, 28(17–18), 2109–2125.
- Nayak, U. V., Rao, K. M. P., Pai, M. A., and Prabhu, K. N. (2016). "Carbonated aqueous media for quench heat treatment of steels." *J. Mater. Eng. Perform.*, 25(9), 3802–3810.
- Pedišić, L., Matijević, B., and Perić, B. (2005). "Influence of quenching oils composition on the cooling rate." *1st Int. Conf. Heat Treat. Surf. Eng. Tools Dies, IFHTSE 2005*, June 8-11, Pula, Croatia, 97–105.
- Penha, R. N., Canale, L. C. F., Totten, G. E., Sarmiento, G. S., and Ventura, J. M. (2010). "Simulation of heat transfer and residual stresses from cooling curves obtained in quenching studies." 3(5), 1–14.
- Perla, S., Kulkarni, S., Balachandran, G., and Balasubramanian, V. (2017). "Influence of section size and grain size on the microstructure evolution and mechanical properties in steel grade AISI 5160." *Trans. Indian Inst. Met.*, 70(9), 2449–2458.
- Philip, J., and Shima, P. D. (2012). "Thermal properties of nanofluids." *Adv. Colloid Interface Sci.*, 183–184, 30–45.
- Prabhu, K. N., and Fernandes, P. (2007). "Determination of wetting behavior, spread activation energy, and quench severity of bioquenchant." *Metall. Mater. Trans. B Process Metall. Mater. Process. Sci.*, 38(4), 631–640.
- Prabhu, K. N., and Prasad, A. (2003). "Metal/quenchant interfacial heat flux transients during quenching in conventional quench media and vegetable oils." *J. Mater. Eng. Perform.*, 12(1), 48–55.
- Pranesh Rao, K. M., and Narayan Prabhu, K. (2017). "Effect of bath temperature on cooling performance of molten eutectic NaNO<sub>3</sub>-KNO<sub>3</sub> quench medium for martempering of steels." *Metall. Mater. Trans. A*, 48(10), 4895–4904.
- Ramesh, G., and Narayan Prabhu, K. (2013). "Wetting kinematics and spreading behaviour of water based aluminium nanofluids during immersion quenching." *Int.*

*Heat Treat. Surf. Eng.*, 7(2), 74–78.

Ramesh, G., and Narayan Prabhu, K. (2014). “Spatial dependence of heat flux transients and wetting behavior during immersion quenching of inconel 600 probe in brine and polymer media.” *Metall. Mater. Trans. B*, 45(4), 1355–1369.

Ramesh, G., and Narayan Prabhu, K. (2016). “Effect of polymer concentration on wetting and cooling performance during immersion quenching.” *Metall. Mater. Trans. B Process Metall. Mater. Process. Sci.*, 47(2), 859–881.

Ramesh, G., and Prabhu, K. N. (2014a). “Wetting and cooling performance of mineral oils for quench heat treatment of steels.” *ISIJ Int.*, 54(6), 1426–1435.

Ramesh, G., and Prabhu, K. N. (2014b). “Wetting kinetics, kinematics and heat transfer characteristics of pongamia pinnata vegetable oil for industrial heat treatment.” *Appl. Therm. Eng.*, 65(1–2), 433–466.

Ramesh, G., and Prabhu, K. N. (2015). “Comparative study of wetting and cooling performance of polymer-salt hybrid quench medium with conventional quench media.” *Exp. Heat Transf.*, 28(5), 464–492.

Ramesh, G., and Prabhu, N. (2012). “Development of clay based nanofluids for quenching.” *Proc. from 6th Int. Quenching Control distortion Conf. Incl. 4th Int. distortion Eng. Conf.*, D. S. MacKenzie, ed., Radisson Blu Aqua Hotel, Chicago, IL, USA: ASM International, 308–318.

Ramesh, G., and Prabhu, N. K. (2011). “Review of thermo-physical properties, wetting and heat transfer characteristics of nanofluids and their applicability in industrial quench heat treatment.” *Nanoscale Res. Lett.*, 6(1), 334.

Rao, K. P. (1991). *Neem (Azadirachta Indica)*.

Rose, A. (1940). “Das abkühlungsvermögen von stahl-abschreckmitteln.” *Arch. für das Eisenhüttenwes.*, 13(8), 345–354.

Said, D., Belinato, G., Sarmiento, G. S., Otero, R. L. S., Totten, G. E., Gastón, A., and Canale, L. C. F. (2013). “Comparison of oxidation stability and quenchant cooling curve performance of soybean oil and palm oil.” *J. Mater. Eng. Perform.*, 22(7), 1929–

1936.

Sarmiento, G. S., Bronzini, C., Canale, A. C., Canale, L. C. F., and Totten, G. E. (2010). "Water and polymer quenching of aluminum alloys: A review of the effect of surface condition, water temperature, and polymer quenchant concentration on the yield strength of 7075-T6 aluminum plate." *ASTM Spec. Tech. Publ.*, 1523 STP(1), 728–753.

Shinde, R. (2013). "Influence of petroleum and biodegradable quenchants on properties of medium carbon steels." 2(11), 2052–2056.

Simencio Otero, R. L., Canale, L. C. F., Totten, G. E., Rhee, I.-S., and Dean, S. W. (2012). "Use of vegetable oils and animal oils as steel quenchants: A historical review—1850-2010." *J. ASTM Int.*, 9(1), 103534.

Souza, E. C., Canale, L. C. F., Sarmiento, G. S., Agaliotis, E., Carrara, J. C., Schicchi, D. S., and Totten, G. E. (2013a). "Heat transfer properties of a series of oxidized and unoxidized vegetable oils in comparison with petroleum oil-based quenchants." *J. Mater. Eng. Perform.*, 22(7), 1871–1878.

Souza, E. C. de, Fernandes, M. R., Augustinho, S. C. M., Campos Franceschini Canale, L. de, and Totten, G. E. (2009). "Comparison of structure and quenching performance of vegetable oils." *J. ASTM Int.*, 6(9), 1–25.

Souza, E. C. De, Friedel, L. F. O., Totten, G. E., and Canale, L. C. F. (2013b). "Quenching and heat transfer properties of aged and unaged vegetable oils." *J. Pet. Sci. Res.*, 2(1), 41–47.

Srinivasan, S., and Ranganathan, S. "Wootz steel: An advanced material of the ancient world." <<http://materials.iisc.ernet.in/~wootz/heritage/WOOTZ.htm>> (Oct. 6, 2017).

Sureshkumar, R., Mohideen, S. T., and Nethaji, N. (2013). "Heat transfer characteristics of nanofluids in heat pipes: A review." *Renew. Sustain. Energy Rev.*

Tensi, H. M., and Lainer, K. "Effect of concave and convex surfaces on the heat transfer and stress development during quenching in synthetic high-performance quenching oils." *Proc. 19th Conf. Heat Treat. Incl. steel heat Treat. new millenium. An Int. Symp. Honor Profr. Georg. Krauss, J. S. Midea and D. G. Pfaffmann, eds., Cincinnati, Ohio,*

USA: ASM heat treating society, 446–451.

Tensi, H. M., and Schwalm, M. (1980). “Wirkung von abschreckfl üssigkeiten unter berücksichtigung specieller wäßriger polyäthylenoxide.” *HTM*, 35, 122–129.

Totten, G. E., Bates, C. E., and Clinton, N. A. (1993). *Handbook of Quenchants and Quenching Technology*. ASM International.

Totten, G. E., Sun, Y. H., Kobasko, N. I., Liscic, B., and Han, S. W. (1998). “Advances in polymer quenching technology.” *Int. Automot. Heat Treat. Conf.*, 1(X), 37–44.

Totten, G. E., Tensi, H. M., and Lainer, K. (1999). “Performance of vegetable oils as a cooling medium in comparison to a standard mineral oil.” *J. Mater. Eng. Perform.*, 8(4), 409–416.

Totten, G. E., Webster, G. M., Bates, C. E., Han, S. W., and Kang, S. H. “Limitations of the use of grossman quench severity factors.” *Heat Treating, Incl. 1997 Int. Induction Heat Treat. Symp. Proc. 17th Heat Treat. Soc. Conf. Expo. 1st Int. Induction Heat Treat. Symp.*, D. L. Milam, ed., Indianapolis, Indiana, USA: ASM International, Heat Treating Society, 1998, 12.

Troell, E., and Kristoffersen, H. (2010). “Influence of ageing and contamination of polymer quenchants on cooling characteristics.” *BHM Berg- und Hüttenmännische Monatshefte*, 155(3), 114–118.

Verhoeven, J. D. (2007). “Steel metallurgy for the non-metallurgist.” *ASM Int.*, 203.

Vivek, and Gupta, A. K. (2004). “Biodiesel production from karanja oil.” *J. Sci. Ind. Res. (India)*., 63(1), 39–47.

Wei, X., and Wang, L. (2010). “Synthesis and thermal conductivity of microfluidic copper nanofluids.” *Particuology*, 8(3), 262–271.

Yu, H., Nicol, J. A., Ramser, R. A., and Hunter, D. E. (1997). “Method of heat treating metal with liquid coolant containing dissolved gas.” Google Patents.

Župan, J., Filetin, T., and Landek, D. (2011). “Cooling characteristics of the water based nanofluids in quenching.” *Proceeding Int. Conf. MATRIB 2011*, 1–10.



**APPENDIX A: COOLING CURVES MEASURED IN THE INCONEL PROBE DURING QUENCHING IN VARIOUS QUENCH MEDIA**

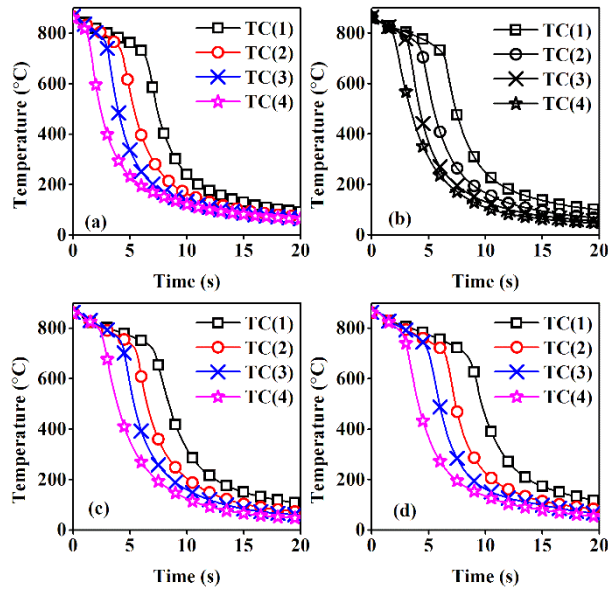


**Figure A.1: Cooling curves measured at 2 mm below the surface of the inconel probe during quenching in 2 lts. of (a) distilled water and (b) 0.01 (c) 0.1 and (d) 0.3 vol.% graphene nanofluids**

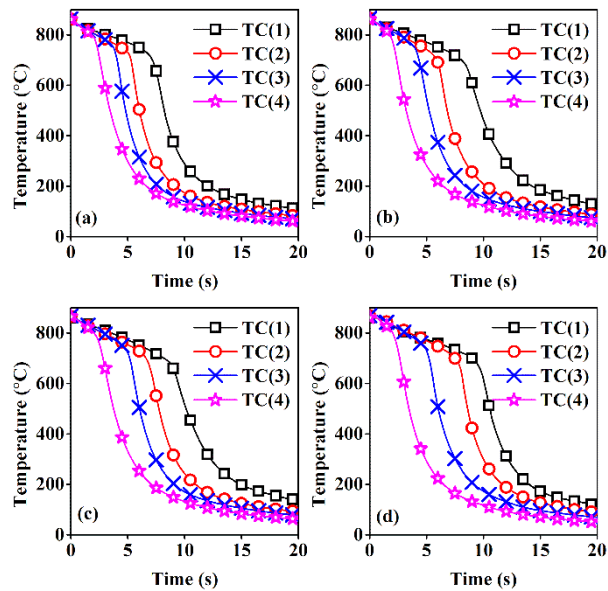


**Figure A.2: Cooling curves measured at 2 mm below the surface of the inconel probe during quenching in 2 lts. of (a) 0.01 (b) 0.05 (c) 0.1 and (d) 1.0 vol.% CuO nanofluids**

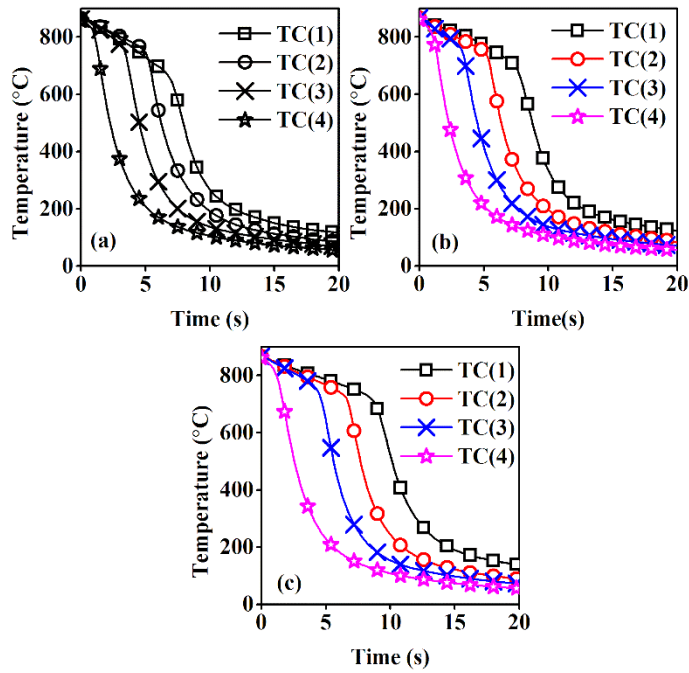


**Figure A.3: Cooling curves measured at 2 mm below the surface of the inconel probe during quenching in 2 lts. of (a) 0.0003 (b) 0.003 and (c) 0.03 vol.% MWCNT nanofluids**

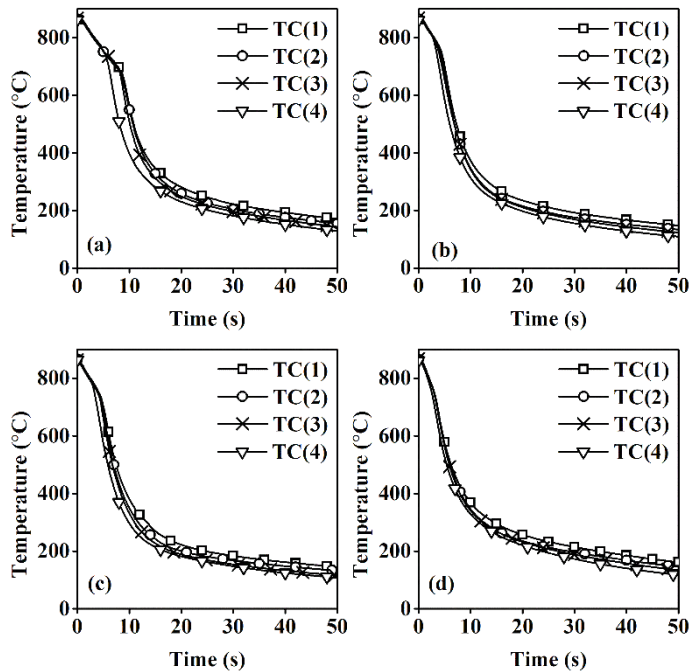


**Figure A.4: Cooling curves measured at 2 mm below the surface of the inconel probe during quenching in 2 lts. of (a) mineral (b) karanja (c) neem and (d) sunflower oil quenching media**

## APPENDIX B: VIDEO IMAGES OF QUENCHING PROCESS

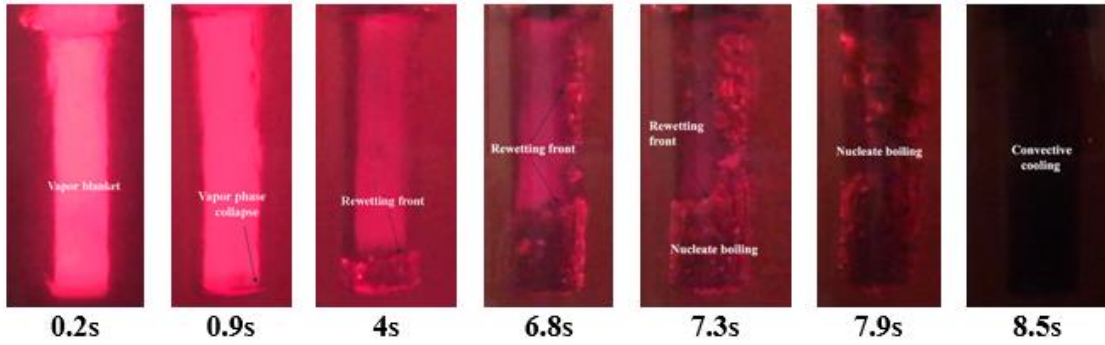


Figure B.1: Video images of quenching of inconel probe in mineral oil

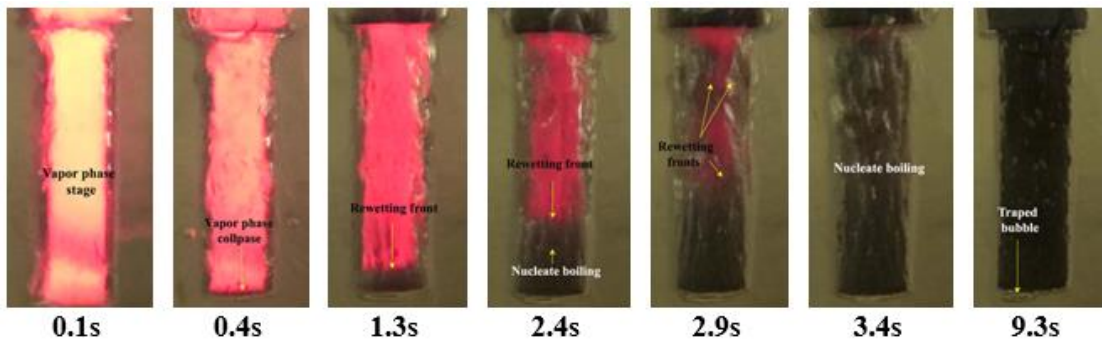
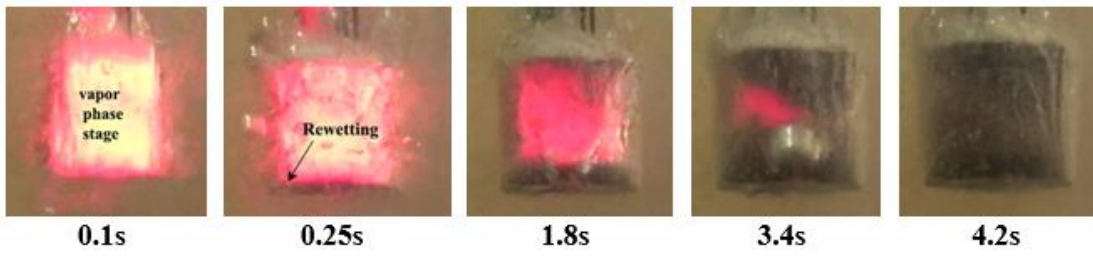


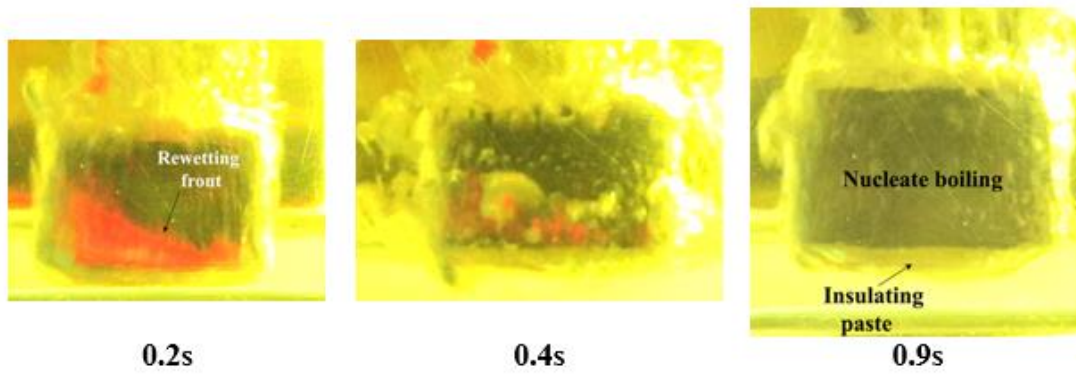
Figure B.2: Video images of quenching of inconel probe in sunflower oil



Figure B.3: Video image taken during quenching of steel probes of (a) 50 and (b) 25 mm in distilled water



**Figure B.4: Video images of 25 mm steel probe quenched in sunflower oil**



**Figure B.5: Video images of 50 mm steel probe quenched in sunflower oil**

**APPENDIX C: CONTACT ANGLE IMAGES OF QUENCH MEDIA**

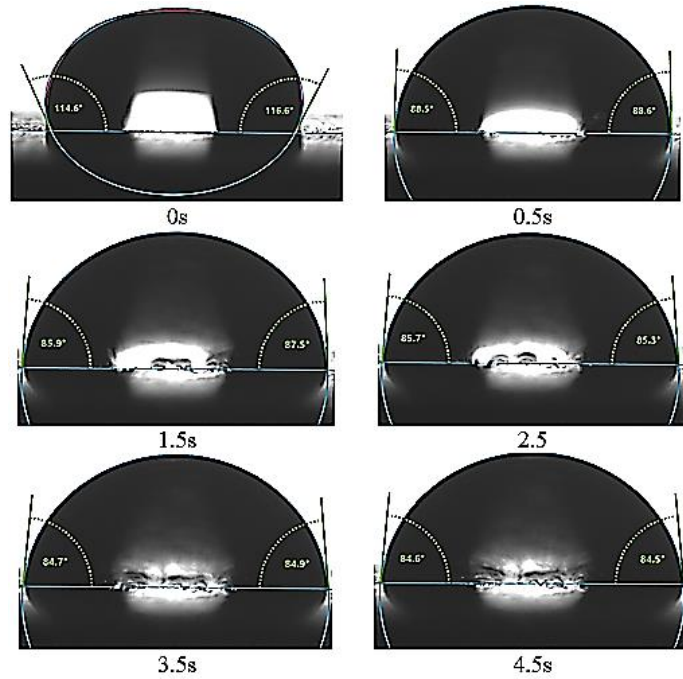


**Figure C.1: Images of contact angle relaxation of water droplet during spreading on an inconel substrate**

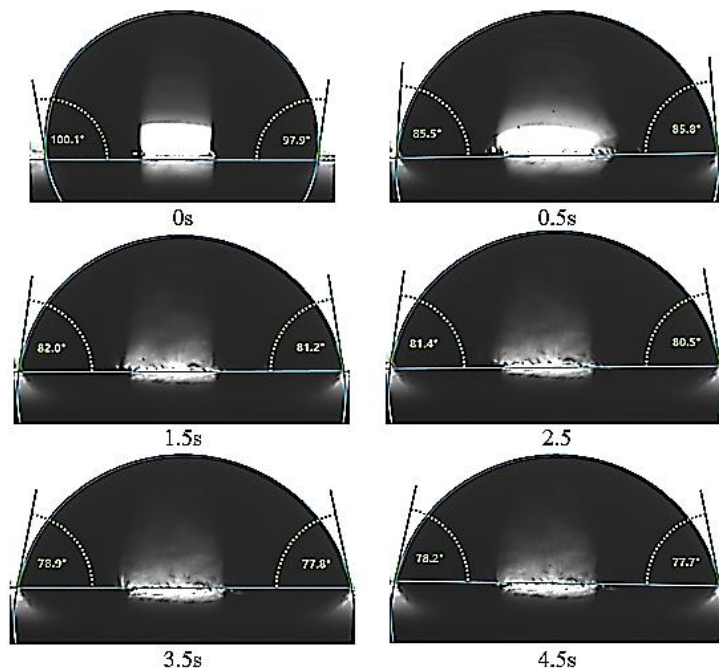


**Figure C.2: Images of contact angle relaxation of 0.01 vol.% CuO nanofluid droplet during spreading on an inconel substrate**

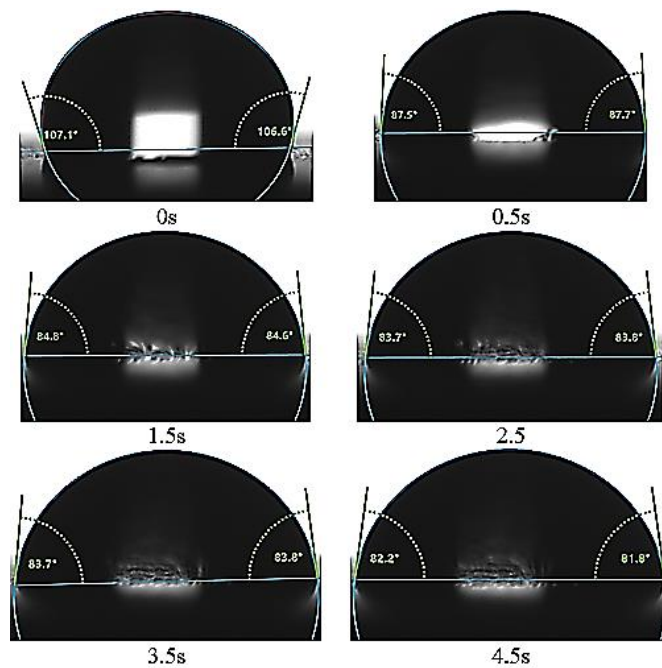


**Figure C.3: Images of contact angle relaxation of 0.05 vol.% CuO nanofluid droplet during spreading on an inconel substrate**

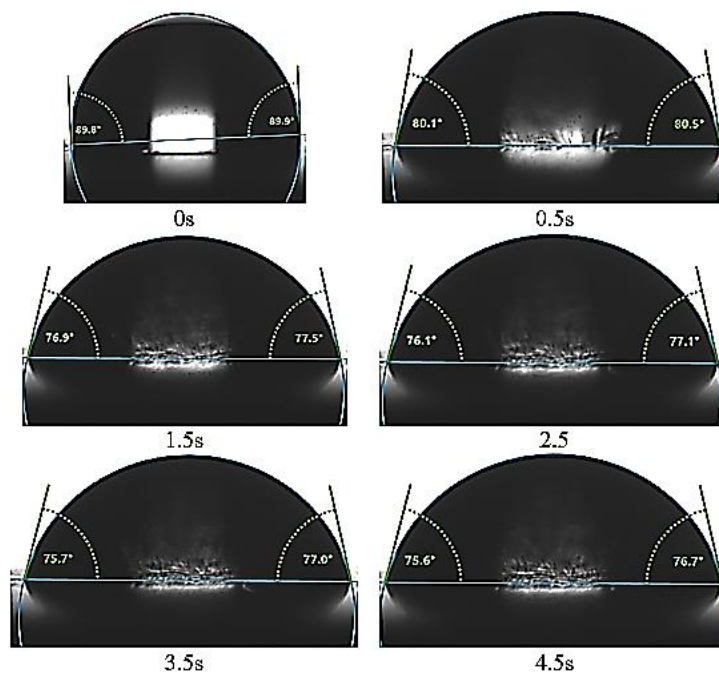


**Figure C.4: Images of contact angle relaxation of 0.1 vol.% CuO nanofluid droplet during spreading on an inconel substrate**



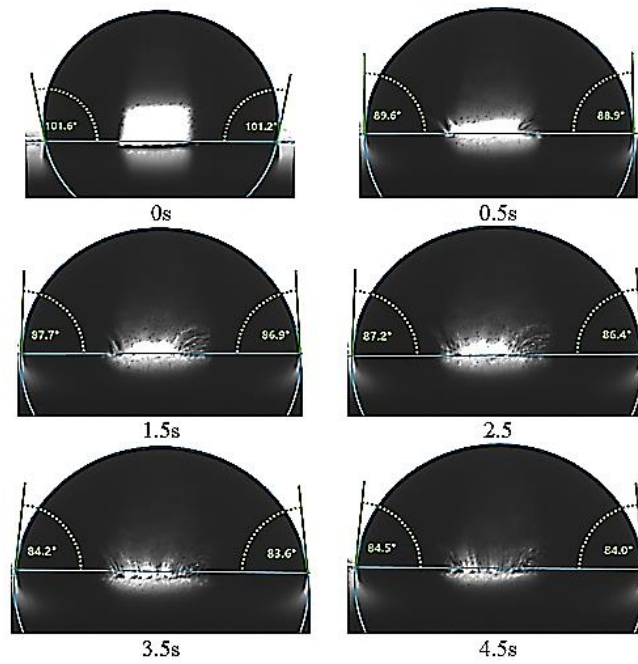


**Figure C.5: Images of contact angle relaxation of 1.0 vol.% CuO nanofluid droplet during spreading on an inconel substrate**

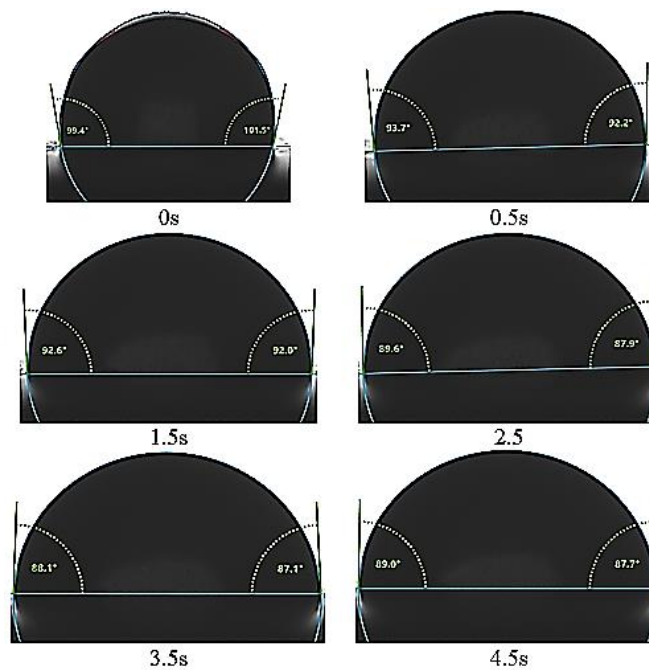


**Figure C.6: Images of contact angle relaxation of 0.1 vol.% graphene nanofluid droplet during spreading on an inconel substrate**

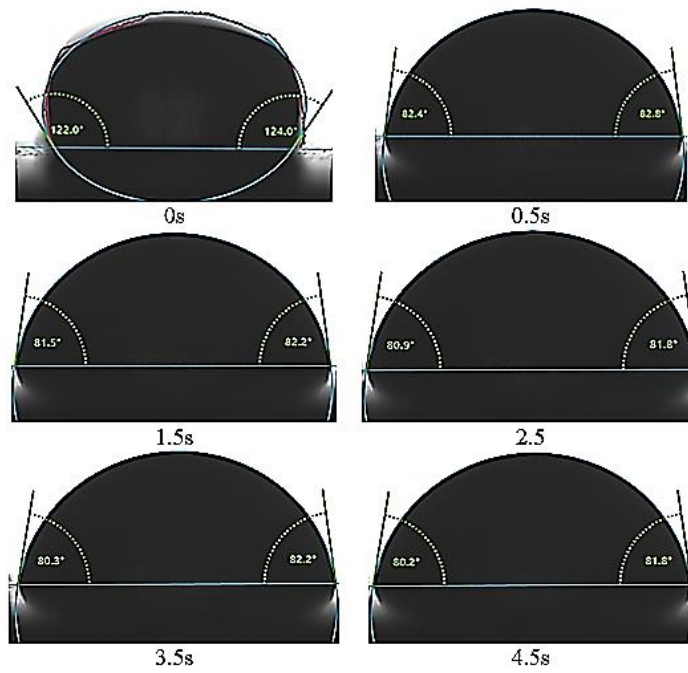


**Figure C.7: Images of contact angle relaxation of 0.3 vol.% graphene nanofluid droplet during spreading on an inconel substrate**

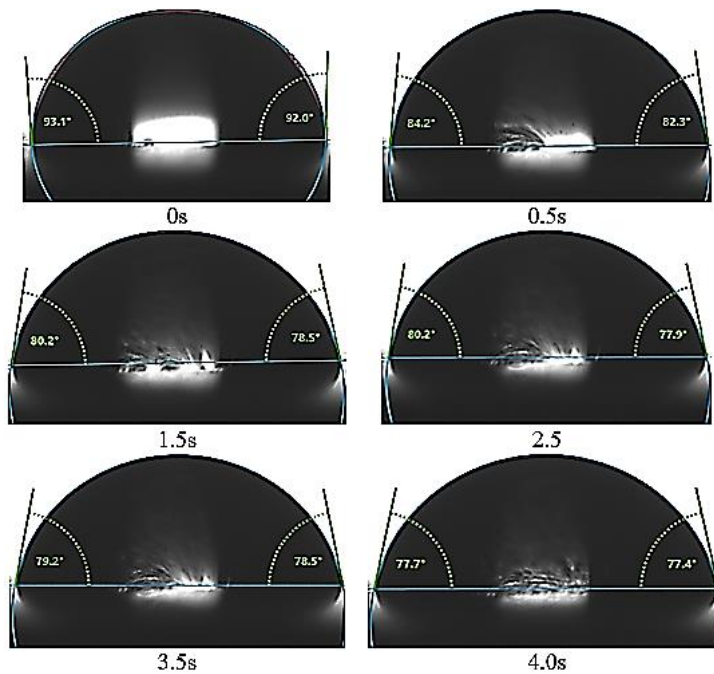


**Figure C.8: Images of contact angle relaxation of 0.0003 vol.% MWCNT nanofluid droplet during spreading on an inconel substrate**



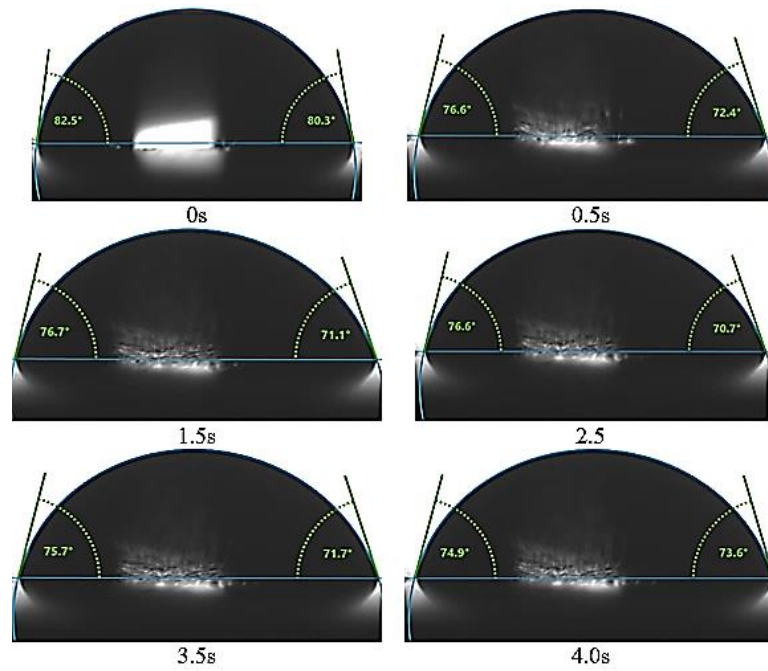


**Figure C.9: Images of contact angle relaxation of 0.003 vol.% MWCNT nanofluid droplet during spreading on an inconel substrate**

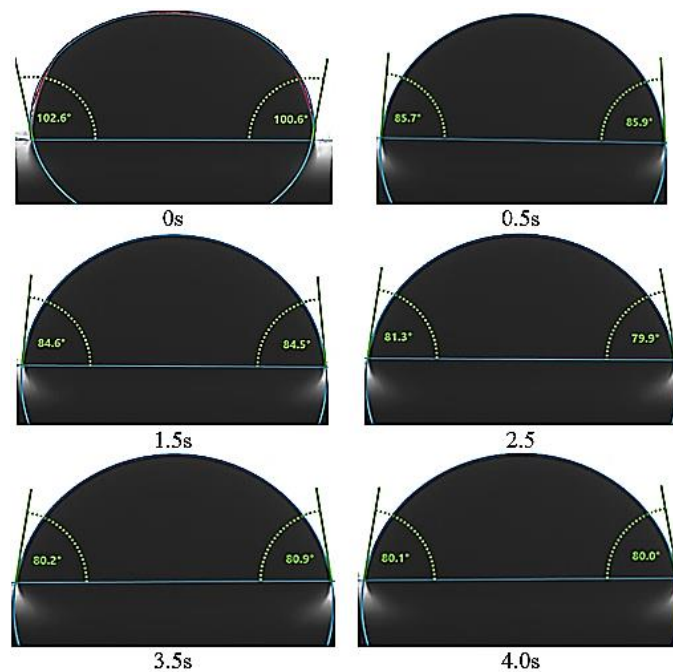


**Figure C.10: Images of contact angle relaxation of 0.03 vol.% MWCNT nanofluid droplet during spreading on an inconel substrate**

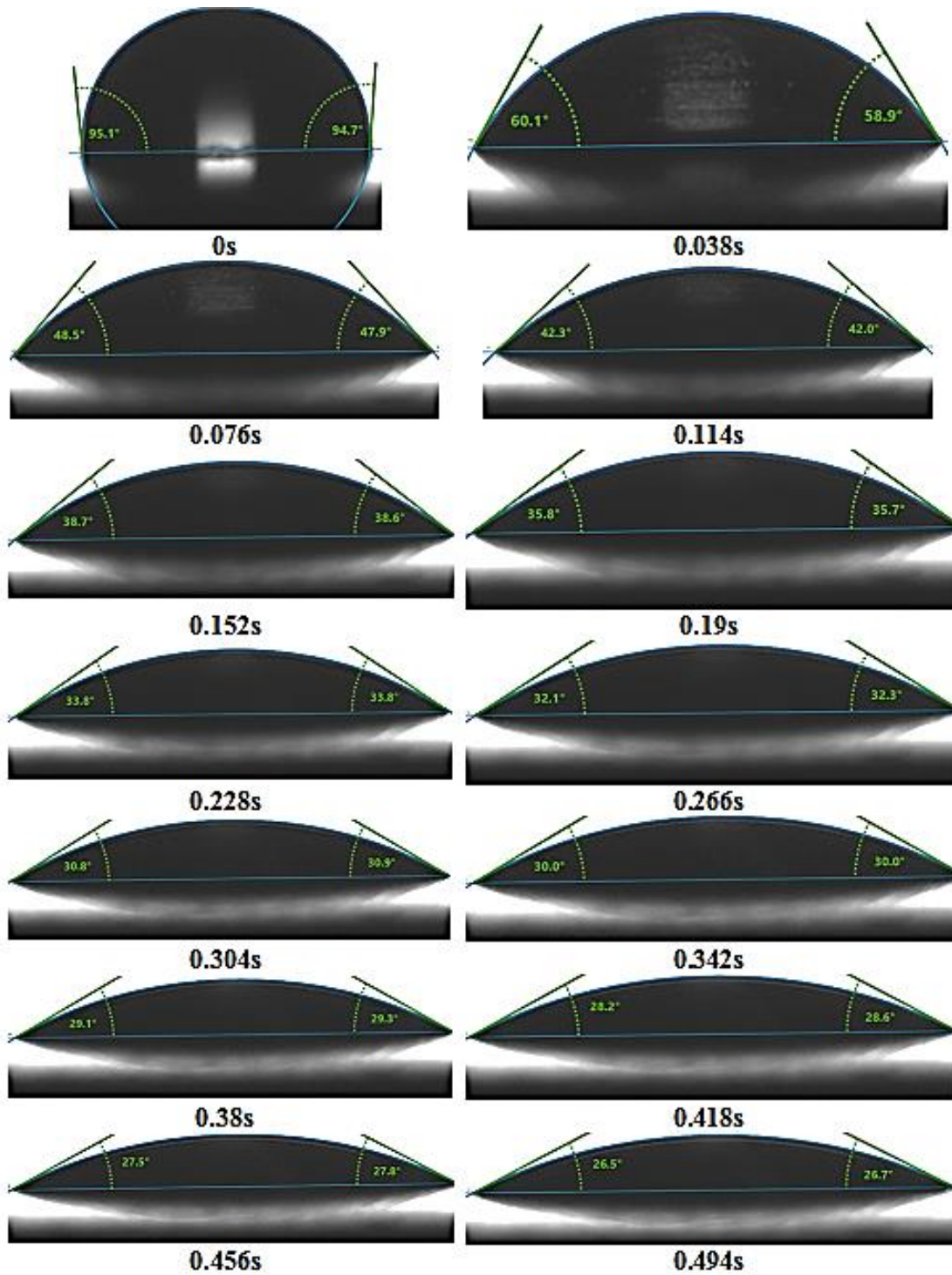


**Figure C.11: Images of contact angle relaxation of mineral oil droplet during spreading on an inconel substrate**

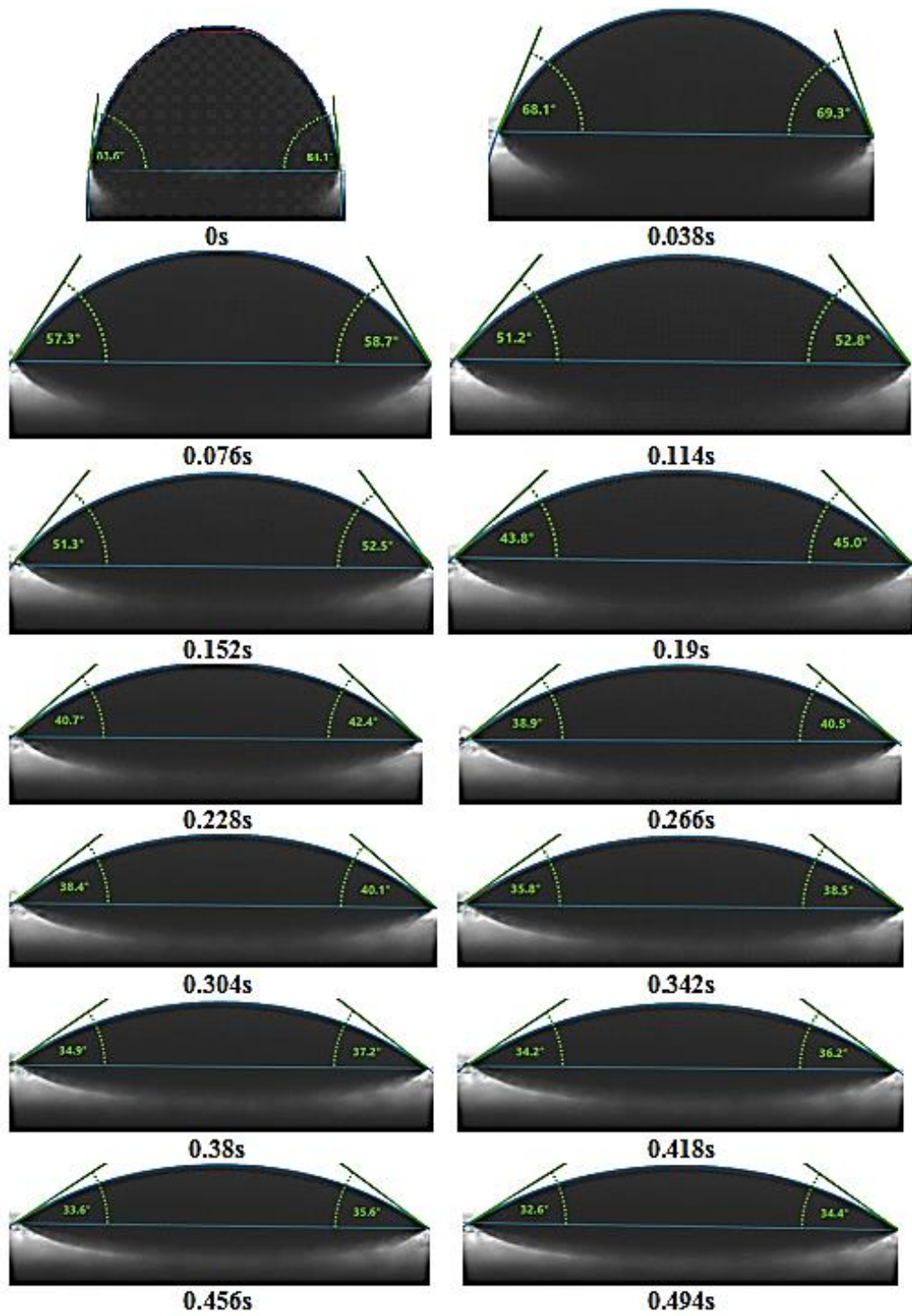


**Figure C.12: Images of contact angle relaxation of karanja oil droplet during spreading on an inconel substrate**

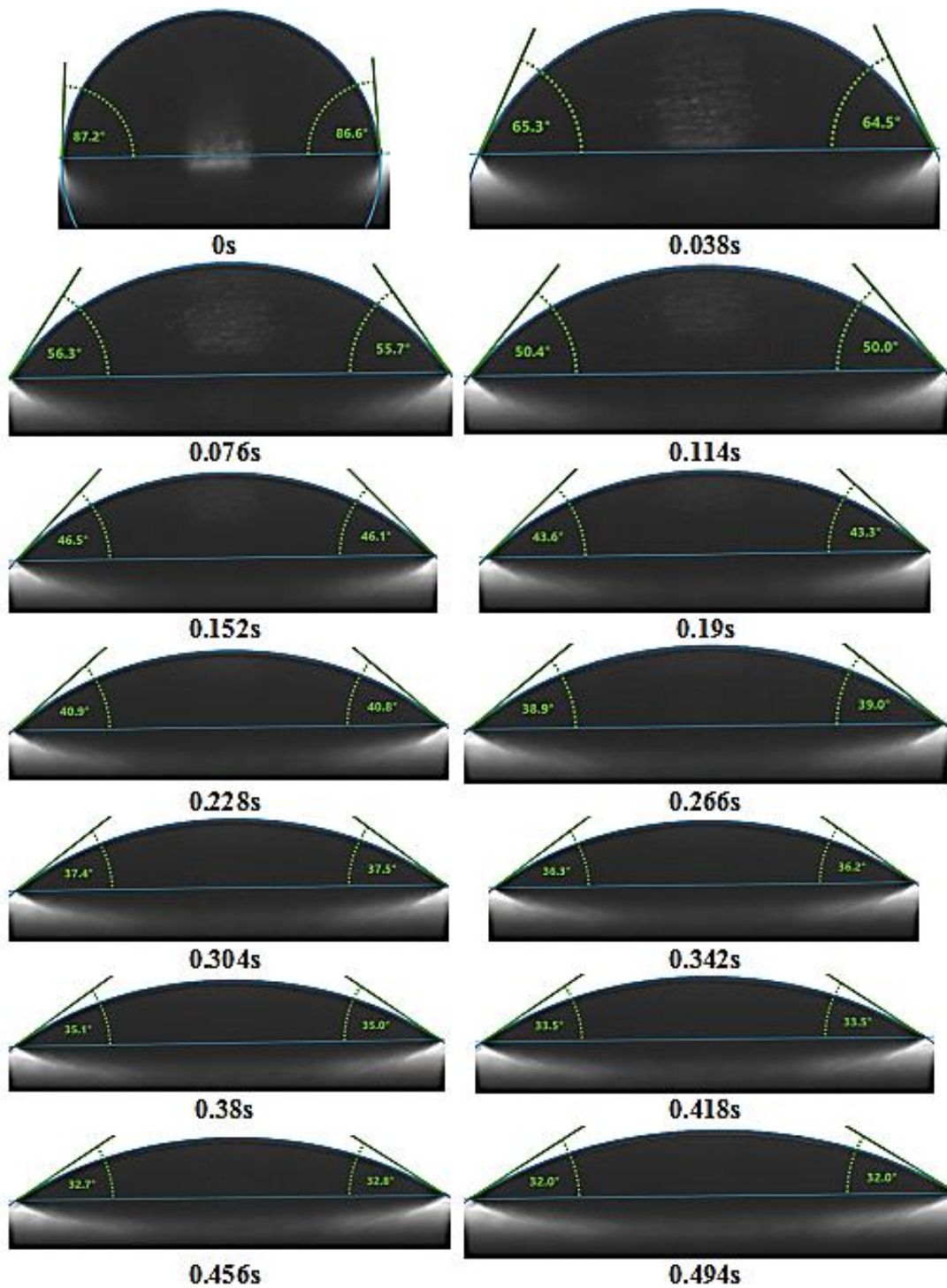


**Figure C.13: Images of contact angle relaxation of neem oil droplet during spreading on an inconel substrate**



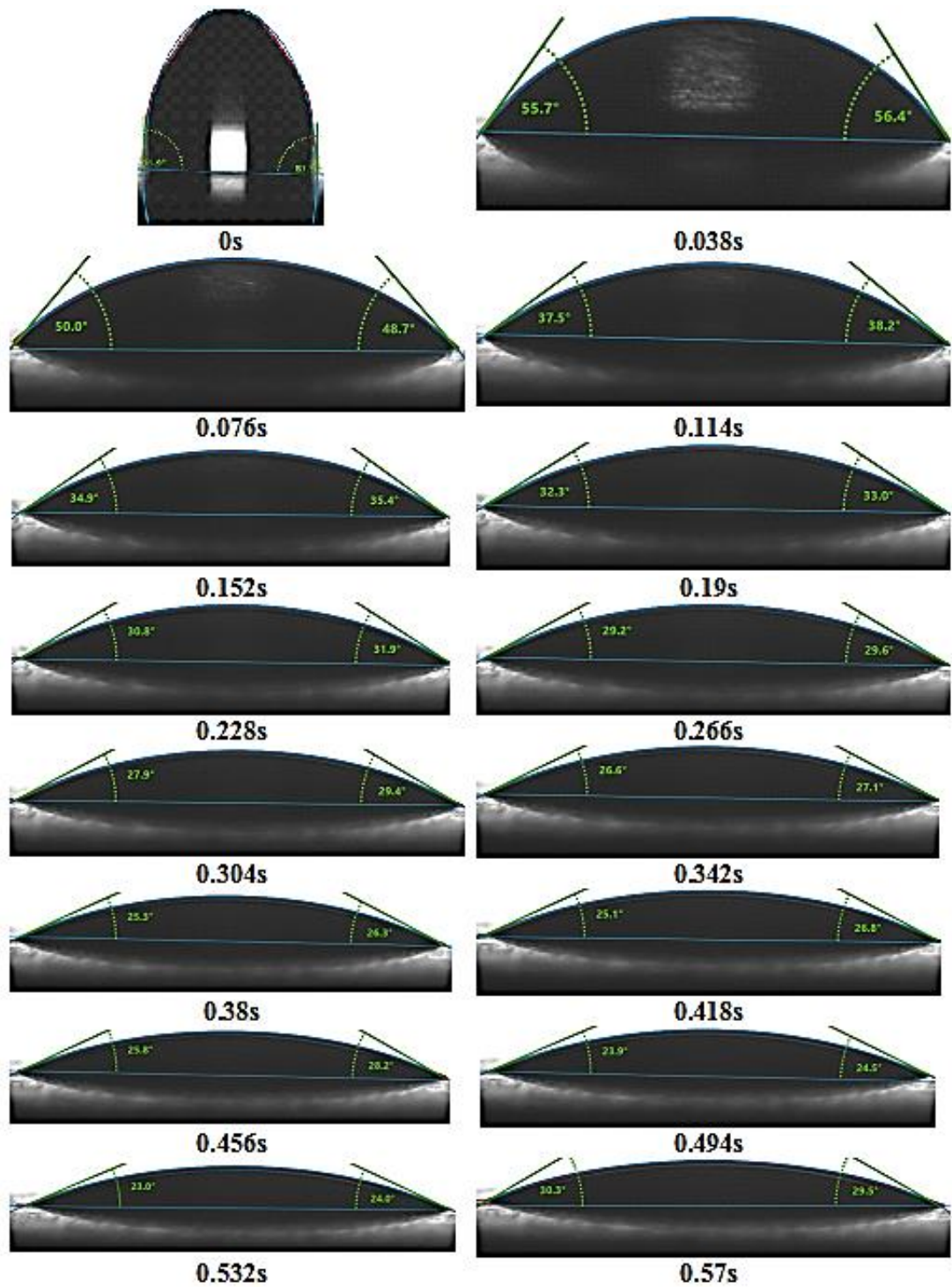


**Figure C.14: Images of contact angle relaxation of sunflower oil droplet during spreading on an inconel substrate**

**APPENDIX D: COOLING CURVES MEASURED IN THE INCONEL PROBE DURING QUENCHING IN VARIOUS QUENCH MEDIA IN THE TENSI AGITATION SYSTEM**

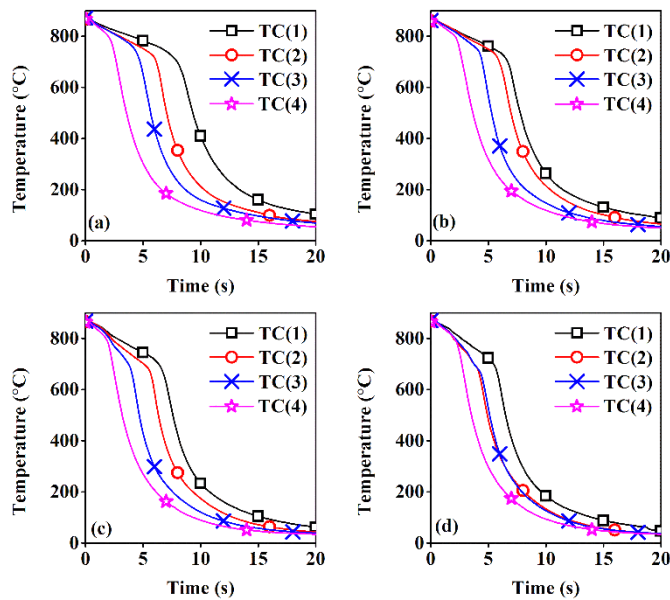


**Figure D.1: Measured cooling curves in the inconel probe during quenching in distilled water under agitation rates of (a) still (b) 500 (c) 1000 and (d) 1500 rpm**

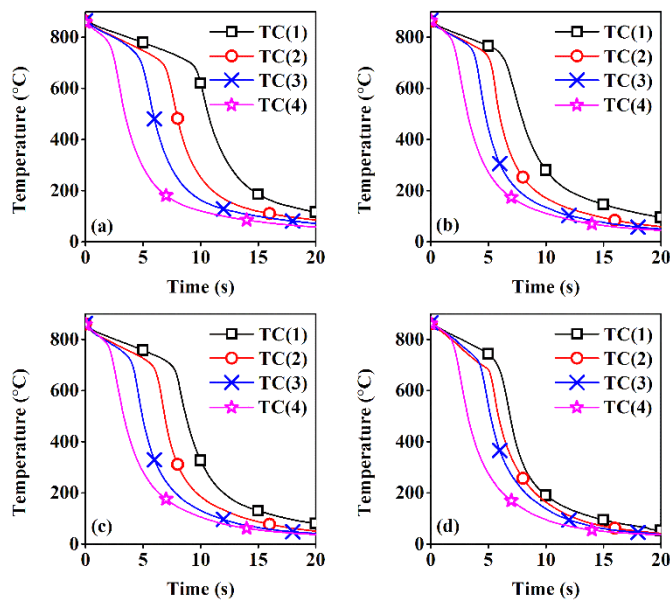


**Figure D.2: Measured cooling curves in the inconel probe during quenching in 0.01 vol.% CuO nanofluid under agitation rates of (a) still (b) 500 (c) 1000 and (d) 1500 rpm**

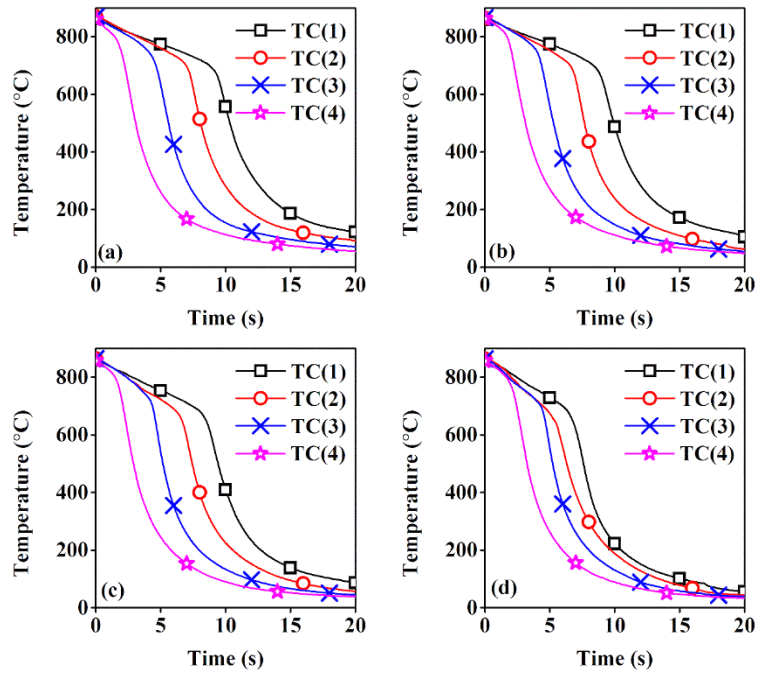


**Figure D.3: Measured cooling curves in the inconel probe during quenching in 0.05 vol.% CuO nanofluid under agitation rates of (a) still (b) 500 (c) 1000 and (d) 1500 rpm**

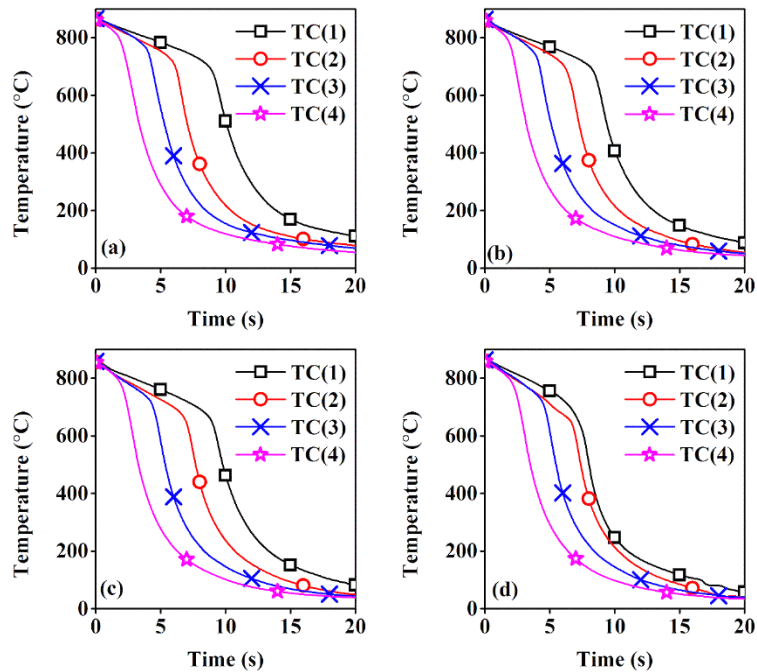


**Figure D.4: Measured cooling curves in the inconel probe during quenching in 0.1 vol.% CuO nanofluid under agitation rates of (a) still (b) 500 (c) 1000 and (d) 1500 rpm**

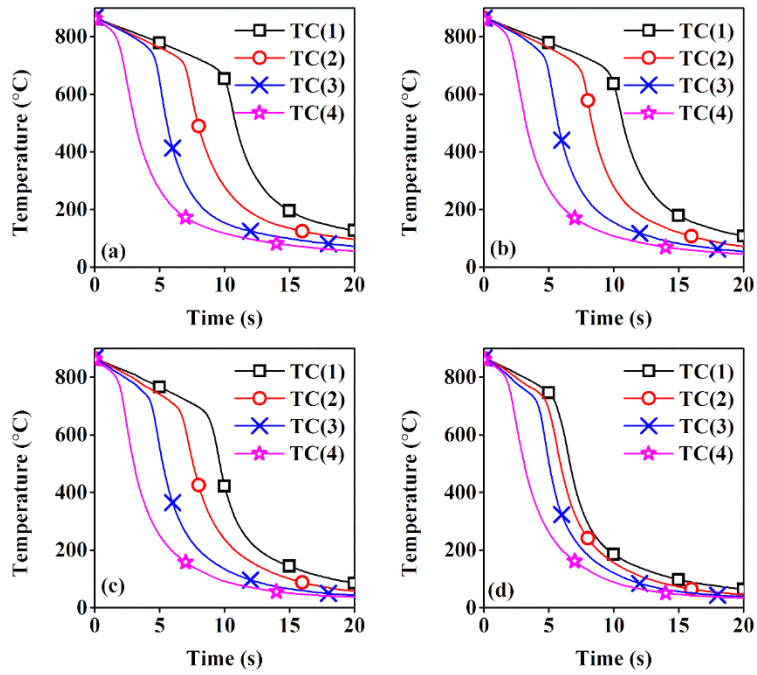


**Figure D.5: Measured cooling curves in the inconel probe during quenching in 1.0 vol.% CuO nanofluid under agitation rates of (a) still (b) 500 (c) 1000 and (d) 1500 rpm**

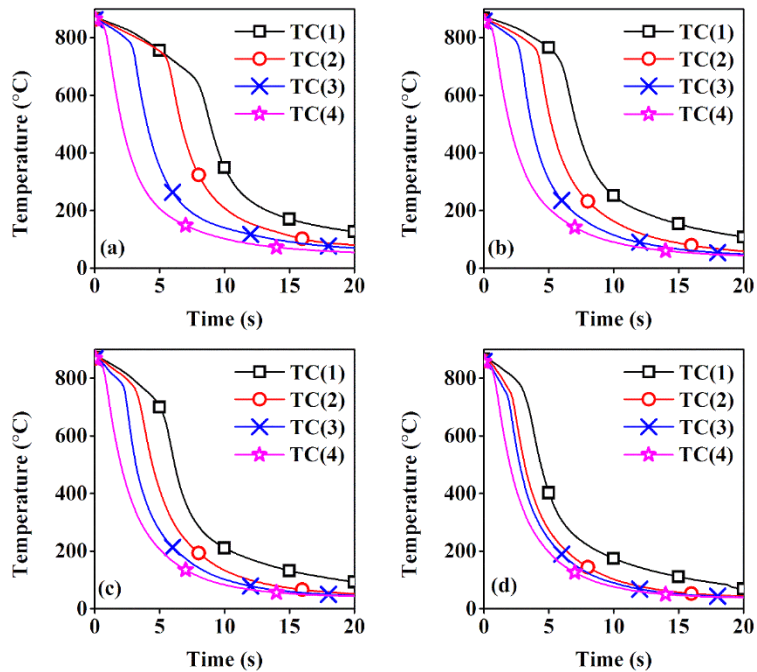


**Figure D.6: Measured cooling curves in the inconel probe during quenching in 0.01 vol.% graphene nanofluid under agitation rates of (a) still (b) 500 (c) 1000 and (d) 1500 rpm**



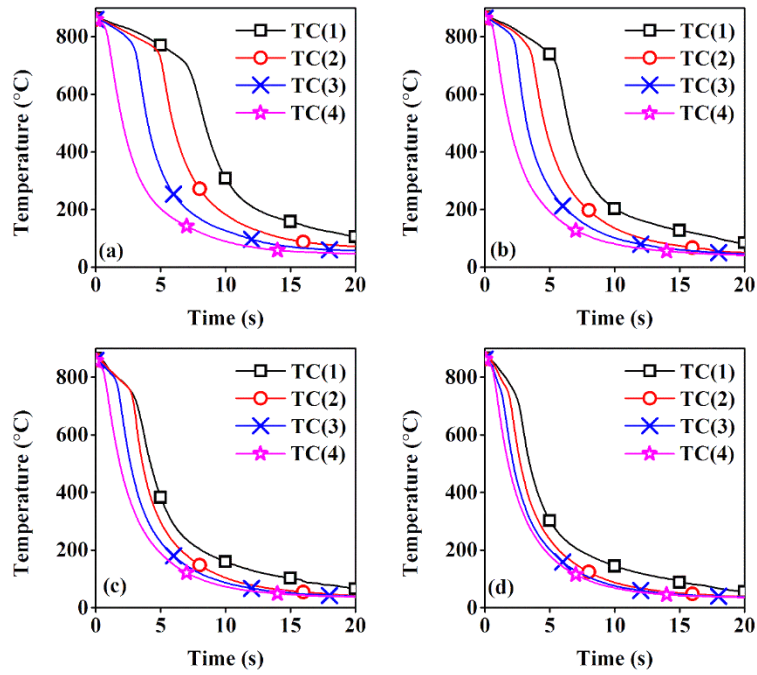


**Figure D.7: Measured cooling curves in the inconel probe during quenching in 0.1 vol.% graphene nanofluid under agitation rates of (a) still (b) 500 (c) 1000 and (d) 1500 rpm**

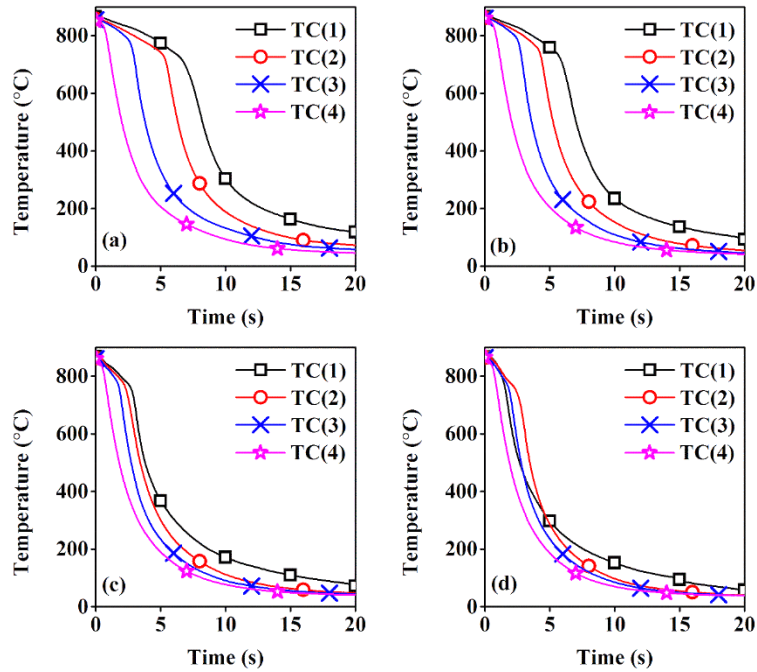


**Figure D.8: Measured cooling curves in the inconel probe during quenching in 0.3 vol.% graphene nanofluid under agitation rates of (a) still (b) 500 (c) 1000 and (d) 1500 rpm**

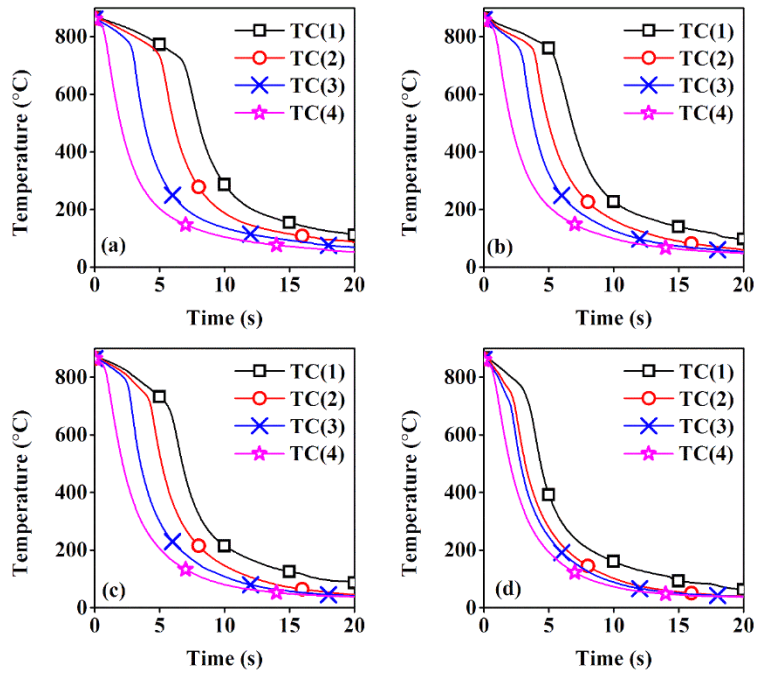


**Figure D.9: Measured cooling curves in the inconel probe during quenching in 0.0003 vol.% MWCNT nanofluid under agitation rates of (a) still (b) 500 (c) 1000 and (d) 1500 rpm**

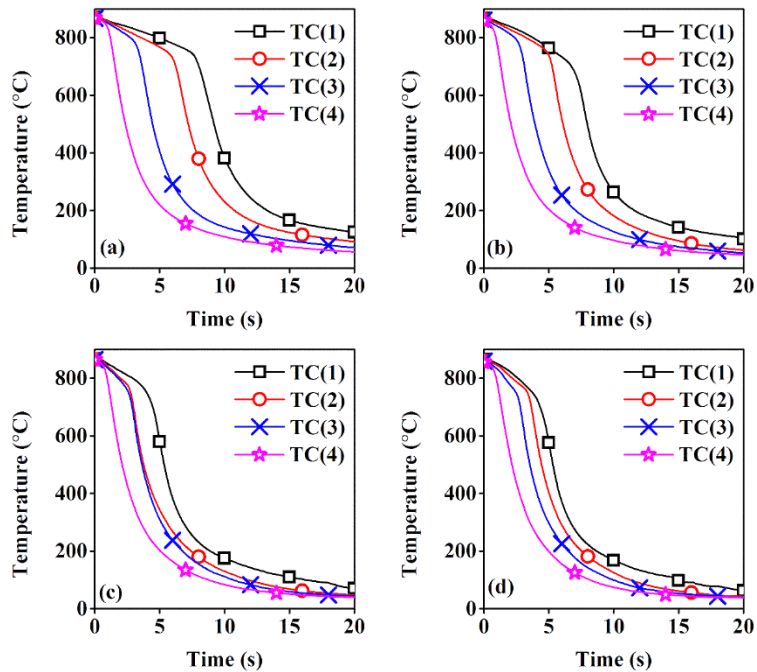


**Figure D.10: Measured cooling curves in the inconel probe during quenching in 0.003 vol.% MWCNT nanofluid under agitation rates of (a) still (b) 500 (c) 1000 and (d) 1500 rpm**

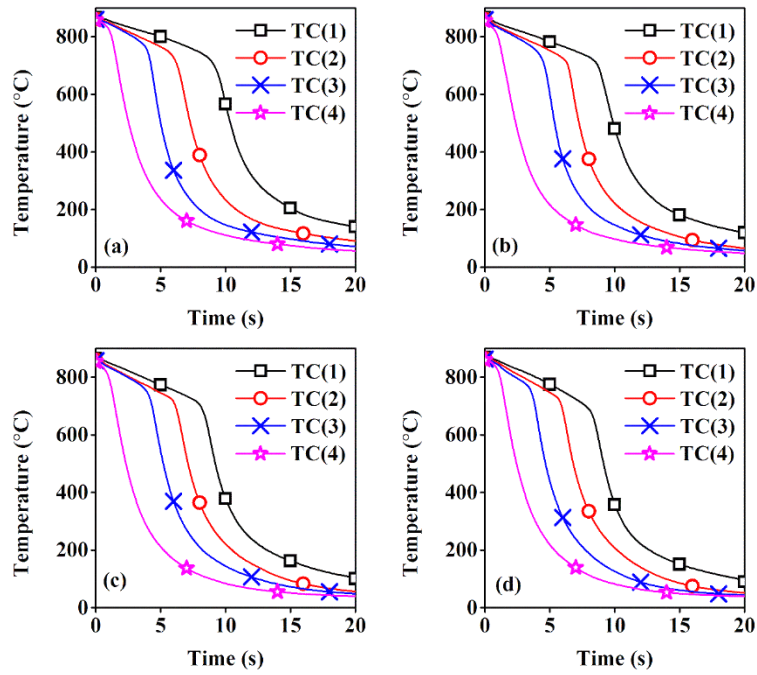


**Figure D.11: Measured cooling curves in the inconel probe during quenching in 0.03 vol.% MWCNT nanofluid under agitation rates of (a) still (b) 500 (c) 1000 and (d) 1500 rpm**

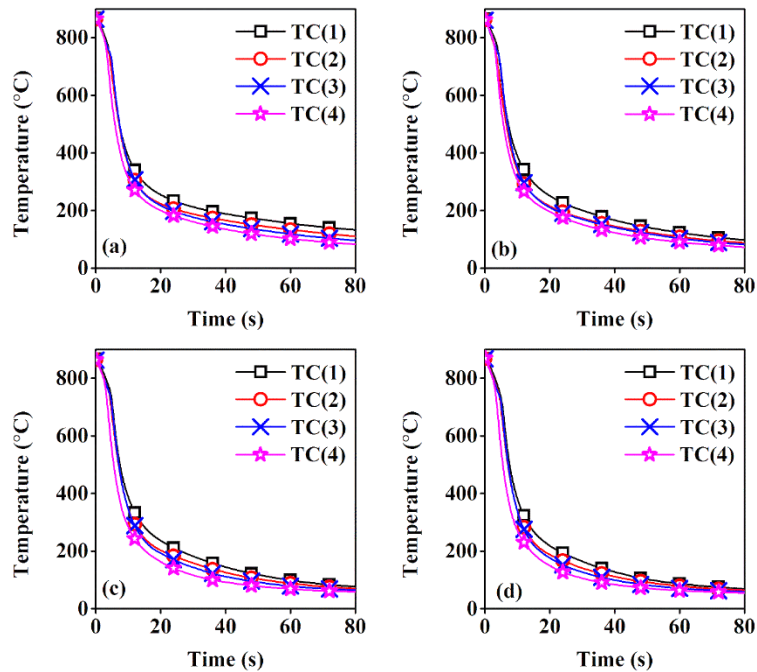


**Figure D.12: Measured cooling curves in the inconel probe during quenching in karanja oil under agitation rates of (a) still (b) 500 (c) 1000 and (d) 1500 rpm**

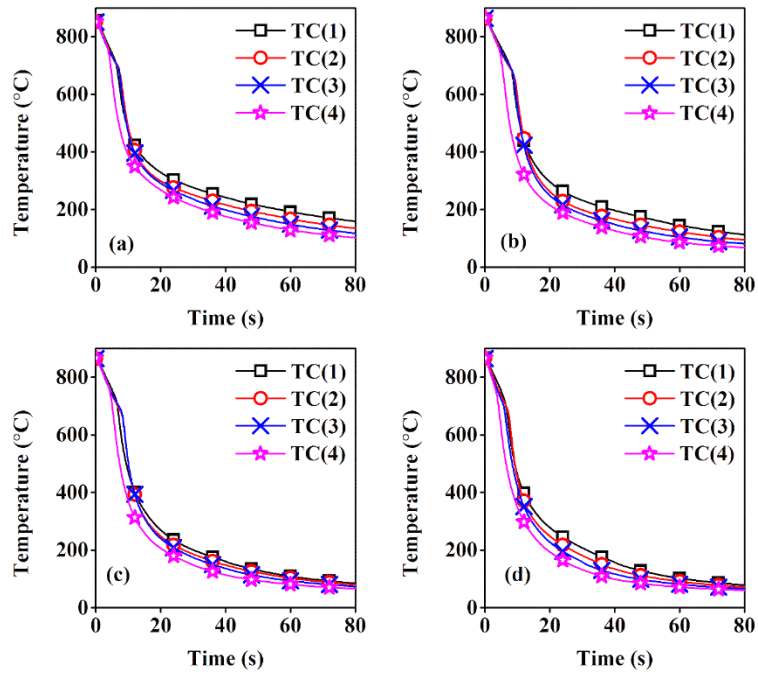


**Figure D.13: Measured cooling curves in the inconel probe during quenching in mineral oil under agitation rates of (a) still (b) 500 (c) 1000 and (d) 1500 rpm**

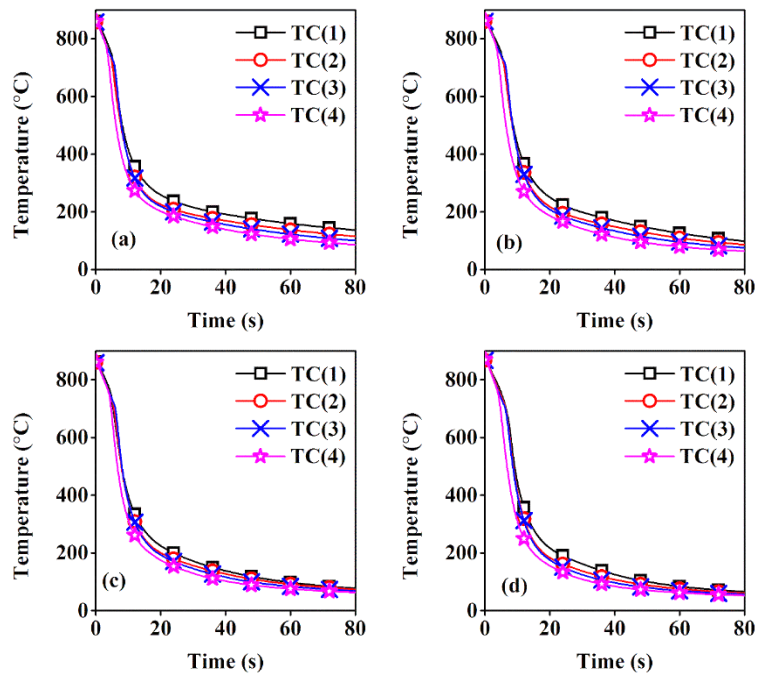


**Figure D.14: Measured cooling curves in the inconel probe during quenching in neem oil under agitation rates of (a) still (b) 500 (c) 1000 and (d) 1500 rpm**

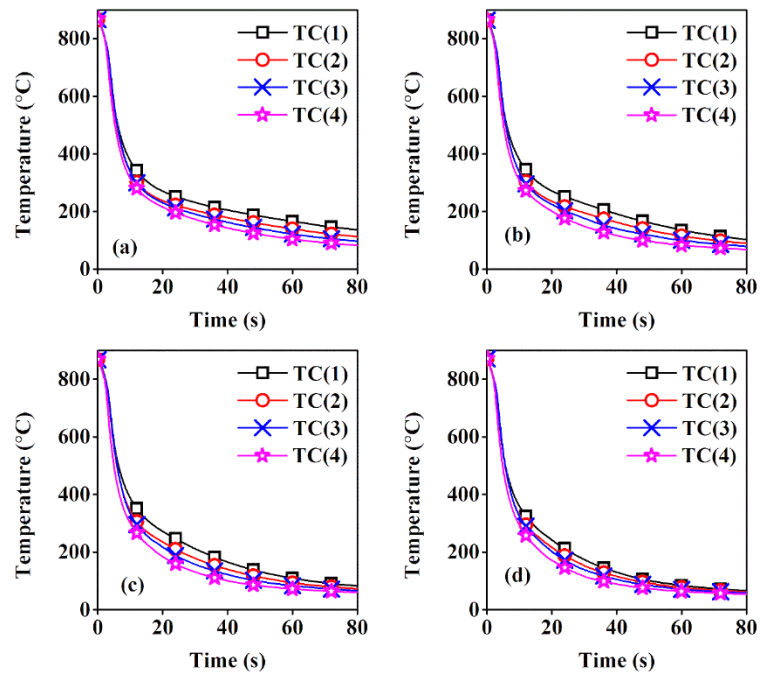


**Figure D.15: Measured cooling curves in the inconel probe during quenching in sunflower oil under agitation rates of (a) still (b) 500 (c) 1000 and (d) 1500 rpm**

**APPENDIX E: COOLING CURVES AND COOLING RATE CURVES  
MEASURED IN THE G 10450 STEEL OF 25 AND 50 MM  
SECTION DIAMETER**

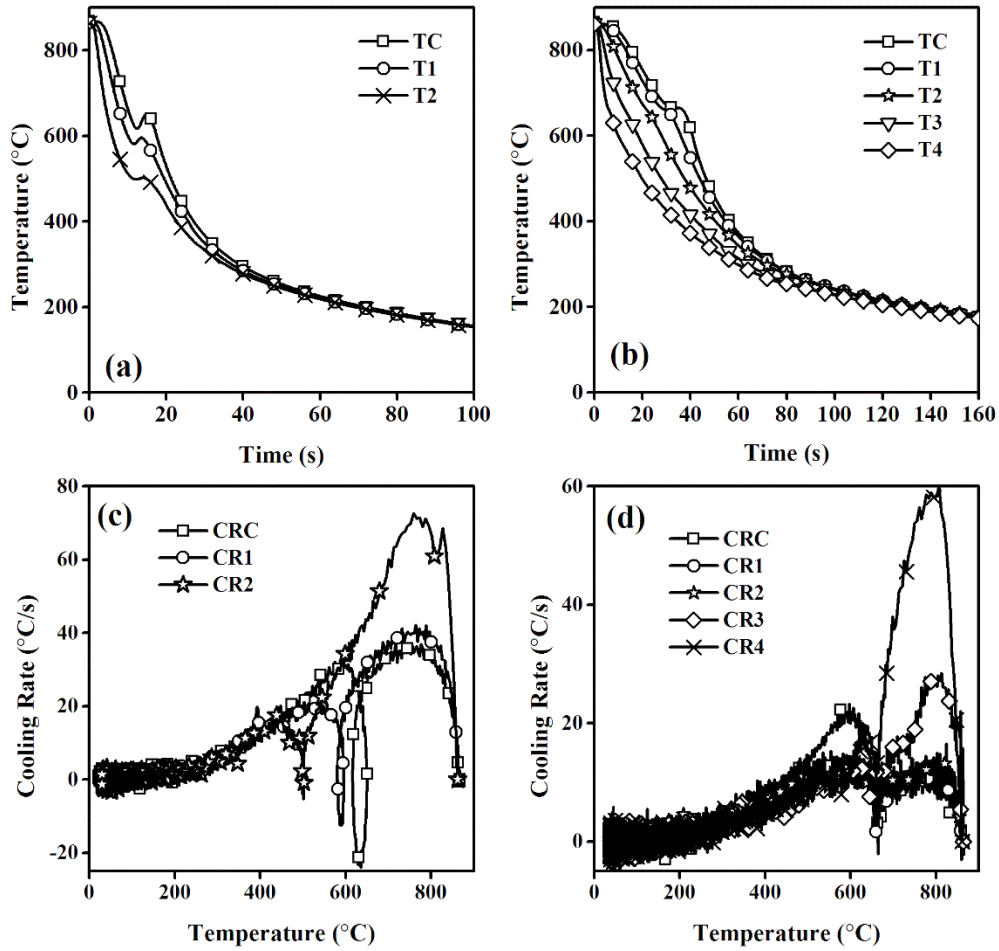


**Figure E.1: Cooling curves obtained at various locations in (a) 25 and (b) 50 mm section diameters of G 10450 steel and their corresponding cooling rate curves in (c) and (d) respectively during quenching in mineral oil quenching medium**

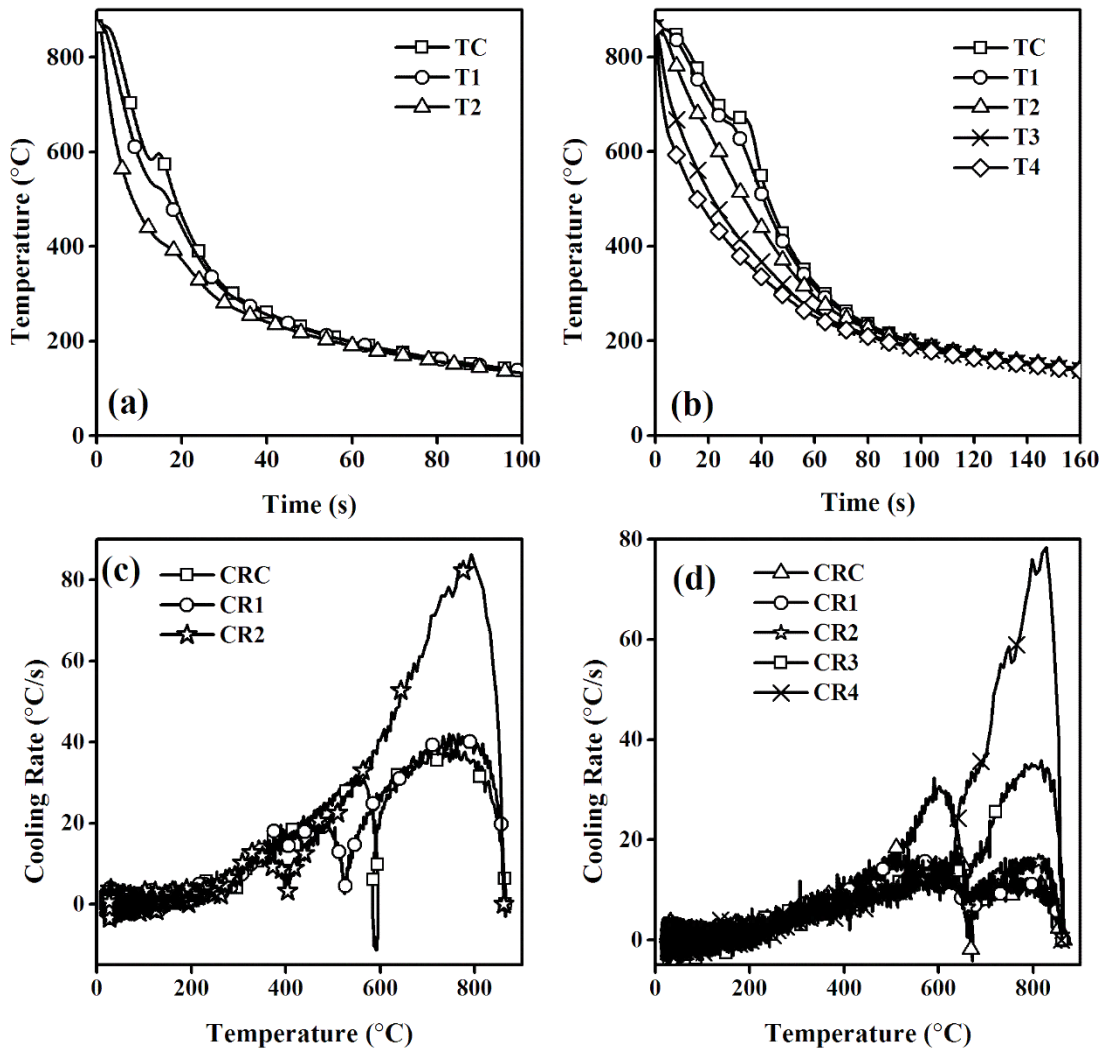


**Figure E.2: Cooling curves obtained at various locations in (a) 25 and (b) 50 mm section diameters of G 10450 steel and their corresponding cooling rate curves in (c) and (d) respectively during quenching in karanja oil quenching medium**

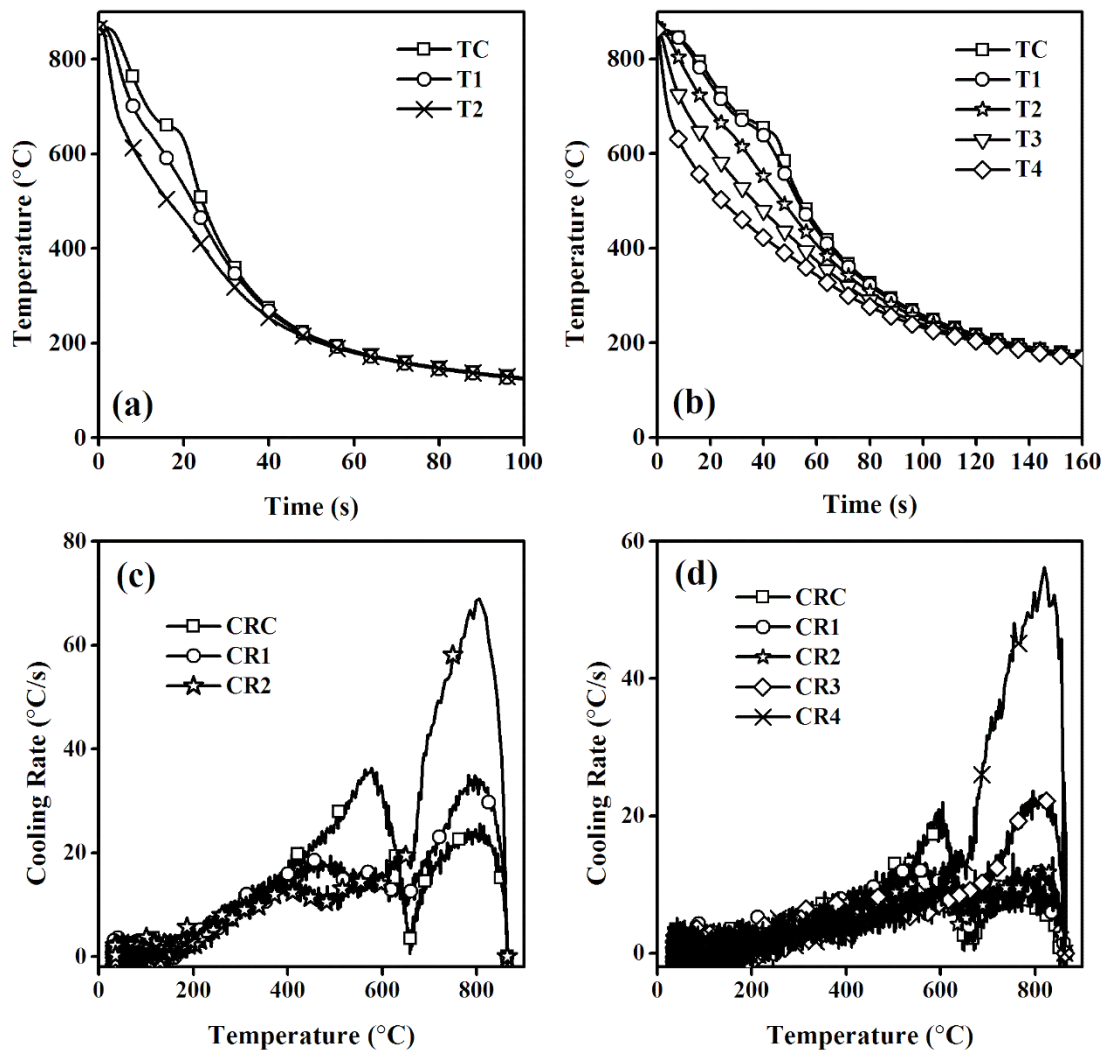


**Figure E.3: Cooling curves obtained at various locations in (a) 25 and (b) 50 mm section diameters of G 10450 steel and their corresponding cooling rate curves in (c) and (d) respectively during quenching in neem oil quenching medium**



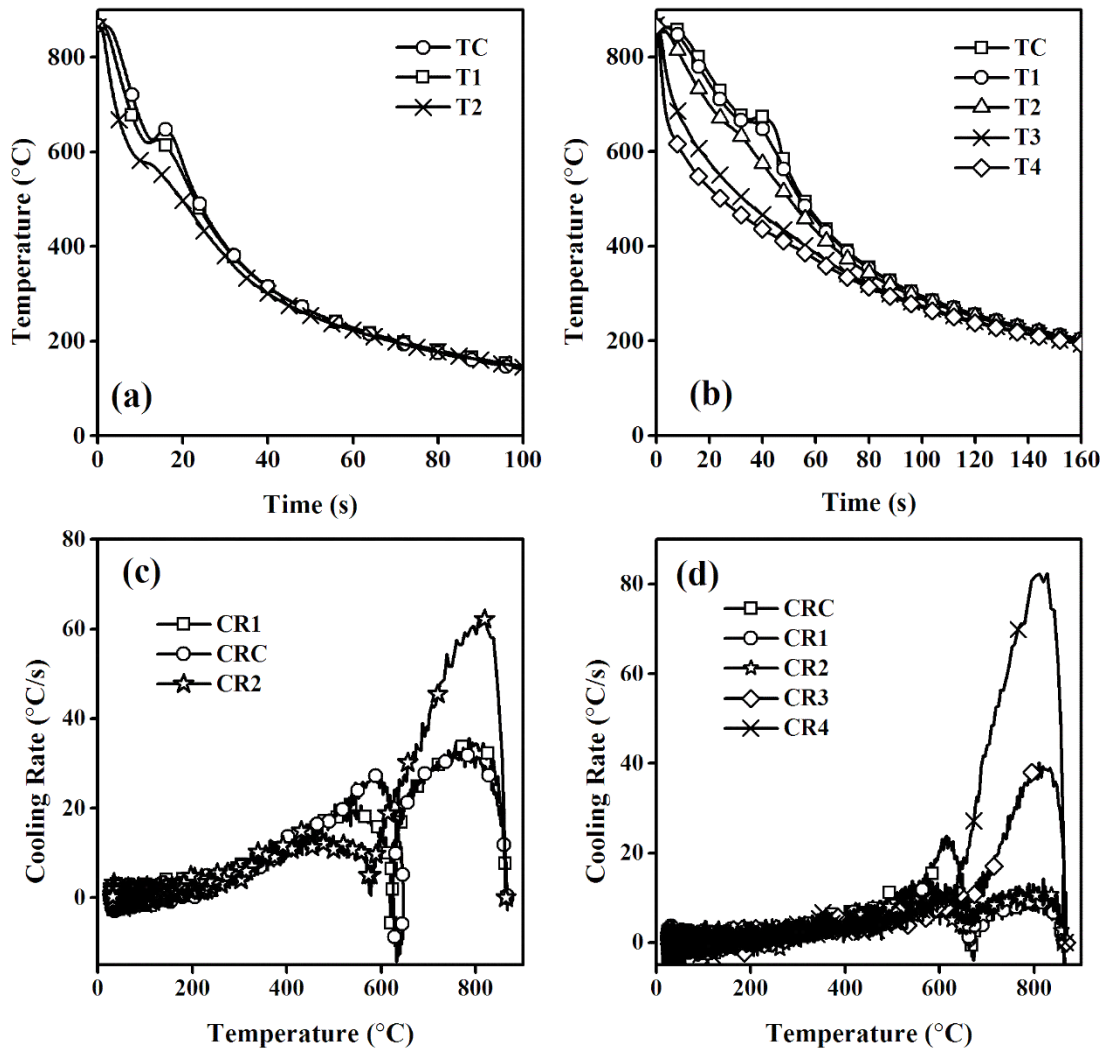


**Figure E.4: Cooling curves obtained at various locations in (a) 25 and (b) 50 mm section diameters of G 10450 steel and their corresponding cooling rate curves in (c) and (d) respectively during quenching in sunflower oil quenching medium**

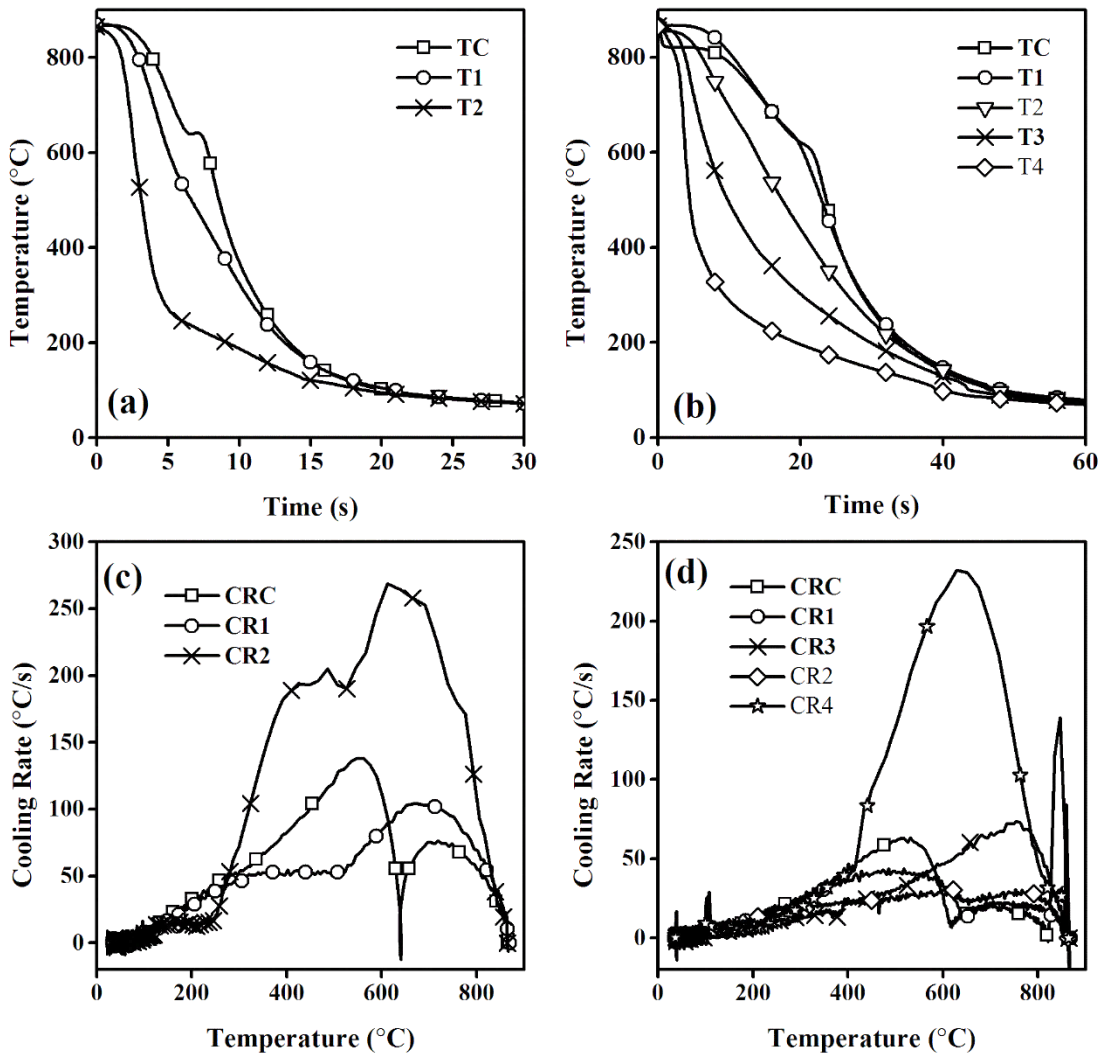


**Figure E.5: Cooling curves obtained at various locations in (a) 25 and (b) 50 mm section diameters of G 10450 steel and their corresponding cooling rate curves in (c) and (d) respectively during quenching in distilled water quenching medium**

**APPENDIX F: COOLING CURVES AND COOLING RATE CURVES  
MEASURED IN THE G 10900 STEEL OF 25 AND 50 mm  
SECTION DIAMETER**

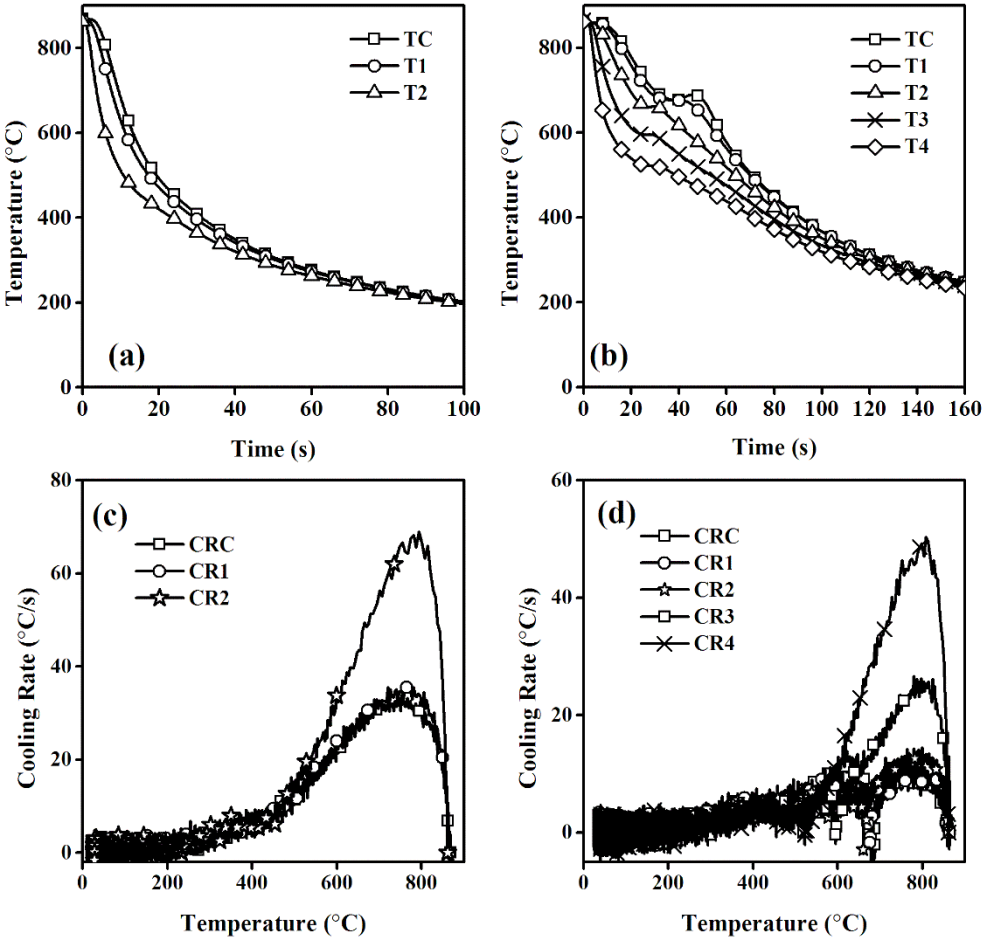


**Figure F.1: Cooling curves obtained at various locations in (a) 25 and (b) 50 mm section diameters of G 10900 steel and their corresponding cooling rate curves in (c) and (d) respectively during quenching in mineral oil quenching medium**

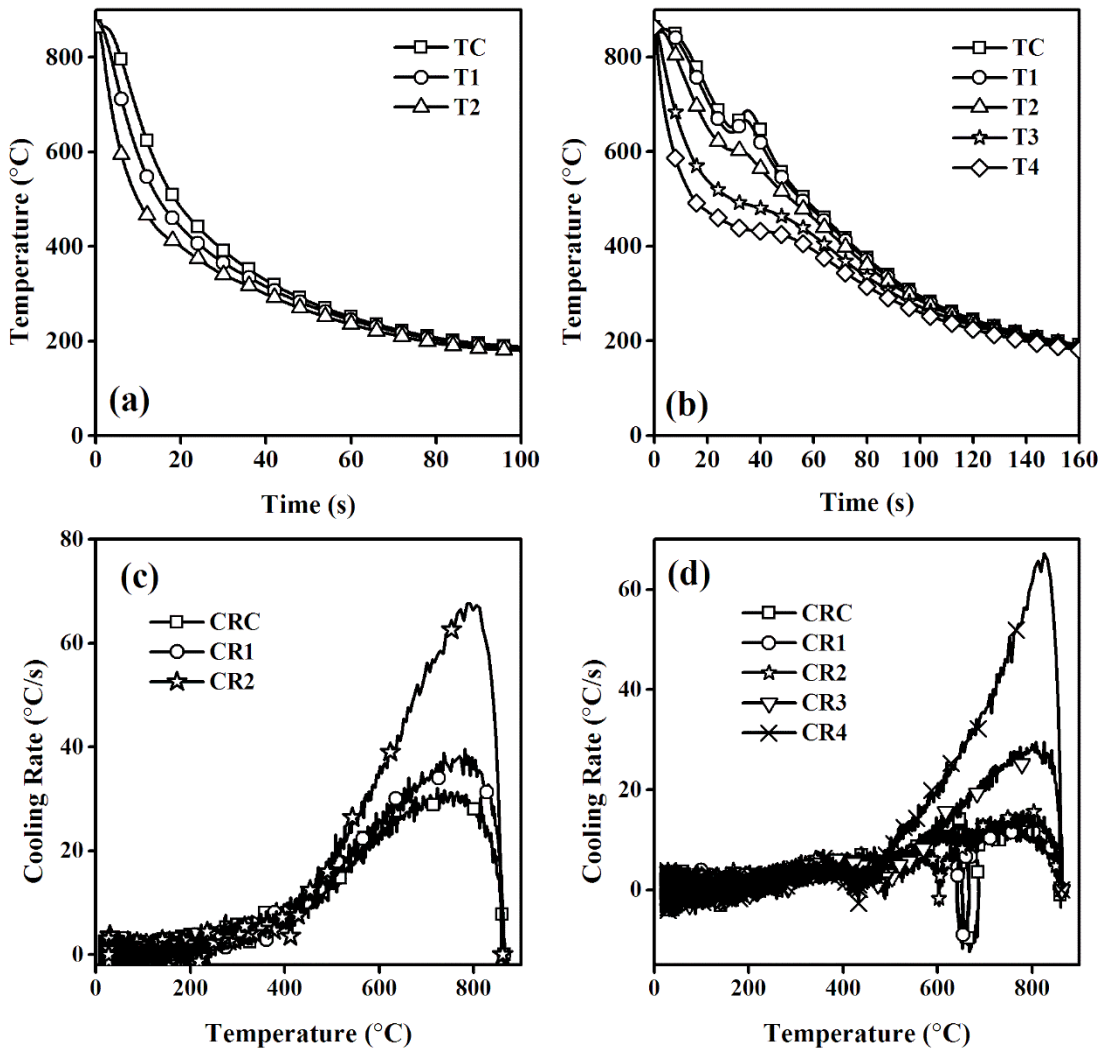


**Figure F.2: Cooling curves obtained at various locations in (a) 25 and (b) 50 mm section diameters of G 10900 steel and their corresponding cooling rate curves in (c) and (d) respectively during quenching in karanja oil quenching medium**

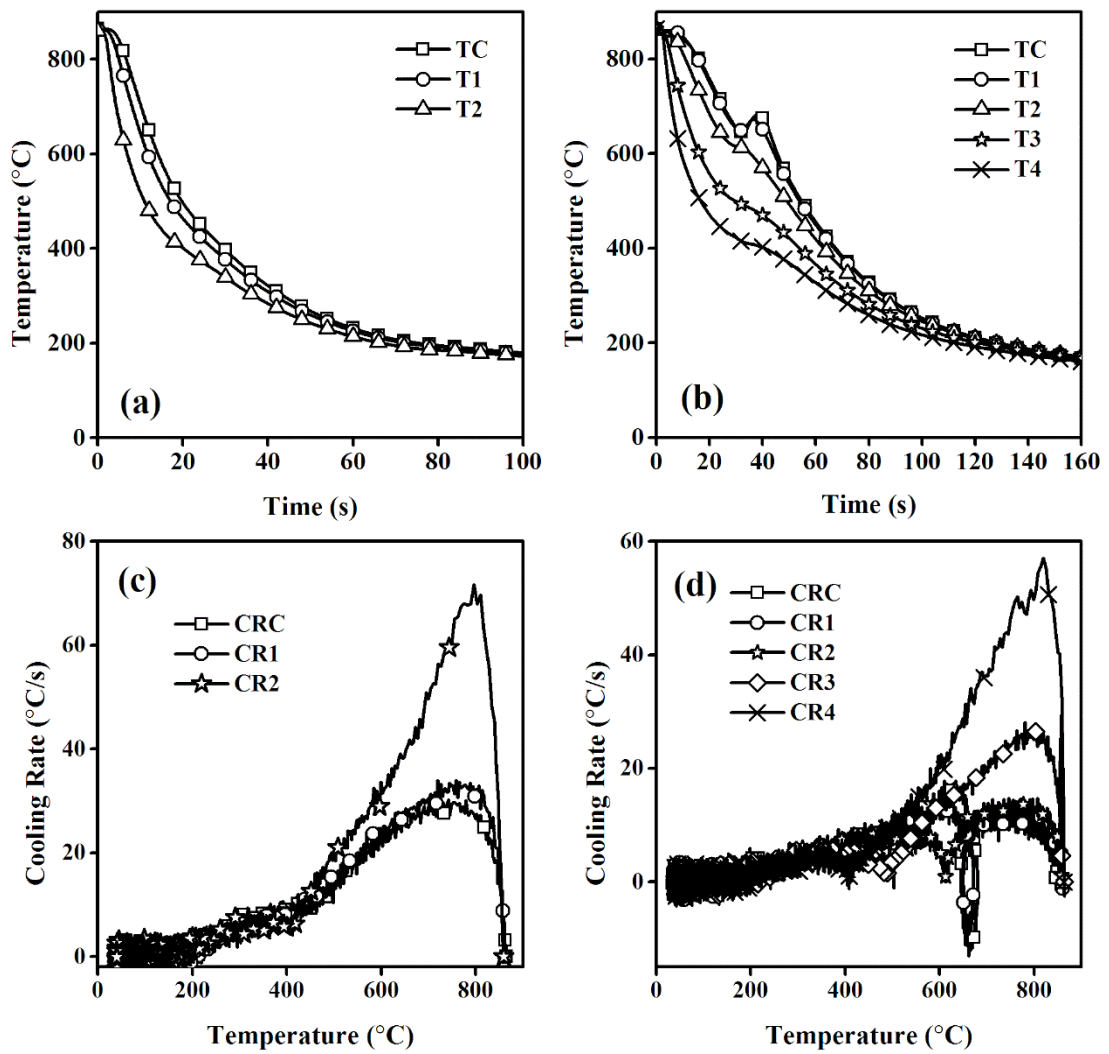


**Figure F.3: Cooling curves obtained at various locations in (a) 25 and (b) 50 mm section diameters of G 10900 steel and their corresponding cooling rate curves in (c) and (d) respectively during quenching in neem oil quenching medium**

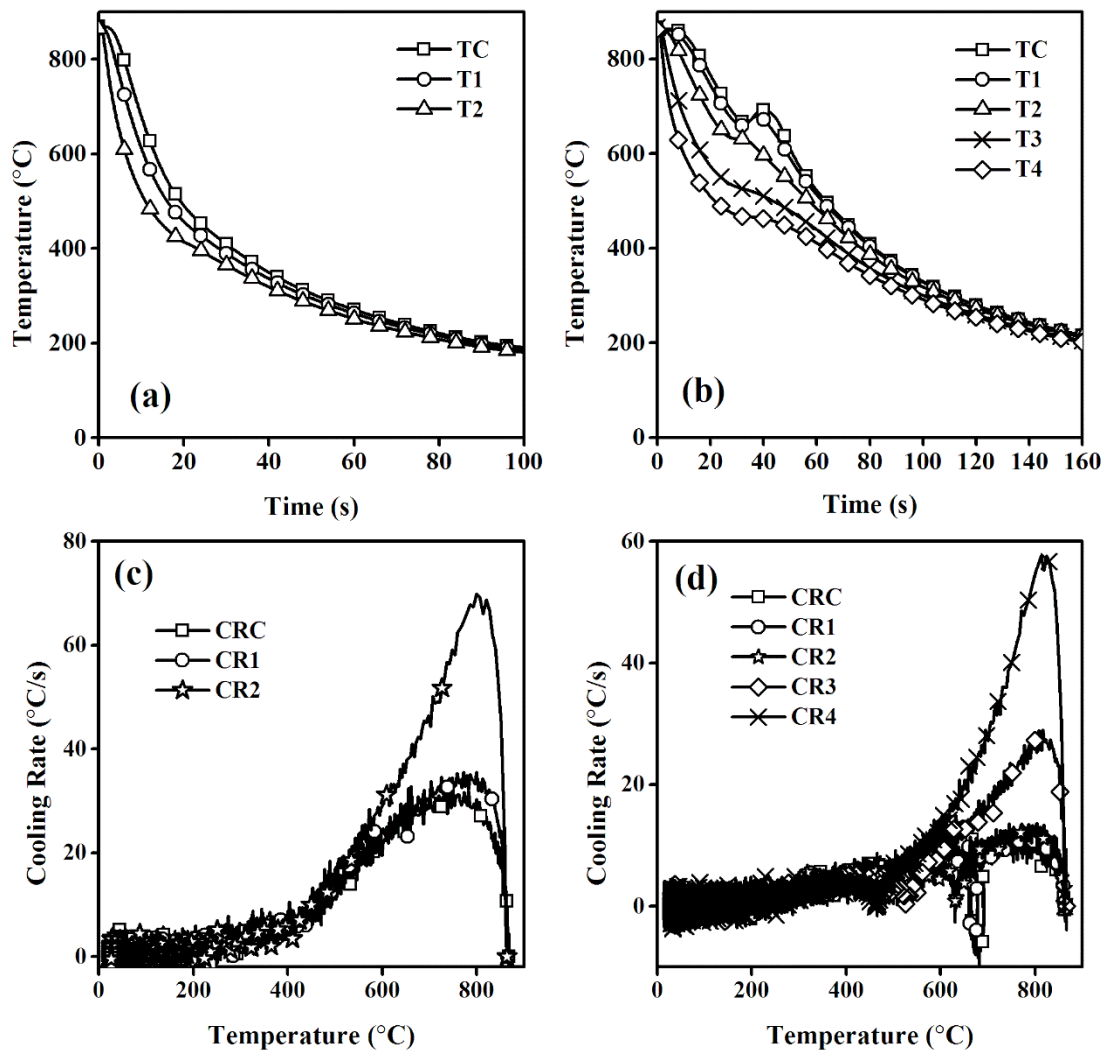


**Figure F.4: Cooling curves obtained at various locations in (a) 25 and (b) 50 mm section diameters of G 10900 steel and their corresponding cooling rate curves in (c) and (d) respectively during quenching in sunflower oil quenching medium**

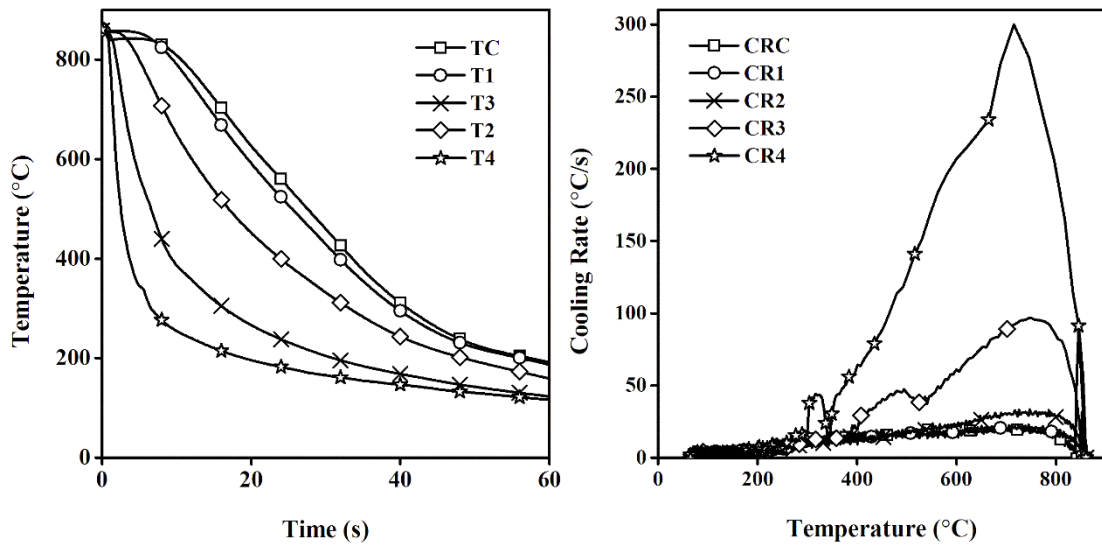


**Figure F.5: (a) Cooling curves and (b) cooling rate curves obtained at various locations in the 50 mm section diameter of G 10900 steel during quenching in distilled water quenching medium**

**APPENDIX G: COOLING CURVES AND COOLING RATE CURVES  
MEASURED IN THE STAINLESS STEEL OF 25 AND 50 mm  
SECTION DIAMETER**

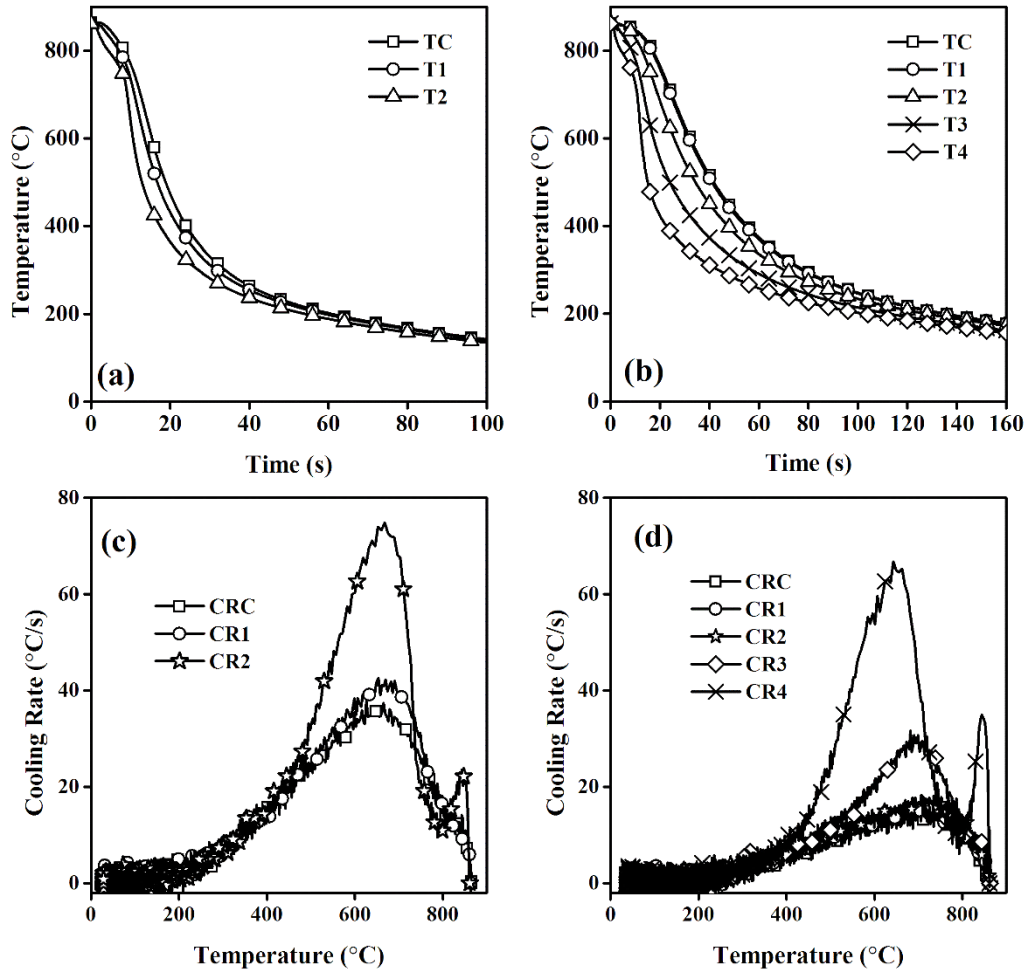


**Figure G.1: Cooling curves obtained at various locations in (a) 25 and (b) 50 mm section diameters of stainless steel and their corresponding cooling rate curves in (c) and (d) respectively during quenching in mineral oil quenching medium**



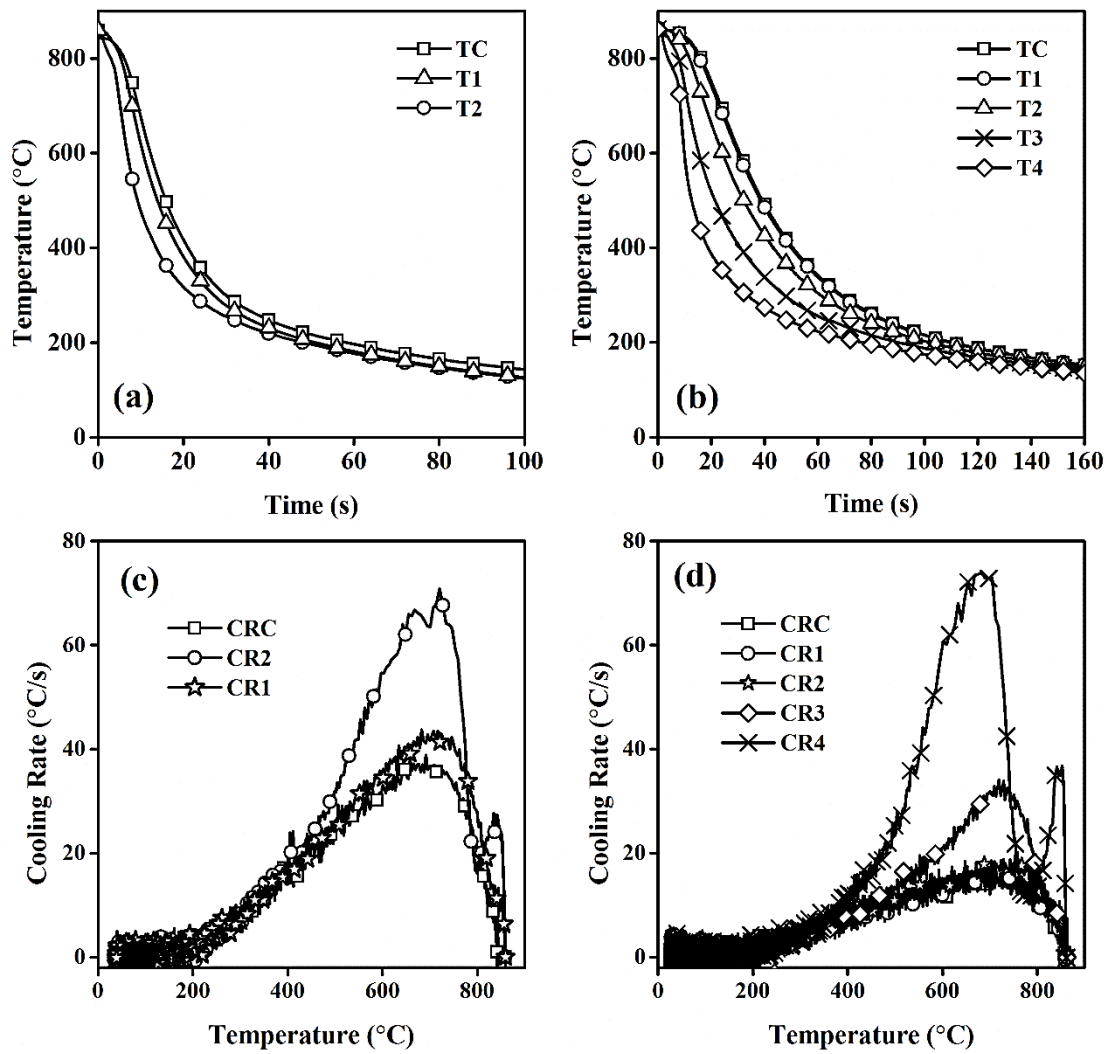


**Figure G.2: Cooling curves obtained at various locations in (a) 25 and (b) 50 mm section diameters of stainless steel and their corresponding cooling rate curves in (c) and (d) respectively during quenching in karanja oil quenching medium**

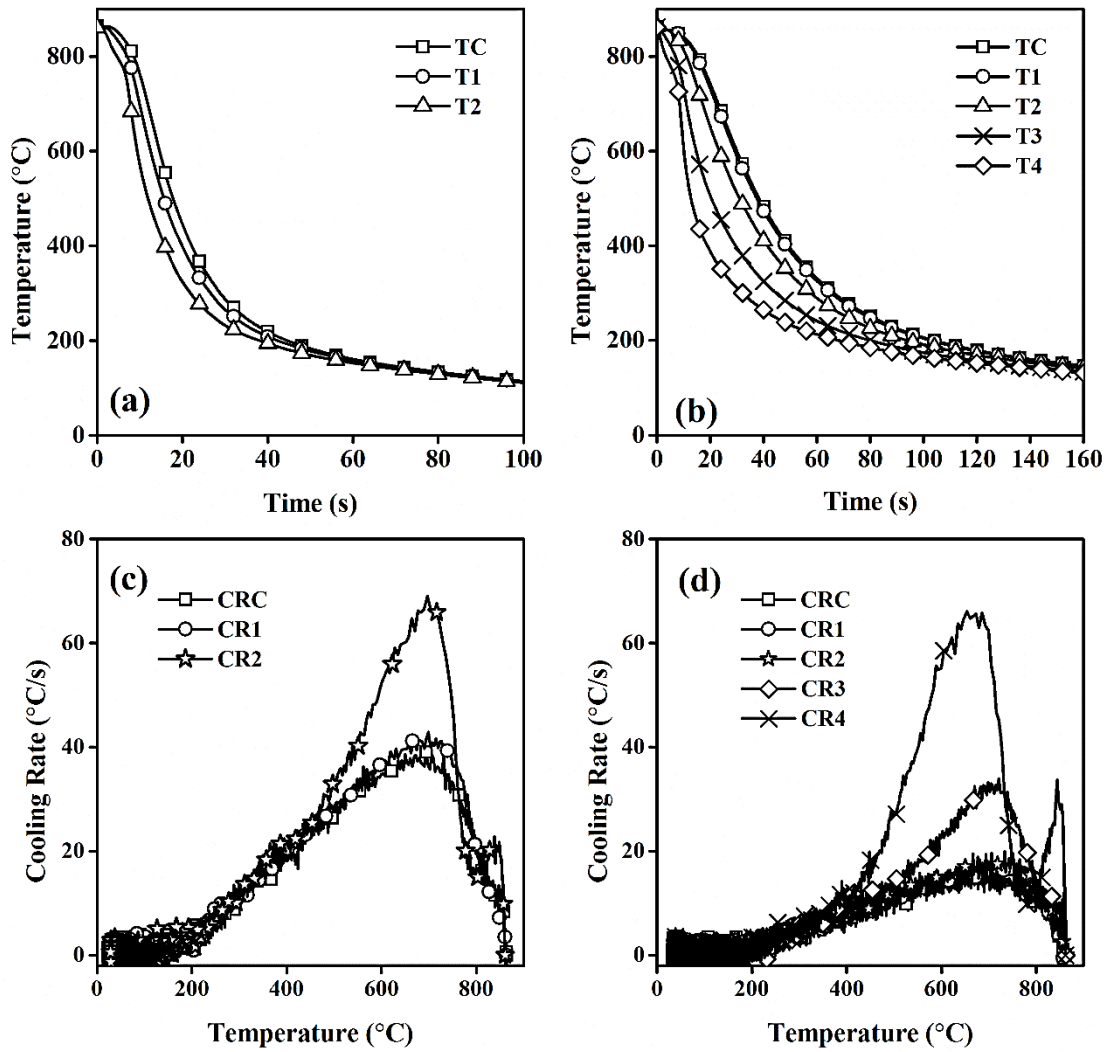


**Figure G.3: Cooling curves obtained at various locations in (a) 25 and (b) 50 mm section diameters of stainless steel and their corresponding cooling rate curves in (c) and (d) respectively during quenching in neem oil quenching medium**

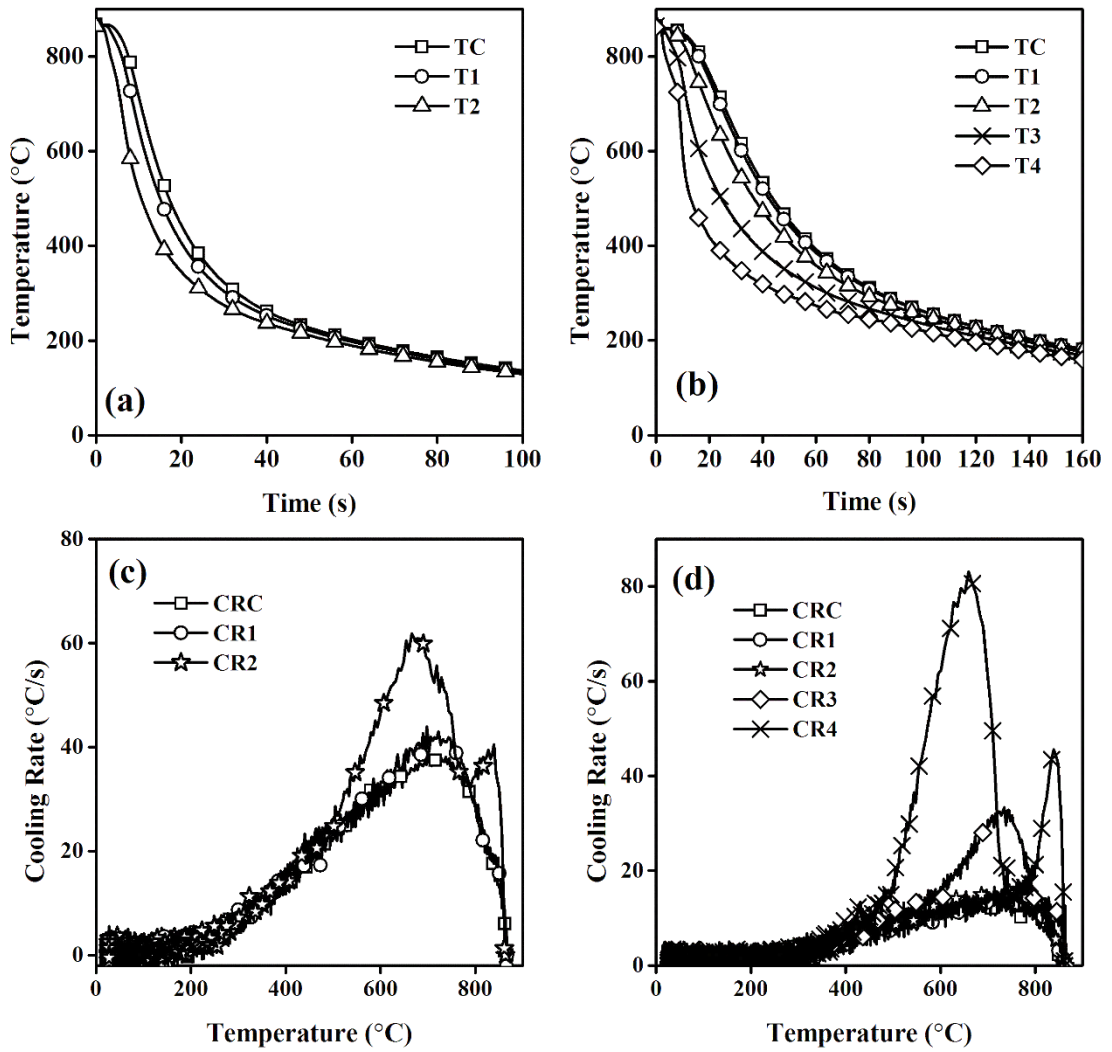


**Figure G.4: Cooling curves obtained at various locations in (a) 25 and (b) 50 mm section diameters of stainless steel and their corresponding cooling rate curves in (c) and (d) respectively during quenching in sunflower oil quenching medium**

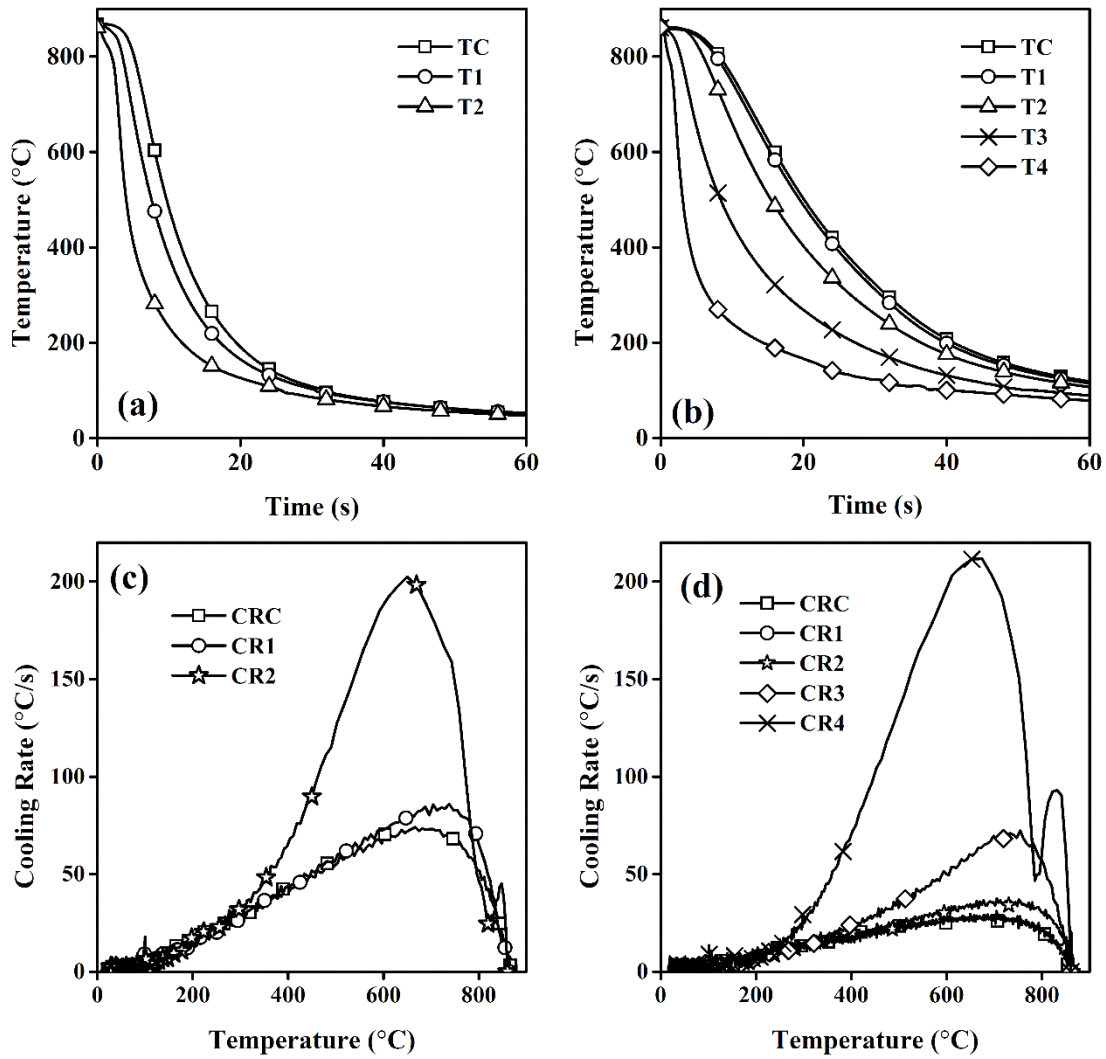


**Figure G.5: Cooling curves obtained at various locations in (a) 25 and (b) 50 mm section diameters of stainless steel and their corresponding cooling rate curves in (c) and (d) respectively during quenching in distilled water quenching medium**

**APPENDIX H: ESTIMATED HEAT FLUX TRANSIENTS DURING QUENCHING OF INCONEL PROBE IN VARIOUS QUENCH MEDIA**

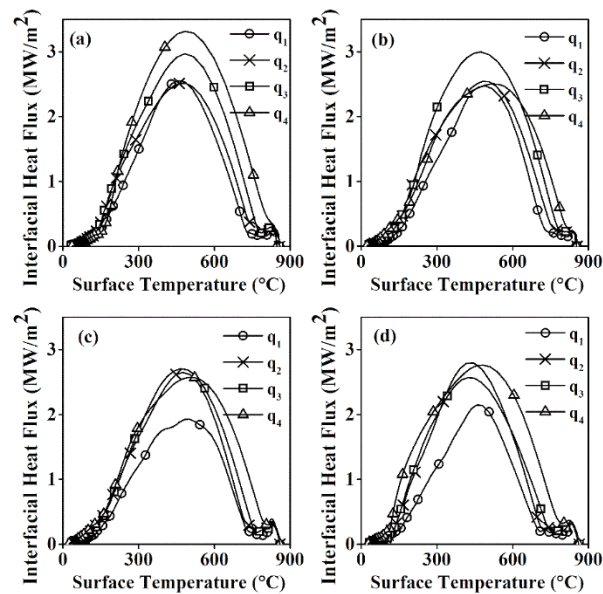


**Figure H.1: Spatiotemporal heat flux obtained during quenching of inconel in (a) distilled water (b) 0.01 (c) 0.1 and (d) 0.3 vol.% graphene nanofluids**

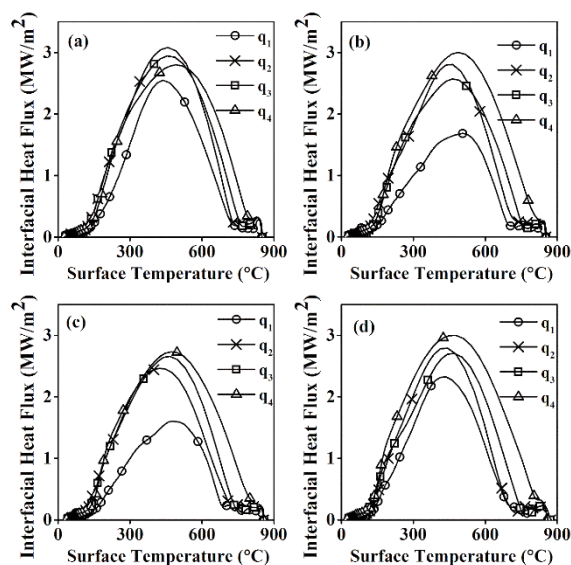


**Figure H.2: Spatiotemporal heat flux obtained during quenching of inconel in (a) 0.01 (b) 0.05 (c) 0.1 and (d) 1.0 vol.% CuO nanofluids**

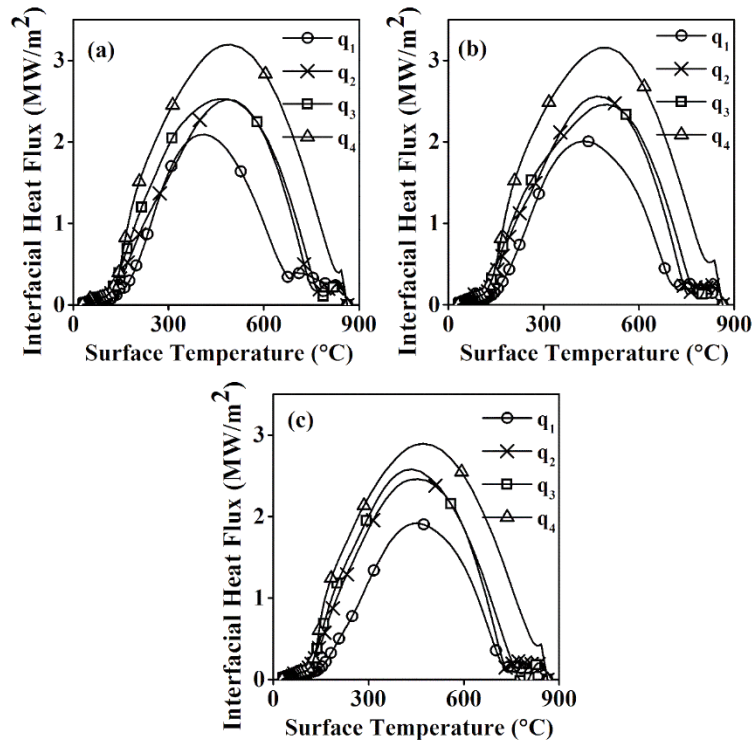


**Figure H.3: Spatiotemporal heat flux obtained during quenching of inconel in (a) 0.0003 (b) 0.003 and (c) 0.03 vol.% MWCNT nanofluids**

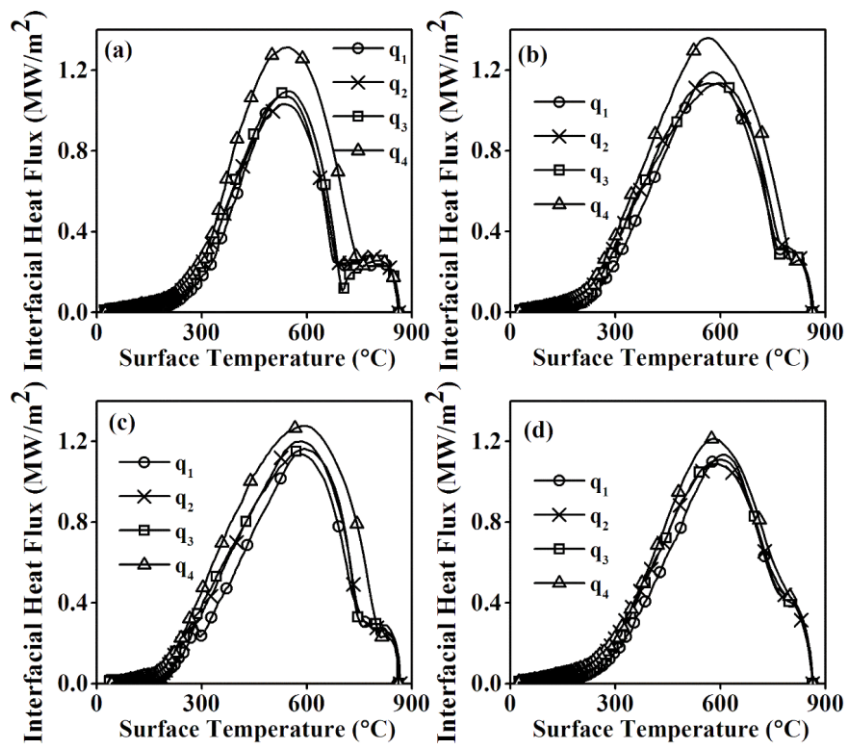


**Figure H.4: Spatiotemporal heat flux obtained during quenching of inconel in (a) mineral (b) karanja (c) neem and (d) sunflower oils**

**APPENDIX I: ESTIMATED HEAT FLUX TRANSIENTS DURING  
QUENCHING OF INCONEL PROBE IN VARIOUS QUENCH  
MEDIA IN THE TENSI AGITATION SYSTEM**

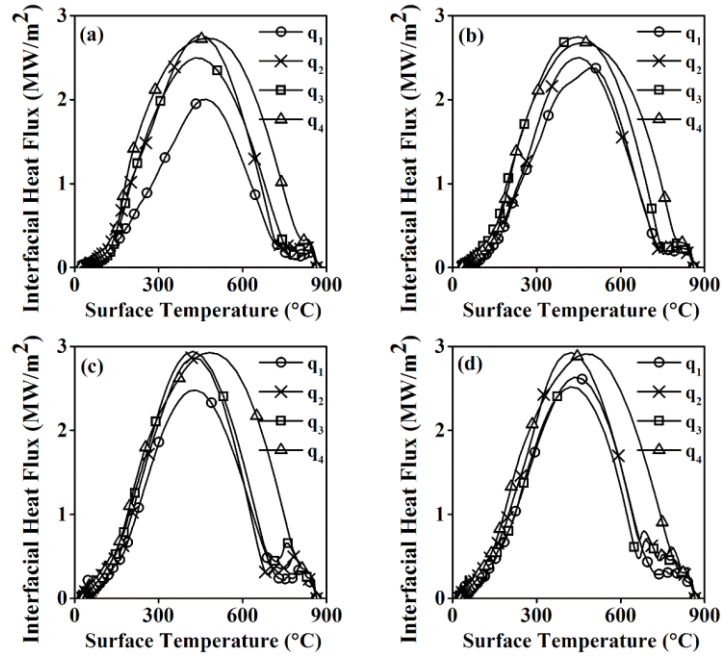


**Figure I.1: Spatiotemporal heat flux estimated at the inconel/water interface at impeller agitation rates of (a) still (b) 500 (c) 1000 and (d) 1500 rpms**

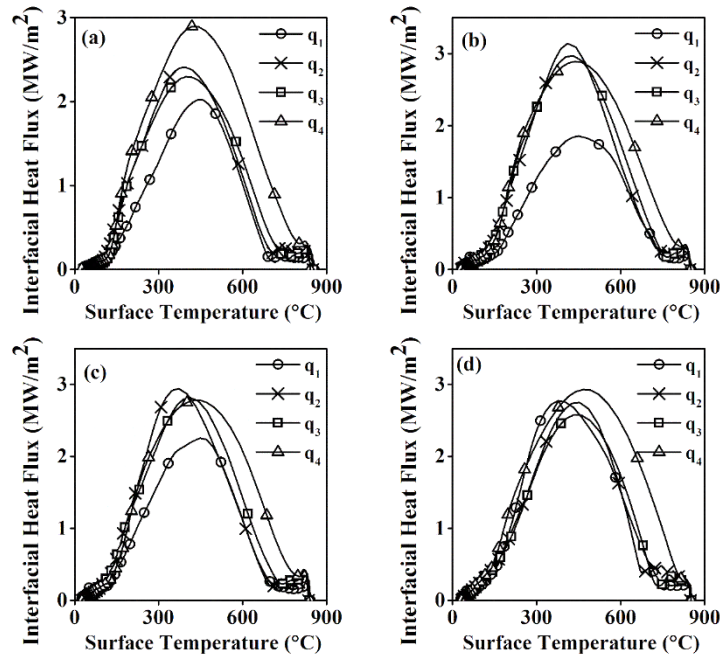


**Figure I.2: Spatiotemporal heat flux estimated at the inconel/0.01 vol.% CuO nanofluid interface at impeller agitation rates of (a) still (b) 500 (c) 1000 and (d) 1500 rpms**

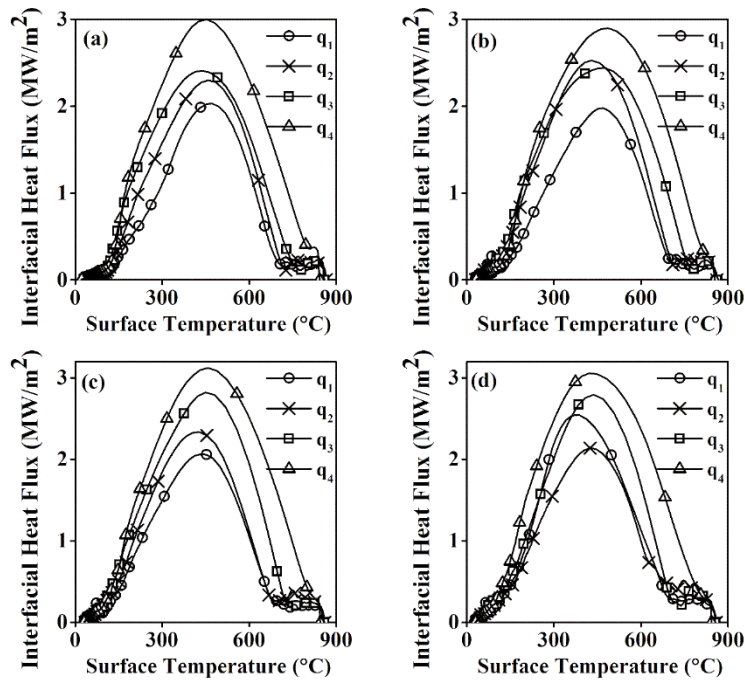


**Figure I.3: Spatiotemporal heat flux estimated at the inconel/0.05 vol.% CuO nanofluid interface at impeller agitation rates of (a) still (b) 500 (c) 1000 and (d) 1500 rpms**

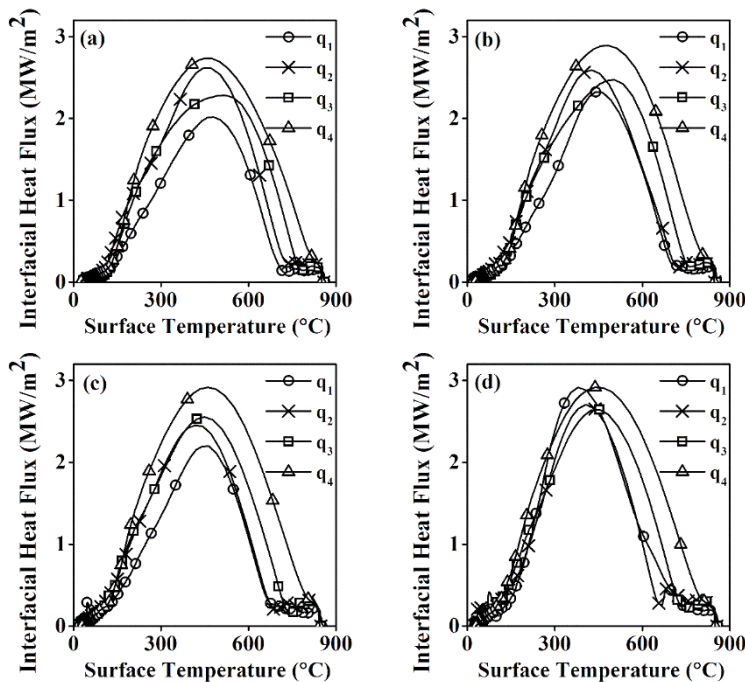


**Figure I.4: Spatiotemporal heat flux estimated at the inconel/0.1 vol.% CuO nanofluid interface at impeller agitation rates of (a) still (b) 500 (c) 1000 and (d) 1500 rpms**



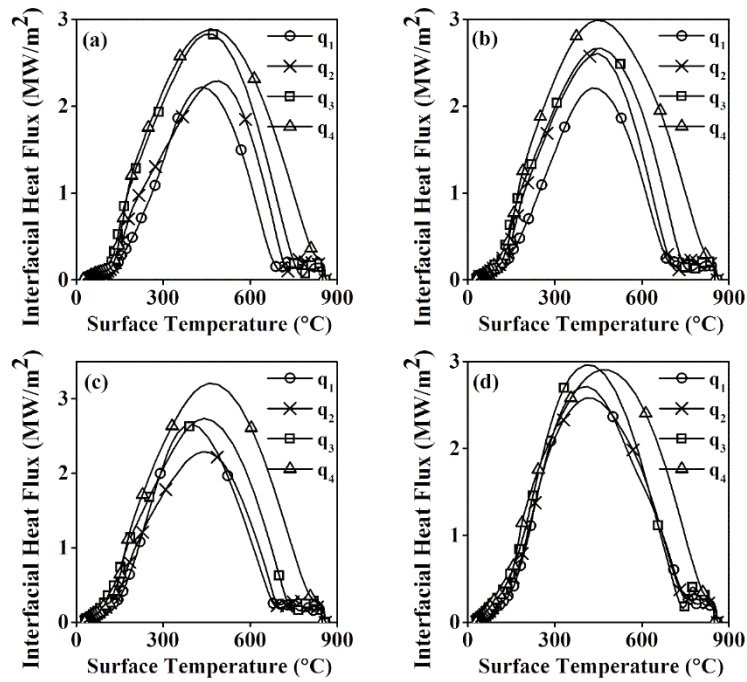


**Figure I.5: Spatiotemporal heat flux estimated at the inconel/1.0 vol.% CuO nanofluid interface at impeller agitation rates of (a) still (b) 500 (c) 1000 and (d) 1500 rpms**

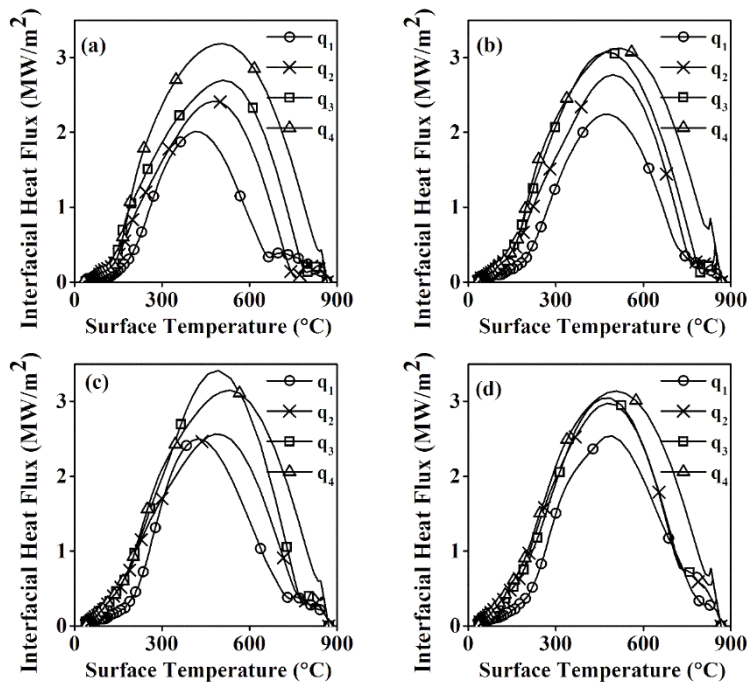


**Figure I.6: Spatiotemporal heat flux estimated at the inconel/0.01 vol.% graphene nanofluid interface at impeller agitation rates of (a) still (b) 500 (c) 1000 and (d) 1500 rpms**

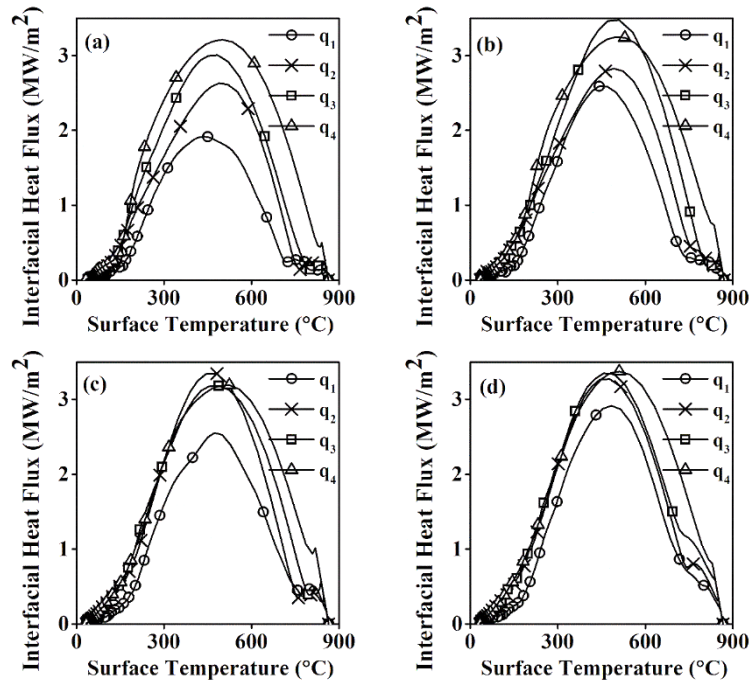


**Figure I.7: Spatiotemporal heat flux estimated at the inconel/0.1 vol.% graphene nanofluid interface at impeller agitation rates of (a) still (b) 500 (c) 1000 and (d) 1500 rpms**

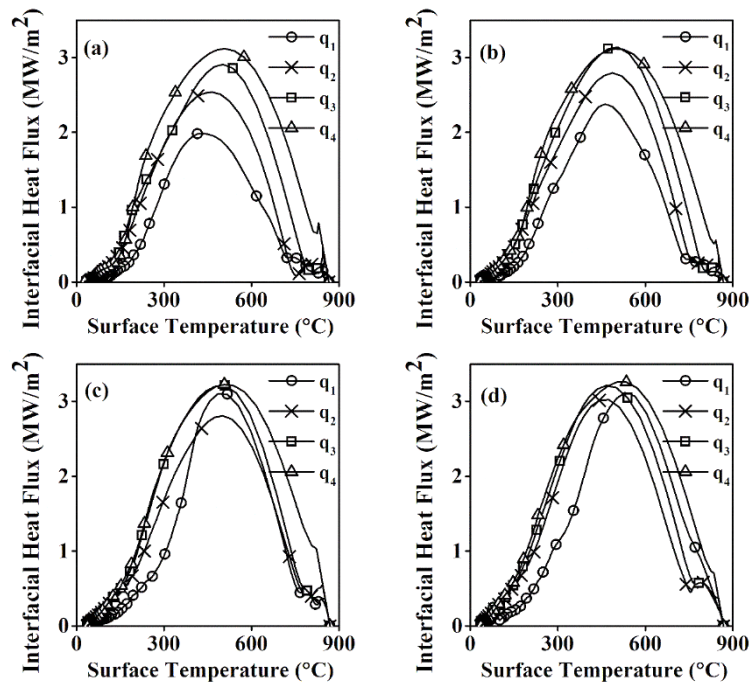


**Figure I.8: Spatiotemporal heat flux estimated at the inconel/0.3 vol.% graphene nanofluid interface at impeller agitation rates of (a) still (b) 500 (c) 1000 and (d) 1500 rpms**

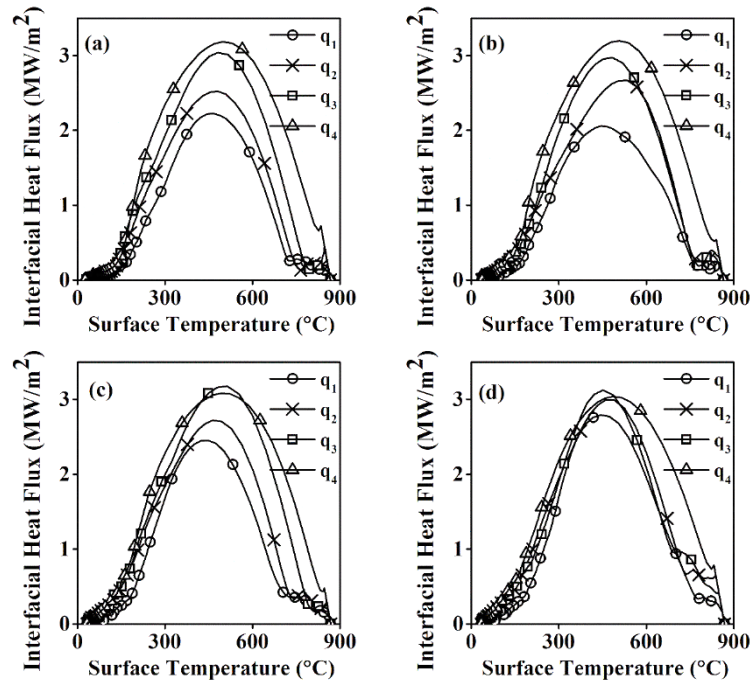


**Figure I.9: Spatiotemporal heat flux estimated at the inconel/0.0003 vol.% MWCNT nanofluid interface at impeller agitation rates of (a) still (b) 500 (c) 1000 and (d) 1500 rpms**

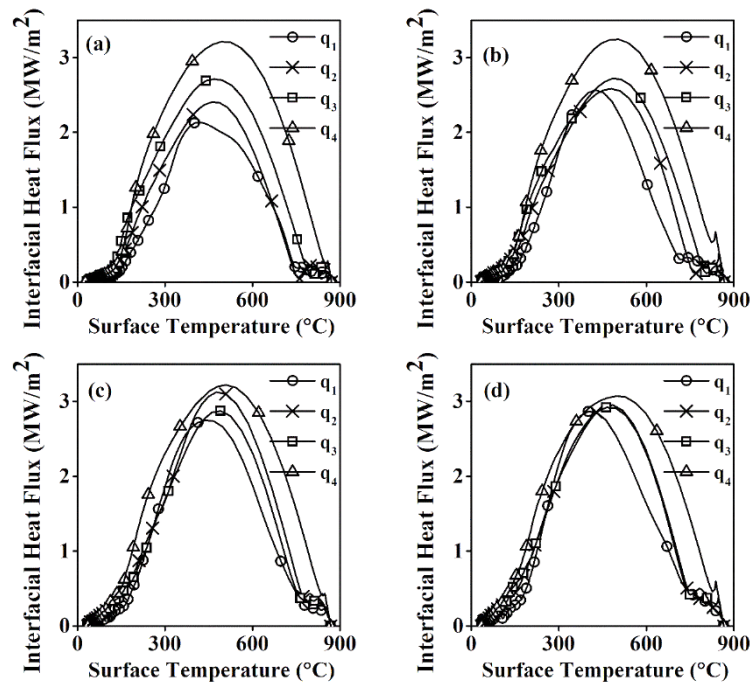


**Figure I.10: Spatiotemporal heat flux estimated at the inconel/0.003 vol.% MWCNT nanofluid interface at impeller agitation rates of (a) still (b) 500 (c) 1000 and (d) 1500 rpms**

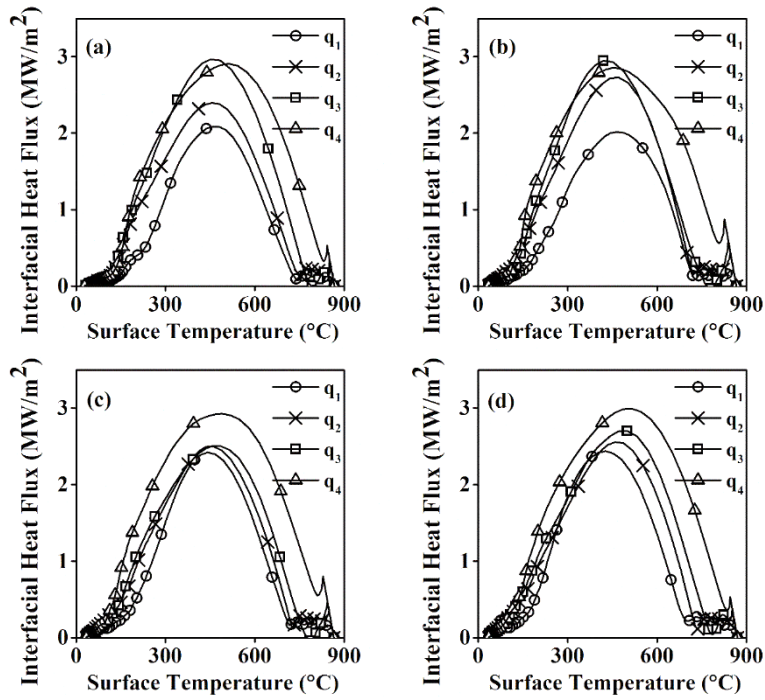


**Figure I.11: Spatiotemporal heat flux estimated at the inconel/0.03 vol.% MWCNT nanofluid interface at impeller agitation rates of (a) still (b) 500 (c) 1000 and (d) 1500 rpms**

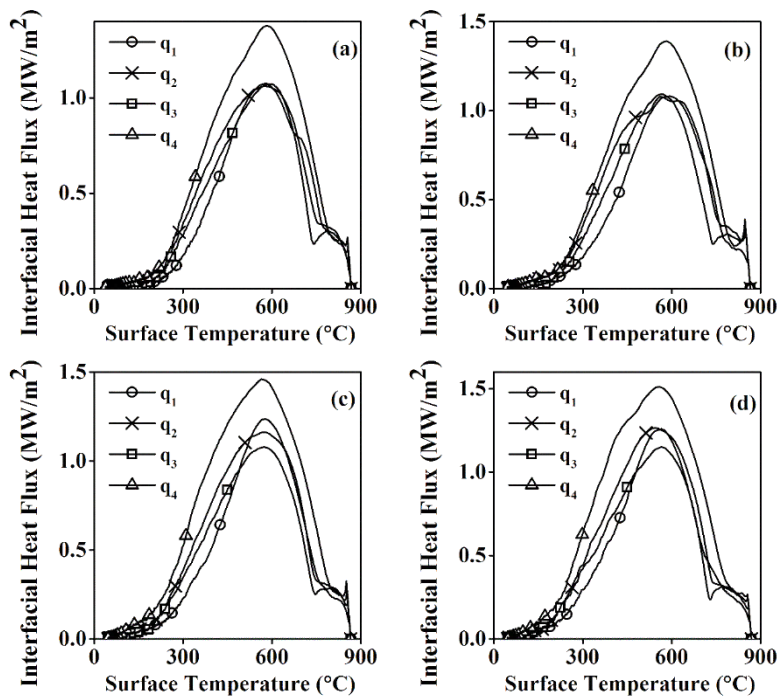


**Figure I.12: Spatiotemporal heat flux estimated at the inconel/karanja oil interface at impeller agitation rates of (a) still (b) 500 (c) 1000 and (d) 1500 rpms**

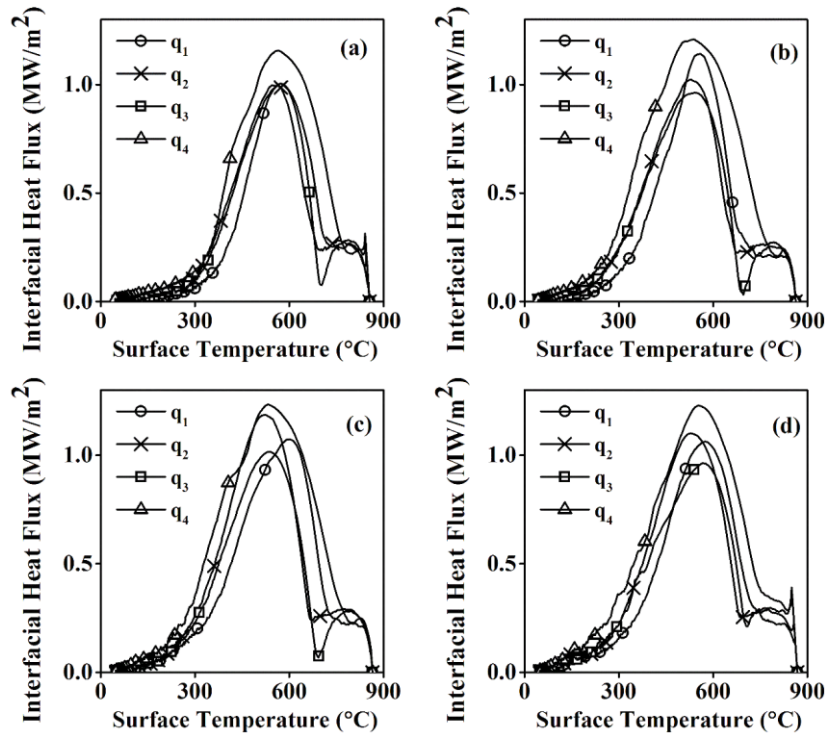


Figure I.13: Spatiotemporal heat flux estimated at the inconel/mineral oil interface at impeller agitation rates of (a) still (b) 500 (c) 1000 and (d) 1500 rpms

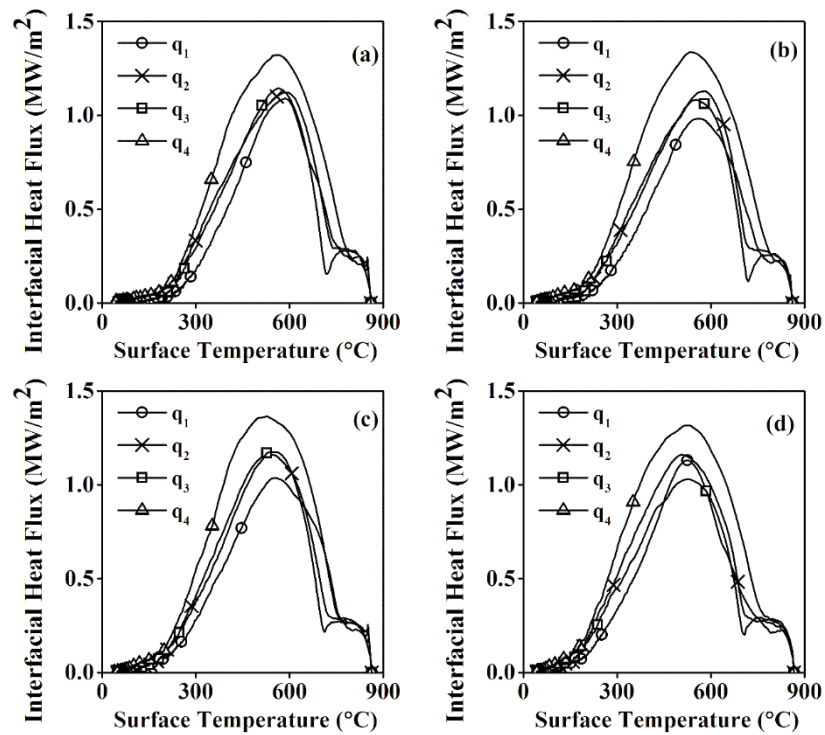
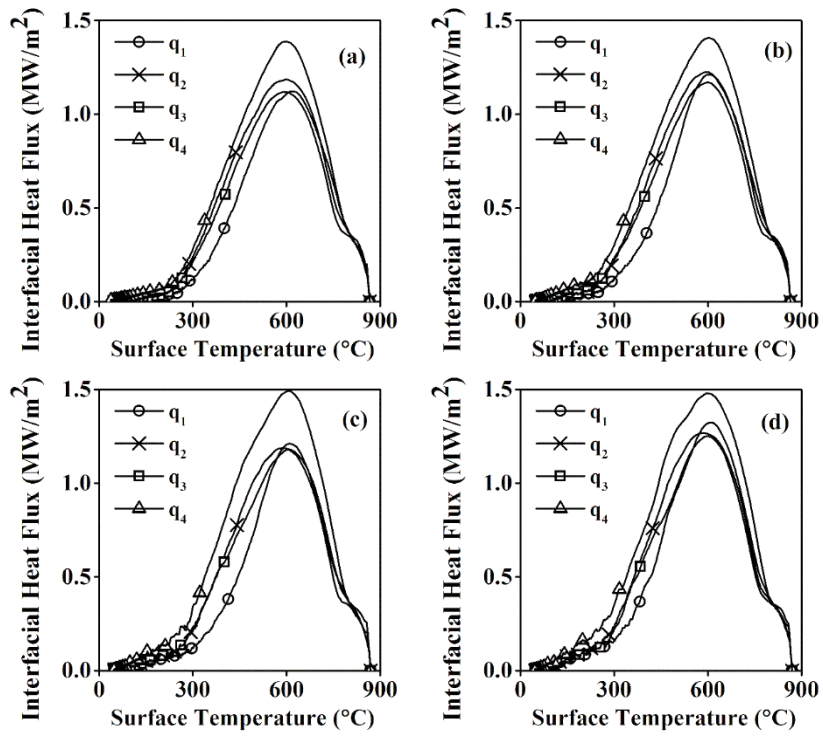
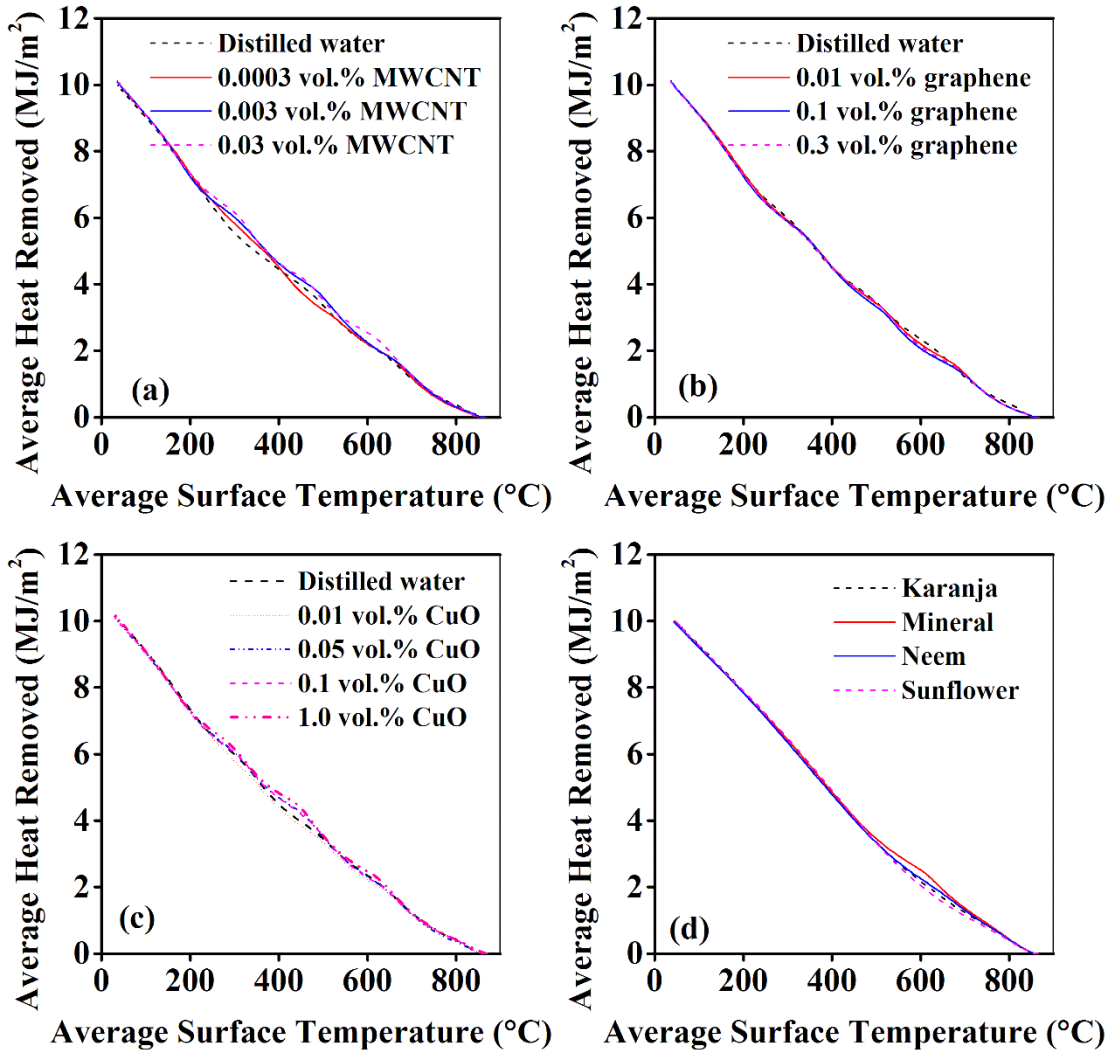


Figure I.14: Spatiotemporal heat flux estimated at the inconel/neem oil interface at impeller agitation rates of (a) still (b) 500 (c) 1000 and (d) 1500 rpms



**Figure I.15: Spatiotemporal heat flux estimated at the inconel/sunflower oil interface at impeller agitation rates of (a) still (b) 500 (c) 1000 and (d) 1500 rpms**

**APPENDIX J: AVERAGE HEAT REMOVED WITH AVERAGE SURFACE TEMPERATURE UNDER AGITATED QUENCH MEDIUM CONDITIONS**



**Figure J.1: Average heat removed as a function of average surface temperature during quenching of the inconel probe in (a) MWCNT (b) graphene (c) CuO nanofluids of various concentrations and (d) oil quenching media under 500 rpm quench condition**



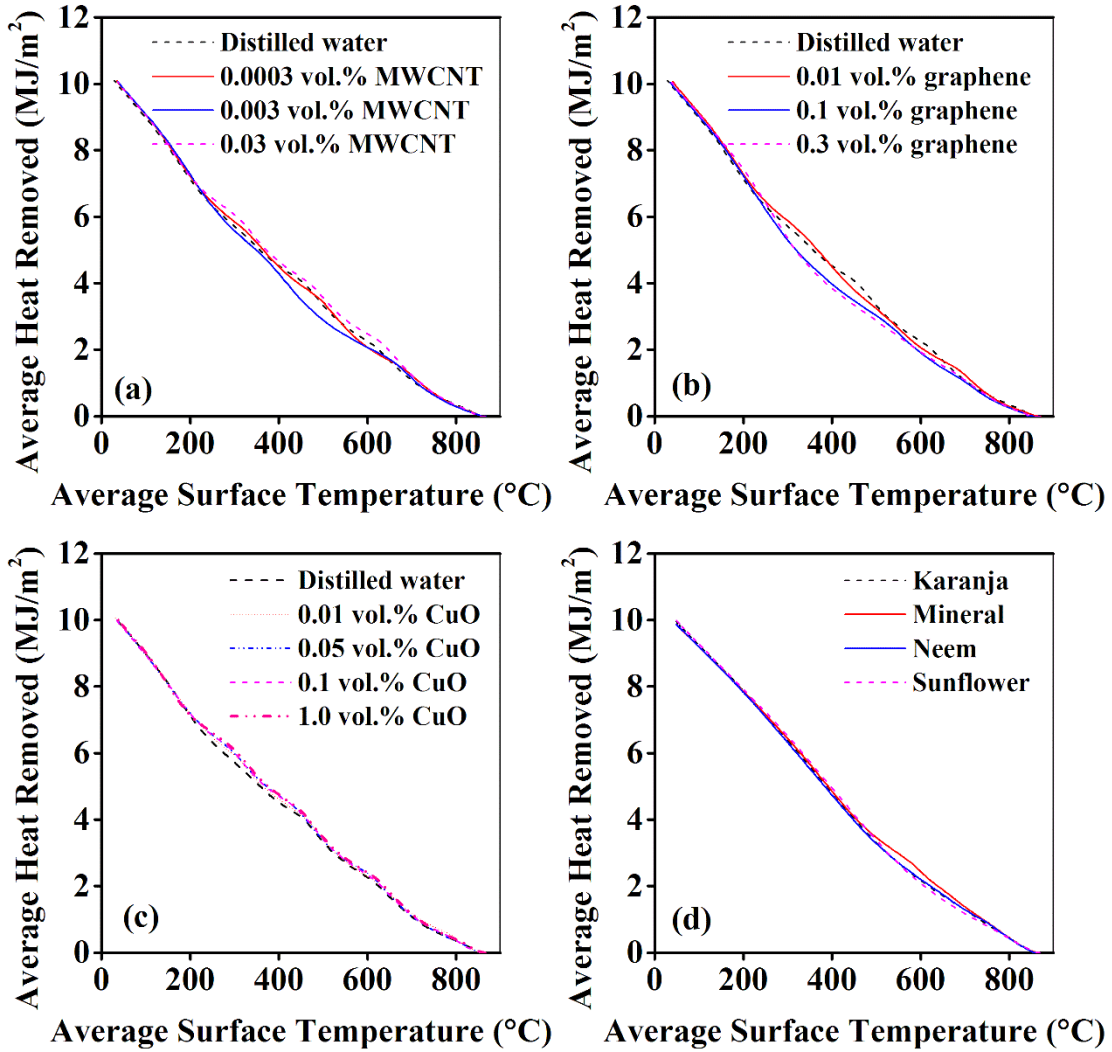


**Figure J.2: Average heat removed as a function of average surface temperature during quenching of the inconel probe in (a) MWCNT (b) graphene (c) CuO nanofluids of various concentrations and (d) oil quenching media under 1000 rpm quench condition**



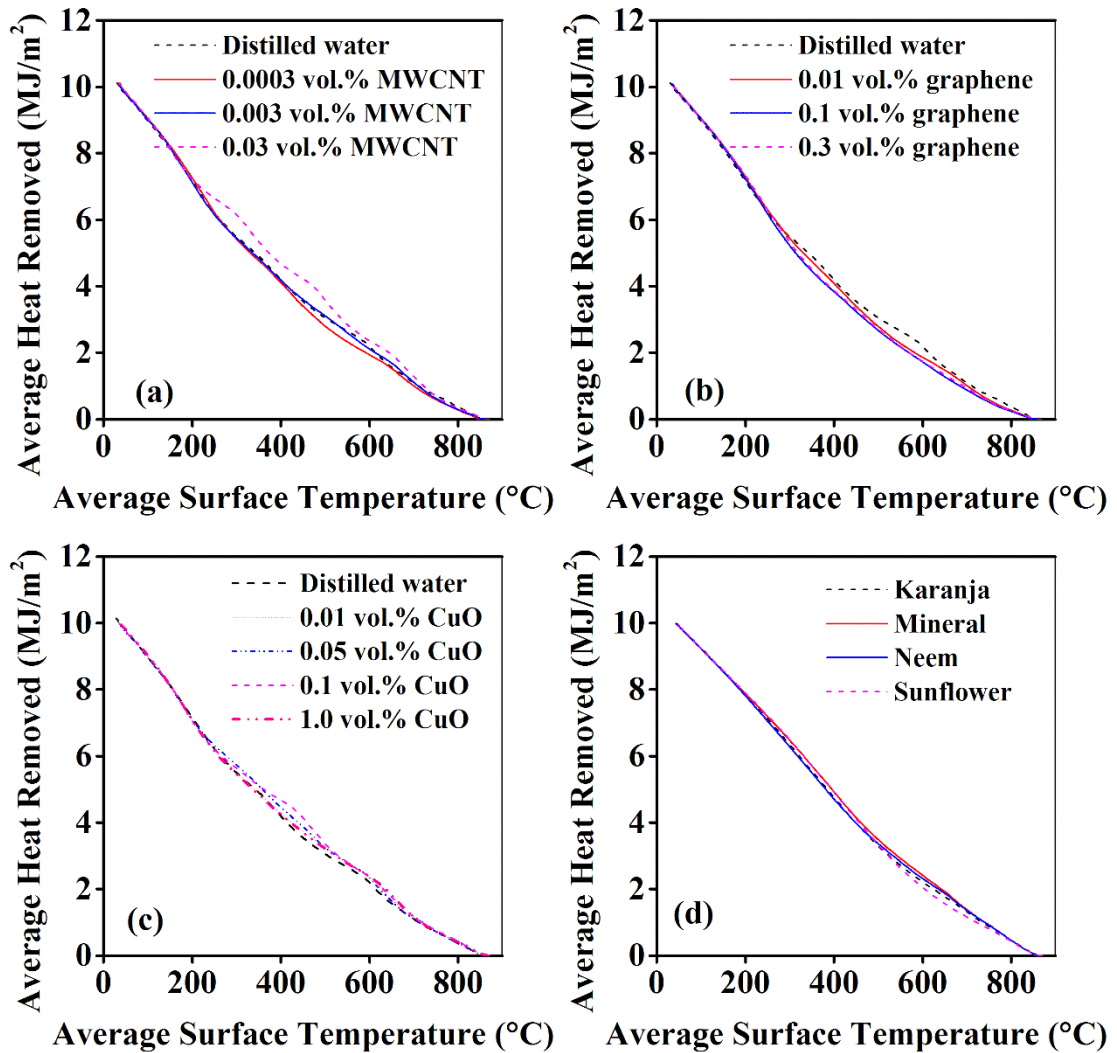


**Figure J.3: Average heat removed as a function of average surface temperature during quenching of the inconel probe in (a) MWCNT (b) graphene (c) CuO nanofluids of various concentrations and (d) oil quenching media under 1500 rpm quench condition**

## LIST OF PUBLICATIONS

### Journal publications

Nayak, U. V., and Prabhu, K. N. (2016). "Heat transfer and quench performance of aqueous CuO nanofluids during immersion quenching." *Int. J. Microstruct. Mater. Prop.*, 11((3/4)), 186–202.

Nayak, V. U., and Prabhu, N. K. (2016). "Wetting behavior and heat transfer characteristics of aqueous graphene nanofluids." *J. Mater. Eng. Perform.*, 25(4), 1474–1480.

Vignesh, N. U., and Narayan P. K., (2015). "Heat transfer during immersion quenching in MWCNT nanofluids." *Mater. Sci. Forum*, 830–831(2015), 172–176.

U. V. Nayak, and K. N. Prabhu, (2018). "Effect of section thickness on heat transfer during quenching in vegetable oil." *Mater. Perform. Charact.*, (In press)

### Conference Proceedings

Vignesh Nayak, U., and Narayan Prabhu, K. (2017). "Comparative study of the effect of section thickness of steel during quenching in neem and mineral oil." *29th Int. Conf. of Heat Treat. Soci.* October 24-26, 2017, Greater Columbus Convention Center Columbus, Ohio, USA. (To be published)

### Conference Presentations

Vignesh Nayak U and Narayan Pabhu K, 'Assessment of heat transfer in MWCNT-water nanofluids for quench heat treatment', Proceedings of the *52nd Nat. Meta. Day including the 68th Ann. Tech. Meet.* on Automotive, Aerospace, Defence and Energy, College of Engineering, Pune, India, 12-15 Nov., 2014.

Vignesh Nayak, U., and Narayan Prabhu, K. (2017). "Heat flux transients for quenching of 50 and 25 mm Stainless steel in mineral and vegetable oils." *Int. Conf. Adv. Mater. Process. ADMAT*, Thiruvananthapuram, Kerala, India, 14-16 Dec., 2017

## **Other publications**

### **Journal publications**

Pai M. A., Vignesh, N. U., Pranesh, R. K. M., and Narayan, P. K. (2015). “Wetting Kinetics and Cooling Performance of PAG Polymer Quenchants.” *Mater. Sci. Forum*, 830–831(2015), 156–159.

Nayak U. V., Rao K. M. P., Pai M. A., and Prabhu K. N. (2016). “Carbonated aqueous media for quench heat treatment of steels.” *J. Mater. Eng. Perform.*, 25(9), 3802–3810.

Nayak, U., Ramesh, G., and Prabhu, K. (2017). “Assessment of spatiotemporal heat flux during quenching in TiO<sub>2</sub> and AlN Nanofluids.” *Mater. Perform. Charact.*, 6(5), 745–756.

### **Book Chapter**

Prabhu, K. N., Nayak U. V., and Rao K. M. P., (2016), Chapter 25: Ploymer Quenchants in “Advances in Polymer Materials and Technology.” CRC press, Boca Raton, USA, A. Srinivasan and S. Bandyopadhyay, eds., 709-740.

## **BIO-DATA**

Name : Vignesh Nayak U  
Date of Birth : 18-08-1988  
Permanent address : Door # 11-1-11/2,  
Opp. Nanadadeep,  
Bhavanthi Street  
Mangalore - 575001  
Email : nayak.vignesh@gmail.com

### **Academic qualification**

- ◆ Bachelor of Engineering (B.E.): Mechanical Engineering; Malnad Engineering College; Hassan ; 2010.
- ◆ Master of Technology (M.Tech.): Process Metallurgy; National Institute of Technology Karnataka; 2012.